Condensed Matter and Interphases

Kondensirovannye sredy i mezhfaznye granitsy

Peer-reviewed scientific journal
Published since January 1999
Periodicity: Quarterly
Volume 27, No. 1, 2025

Full-text version is available in the Russian language on the website: https://journals.vsu.ru/kcmf

Condensed Matter and Interphases (Kondensirovannye Sredy i Mezhfaznye Granitsy) publishes articles in Russian and English dedicated to key issues of condensed matter and physicochemical processes at interfaces and in volumes.

The mission of the journal is to provide open access to the results of original research (theoretical and experimental) at the intersection of contemporary condensed matter physics and chemistry, material science and nanoindustry, solid state chemistry, inorganic chemistry, and physical chemistry, and to share scientific data in the **following sections**: atomic, electron, and cluster structure of solids, liquids, and interphase boundaries; phase equilibria and defect formation processes; structure and physical and chemical properties of interphases; laser thermochemistry and photostimulated processes on solid surfaces; physics and chemistry of surface, thin films and heterostructures; kinetics and mechanism of formation of film structures; electrophysical processes in interphase boundaries; chemistry of surface phenomena in sorbents; devices and new research methods.

The journal accepts for publication: reviews, original articles, short communications by leading Russian scientists, foreign researchers, lecturers, postgraduate and undergraduate students.

FOUNDER AND PUBLISHER:
Voronezh State University

The journal is registered by the Russian Federal Service for Supervision of Communications, Information Technology and Mass Media, Certificate of Registration ПИ № ФС77-78771 date 20.07.2020

The journal is included in the List of peer reviewed scientific journals published by the Higher Attestation Commission in which major research results from the dissertations of Candidates of Sciences (PhD) and Doctor of Science (DSc) degrees are to be published. Scientific specialties of dissertations and their respective branches of science are as follows: 1.4.1. – Inorganic Chemistry (Chemical sciences); 1.4.4. – Physical Chemistry (Chemical sciences); 1.4.6. – Electrochemistry (Chemical sciences); 1.4.15. – Solid State Chemistry (Chemical sciences); 1.3.8. – Condensed Matter Physics (Physical sciences).

The journal is indexed and archived in: Russian Scientific Index Citations, Scopus, Chemical Abstract, EBSCO, DOAJ, CrossRef

Editorial Board and Publisher Office:
1 Universitetskaya pl., Voronezh 394018
Phone: +7 (432) 2208445
https://journals.vsu.ru/kcmf
E-mail: kcmf@main.vsu.ru

When reprinting the materials, a reference to the Condensed Matter and Interphases must be cited

The journal's materials are available under the Creative Commons "Attribution" 4.0 Global License

© Voronezh State University, 2025

EDITOR-IN-CHIEF:
Victor N. Semenov, Dr. Sci. (Chem.), Full Professor, Voronezh State University (Voronezh, Russian Federation)

VICE EDITORS-IN-CHIEF:
Evelina P. Domashevskaya, Dr. Sci. (Phys.–Math.), Full Professor, Voronezh State University (Voronezh, Russian Federation)
Polina M.Volovitch, Ph.D. (Chem.), Associate Professor, Institut de Recherche de Chimie (Paris, France)

EDITORIAL BOARD:
Nikolay N. Afonin, Dr. Sci. (Chem.), Voronezh State Pedagogical University (Voronezh, Russian Federation)
Vera I. Vasil'eva, Dr. Sci. (Chem.), Full Professor, Voronezh State University (Voronezh, Russian Federation)
Aleksandr V. Vvedenskii, Dr. Sci. (Chem.), Full Professor, Voronezh State University (Voronezh, Russian Federation)
Victor V. Gusarov, Dr. Sci. (Chem.), Associate Member of the RAS, Ioffe Physical-Technical Institute RAS (St. Petersburg, Russian Federation)
Vladimir E. Guterman, Dr. Sci. (Chem.), Full Professor, Southern Federal University (Rostov-on-Don, Russian Federation)
Boris M. Darinskii, Dr. Sci. (Phys.–Math.), Full Professor, Voronezh State University (Voronezh, Russian Federation)
Vladimir P. Zlomanov, Dr. Sci. (Chem.), Full Professor, Moscow State University (Moscow, Russian Federation)
Valentin M. Ievlev, Dr. Sci. (Phys.–Math.), Full Member of the RAS, Moscow State University (Moscow, Russian Federation)
Oleg A. Kozaderov, Dr. Sci. (Chem.), Associate Professor, Voronezh State University (Voronezh, Russian Federation)
Andrey I. Marshakov, Dr. Sci. (Chem.), Full Professor, Frumkin Institute of Physical Chemistry and Electrochemistry RAS (Moscow, Russian Federation)
Irina Ya. Mittova, Dr. Sci. (Chem.), Full Professor, Voronezh State University (Voronezh, Russian Federation)
Victor V. Nikonenko, Dr. Sci. (Chem.), Full Professor, Kuban State University (Krasnodar, Russian Federation)
Oleg V. Ovchinnikov, Dr. Sci. (Phys.–Math.), Full Professor, Voronezh State University (Voronezh, Russian Federation)
Sergey N. Saltykov, Dr. Sci. (Chem.), Associate Professor, Novolipetsk Steel (Lipetsk, Russian Federation)
Vladimir F. Selemenev, Dr. Sci. (Chem.), Full Professor, Voronezh State University (Voronezh, Russian Federation)
Pavel V. Seredin, Dr. Sci. (Phys.-Math.), Associate Professor, Voronezh State University (Voronezh, Russian Federation)
Evgeny A. Tutov, Dr. Sci. (Chem.), Associate Professor, Voronezh State Technical University (Voronezh, Russian Federation)
Pavel P. Fedorov, Dr. Sci. (Chem.), Full Professor, Prokhorov General Physics Institute RAS (Moscow, Russian Federation)
Vitaly A. Khonik, Dr. Sci. (Phys.–Math.), Full Professor, Voronezh State Pedagogical University (Voronezh, Russian Federation)
Andrey B. Yaroslavtsev, Dr. Sci. (Chem.), Full Member of the RAS, Kurnakov Institute of General and Inorganic Chemistry RAS (Moscow, Russian Federation)

INTERNATIONAL MEMBERS OF THE EDITORIAL BOARD:
Mahammad Babanly, Dr. Sci. (Chem.), Associate Member of the ANAS, Institute of Catalysis and Inorganic Chemistry ANAS (Baku, Azerbaijan)
Tiziano Bellezze, Dr. Sci. (Chem.), Marche Polytechnic University (Ancona, Italy)
Mane Rahul Maruti, Ph.D. (Chem.), Shivaji University (Kolhapur, India)
Nguyen Anh Tien, Ph.D. (Chem.), Associate Professor, University of Pedagogy (Ho Chi Minh City, Vietnam)
Vladimir V. Pankov, Dr. Sci. (Chem.), Full Professor, Belarusian State University (Minsk, Belarus)
Fritz Scholz, Dr. Sci., Professor, Institut für Biochemie Analytische Chemie und Umweltchemie (Greifswald, Germany)
Mathias S. Wickleder, Dr. Sci., Professor, University of Cologne (Koln, Germany)
Vladimir Sivakov, Dr. rer. nat., Leibniz Institute of Photonic Technology (Jena, Germany)

EXECUTIVE SECRETARY:
Vera A. Logacheva, Cand. Sci. (Chem.), Voronezh State University (Voronezh, Russian Federation)

CONTENTS

Special issue of the journal “Condensed Matter and Interphases”: “Physicochemical Analysis in Materials Science” (continued)

Review

Bulanov A. D., Gavva V. A., Troshin O. Yu.
Features of synthesis and properties of new materials based on monoisotopic silicon and germanium. Review 3

Velmuzhov A. P., Sukhanov M. V., Tyurina E. A., Shiryaev V. S.
Advanced methods for preparing especially pure glasses based on germanium and gallium chalcogenides. Part 1. Synthesis via volatile and low-melting compounds. Review 16

Zavraznov A. Yu., Brezhnev N. Yu., Nekrylov I. N., Kosyakov A. V.
Phases with layered (AB) and “defective” (A_2B_3) structures in A^{III}–B^{VI} systems. Part 2. Phase diagrams and approaches to some problems of reproducible synthesis in A^{III}– B^{VI} systems. Review 29

Original articles

Aghayeva A. R., Mammadova S. H., Babanly D. M., Jafarov Ya. I., Tagiyev D. B.
Thermodynamic study of zinc antimonides by the electromotive force measurements 48

Mammadov F. M., Imamaliyeva S. Z., Ismailova E. N., Amiraslanov I. R., Akhmedov E. I., Babanly M. B.
Refinement of the phase diagram of the MnSe–In_2Se_3 system and the crystal structures of $MnIn_2Se_4$ and $Mn_2In_2Se_5$ compounds 57

Charykov N. A., Rumyantsev A. V., Keskinov V. A., Semenov K. N., German V. P., Kulenova N. A., Charykova M. V., Keskinova M. V., Arshinov M. Yu.
A universal algorithm for the calculation of vapor-liquid equilibrium diagrams in quasi-simple multicomponent systems 67

Articles of issue 1
Original articles

Vasilkova E. I., Pirogov E. V., Nevedomsky V. N., Barantsev O. V., Voropaev K. O., Vasiliev A. A., Karachinsky L. Ya., Novikov I. I., Sobolev M. S.
Analysis of the crystalline quality of bulk $In_{0.83}Ga(Al)_{0.17}$ layers formed on metamorphic InAlAs/InP buffer layers with linear and nonlinearcomposition gradients 86

Vakhtel V. M., Velichkov A. I., Karaivanov D. V., Milanova M. M., Segal Yu. G., Temerbulatova N. T., Filosofov D. V., Tsvetkov M. P.
Study of hyperfine interactions in spinel cobalt ferrite $CoFe_2O_4$ doped with Hf, Lu, and Yb using Mössbauer spectroscopy and perturbed γ-γ angular correlation 96

Markelova M. N., Hafizov A. A., Shi Xiaoyu, Graboy I. E., Shanin M. S., Konnikova M. R., Shkurinov A. P., Kaul A.R.
Chemical vapor deposition of $Tm_3Fe_5O_{12}$ epitaxial films, investigation of their structure and properties in the terahertz range 104

Petukhov I. V., Medvedeva N. A.
Topography and microrelief electroless Ni-P coatings at different loading densities 115

Petukhova E. A., Ershova V. S., Terentyev A. V., Ruban E. A., Pichugov R. D., Konev D. V., Usenko A. A.
Coulometric analysis method for determining the concentration and degree of oxidation of vanadium in the electrolyte of a vanadium flow battery using a hydrogen vanadium cell 128

Yushchenko E. V., Belchinskaya L. I., Kostyuchenko A. V., Zhukalin D. A.
The role of nanofillers of various nature in the morphological changes of the polymer binder for plywood production 139

Manyakin M. D., Kurganskii S. I., Kakuliia I. S., Titova S. S., Chuvenkova O. A., Turishchev S. Yu.
Theoretical and experimental study of the niobium dioxide electronic structure 146

Short communication

Ermolov Y. M., Vasilchenko A. A., Mischinenko V. B.
Monte Carlo simulation of interfacial adhesion between geopolymer binders and mineral aggregates 154

Guide for Authors – 2025 160

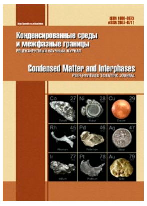

ISSN 1606-867X (Print)
ISSN 2687-0711 (Online)
Condensed Matter and Interphases
Kondensirovannye Sredy i Mezhfaznye Granitsy
https://journals.vsu.ru/kcmf/

Special issue of the journal "Condensed Matter and Interphases":
"Physicochemical Analysis in Materials Science"
(continued)

Review

Review article
https://doi.org/10.17308/kcmf.2025.27/12483

Features of synthesis and properties of new materials based on monoisotopic silicon and germanium. Review

A. D. Bulanov[1], V. A. Gavva[1], O. Yu. Troshin[1]✉

[1]*G. G. Devyatykh Institute of Chemistry of High-Purity Substances, Russian Academy of Sciences,*
49 Tropinina st., Nizhny Novgorod 603951 Russian Federation

Abstract

This paper reviews scientific works on the preparation and properties of isotopically enriched silicon and germanium, along with their compounds. It covers the technological aspects and peculiarities of synthetic methods with the deep purification processes for obtaining isotopically enriched silicon and germanium compounds. The review also discusses the production of polycrystalline and single-crystal samples with varying degrees of isotopic and chemical purity. The results of a study investigating the physicochemical characteristics of both simple and complex substances derived from isotopically enriched silicon and germanium are presented. These studies indicate that the isotopic composition of silicon and germanium significantly affects heat capacity, thermal conductivity, and light absorption processes. Finally, the paper explores current applications of substances and materials based on isotopically enriched silicon and germanium.

Keywords: Silicon, Germanium, Isotopes, Hydrides, Materials

Funding: The study was supported by the Ministry of Science and Education of the Russian Federation within the framework of the government order, FFSR-2022-0003.

For citation: Bulanov A. D., Gavva V. A., Troshin O. Yu. Features of synthesis and properties of new materials based on monoisotopic silicon and germanium. Review. *Condensed Matter and Interphases*. 2025;27(1): 3–15. https://doi.org/10.17308/kcmf.2025.27/12483

Для цитирования: Буланов А. Д., Гавва В. А., Трошин О. Ю. Особенности синтеза и свойства новых материалов на основе моноизотопных кремния и германия. Обзор. *Конденсированные среды и межфазные границы*. 2025;27(1): 3–15. https://doi.org/10.17308/kcmf.2025.27/12483

✉ Oleg Yu. Troshin, e-mail: troshin@ihps-nnov.ru

© Bulanov A. D., Gavva V. A., Troshin O. Yu., 2025

The content is available under Creative Commons Attribution 4.0 License.

Conventionally, the characteristics that determine the set of physical and chemical properties of substances and materials include morphology, the level of chemical purity, and structural perfection. However, as a rule, the presence of several isotopes in the natural composition of most chemical elements is often ignored. Yet, these isotopes can be considered as a combination of the main and impurity isotopes of the chemical element [1, 2].

Differences in the properties of isotopically modified substances (the so-called isotopic effect) are due to the difference in the molar masses of isotopes. What is more, they are more noticeable in the chemical elements in periods 1–2 of the Mendeleev periodic table [3]. A detailed study and expansion of the database of properties of individual isotopes of chemical elements in the form of simple substances and compounds is important for fundamental and applied science. This information is relevant for predicting the properties and for the manufacturing of isotopic compositions, i.e. mixtures with desired properties, as part of isotopic engineering [4].

In the case of chemical elements with a relatively small difference in the mass numbers of isotopes, it is necessary to obtain corresponding substances with high chemical purity and structural perfection which will allow a definitive determination of the isotopic effects. High-tech semiconductor materials, monocrystalline silicon and germanium, are the most convenient for the study of isotopic effects. They are currently considered as the most advanced materials in terms of structural perfection and chemical purity.

Silicon is represented in nature by three stable isotopes: ^{28}Si (92.230%), ^{29}Si (4.683%), and ^{30}Si (3.087%). Among the radioactive isotopes of silicon, ^{32}Si ($T_{1/2}$ ~ 150 years) is the longest-lasting [3]. Germanium consists of four stable isotopes, ^{70}Ge (20.84%), ^{72}Ge (27.54%), ^{73}Ge (7.73%), ^{74}Ge (36.28%), and ^{76}Ge (7.61%), with a half-life of about $2{\cdot}10^{21}$ years [3]. Gas ultracentrifugation of volatile fluorides is mainly used to separate the isotopes of these chemical elements [5–7]; monogermane is also used in the separation of germanium isotopes [8, 9].

The first works dedicated to the production and properties of monoisotopic silicon and germanium were published in the 1990s. In paper [10] the Czochralski technique with a natural silicon seed was used to produce a single crystal of silicon-28 with a weight of about 300 g and an isotope content of ^{28}Si at 99 mol %. This single crystal was used to measure the parameter of the silicon-28 lattice and to determine the Avogadro's number. The initial silicon-28 was obtained by aluminum reduction of silicon dioxide-28 with a 99.88% silicon-28 enrichment. The content of oxygen, carbon, and boron impurities in silicon-28 was 10^{16} - 10^{18} atoms/cm^3. The authors of [11] obtained a single crystal of silicon-28 with a diameter of 4 mm and a length of 50 mm and a 99.924 at. % isotope content of ^{28}Si. The silicon powder obtained by the aluminum reduction of silicon oxide-28 was compressed, sintered, and zone-melted. The resulting sample had a *p*-type conductivity and contained an aluminum impurity at $1{\cdot}10^{-3}$ at. %. According to the authors, isotopically enriched silicon was a promising material for the development of a quantum computer.

In [12], the liquid-phase epitaxy was used to obtain a film of silicon-28 with a 99.7% enrichment and a thickness of 11.7 microns from the indium melt. The film was produced on a natural silicon substrate, on which an aluminum layer with a thickness of about 1000 Å was sprayed. After measuring the thermal conductivity of the sample, it was found that the thermal conductivity of isotopically enriched ^{28}Si at 298 K was about 60% higher than that of silicon with a natural isotopic composition. However, as a result of interlaboratory measurements using the technique of stationary heat flux, it was found that the difference in the thermal conductivity of isotopically enriched ^{28}Si and natural silicon did not exceed 10±2% [13]. The significant discrepancy in the value of the thermal conductivity of silicon-28 obtained in [12] could be due to the contamination of the sample.

The researchers also obtained isotopically enriched samples of ^{29}Si and ^{30}Si in the form of single crystals [5,14] and epitaxial films [15] with the degree of enrichment in the main isotope of silicon that did not exceed 99.9%. In [5], polycrystalline silicon-29 and silicon-30 were produced by the thermal decomposition of monosilane which had been obtained by the reaction between silicon tetrafluoride ($^{29}SiF_4$,

$^{30}SiF_4$) and calcium hydride. Monoisotopic silicon was deposited on a molybdenum wire, resulting in granules with a size of 0.3 – 0.5 mm. To minimize isotopic dilution at the stage of growing single crystals by the Czochralski technique, small-volume crucibles with a coating of $^{29}SiO_2$ or $^{30}SiO_2$ with a thickness of 100-150 microns were used. The content of the main isotope of silicon in the obtained ^{29}Si and ^{30}Si single crystals was 99.225±0.023 at. % and 99.742±0.015 at. %; in the initial $^{29}SiF_4$ and $^{30}SiF_4$, the content of ^{29}Si, ^{30}Si in the composition of silicon was 99.576±0.105 at. % and 99.829 ± 0.060 at. %. In [14], silicon-29 was precipitated on a graphite substrate, after the removal of which the resulting silicon-29 was melted into a rod. A natural silicon seed was used to produce a single crystal of silicon-29.

The authors of [16] measured the temperature dependence of the thermal conductivity of a single crystal of isotopically enriched silicon-29 (99.919%) in the range of 2.4 - 410 K. It was found that at low temperatures ($T < 6$ K) in the mode of boundary phonone scattering, the thermal conductivity of the ^{29}Si crystal was higher than that of the ^{28}Si crystal (99.983%). In the high temperature region, where thermal conductivity is determined by anharmonic processes of phonon scattering, the value of thermal conductivity of ^{29}Si was lower than that of ^{28}Si.

To obtain significant quantities of silicon-28, as well as samples of silicon-29 and silicon-30, the Institute of Chemistry of High Purity Substances of the Russian Academy of Sciences developed a laboratory technology for the synthesis, deep purification, and thermal decomposition of monosilane for the production of polycrystalline silicon-28 [1,2]. Further studies aimed at obtaining and improving the isotopic and chemical purity were triggered by using monoisotopic silicon-28 to determine the Avogadro's number and creating a physically justified kilogram standard within the framework of the *Avogadro* and *Kilogram* projects [6, 7, 10, 17, 18]. Silicon tetrafluoride SiF_4 was used as the starting material. It was enriched by gas ultracentrifugation (ZAO *Tsentrotekh-SPb*, AO *Production Association "Electrochemical Plant"*) to the content of silicon-28 of over 99.99% [7]. The content of molecular impurities in samples of isotopically enriched $^{28}SiF_4$ according to high-resolution Fourier IR spectroscopy [19] and gas chromatography [20] was: Si_2F_6O – $2\cdot10^{-1}$ mol %; CO_2 – $1\cdot10^{-2}$ mol %; H_2O – $6\cdot10^{-3}$ mol %; HF – $3\cdot10^{-4}$ mol %; hydrocarbons C_1-C_4 (methane, ethane, ethylene, propane, butane) – $n\cdot10^{-3}$–$n\cdot10^{-5}$ mol % [21]. The content of metal impurities in isotopically enriched silicon tetrafluoride, determined by the atomic emission with matrix distillation for the concentration of non-volatile impurities, was at $n\cdot10^{-7}$ wt. % [22, 23]. The content of silicon isotopes in the composition of silicon tetrafluoride, as well as monosilane and crystalline silicon, was determined by mass spectrometry [24].

$^{28}SiH_4$ was synthesized by the reaction of $^{28}SiF_4$ with ground calcium hydride in a hydrogen flow reactor. Calcium hydride was synthesized from distilled calcium and hydrogen [25] and ground before the synthesis *(in situ)*; calcium hydride was ground to a particle size of less than 1 mm and was loaded into the monosilane synthesis reactor in boxes with an inert nitrogen atmosphere. This ensured a low content of oxygen-containing impurities in calcium hydride, which are formed upon contact with atmospheric moisture, and a high isolated yield of monosilane. The productivity of the laboratory synthesis was 3 kg of $^{28}SiH_4$ per month. However, this technique for monosilane synthesis has a disadvantage, i.e. the low degree of conversion of the solid-phase reagent, CaH_2, which does not exceed 15% [26]. Therefore, it is important to increase the degree of conversion of calcium hydride. One of the solutions can be to carry out the conversion process at an elevated pressure [27] or to use mechanical activation, i.e. grinding the solid-phase reagent in the process of producing monosilane in a rotating flow reactor [28].

The isolated yield of $^{28}SiH_4$ over $^{28}SiF_4$ was 92–96%. According to [26], the obtained monosilane contains impurities of hydrocarbons, siloxanes, and polysilanes at $n\cdot10^{-3}$ – $n\cdot10^{-5}$ mol %. One of the sources of hydrocarbon impurities in monosilane is the hydrogenation of impurity carbon in calcium during the contact of calcium hydride with hydrogen at an elevated temperature [21]. Preliminary purging of the reactor with calcium hydride with high-purity hydrogen at 200 °C allows reducing the content of unsaturated hydrocarbons in the resulting silane and disiloxane impurities by about an order of magnitude [29].

A combination of cryofiltration and low-temperature rectification was used for deep purification of isotopically enriched monosilane [30]. Cryofiltration on a Petryanov filter at a temperature of about 165 K allowed separating the higher-boiling impurities of siloxanes and higher silanes (disilane, trisilane). Rectification was carried out in metal rectification columns with a middle feeding tank in the mode of discrete choice of impurities from the lower and upper sections filled with a nichrome wire spiral-prismatic nozzle [29]. The yield of the high-purity product at the purification stages was 80–90%. The content of chemical impurities in samples of high-purity monosilane was: alkylsilanes at $n\cdot10^{-6}$ mol %, hydrocarbons C_1-C_9 at $n\cdot10^{-5}$ mol %, disiloxane at 10^{-3} mol %, and higher silanes at $n\cdot10^{-2}$ mol %.

Monoisotopic polycrystalline silicon (^{28}Si, ^{29}Si, ^{30}Si) was obtained by the pyrolysis of high-purity isotopically enriched monosilane in SAA-20 and SAA-800 monosilane decomposition plants (Steremat Electrowarme), which differed in the maximum amount of obtained material (150 g and 6 kg, respectively). In the absence of rods from isotopically enriched material and due to the restrictions regarding the usage of silicon rods of natural isotopic composition to avoid isotopic dilution, monoisotopic silicon was deposited on molybdenum substrates. This involved obtaining silicon polycrystals, which were connected into a tape by means of contactless high-frequency welding. The resulting tape was used as a substrate for silicon precipitation [31]. Thin walled stainless steel tubes (12X18H10T) can also be used as a substrate for precipitation. After precipitation, the substrate material dissolved in hydrochloric acid and the resulting silicon tube was melted into a rod of the specified diameter by crucibleless melting. This technique is simpler and reduces the cost for the production of seed rods, which is especially important when obtaining samples of monoisotopic silicon of various nature and variable isotopic composition.

The manufacture of monocrystalline silicon samples involved using crucibleless melting and the Czochralski technique. To avoid isotopic dilution when using the Czochralski technique with quartz crucibles, special techniques were developed for applying protective coatings from isotopically enriched silicon dioxide by oxidizing monosilane $^{28}SiH_4$ [32].

One of the results of the *Avogadro* international project was the production of two spheres of monocrystalline silicon-28 with a diameter of 96.3 mm and a mass of 1 kg. Measuring its volume, density, atomic lattice constant, and molar mass allowed obtaining the Avogadro constant, $N_A = 6.022\ 14082(18)\cdot10^{23}$ mol^{-1} with a relative error of $2\cdot10^{-8}$ [7].

The properties of isotopically enriched silicon samples are presented in [13,16,33–41] and generalized in [2]. The difference in the properties of samples of monoisotopic silicon and silicon of the natural isotopic composition is associated with a different value of the average atomic mass and with an uneven distribution of isotopes in the sample. A number of properties dependent on spin interactions (nuclear magnetic resonance spectra, electron paramagnetic resonance, and the parameters of spin-spin and spin-lattice interactions) are affected by the concentration of silicon-29 with a non-zero nuclear spin. Table 1 shows the properties of monocrystalline samples of ^{28}Si, ^{29}Si, and ^{30}Si and pure silicon of the natural isotopic composition ^{nat}Si [2].

Samples of isotopically enriched germanium were obtained using a hydride technology [42]. Unlike the production of silicon isotopes, germanium did not require converting the working gas into volatile hydride for ultracentrifugation. Monogermane was used to separate germanium isotopes [8]. The technique for obtaining high-purity germanium isotopes included the stages of low-temperature rectification and thermal decomposition of monogermane and additional purification of germanium by zone melting [9]. Rectification purification of monogermanes was carried out on a metal column with a middle cube, equipped with an automated refrigerant supply system and a gas chromatograph for operational control of the impurity composition of the fractions. The weight of the monogermane loaded into the column was about 250 g, the duration of purification was about 40 hours, the isolated yield of the rectified product was 75–80%. The content of molecular impurities (C_1-C_9 hydrocarbons and their halogen derivatives, alkyl and halogen germanes, etc.) in purified monogermane samples according to chromatography-mass spectrometry [43] was at $n\cdot10^{-5}$ – $n\cdot10^{-6}$ mol %.

Table 1. Properties of samples of ^{28}Si, ^{29}Si, ^{30}Si and high-purity silicon of natural isotopic composition ^{nat}Si [2]

Property	Sample				The content of the main isotope, %
	^{28}Si	^{29}Si	^{30}Si	^{nat}Si	
Density at 20 °C, g·cm^{-3}	2.320071	–	-	2.329045	^{28}Si – 99.99
Debye temperature, K	641	627	616	638	^{28}Si – 99.98 ^{29}Si – 99.0 ^{30}Si – 99.0
Heat capacity at 100 K, J·mol^{-1}·K^{-1}	7.24	7.40	7.61	7.24	^{28}Si – 99,98 ^{29}Si – 99,0 ^{30}Si – 99,0
Thermal conductivity at 25 K, W·cm^{1}·K^{1}	288	214	–	45.6	^{28}Si – 99.98 ^{29}Si – 99.92
Raman shift at 20 °C, cm^{-1}	521.4	512.3	503.9	520.8	^{28}Si – 99.993 ^{29}Si – 99.92 ^{30}Si – 99.97
Refractive index at 293 K, λ=1.5 microns	3.48207	3.48171	3.48112	3.48191	^{28}Si – 99.993 ^{29}Si – 99.92 ^{30}Si – 99.97

Thermal decomposition of monogermane was performed at a temperature of 500 °C in a quartz tube with a pyrocarbon coating. As a result of the monogermane decomposition, polycrystalline and powdered germanium was formed in the reactor, which was then melted into an ingot; the isolated yield of germanium was about 95%. Additional purification of monoisotopic germanium was carried out by zone melting in quartz boats coated with amorphous silicon dioxide in the pure hydrogen atmosphere. Germanium single crystals were grown by the Bridgman technique and the Czochralski technique [2, 5–7].

When crystals of isotopically enriched germanium are grown by the Czochralski technique, there is a problem associated with the lack of oriented isotopically enriched monocrystalline seeds. Growing single crystals of isotopically enriched germanium using a germanium seed of a natural isotopic composition leads to isotopic dilution, which can reach $n\cdot10^{-1}$%. To reduce the isotopic dilution of germanium, crystals were grown stage by stage: the first stage involved growing in a quartz crucible a single crystal with a diameter of 5 mm and a length of 50 mm on a seed from germanium of a natural isotopic composition using a small amount of melt of isotopically enriched germanium. This single crystal was then used as a seed for growing a single crystal of isotopically enriched germanium. It is also possible to use a seed from previously obtained isotopically enriched germanium to minimize a certain germanium isotope. For example, when obtaining a single crystal of germanium-70, germanium-74 was used as a seed [42].

The isotopic composition of germanium in samples of isotopically enriched monogermane and germanium was determined by mass spectrometry [44]. To date, the Institute of Chemistry of High Purity Substances of the Russian Academy of Sciences have obtained and described all stable isotopes of germanium with a content of the main substance of over 99% [42, 45]. Table 2 shows the isotopic composition of germanium in high-purity monogermanes and isotopically enriched germanium [2, 42].

Some properties of the samples of isotopically enriched germanium and its hydrides were studied in [46–53].

In [46], differential scanning calorimetry was used to determine the melting point for the samples of germanium isotopes ^{72}Ge, ^{73}Ge, ^{74}Ge, and ^{76}Ge with the content of the main isotope of 99.98439%, 99.8995%, 99.9365%, and 88.21%, respectively. It was established that the melting point of samples of isotopically enriched germanium decreased with an increase in the atomic mass of the isotope. The change was 0.15 K per unit of atomic mass, which is

Table 2. The content of germanium isotopes in the composition of the obtained samples of high-purity monogermans and isotopically enriched germanium

Sub-stance	The content of the germanium isotope, at. %				
	^{70}Ge	^{72}Ge	^{73}Ge	^{74}Ge	^{76}Ge
^{70}GeH$_4$	99.99303±0.00012	0.00678±0.00009	0.00005±0.00003	0.00012±0.00005	<0.00001
^{70}Ge	99.99329±0.00006	0.00669±0.00005	0.00002±0.00001	0.00001	0.00001
^{72}GeH$_4$	0.005±0.001	99.953±0.008	0.018±0.003	0.023±0.006	0.002±0.001
^{72}Ge	0.00009±0.00002	99.98439±0.00091	0.01191±0.00073	0.00356±0.00030	0.00005±0.00001
^{73}GeH$_4$	0.0012±0.0005	0.0415±0.0080	99.8942±0.0100	0.0626±0.0100	0.0005±0.0003
^{73}Ge	0.0001±0.0001	0.0391±0.0027	99.8995±0.0155	0.0611±0.0102	0.0002±0.0001
^{74}GeH$_4$	0.0007±0.0003	0.0017±0.0004	0.059±0.003	99.9377±0.0031	0.0033±0.0006
^{74}Ge	0.0001±0.0001	0.0009±0.0004	0.0595±0.0010	99.9365±0.0011	0.0030±0.0003
^{76}GeH$_4$	0.12±0.01	0.17±0.01	0.07±0.01	11.50±0.50	88.14±0.55
^{76}Ge	0.060±0.009	0.090±0.009	0.051±0.009	11.592±0.192	88.207±0.188

qualitatively consistent with the value calculated by the Lindemann’s formula, taking into account the effect of “isotopic compression” of the unit cell. The dependence of the melting point T_m(°C) on the average atomic mass M can be described by the equation $T_m = 949.3 - 0.153 \cdot M$.

In [47], differential scanning calorimetry was used to remeasure the melting point of the samples studied in [46] ^{72}Ge, ^{73}Ge, ^{74}Ge, and ^{76}Ge and to measure the melting point of the sample of germanium-70 with a content of the main isotope of 99.99329%. The melting point for samples ^{70}Ge, ^{72}Ge, ^{73}Ge, ^{74}Ge, and ^{76}Ge was 1,212.0 K, 1,211.6 K, 1,211.3 K, 1,211.1 K, and 1,210.8 K, respectively.

The temperature dependence of the thermal conductivity of single crystals of isotopically enriched germanium ^{70}Ge (degree of enrichment 99.926%), ^{72}Ge (99.980%), ^{74}Ge (99.921%) in the temperature range of 80–310 K was measured in [48]. In the studied temperature range, the thermal conductivity of germanium was determined by anharmonic processes of phonon scattering. A decrease in the value of thermal conductivity was also experimentally observed with an increase in the mass of the germanium isotope.

Optical spectroscopy was used to study the optical transmission of the germanium isotopes ^{70}Ge, ^{72}Ge, ^{73}Ge, ^{74}Ge, and ^{76}Ge in the terahertz spectral range of up to 3,000 μm [49]. It was shown that the minimum absorption within the wavelength range of 30–3,000 μm was within the range of 200–800 μm, and the corresponding absorption coefficient for this range was less than 1 cm^{-1} for most of the studied monocrystalline samples. Within the range of 1,000–3,000 μm, there was a trend towards an increase in the absorption coefficient with an increase in the mass number of the germanium isotope.

Paper [50] presents the results of the precision measurement of the refractive index of stable single crystals of germanium isotopes ^{72}Ge, ^{73}Ge, ^{74}Ge, and ^{76}Ge with high enrichment by Fourier transform interference refractometry in the range of 1.94–20 μm with a resolution of 0.1 cm^{-1}. This paper provides coefficients of the generalized Cauchy dispersion function, approximating experimental values for the refractive index over the entire measurement range, and the transmission and Raman light scattering spectra.

The authors of [51] conducted a single experiment to investigate the dependence of the position of phonon absorption peaks in the range of 11–40 μm for five single-crystal samples of germanium, ^{70}Ge, ^{72}Ge, ^{73}Ge, ^{74}Ge, and ^{76}Ge. The obtained dependence can be used to identify the nature of single crystals of isotopically enriched germanium [52].

The authors of [53] calculated the standard thermodynamic functions of isotopically enriched monogermanes, ^{70}GeH$_4$, ^{72}GeH$_4$, ^{73}GeH$_4$, ^{74}GeH$_4$, and ^{76}GeH$_{4,}$ in the temperature range of 200–700 K in the approximations “harmonic generator – rigid rotator”, “anharmonic generator – oscillating non-rigid rotator”, as well as by the direct summation of experimental energy values. They established the influence of the isotopic effect on the values of the standard isobaric heat capacity, entropy, enthalpy of heating and the reduced isobaric-isothermal potential of germanium. The authors formulated the limiting requirements for the accuracy of spectral parameters used to identify the influence of the isotopic effect on thermodynamic functions and interatomic distances in the germane molecule.

In addition to fundamental and metrological studies, isotopically enriched silicon and germanium, monosilane and monogermane were investigated in the works dedicated to creating prototypes of quantum devices. State and private programs for the development and application of quantum devices are run in many countries all over the world [54]. In Russia, the systematic development of quantum technologies is carried out according to the Roadmap for the Development of the High-Tech Area "Quantum Computing" [55], which provides for various approaches to the implementation of quantum devices. One of the most promising areas is the model of a solid-state quantum computer using the state of the nuclear spin of an atom as a carrier of quantum information, a qubit [56]. An ensemble of qubits is created by implanting atoms of elements with a non-zero nuclear spin into a crystalline matrix. In the case of silicon, these are atoms of silicon-29 (nuclear spin 1/2+) distributed in a crystalline matrix of silicon-28 atoms, while in the case of germanium, these are atoms of germanium-73 (nuclear spin 9/2+) in a matrix of atoms of a common isotope (^{70}Ge, ^{72}Ge, ^{74}Ge). Of interest are heterostructures based on silicon and germanium isotopes [57], for the creation of which molecular beam epitaxy and vapor deposition methods are used. The precursors for the production of epitaxial structures by molecular beam epitaxy are elementary silicon and germanium, whereas their volatile hydrides are the precursors for chemical vapor deposition (monosilane and monogermane).

To establish the influence of the degree of isotopic enrichment on the performance of silicon-based qubits in order to determine the limiting, physically justified values of silicon and germanium enrichment for the creation of qubits, we need isotopically enriched substances (silicon, germanium, monosilane, and monogermane) with different isotope content of ^{29}Si, ^{73}Ge. Samples of these isotopically enriched substances were prepared according to the techniques described above. Isotopically enriched silicon tetrafluoride with the content of the main isotope ^{28}Si at 99.9%, 99.99%, 99.999% and monogermane with the content of the main isotope ^{72}Ge at 99.9% were used as starting substances [58].

Table 3 shows the content of silicon isotopes in the composition of samples of ^{28}SiF$_4$, ^{28}SiH$_4$, ^{28}Si with different levels of enrichment.

From Table 3, it can be concluded that there was a statistically significant dilution of sample №3 with an isotopic enrichment of 99.999% at the stage of silicon-28 tetrafluoride conversion to monosilane, which may be due to the intake of ^{29}Si, ^{30}Si from the material of the synthesis equipment or storage tanks.

Table 4 provides information on the content of impurities of a number of substances (hydrocarbons, halogen derivatives

Table 3. The content of silicon isotopes in samples of isotopically enriched silicon tetrafluoride-28 with different levels of enrichment

Sample		The content of the silicon isotope, wt. %		
		^{28}Si	^{29}Si	^{30}Si
№1 (3N)	^{28}SiF$_4$	99.96034±0.00160	0.03957±0.00160	0.00009±0.00006
	^{28}SiH$_4$	99.9668±0.0015	0.0329±0.0015	0.0003±0.0001
	^{28}Si	99.9657±0.0015	0.0340±0.0008	0.0003±0.0001
№2 (4N)	^{28}SiF$_4$	99.99623±0.00022	0.00369±0.00022	0.00008±0.00002
	^{28}SiH$_4$	99.99577±0.00028	0.00418±0.00028	0.00005±0.00001
	^{28}Si	99.99581±0.00045	0.00411±0.00043	0.00008±0.00002
№3 (5N)	^{28}SiF$_4$	99.99917±0.00011	0.00080±0.00011	0.00003±0.00001
	^{28}SiH$_4$	99.99882±0.00010	0.00112±0.00010	0.00006±0.00001
	^{28}Si	99.99881±0.00010	0.00114±0.00010	0.00005±0.00001

Table 4. The content of molecular impurities in high-purity $^{28}SiH_4$

Impurity	Content, % mol.	Impurity	Content, % mol.
Ar	$(4.3 \pm 0.6) \cdot 10^{-5}$	trans-1,2-$C_2H_2F_2$	$<5 \cdot 10^{-7}$
CO_2	$<2 \cdot 10^{-6}$	cis-1,2-$C_2H_2F_2$	$<4 \cdot 10^{-7}$
CH_4	$<5 \cdot 10^{-6}$	1,1,1,2-$C_2H_2F_4$	$<5 \cdot 10^{-7}$
C_2H_2	$<2 \cdot 10^{-6}$	1,1,2,2-$C_2H_2F_4$	$<5 \cdot 10^{-7}$
C_2H_4	$<2 \cdot 10^{-6}$	CH_3Cl	$<5 \cdot 10^{-7}$
C_2H_6	$<2 \cdot 10^{-6}$	CF_3Cl	$<5 \cdot 10^{-7}$
C_3H_6	$<2 \cdot 10^{-6}$	Si_2H_6O	$<2 \cdot 10^{-6}$
C_3H_8	$<1 \cdot 10^{-6}$	$Si_3H_8O_2$	$(1.3 \pm 0.4) \cdot 10^{-6}$
i-C_4H_{10}	$<2 \cdot 10^{-6}$	*i*-$Si_4O_3H_{10}$	$<2 \cdot 10^{-7}$
n-C_4H_{10}	$<2 \cdot 10^{-6}$	*n*-$Si_4O_3H_{10}$	$<2 \cdot 10^{-7}$
C_4H_8 1-buten	$<2 \cdot 10^{-6}$	$Si_2OH_4F_2$	$<7 \cdot 10^{-7}$
C_4H_8 2-buten	$<2 \cdot 10^{-6}$	Si_2OH_5F	$(1.8 \pm 0.5) \cdot 10^{-6}$
n-C_5H_{12}	$<2 \cdot 10^{-6}$	$Si_3O_2H_6F_2$	$<3 \cdot 10^{-7}$
n-C_6H_{14}	$<2 \cdot 10^{-6}$	$Si_3O_2H_7F$	$<4 \cdot 10^{-7}$
n-C_7H_{16}	$<2 \cdot 10^{-6}$	Si_2H_6	$<3 \cdot 10^{-6}$
n-C_8H_{18}	$<5 \cdot 10^{-6}$	Si_3H_8	$<6 \cdot 10^{-7}$
C_6H_6	$<1 \cdot 10^{-6}$	*i*-Si_4H_{10}	$<6 \cdot 10^{-7}$
C_6H_5-CH_3	$<4 \cdot 10^{-7}$	*n*-Si_4H_{10}	$<3 \cdot 10^{-7}$
GeH_4	$<3 \cdot 10^{-6}$	*i*-Si_5H_{12}	$<3 \cdot 10^{-6}$
PH_3	$<1 \cdot 10^{-6}$	*n*-Si_5H_{12}	$<3 \cdot 10^{-6}$
AsH_3	$<3 \cdot 10^{-6}$	CH_3SiH_3	$<1 \cdot 10^{-6}$
H_2S	$<5 \cdot 10^{-6}$	$C_2H_5SiH_3$	$<1 \cdot 10^{-6}$
CF_4	$<4 \cdot 10^{-7}$	$(SiH_3)_2CH_2$	$<3 \cdot 10^{-7}$
CHF_3	$<5 \cdot 10^{-6}$	$(CH_3)_3SiH$	$<5 \cdot 10^{-7}$
C_2F_4	$<3 \cdot 10^{-7}$	$(C_2H_5)_2SiH_2$	$<6 \cdot 10^{-7}$
1,1,1-$C_2H_3F_3$	$<7 \cdot 10^{-7}$	$Si_2H_5CH_3$	$<1 \cdot 10^{-6}$

of hydrocarbons, siloxanes, homologues of monosilane, and hydrides of a number of chemical elements) in an isotopically enriched monosilane – rectifier $^{28}SiH_4$, according to the chromatography-mass spectrometry data.

Fig. 1 shows an image of a sample of a single-crystal silicon–28 (content of the main isotope 99.9988 wt. %) weighing 90 g.

Table 5 shows the content of germanium isotopes in the composition of samples of isotopically enriched monogermane $^{72}GeH_4$ and germanium-72 obtained from it according to inductively coupled plasma mass spectrometry.

From Table 5, it can be concluded that there is no statistically significant isotopic dilution at the stage of obtaining crystalline germanium-72.

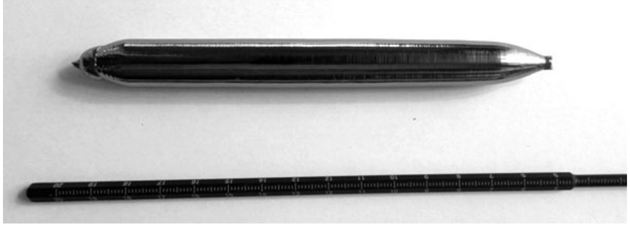

Fig. 1. Image of a single crystal silicon sample – 28

Table 6 provides information on the content of a number of impurities (hydrocarbons, halogen derivatives of hydrocarbons, siloxanes, homologues of monosilane, hydrides of a number of chemical elements) in isotopically enriched monogermane – rectifier $^{72}GeH_4$ according to chromatography-mass spectrometry data.

Table 5. The content of germanium isotopes in the composition of isotopically enriched monogermane samples $^{72}GeH_4$ and germanium-72

Substance	The content of the germanium isotope, wt. %				
	^{70}Ge	^{72}Ge	^{73}Ge	^{74}Ge	^{76}Ge
$^{72}GeH_4$	0.00035±0.00007	99.98460±0.00020	0.01140±0.00015	0.00357±0.00012	0.00008±0.00004
^{72}Ge	0.00011±0.00002	99.98576±0.00105	0.01099±0.00096	0.00310±0.00030	0.00004±0.00001

Table 6. The content of molecular impurities in high-purity monohermane $^{72}GeH_4$

Impurity	Impurity content, mol. %	Impurity	Impurity content, mol. %
Ar	$(2.8±0.3)·10^{-5}$	i-C_4H_{10}	$<2·10^{-6}$
CO_2	$(3±1)·10^{-6}$	n-C_5H_{12}	$<1·10^{-6}$
N_2O	$<2·10^{-6}$	n-C_6H_{14}	$<1·10^{-6}$
Kr	$<3·10^{-7}$	i-C_7H_{16}	$<1·10^{-6}$
Xe	$<3·10^{-7}$	C_7H_{16} 3-metylhexane	$<1·10^{-6}$
SiH_4	$<1·10^{-6}$	n-C_7H_{16}	$<9·10^{-7}$
PH_3	$<1·10^{-6}$	n-C_8H_{18}	$<2·10^{-6}$
AsH_3	$<2·10^{-6}$	C_6H_6	$<2·10^{-7}$
H_2S	$<3·10^{-6}$	$C_6H_5CH_3$	$<2·10^{-7}$
CH_4	$<1·10^{-5}$	C_2H_5Cl	$<5·10^{-7}$
C_2H_2	$<2·10^{-6}$	CH_2Cl_2	$<5·10^{-7}$
C_2H_4	$<1·10^{-6}$	2–C_3H_7Cl	$<9·10^{-7}$
C_2H_6	$<2·10^{-6}$	C_4H_9F	$<4·10^{-6}$
C_3H_6	$<1·10^{-6}$	$C_2H_5GeH_3$	$<1·10^{-5}$
C_3H_8	$<1·10^{-6}$	$C_2H_5Ge_2H_5$	$<1·10^{-5}$
C_4H_8 2-metyl-1-propen	$<2·10^{-6}$	1,1,2–$C_2F_3Cl_3$	$<4·10^{-7}$
C_4H_8 1-buten	$<2·10^{-6}$	1,1,2–$C_2H_3Cl_3$	$<6·10^{-7}$
C_4H_8 2-buten	$<2·10^{-6}$	CH_3GeH_3	$<1·10^{-6}$
n-C_4H_{10}	$<2·10^{-6}$	CS_2	$<4·10^{-7}$

Currently, high-purity isotopically enriched monosilane and monogermane, as well as samples of monoisotopic silicon and germanium with a controlled content of isotopes with a non-zero nuclear spin, produced at the Institute of Chemistry of High Purity Substances of the Russian Academy of Sciences, are widely used in scientific research dedicated to the creation of quantum computing devices in Russia and abroad.

Research on the properties of isotopically enriched binary and complex substances is of fundamental scientific interest. Of particular interest is the production and study of the effect of the isotopic composition on the properties of optical materials, such as quartz glass. A theoretical evaluation provided in a number of works [59, 60] allows concluding that optical losses can be reduced and the optical fiber transparency window can be expanded by the $^{30}Si^{18}O_2$-based light-conducting core and the $^{28}Si^{16}O_2$-based shell. According to the authors, it is also possible to ensure the effect of total internal reflection in such a quartz light-guiding structure due to the difference in the isotopic composition of silicon and oxygen without the use of alloying additives [4]. Silicon tetrachloride is used to obtain high-purity quartz glass by various techniques (vapor deposition, sol-gel method), while its tetrafluoride is used to separate silicon isotopes by gas centrifugation. For the synthesis of $^{28}SiCl_4$, a technique was developed which involves the conversion of isotopically enriched silicon tetrafluoride in static conditions using aluminum(III) chloride [61]; the isolated yield is about 95%, the productivity is 3–4 g of $^{28}SiCl_4$/hour. The reaction of silicon tetrafluoride with aluminum(III) chloride proceeds successively with the formation of silicon fluoride-chlorides [62]; the equilibrium of liquid-vapor in the system $SiCl_4$ – $SiCl_{4-n}F_n$ impurities (n = 1÷4) [63] was also studied. A technique has been developed for the synthesis of silicon-28 tetrachloride from simple substances in a quartz reactor (productivity 20 g/h), which, in combination with isothermal distillation, allows obtaining samples of $^{28}SiCl_4$ with enrichment at 99.99% and the content of impurities of common chemical elements (sodium, aluminum, calcium, iron) at $n{\cdot}10^{-5}$ wt. %.

High-purity silicon-28 tetrachloride has been used for the manufacture of preforms and fiber light carriers based on isotopically enriched quartz glass by the MCVD method [64]. Deposition of isotopically enriched silicon dioxide was carried out on a support tube with a natural content of isotopes; isotopically enriched $^{28}SiF_4$ with a degree of enrichment in silicon-28 of 99.99782±0.00012% was used as a substance for doping with fluorine and reducing the refractive index of the light-reflecting shell. This resulted in obtaining a piece with a light-guiding structure based on isotopically enriched quartz glass, from which the light-guide was extracted. The refractive index profile of the obtained piece was measured, as well as the spectral dependence of the level of optical losses of the light guide based on isotopically enriched silicon-28 dioxide in the range of 900–1,750 nm [64]. Figure 2 shows the distribution profile of silicon isotopes in a preform based on isotopically enriched $^{28}SiO_2$ according to secondary ion mass spectrometry.

The content of silicon isotopes ^{28}Si, ^{29}Si, and ^{30}Si in the central part of the preform was 99.89±0.10%, 0.087±0.080%, and 0.023±0.020%, respectively. These results indicate a marked decrease in the content of the isotope of silicon-28 in the preform relative to its content in the starting substances ($^{28}SiCl_4$ and $^{28}SiF_4$) to a level of 99.9%. Most likely this was caused by the diffusion of silicon isotopes ^{29}Si, ^{30}Si from a support quartz tube with a natural isotopic composition of silicon at the stage of the porous layer melting.

Further research in the field of obtaining isotopically enriched substances and materials based on them should be focused on increasing the level of isotopic purity and obtaining samples of binary substances enriched in the basic chemical elements in their composition.

Contribution of the authors

The authors contributed equally to this article.

Conflict of interests

The authors declare that they have no known competing financial interests or personal relationships that could have influenced the work reported in this paper.

References

1. Devyatykh G. G., Bulanov A. D., Gusev A. V... Pohl H.-J. *Doklady Chemistry*.2001;376(4/6), 47–48. https://doi.org/10.1023/a:1018864208808

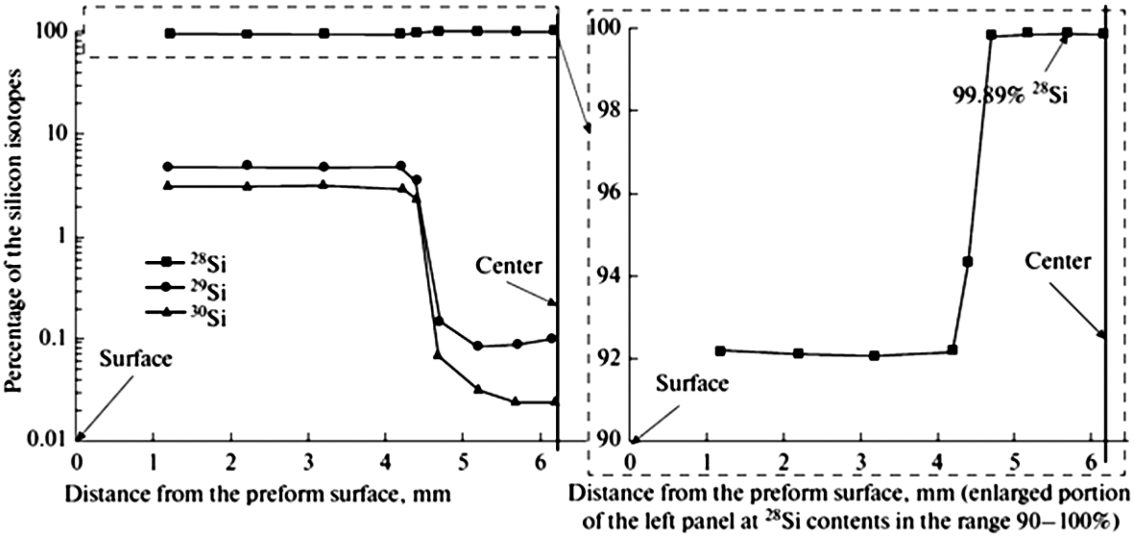

Fig. 2. The distribution profile of silicon isotopes in a preform based on isotopically enriched $^{28}SiO^2$ [64]

2. *High-purity substances**. M. F. Churbanov, Yu. A. Karpov, P. V. Zlomanov, V. A. Fedorov (eds.). Moscow: Nauchnyj Mir Publ., 2018. 996 p. (In Russ.)

3. *Isotopes: properties, production, application**. In 2 volumes. Vol. 1. V. Yu. Baranov (ed.). Moscow: Fizmatlit Publ., 2005. 600 p. (In Russ.)

4. Plekhanov V. G. Isotope engineering. *Physics-Uspekhi*. 2000:170(11): 1245–1252. https://doi.org/10.1070/pu2000v043n11abeh000264

5. Itoh K. M., Kato J., Uemura M., … Rieman H. High purity isotopically enriched ^{29}Si and ^{30}Si single crystals: isotope separation, purification, and growth. *Japanese Journal of Applied Physics*. 2003;42: 6248–6251. https://doi.org/10.1143/JJAP.42.6248

6. Devyatykh G. G., Bulanov A. D., Gusev A. V., … Abrosimov N. V. High-purity single-crystal monoisotopic silicon-28 for precise determination of Avogadro's number. *Doklady Chemistry*. 2008(421): 157–160. https://doi.org/10.1134/S001250080807001X

7. Abrosimov N. V., Aref'ev D. G., Becker P., … Zakel S. A new generation of 99.999 % enriched ^{28}Si single crystals for the determination of Avogadro constant. *Metrologia*. 2017;54: 599–609. https://doi.org/10.1088/1681-7575/aa7a62

8. Arefiev D. G., Bulanov A. D., Vasin S. A., … Churbanov M. F. *Method for separating germanium isotopes**: RF Patent: No. 2412747. Publ. 02.27.2011, bull. No. 6. (In Russ.)

9. Churbanov M. F., Gavva V. A., Bulanov A. D., … Gusev A. V. Production of germanium stable isotopes single crystals. *Crystal Research and Technology*. 2017;52(4): 1700026. https://doi.org/10.1002/crat.201700026

10. Seyfried P., Spieweck F., Bettin H., …, Holm C. ***T**he silicon-28 path to the Avogadro constant – first experiments and outlook. *Proceedings of Conference on Precision Electromagnetic Measurements Digest.* 1995;44(2): 522–525. https://doi.org/10.1109/CPEM.1994.333372

11. Takyu K., Itoh K. M., Oka K., Saito N., Ozhogin V. I. Growth and characterization of the isotopically enriched ^{28}Si bulk single crystal. *Japanese Journal of Applied Physics*. 1999;38: L1493–L1495. https://doi.org/10.1143/jjap.38.l1493

12. Capinski W. S., Maris H. J., Bauser E., Silier … Gmelin E. Thermal conductivity of isotopically enriched Si. *Applied Physics Letters*. 1997;71(15): 2109–2111. https://doi.org/10.1063/1.119384

13. Kremer R. K., Graf K., Cardona M., Gusev A. V., Inyushkin A. V., Taldenkov A. Thermal conductivity of isotopically enriched 28Si: revisited. *Solid State Communications*. 2004;131: 499–503. https://doi.org/10.1016/j.ssc.2004.06.022

14. Gusev A. V., Gavva V. A., Kozyrev E. A., Potapov A. M., Plotnichenko V. G. Preparation of single-crystal 29Si. *Inorganic Materials*. 2011;47(7): 691–693. https://doi.org/10.1134/s0020168511070119

15. Nakabayashi Y., Segawa T., Osman H. I., … Abe T. Epitaxial growth of pure ^{30}Si layers on a natural Si(100) substrate using enriched $^{30}SiH_4$. *Japanese Journal of Applied Physics*. 2000;39(11B): L1133–L1134. https://doi.org/10.1143/JJAP.39.L1133

16. Inyushkin A. V., Taldenkov A. N., Gusev A. V., Gibin A. M., Gavva V. A., Kozyrev E. A. Thermal conductivity of the single-crystal monoisotopic 29Si in the temperature range 2.4–410 K. *Physics of the Solid State*; 2013;55(1): 235–239. https://doi.org/10.1134/s1063783413010150

17. Becker *P.*, Schiel D., Pohl H.-J., … Dianov E. M. Large-scale production of highly enriched ^{28}Si for the precise determination of the Avogadro constant. *Measurement Science and Technology*. 2006;17: 1854–1860. https://doi.org/10.1088/0957-0233/17/7/025

18. Andreas B., Azuma Y., Bartl G., … Zakel S. Counting the atoms in a ^{28}Si crystal for a new kilogram definition. *Metrologia*. 2011;48: S1–S13. https://doi.org/10.1088/0026-1394/48/2/S01

19. Chuprov L. A., Sennikov P. G., Tokhadze K. G., Ignatov S. K., Schrems O. High-resolution Fourier-transform IR spectroscopic determination of impurities in silicon tetrafluoride and silane prepared from it. *Inorganic Materials*. 2006;42(8): 924–931. https://doi.org/10.1134/s0020168506080231

20. Krylov V. A., Sorochkina T. G. Gas-chromatographic determination of C1-C4 hydrocarbon trace impurities in silicon tetrafluoride. *Journal of Analytical Chemistry*. 2005;60(12): 1125–1128. https://doi.org/10.1007/s10809-005-0254-z

21. Bulanov A. D., Sennikov P. G., Krylov V. A., … Troshin O. Yu. (2007). Hydrocarbon impurities in SiF_4 and SiH_4 prepared from it. *Inorganic Materials*. 2007;43(4): 364–368. https://doi.org/10.1134/s0020168507040061

22. Pimenov V. G., Bulanov A. D. Analysis of high-purity silicon tetrafluoride by atomic-emission method with concentration of impurities by matrix sublimation. *Analitika i kontrol'*. 2004; 8(4): 315–321. (In Russ.). Available at: https://elar.urfu.ru/bitstream/10995/57605/1/aik-2004-04-02.pdf

23. Bulanov A. D., Pimenov V. G. Determination of impurities in monoisotopic silicon tetrafluoride. *Inorganic Materials*. 2004;40(7): 754–759. https://doi.org/10.1023/b:inma.0000034777.13686.f8

24. Kovalev I. D., Potapov A. M.,Bulanov A. D. Measurement of the isotopic composition of the isotopic enriched silicon and its volatile compounds by laser ionization mass spectrometry. *Mass-spektrometria*. 2004; 1(1): 37–44. (In Russ., abstract in Eng.). Available at: https://elibrary.ru/item.asp?id=9290214

25. Bulanov A. D., Troshin O. Yu., Balabanov V. V. Synthesis of high-purity calcium hydride. *Russian Journal of Applied Chemistry*. 2004;77(6): 875–877. https://doi.org/10.1023/b:rjac.0000044107.80122.61

26. Bulanov A. D., Balabanov V. V., Pryakhin D. A., Troshin O. Yu. Preparation and fine purification of SiF_4 and $^{28}SiH_4$. *Inorganic Materials*. 2002;38(3): 283–287. https://doi.org/10.1023/A:1014735203351

27. Arefiev D. G., Bulanov A. D., Vasin S. A., … Churbanov M. F. *Method for separating germanium isotopes**: Patent RF No. 2412747. Publ. 02.27.2011, bull. No. 6.

28. Troshin O. Yu., Bulanov A. D., Mikheev V. S., Lashkov A. Yu. Mechanically activated synthesis of monosilane by the reaction of calcium hydride with silicon tetrafluoride. *Russian Journal of Applied Chemistry*. 2010;83(6): 984–988. https://doi.org/10.1134/S1070427210060108

29. Bulanov A. D., Sennikov P. G., Sozin A. Yu., Lashkov A. Yu., Troshin O. Yu. Formation of impurity Si_2OH_6 in silane syntezed from silicon tetrafluoride. *Russian Journal*

of Inorganic Chemistry. 2011;56(4): 510–512. https://doi.org/10.1134/S0036023611040061

30. Bulanov A. D., Moiseev A. N., Troshin O. Yu., Balabanov V. V., Isaev D. V. Fine purification of monoisotopic silanes $^{28}SiH_4$, $^{29}SiH_4$ and $^{30}SiH_4$ via distillation. *Inorganic Materials*. 2004;40(6): 555–557. https://doi.org/10.1023/b:inma.0000031984.83652.87

31. Gusev A. V., Bulanov A. D. High-purity silicon isotopes ^{28}Si, ^{29}Si and $^{30}SiH_4$. *Inorganic Materials*. 2008;44(13): 1395–1408. https://doi.org/10.1134/S0020168508130013

32. Gusev A. V., Gavva V. A., Kozyrev E. A., Riemann H., Abrosimov N. V. Crucibles for Czochralski growth of isotopically enriched silicon single crystals. *Inorganic Materials*. 2013;49(12): 1167–1169. https://doi.org/10.1134/s0020168513120078

33. Andreas B., Azuma Y., Bartl G., ... Waseda A. An accurate determination of the Avogadro constant by counting the atoms in a ^{28}Si crystal. *Physical Review Letters*. 2011;106(3): 030801(1-4). https://doi.org/10.1103/PhysRevLett.106.030801

34. . Gibin A. M., Devyatykh G. G., Gusev A. V., Kremer R. K., Cardona M., Pohl H.-J. Heat capacity of isotopically enriched ^{28}Si, ^{29}Si and ^{30}Si in the temperature range 4 K < T< 100 K. *Solid State Communications*. 2005;133(9): 569–572. https://doi.org/10.1016/j.ssc.2004.12.047

35. Plotnichenko V. G., Nazaryants V. O., Kryukova E. V., ... Dianov E. M. Refractive index spectral dependence, Raman spectra, and transmission spectra of high-purity ^{28}Si, ^{29}Si, ^{30}Si, and Sinat single crystals. *Applied Optics*. 2011;50(23): 4633–4641. https://doi.org/10.1364/AO.50.004633

36. Ramdas A. K., Rodriguez S.,Tsoi S., Haller E. E. Electronic band gaps of semiconductors as influenced by theirisotopic composition. *Solid State Communications*. 2005;133(11): 709–714. https://doi.org/10.1016/j.ssc.2004.12.038

37. Sanati M., Estreicher S. K., Cordona M. Isotopic dependence of the heat capacity of c-C, Si, and Ge:An ab-initio calculation. *Solid State Communications*. 2004;131: 229–233. https://doi.org/10.1016/j.ssc.2004.04.043

38. Cardona M., Ruf T. Phonon self-energies in semiconductors: Anharmonic and isotopic contributions. *Solid State Communications*. 2001;117: 201–212. https://doi.org/10.1016/S0038-1098(00)00443-9

39. Wille H.-C., Shvyd'ko Yu. V., Gerdau E., ... Zegenhagen J. Anomalous isotopic effect on the lattice parameter of silicon. *Physical Review Letters*. 2002;89: 285901. https://doi.org/10.1103/PhysRevLett.89.285901

40. Cardona M., Thewalt M. L. W. Isotope effects on the optical spectra of semiconductors. *Reviews of Modern Physics*. 2005;77: 1173–1223. https://doi.org/10.1103/RevModPhys.77.1173

41. Haller E. E. Isotopically controlled semiconductors. *Solid State Communications*. 2005;133(11): 693–707. https://doi.org/10.1016/j.ssc.2004.12.021

42. Gavva V. A., Troshin O. Yu., Adamchik S. A., ... Bulanov A. D. Preparation of single-crystal isotopically enriched ^{70}Ge by a hydride method. *Inorganic Materials*. 2022;58(3): 246–251. https://doi.org/10.1134/s0020168522030050

43. Sozin A. Yu., Krylov V. A., Chernova O. Yu., ... Lashkov A. Yu. Study of the impurity composition of isotope enriched german $^{70}GeH_4$ by the method of gas chromatography-mass spectrometry. Perspektivnye Materialy. 2022;2: 70–82. https://doi.org/10.30791/1028-978x-2022-2-70-82

44. Potapov A. M., Kurganova A. E., Bulanov A. D., Troshin O. Yu., Zyryanov S. M. Isotope analysis of $^{72}GeH_4$, $^{73}GeH_4$, $^{74}GeH_4$, and $^{76}GeH_4$ monogermanes by inductively-coupled plasma high-resolution mass spectrometry (ICP–MS). Journal of Analytical Chemistry. 2016;71(7): 667–675. https://doi.org/10.1134/s1061934816050087

45. Churbanov M. F., Gavva V. A., Bulanov A. D., ... Abrosimov N. V. Production of germanium stable isotopes single crystals. *Crystal Research and Technology*. 2017;52(4): 1700026. https://doi.org/10.1002/crat.201700026

46. Gavva V. A., Bulanov A. D., Kut'in A. M., Plekhovich A. D., Churbanov M. F. Melting point of high-purity germanium stable isotopes. *Physica B: Condensed Matter*. 2018;537: 12–14. https://doi.org/10.1016/j.physb.2018.01.056

47. Kutyin A. M., Plekhovich A. D., Gavva V. A., Bulanov A. D. Development of an applied version of the Kolmogorov–Johnson–Meyl crystallization theory for processing thermal analysis data on the melting temperature and enthalpy of germanium isotopes. *Doklady Rossijskoj Akademii Nauk. Himiya, Nauki o Materialah*. 2024;516(1):30-38. https://doi.org/10.31857/S2686953524030046

48. Gibin A. M., Abrosimov N. V., Bulanov A. D., Gavva V. A.Thermal conductivity of single-crystals isotopically enriched ^{70}Ge, ^{72}Ge, ^{74}Ge in the temperature range of 80-310 K. *Physics of the Solid State*. 2023;65(8): 1393–1396. https://doi.org/10.21883/FTT.2023.08.56167.65

49. Kropotov G. I., Kaplunov I. A., Rogalin V. E., Shakhmin A. A., Bulanov A. D. Particular of radiation transmission of monoisotopic germanium single crystals in the terahertz spectral range. *Applied Physics (Prikladnaya Fizika)*. 2024(1): 80–83. https://doi.org/10.51368/1996-0948-2024-1-80-84

50. Lipskiy V. A., Kotereva T. V., Bulanov A. D., Gavva V. A., Churbanov M. F., Nazaryants V. O., Koltashev V. V., Plotnichenko V. G. Refractive index spectral dependence, Raman spectra, and transmission spectra of high-purity ^{72}Ge, ^{73}Ge, ^{74}Ge, ^{76}Ge, and ^{nat}Ge single crystals. *Applied Optics*. 2019;58(27): С. 7489–7496. https://doi.org/10.1364/AO.58.007489

51. Kropotov G. I., Bulanov A. D., Rogalin V. E., Kaplunov I. A., Shakhmin A. A. (2023). Dependence of the position of phonon IR absorption bands of germanium isotopes on their mass number. *Doklady Rossijskoj Akademii Nauk. Fizika, Tekhnicheskie Nauki*.2023;511(1), 10–15. (In Russ., abstract in Eng.). https://doi.org/10.31857/s2686740023040077

52. Kaplunov I. A., Rogalin V. E., Filin S. A., Kropotov G. I., Shakhmin A. A., Bulanov A. D. *Method of express analysis of objective identification of isotopically pure germanium single crystal*®. Patent RF: No. 2813061. Publ. 06.02.2024. (In Russ.)

53. Velmuzhova I. A., Koshelev M. A., Velmuzhov A. P., Ulenikov O. N., Gromova O. V. Thermodynamic functions of germane isotopologues $^{A}GeH_4$ (A = 70, 72, 73, 74, 76) calculated from high-resolution IR spectra. *Journal of Molecular Spectroscopy*. 2024;402: 111914. https://doi.org/10.1016/j.jms.2024.111914

54. Fedorov A. K. Quantum technologies: from scientific discoveries to new applications. *PHOTONICS Russia*.

2019;13(6): 574–583. (In Russ., abstract in Eng.). https://doi.org/10.22184/1993-7296.FRos.2019.13.6.574.583

55. Fedorov A. K., Akimov A. V., Biamonte J. D., ... Zheltikov A. M. Quantum technologies in Russia. *Quantum Science and Technology*. 2019;4: 40501. https://doi.org/10.1088/2058-9565/ab4472

56. Valiev K. A. Quantum computers and quantum computations. *Uspekhi Fizicheskih Nauk*. 2005;175(1):, 3. https://doi.org/10.3367/ufnr.0175.200501a.0003

57. Vrijen R., Di Vincenzo D. Electron spin resonance transistor for quantum computation in silicon-germanium heterostructure. *Physical Review A*. 2000;62: 012306(1–10). https://doi.org/10.1103/PhysRevA.62.012306

58. Troshin O. Yu., Gavva V. A., Lashkov A. Yu., ... Bulanov A. D. Isotopically modified silicon, germanium and their hydrides for the development of quantum computing devices*. *Neorganičeskie materialy*. 2023;59(11): 1201–1210. https://doi.org/10.31857/S0002337X23110143

59. Heitmann W., Klein K. F. *Glass for optical waveguides or the like*. US Patent: No. 6490399. Published 03.12.2002.

60. Kelsey V., Alexander J.E., Burden S.J. *Isotopically engeneered optical materials*. US Patent: No. 20030039865. Publ. 27.02.2003.

61. Churbanov M. F., Bulanov A. D., Troshin O. Yu., Grebenkov K. S. *Method for producing isotopically enriched silicon tetrachloride**. R F Patent: No. 2618265. Publ. 03.05.2017, bull. No. 13.

62. Troshin O. Yu., Bulanov A. D., Kirillov Yu. P., ... Ermakov A. A. Preparation of high-purity silicon-28 tetrachloride from silicon-28 tetrafluoride. *Inorganic Materials*. 2022;58(8): 854–859. https://doi.org/10.1134/s002016852208012x

63. Troshin O. Yu., Bulanov A. D., Chernova O. Yu. Liquid–vapor equilibria in the $SiCl_4$–A (A = $SiCl_{4-n}F_n$ (n = 1–4) impurity) systems. *Inorganic Materials*. 2018;54(8): 840–843. https://doi.org/10.1134/s0020168518080162

64. Troshin O. Yu., Bulanov A. D., Salgansky M. Yu., ... Drozdov M. N. $^{28}SiO_2$-based isotopically enriched silica fiber. *Inorganic Materials*. 2023;59(6): 591-596. https://doi.org/10.1134/s0020168523060158

* *Translated by author of the article*

Information about the authors

Andrey D. Bulanov, Corresponding Member of the Russian Academy of Sciences, Dr. Sci (Chem.), Chief Researcher, Devyatykh Institute of Chemistry of High-Purity Substances, Russian Academy of Sciences (Nizhny Novgorod, Russian Federation).

https://orcid.org/0000-0001-5717-0527
bulanov@ihps-nnov.ru

Vladimir A. Gavva, Cand. Sci. (Chem.), Leading Researcher, Devyatykh Institute of Chemistry of High-Purity Substances, Russian Academy of Sciences (Nizhny Novgorod, Russian Federation).

https://orcid.org/0000-0003-3071-8884
gavva@ihps-nnov.ru

Oleg Yu. Troshin, Cand. Sci. (Chem.), Senior Researcher, Devyatykh Institute of Chemistry of High-Purity Substances, Russian Academy of Sciences (Nizhny Novgorod, Russian Federation).

https://orcid.org/0000-0001-6996-1561
troshin@ihps-nnov.ru

Received 05.07.2024; approved after reviewing 24.09.2024; accepted for publication 15.10.2024; published online 25.03.2025.

Translated by Irina Charychanskaya

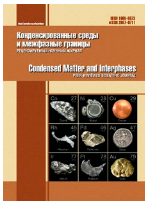

ISSN 1606-867X (Print)
ISSN 2687-0711 (Online)
Condensed Matter and Interphases
Kondensirovannye Sredy i Mezhfaznye Granitsy
https://journals.vsu.ru/kcmf/

Review

Review article
https://doi.org/10.17308/kcmf.2025.27/12482

Advanced methods for preparing especially pure glasses based on germanium and gallium chalcogenides. Part 1. Synthesis via volatile and low-melting compounds. Review

A. P. Velmuzhov✉**, M. V. Sukhanov, E. A. Tyurina, V. S. Shiryaev**

G. G. Devyatykh Institute of Chemistry of High-Purity Substances, Russian Academy of Sciences,
49 Tropinina st., Nizhny Novgorod 603951 Russian Federation

Abstract

Glasses based on germanium and gallium chalcogenides are promising optical materials for the near and mid-infrared (IR) regions. They are used to develop fiber-optic sensors, sources of supercontinuum, luminescent and laser radiation, glass-ceramic materials with improved mechanical properties, memory cells, and other optical and optoelectronic devices. The most important characteristic of chalcogenide glasses is the content of limiting impurities that have the most negative effect on their optical properties. Conventional methods for producing these materials include melting simple substances with getters in evacuated silica-glass ampoules and then distilling the melt. These methods do not allow achieving extremely low concentrations of impurities that do not affect optical transparency of glasses. Therefore, new approaches need to be developed.

The purpose of the review is to systematize the scientific information related to the methods for preparing especially pure chalcogenide glasses which have been developed over the past 15 years at the Institute of Chemistry of High Purity Substances of the Russian Academy of Sciences. The methods discussed in the first part of the paper include: 1) synthesis of *p*-element chalcogenides via volatile iodides; 2) preparing a batch by thermal decomposition of germanium sulfide and selenide iodides; 3) synthesis and deep purification of germanium monochalcogenides. The developed methods made it possible to reduce the content of hydrogen, oxygen, and carbon impurities and heterogeneous inclusions in chalcogenide glasses by 1–2 orders of magnitude as compared to conventional methods. In conclusion, the article discusses the possibilities for further reduction of the content of impurities in glasses based on germanium and gallium chalcogenides to achieve extremely low optical losses.

Keywords: Chalcogenide glasses, Especially pure substances, Optical materials, Synthesis, IR spectrometry, Chemical transport reactions

Funding: The research was carried out with the financial support of the national project “Science and Universities” at the laboratory “Ultra-pure chalcogenide glasses for mid-infrared photonics”, state order FFSR-2024-0001 and the Research and Education Centre of the Nizhny Novgorod Region within the framework of the “Technoplatform 2035” project.

For citation: Velmuzhov A. P., Sukhanov M. V., Tyurina E. A., Shiryaev V. S. Advanced methods for preparing especially pure glasses based on germanium and gallium chalcogenides. Part 1. Synthesis via volatile and low-melting compounds. Review. *Condensed Matter and Interphases*. 2025;27(1): 16–28. https://doi.org/10.17308/kcmf.2025.27/12482

Для цитирования: Вельмужов А. П., Суханов М. В., Тюрина Е. А., Ширяев В. С. Современные способы получения особо чистых стекол на основе халькогенидов германия и галлия. Часть 1. Синтез через летучие и легкоплавкие соединения. Обзор. *Конденсированные среды и межфазные границы*. 2025;27(1): 16–28. https://doi.org/10.17308/kcmf.2025.27/12482

✉ Alexander P. Velmuzhov, e-mail: velmuzhov.ichps@mail.ru

© Velmuzhov A. P., Sukhanov M. V., Tyurina E. A., Shiryaev V. S., 2025

The content is available under Creative Commons Attribution 4.0 License.

1. Introduction

Chalcogenide glasses are a promising material for mid-infrared (IR) optics. It is a broad class of glassy inorganic materials based on sulfides, selenides, and tellurides of elements belonging to groups 13–15 of the periodic system. These glasses have a wide transparency region in the IR range (Fig. 1), high optical nonlinearity, and pronounced semiconductor and acoustooptical properties [1–3]. Typical chalcogenide glass forming systems include: As – S, As – Se, As – S – Se, As – Se – Te, Ge – S, Ge – Se, Ge – As – S, Ge – As – Se, Ga – Ge – S, Ga – La – S, Ge – Sb – S, Ga – Ge – Se, Ga – Ge – Te, etc. [4, 5]. There is an increasing interest in glasses based on gallium and antimony chalcogenides, which do not contain arsenic or germanium [6, 7]. This is due to their better transparency in the long-wave IR range.

Chalcogenide glasses are widely used as materials for IR lenses in night vision equipment and thermal visors and for the manufacture of fiber-optic light carriers used in aircraft protection systems [8, 9]. Chalcogenide glasses are used to develop fiber-optic sensors, supercontinuum sources, memory cells, and other optical and optoelectronic devices [10–12]. These materials can also be used to manufacture optical glass-ceramics with improved mechanical and thermophysical properties as compared to glass [13]. The most important area of application of chalcogenide glasses doped with rare earth elements (REE) is the development of mid-infrared luminescent and laser sources [14, 15].

The key characteristic of chalcogenide glasses, which largely determines their practical application, is the content of limiting impurities that have the most negative effect on their optical properties. Among such impurities are: 1) hydrogen in the form of SH-, SeH-, TeH-, and OH-groups and water; 2) oxygen in the form of oxides of glass components and impurity elements; 3) carbon-containing compounds: CS_2, CO_2, COS, and organic substances; 4) transition metals; 5) heterogeneous impurity inclusions, which, first of all, include silicon(IV) oxide used as a material for glass synthesis equipment. These impurities have intense absorption bands within the region of optical transparency of chalcogenide glasses (Table 1) [16–19]. Heterogeneous inclusions reduce the overall transparency in a wide spectral range due to the scattering of IR radiation [20]. The influence of heterogeneous inclusions on the optical transparency of glasses is mainly determined by their size. For $Ge_{25}Sb_{10}S_{65}$ glass, it was shown that with a SiO_2 particle size of 0.1 μm and a concentration of 10^9 cm^{-3} optical losses in the fiber are at least 1 dB/m in the spectral range of 1.1–7.4 μm. Particles with a size of 1 μm cause the same losses but at concentrations of 10^5 cm^{-3} [21].

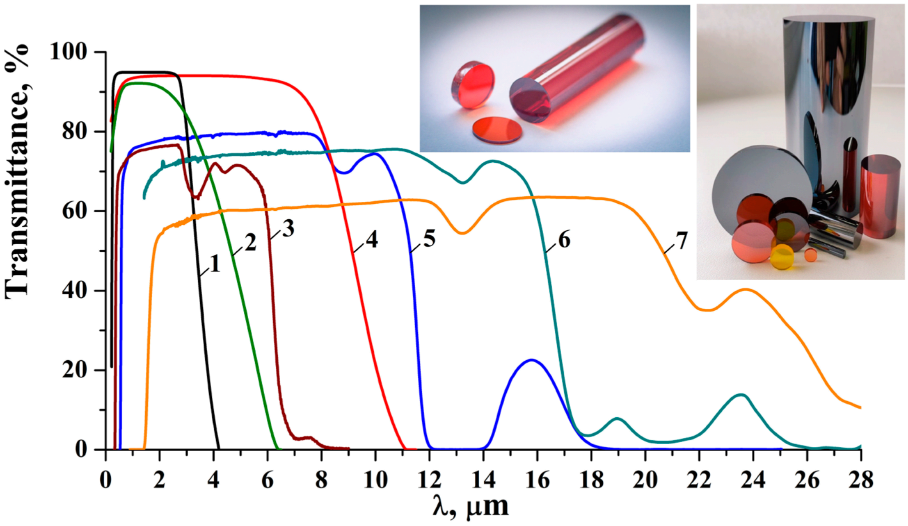

Fig. 1. Transparency windows of several optical materials in the near and middle IR ranges. *1* – silica glass; *2* – Al_2O_3; *3* – ZnO–TeO_2 tellurite glass; *4* – CaF_2; *5* – $Ga_5Ge_{35}S_{60}$ sulfide glass; *6* –$Ge_{28}Sb_{12}Se_{60}$ selenide glass; *7* – $(GeTe_4)_{50}(AgI)_{50}$ telluride glass. An optical path-length of samples can be different, therefore a comparison of transparency spectra is estimate. Inserts give photos of chalcogenide glasses prepared at the Institute of Chemistry of High-Purity Substances of the Russian Academy of Sciences

Table 1. The position of the absorption bands of impurities, $\lambda_{max.}$; their absorption coefficients, ε; and their limiting contents in As_2S_3 glass corresponding to the intrinsic optical losses, $C_{lim.}$ [16–19, 24]

Impurity	λ_{max}, μm	ε, dB/km/ppm(wt.)	C_{lim}, ppb(wt.)	Impurity	λ_{max}, μm	ε, dB/km/ppm(wt.)	C_{lim}, ppb(wt.)
SH	4.0	2,500 ppm(at.)	0.4	SO_2	8.63	43	2300
SeH in As_2Se_3 glass	4.5	1,000 ppm(at.)	0.1	Se–O in As_2Se_3 glass	10.6	380	2.6
GeH	4.85	–	–	Te–O	13.1	–	–
OH (in SiO_2)	2.92	10^4	0.3	Ga – O	15–20	–	–
Ge–O in $Ge_{25}Se_{15}Te_{60}$ glass	7.8	2610	0.4	Si–O	9.1	28000	–
	12.5	99000	0.01	CO_2	4.33	$1.5\cdot10^4$	0.04
As_2O_3 in As_2Se_3 glass	12.65	$4.3\cdot10^4$	100	COS	4.95	10^5	0.004
	9.5	1030	400	CS_2	6.68	$4.8\cdot10^5$	0.2

The intrinsic (excluding the effect of impurities) optical losses in As_2S_3 glass, calculated from the absorption spectra of an ultra-pure bulk sample, are <20 dB/km in the spectral range of 2–6 μm with a minimum of about 0.3 dB/km at 5.2 μm [22]. According to the theoretical evaluation, the minimum optical losses for As_2Se_3 glass in the range of 2.5–6.6 μm do not exceed 1 dB/km [23]. From the known absorption coefficients of impurities [24], it was calculated that their content in As_2S_3 glass, corresponding to the intrinsic optical losses, should not exceed 0.4 ppb(wt.) for hydrogen in the form of SH-groups and 0.2, 0.004, and 0.04 ppb(wt.) for carbon in the form of CS_2, COS, and CO_2, respectively. To provide minimum optical losses in As_2Se_3 glass, the content of hydrogen impurity in the form of SeH-groups should not exceed 0.1 ppb(wt.), of oxygen in the form of oxides 0.1 ppm(wt.), and carbon 0.1–0.01 ppm(wt.) [25]. The content of impurities in samples of chalcogenide glasses prepared by the conventional method including the purification of the melt by distillation is 3–4 orders of magnitude higher than the permissible values [16]. This significantly limits the practical use of such materials for the manufacture of fiber-optic light carriers and makes it impossible to use them to manufacture laser radiation sources. The intrinsic optical losses in glasses based on germanium and gallium chalcogenides have so far been only evaluated for the $Ge_3PS_{7.5}$ composition [26], which makes it difficult to determine the maximum permissible concentration of impurities in these materials.

The purpose of this review is to systematize the scientific information related to the methods for preparing ultra-pure chalcogenide glasses which have been developed over the past 15 years at the Institute of Chemistry of High Purity Substances of the Russian Academy of Sciences. The key idea of the new methods was to use germanium and gallium compounds, which are more volatile, low-melting, and have better reactive properties as compared to the simple substances which had been used traditionally. Among such compounds were: germanium(IV) iodide, gallium(III) iodide, germanium sulfide and selenide iodides, and germanium(II) chalcogenides.

2. Traditional method for preparing chalcogenide glasses

Traditionally, chalcogenide glasses are prepared by the interaction of especially pure substances of grades 4–7 N in evacuated silica-glass ampoules [27]. The synthesis temperature is determined by the glass composition and is usually in the range of 750–950 °C. To ensure the uniformity of the glasses, the process is carried out in rocking furnaces. The melt is usually quenched in air or in water, depending on the crystallization stability of the glasses. To relieve mechanical stresses after quenching, the samples are annealed at the glass transition temperature.

The main method of reducing the content of impurities in chalcogenide glasses involves adding getters to the batch, which selectively bind impurities and convert them into a form which can be easily removed, and a subsequent purification of the melt by distillation [27]. Aluminum and magnesium is used to bind oxygen impurities, while tellurium(IV) chloride and aluminum(III) chloride contribute to a decrease in hydrogen content. This method allows reducing the concentration of impurities in glasses by 1–2 orders of magnitude. In the best samples of germanium-containing glasses prepared by the traditional method, the content of hydrogen impurity in the form of SH-groups was 7.5 ppm(at.) in $Ge_{25}Sb_{10}S_{65}$ [17]; the content of hydrogen impurity in the form of SeH-groups was 2.7 ppm(at.) and the content of oxygen in the form of germanium oxides was 0.2 ppm(wt.) in $Ge_{20}Se_{80}$ [28].

The disadvantage of using getters is their interaction with the walls of the silica-glass reactor, which leads to the introduction of impurities into the chalcogenide melt.

$$2Al + 3SiO_2 \rightleftarrows Al_2O_3 + 3SiO, \quad (1)$$

$$xAl_2O_3 + ySiO_2 \rightleftarrows xAl_2O_3{\cdot}ySiO_2, \quad (2)$$

$$4Mg + SiO_2 \rightleftarrows 2MgO + Mg_2Si. \quad (3)$$

During subsequent purification of the glass-forming melt by distillation, reaction products (1)–(3), which have low solubility in the chalcogenide melt, can be only partly removed. This results in the appearance of heterogeneous impurity inclusions and absorption bands in the glasses in the regions of 9.1 μm (Si–O) and 13.2 μm (Al-O) [19]. The interaction of aluminum with the walls of the silica-glass reactor can lead to its rupture during cooling of the melt. This significantly complicates the production of chalcogenide glasses and makes synthesis more hazardous.

The main disadvantage of the purification of the batch by distillation is the high temperature and duration of the process. They are due to the relatively low volatility of germanium dichalcogenides and the need for slow evaporation of the melt for its effective purification from heterogeneous impurities. High temperatures contribute to the entry of hydrogen, metal, and silicon oxide impurities from the walls of the silica-glass reactor into the chalcogenide melt [22, 29]. During preparation of telluride-germanium glasses, there is another limitation of purification by distillation, i.e. the dissociative evaporation of GeTe, which makes it difficult to obtain charge of a specified chemical composition [30].

The main challenge for the production of especially-pure glasses containing gallium is related with the low volatility of this metal and its chalcogenides [31, 32]. This makes the purification of the glass-forming melt by distillation impossible. Therefore, gallium is added to the batch by loading the sample in air or into a glove box with an inert atmosphere. When using this method, gallium oxide and hydroxide impurities, which are present on its surface and which form during the reactor soldering, enter the glass-forming melt. These impurities significantly reduce the transparency of chalcogenide glasses in the mid IR range.

These problems associated with the production of optical materials based on especially pure chalcogenide glasses mean that novel approaches to their synthesis need to be developed. Reducing the content of absorbing and scattering impurities by 2–3 orders of magnitude will significantly improve the optical characteristics of chalcogenide glasses. This will expand the scope and the efficiency of their application. To improve the purity of chalcogenide glasses, it is highly important to establish the nature and limits of the influence of impurities on the properties of these materials.

3. Preparation of chalcogenide glasses via volatile iodides

The main idea of the developed method was to synthesize batch components by the interaction between iodides and chalcogen [33–35]. Using the Ge – Sb – S – I and Ge – Sb – Se – I systems, germanium and antimony chalcogenides were synthesized by reactions of the following type:

$$GeI_4 + 2S(Se) \rightleftarrows GeS(Se)_2 + 2I_2\uparrow, \quad (4)$$

$$2SbI_3 + 3S(Se) \rightleftarrows Sb_2S(Se)_3 + 3I_2\uparrow. \quad (5)$$

According to the thermodynamic modeling of reactions (4) and (5), the degree of iodides conversion to the corresponding chalcogenides under equilibrium conditions was expected to be low, up to 26% for sulfides and up to 11% for selenides at a temperature of 500 °C [36]. A significant increase in the yield of chalcogenides was possible due to the selective isolation of iodine from the reaction melt. In practice, this involved using a vertical unit made of silica-glass and consisting of three parts which were successively soldered together: 1) reactor; 2) mass transfer section; 3) iodine receiver. Batch components were synthesized at a temperature of 500–650 °C. Heating of the reaction mixture resulted in the release of iodine vapors by reactions (4) and (5) and their entering the receiver. One part of the iodine condensed as crystals, the other part in the form of liquid drained back into the reactor. The presence of the mass transfer section allowed selectively extracting iodine from the reaction melt without the significant removal of volatile iodides from it. As the synthesis proceeded, the batch was depleted of iodine and its viscosity increased, which required a gradual increase in the reactor temperature to ensure the batch was molten.

The content of metal impurities in the prepared glass samples did not exceed 0.5 ppm(wt.); the content of silicon, which was the main source of heterogeneous inclusions, was 0.02–0.1 ppm(wt.); the content of the impurities which were the most difficult to remove, impurities of hydrogen in the form of SH- and SeH-groups, was 0.1–0.3 ppm(at.) [33, 34]. This was 1–2 orders of magnitude lower than in glasses prepared by the interaction of simple substances with purification of the melt by distillation. The achieved purity was provided by the following main advantages of the method:

– Before the synthesis of the batch component, iodides of *p*-elements were subjected to deep purification from hydrogen, oxygen, and carbon impurities and heterogeneous inclusions by vacuum distillation at temperatures that did not exceed 200 °C. The content of these impurities in the corresponding simple substances of especially pure grades was not controlled and could be significant.

– Iodides were loaded into the reactor by vacuum evaporation, which excluded the contact of reagents with atmospheric impurities (oxygen, water, organic substances, dust, etc.).

– The synthesis temperature of the glass-forming components of the batch did not exceed 650 °C, which significantly reduced the contamination effect of the silica-glass reactor.

– Iodides of *p*-elements converted the hydrogen impurity in the form of SH- and SeH-groups into an easily removable form due to the following chemical reactions:

$$GeI_4 + 2H_2S(Se) \rightleftarrows GeS(Se)_2 + 4HI\uparrow, \quad (6)$$

$$2SbI_3 + 3H_2S(Se) \rightleftarrows Sb_2S(Se)_3 + 6HI\uparrow, \quad (7)$$

$$I_2 + H_2S(Se) \rightleftarrows S(Se) + 2HI\uparrow. \quad (8)$$

The formed hydrogen iodide was removed from the reaction melt and concentrated in the iodine receiver.

The main disadvantage of the method is the difficulty of providing a specified chemical composition of the glass by a controlled removal of iodine from the reaction mixture. Deviations in the content of components can reach 3–5 at. %.

The developed method was used for the synthesis of crystalline binary and complex sulfides and selenides of *p*-elements with the actual yield of 70–98% and a residual iodine content of <0.1 to 2 at. %. [37–40] (Table 2). Such amount of iodine did not have a noticeable negative effect on the optical properties of chalcogenides, but allowed growing their single crystals by chemical transport directly in the synthesis reactor [42]. This

Table 2. Chemical composition and actual yield of some chalcogenides prepared via volatile iodides

Sample	Element concentration, at. %				Yield, %
	p-element	Zn	S(Se)	I	
Ga_2S_3	40.2	–	59.7	0.04	95
In_2S_3	39.1	–	59.4	1.5	72
Sb_2S_3	38.2	–	61.2	0.6	88
GeS_2	33.9	–	65.9	0.2	92
ZnS	–	50.5	48.7	0.8	91
Ga_2Se_3	41.3	–	57.3	1.4	82
In_2Se_3	42.3	–	56.1	1.6	70
$GeSe_2$	36.4	–	63.4	0.2	90
ZnSe	–	50.9	48.3	0.8	90
$ZnGa_2S_4$	29.2	14.8	55.6	0.4	94
$ZnGa_2Se_4$	26.9	16.2	56.5	0.4	88

means there was no need in the extra step which involves adding a transport agent and leads to the contamination of the material. It was theoretically predicted and experimentally confirmed that the yield of chalcogenides of *p*-elements increases with a decrease in the atomic mass of the element in the group and with the transition from selenides to sulfides. Synthesis was most effective when aluminum(III) iodide and gallium(III) iodide interacted with sulfur. To prepare Ga_2S_3 and complex sulfides based on it, a reactor with two temperature zones without a mass transfer section was used. At synthesis temperatures of up to 550 °C, γ-Ga_2S_3 with the cubic structure of the unit cell was formed (Fig. 2a). Annealing the resulting sulfide at higher temperatures led to the formation of monoclinic β-Ga_2S_3. The synthesis of indium, germanium, antimony, and bismuth chalcogenides was complicated by the formation of relatively stable sulfide and selenide iodides as intermediate products (Fig. 2b, 2c). The decomposition of these compounds led to the formation of chalcogenides, for example, by reactions:

$$3SbSI \rightleftarrows Sb_2S_3 + SbI_3, \qquad (9)$$

$$Bi(Bi_2S_3)_9I_3 \rightleftarrows 9Bi_2S_3 + BiI_3. \qquad (10)$$

Preparing tellurides of *p*-elements of groups 13–15 by the proposed method is complicated due to thermodynamic limitations with regard to the high melting point of tellurium (T_m = 451 °C [43]) and the formation of relatively stable TeI_4.

4. Preparation of glasses of the Ge – S(Se) – I system by thermal decomposition of germanium sulfide and selenide iodides

It is known that the Ge – S – I system has low-melting compounds of the $GeSI_2$ (T_m = 150 °C) [44] and $Ge_2S_3I_2$ (T_m = 310 °C) composition [45], which form stable glasses. Thermal decomposition of these sulfide iodides in a temperature gradient was accompanied by the release of germanium(IV) iodide and the formation of germanium(IV) sulfide [46] (Fig. 3), which in a simplified way can be described by the following chemical reactions:

$$2GeSI_2 \rightleftarrows GeS_2 + GeI_4\uparrow, \qquad (11)$$

$$2Ge_2S_3I_2 \rightleftarrows 3GeS_2 + GeI_4\uparrow. \qquad (12)$$

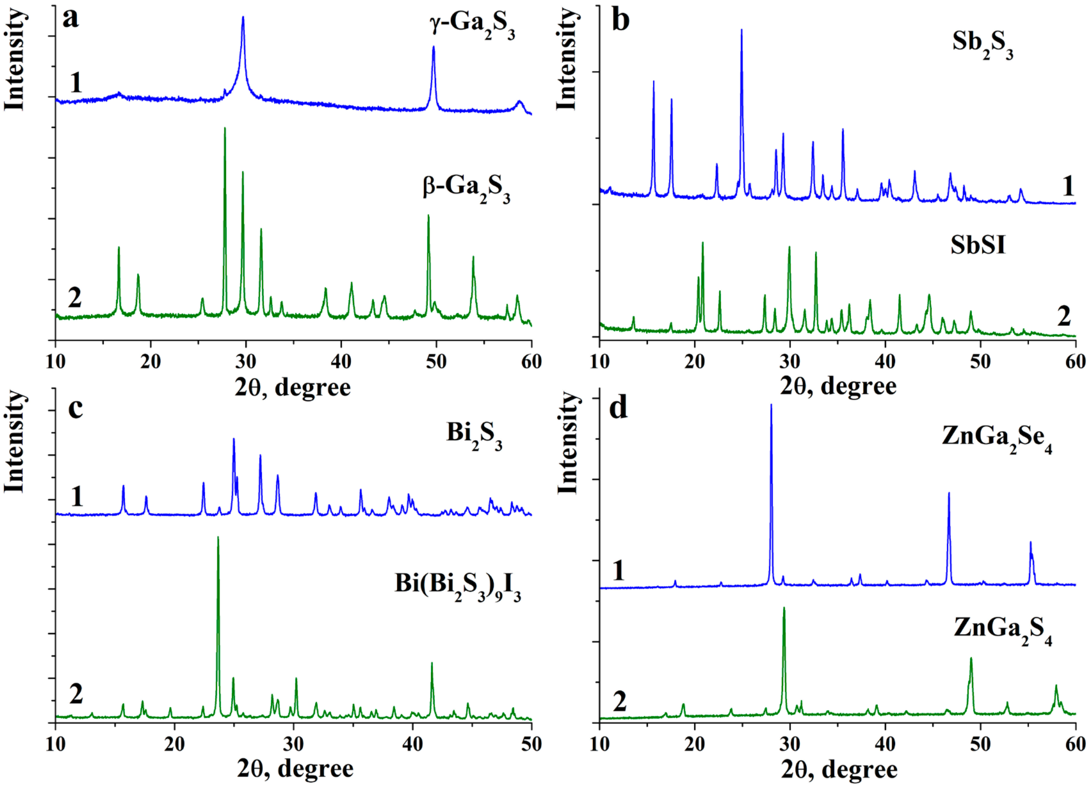

Fig. 2. X-ray diffraction patterns of the reaction products of some iodides with chalcogens; a1 – GaI_3 + S <550 °C (PDF 49-1361 [41]); a2 – GaI_3 + S >550 °C (PDF 76-0752); b1 – SbI_3 + S (PDF 75-1310); b2 – SbI_3 + S intermediate product (PDF 74-2244); c1 – BiI_3 + S (PDF 84-0279); c2 – BiI_3 + S intermediate product (PDF 73-1157); d1 – ZnI_2 + GaI_3 + Se (PDF 47-1590); d2 – ZnI_2 + GaI_3 + S (PDF 84-2007)

By controlling the degree of decomposition of sulfide iodides, it is possible to specify the composition of the non-volatile reaction product. The method for preparing glasses of the Ge – S – I system at low temperatures is based on this idea [47, 48].

The synthesis of the glassy $Ge_2S_3I_2$, its subsequent thermal decomposition, and melting of the resulting batch were carried out in one evacuated silica-glass reactor, which excluded contamination of the melt with impurities from the atmosphere [47]. $Ge_2S_3I_2$ was prepared by the reaction between germanium(IV) iodide, germanium, and sulfur at a temperature of 550 °C

$$GeI_4 + 3Ge + 6S \rightleftarrows 2Ge_2S_3I_2. \qquad (13)$$

When a temperature gradient from 550 °C to room temperature was created in the reactor, the resulting sulfide-iodide was thermally decomposed. The degree of decomposition was controlled by its duration (from 1 to 5 hours) according to a predetermined experimental dependence of the glass composition on the duration of the process. This allowed specifying the content of components with deviations of no more than ± 2 at. %. Further, the evaporator with the resulting batch was sealed-off from the unit and the glass-forming melt was homogenized at 750 °C under the stirring action of a rocking furnace. Similarly, glasses of the Ge – Se – I system were prepared by the thermal decomposition of $Ge_2Se_3I_2$ [49].

According to the results of the IR Fourier analysis, in the best samples of the prepared glasses, the content of hydrogen impurity in the form of SH- and SeH-groups was 0.1–0.5 ppm(at.); OH-groups <0.05 ppm(wt.); oxygen chemically bound to germanium up to 0.5 ppm(wt.), and carbon in the form of CO_2, CS_2, and COS <0.01 ppm(wt.). The achieved content of absorbing impurities was due to a significant decrease in the synthesis temperature and effective removal of highly volatile impurity compounds at the stage of thermal decomposition of $Ge_2S_3I_2$ and $Ge_2Se_3I_2$.

The main limitation of the developed method is that it can only be applied to two glass-forming systems: Ge – S – I and Ge – Se – I. To prepare glasses of the compositions beyond the $GeS(Se)_2$ – GeI_4 quasi-binary section, it is necessary to use source alloys with a corresponding excess (*y*) or deficiency (-*y*) of chalcogen:

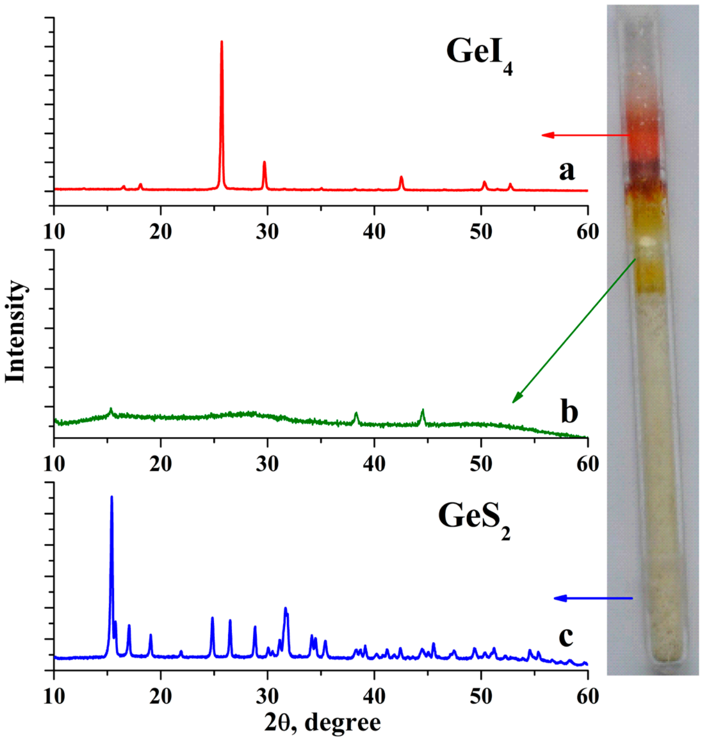

Fig. 3. X-ray diffraction patterns of the thermal decomposition products of $Ge_2S_3I_2$ glass. a – cold section of the reactor, corresponds to GeI_4 (PDF 75-0982); b – intermediate section, amorphous product with weak reflections from GeS_2; c – high-temperature section, corresponds to GeS_2 (PDF 71-0003). The insert on the right shows a photo of the reactor

$$2Ge_2S_{(3+y)}I_2 \rightleftarrows 3GeS_{(2+2/3y)} + GeI_4\uparrow. \qquad (14)$$

Along with the use of sulfide and selenide iodides, the glasses of the Ge – S and Ge – Se systems can be prepared by thermal decomposition of $GeSBr_2$ and $Ge_2S_3Br_2$ [50]. The disadvantage of this method is the need to use liquid bromine to synthesize starting compounds.

5. Preparation of glasses via germanium monochalcogenides

5.1. Ge – S, Ge – Se systems

Another approach was aimed at alleviating the disadvantages of the conventional vacuum distillation of the chalcogenide melt described in paragraph 2. The novel method involved synthesis and purification of germanium monochalcogenides. The synthesis was carried out by passing chalcogen vapors over a mixture of germanium granules with a getter [51, 52]. The by-products of the proposed method for the germanium monochalcogenide synthesis were dichalcogenides. According to the results of thermodynamic modeling of the Ge – S and Ge – Se systems by the method of equilibrium constants, the formation of GeS and GeSe is facilitated by an increase in the reactor temperature and a decrease in the temperature of the chalcogen evaporator [51, 53]. The results of thermodynamic modeling are in good agreement with the experimental values of the optimal conditions for the synthesis of germanium monochalcogenides: reactor temperature of 550–600 °C and chalcogen evaporator temperature of 240–260 °C for sulfur and 330–350 °C for selenium.

The developed method was used to prepare especially pure glasses of the $Ge_{20}Se_{80}$ composition [54]. The content of impurities in the optical fibers fabricated from such glass was as following: hydrogen in the form of SeH-groups was 1.8±0.1 ppm(at.); oxygen chemically bound to germanium was 0.013±0.002 ppm(wt.). According to these values, the obtained fibers were the best among those made of glasses based on germanium selenides. The minimum optical losses in the fiber were 0.77 dB/m at a wavelength of 5.6 μm (Fig. 4). The relatively high losses may be due to partial crystallization of the glass due to unoptimized conditions for fiber drawing. The lowest losses in germanium selenide optical fibers ‑ obtained to date [28] are 0.1 dB/m at a wavelength of 6.5 μm. The content of hydrogen impurities in the form of SeH-groups and oxygen chemically bound to germanium in this fiber was 2.7 ppm(at.) and 0.2 ppm(wt.), respectively.

For sulfide systems, the developed method in combination with the synthesis of gallium(III) sulfide by the interaction of gallium(III) iodide with sulfur was used to especially pure $Ga_5Ge_{35}S_{60}$ and $Ga_8Sb_{32}S_{60}$ glasses [53]. The absorption spectra of the samples and the photographs of diffraction spots caused by submicron inclusions recorded by 3D laser ultramicroscopy are shown in Fig. 5. The content of hydrogen impurities in the samples in the form of SH-groups was 0.2–0.6 ppm(at.), which was 2 orders of magnitude lower than during the synthesis from simple substances. In the glasses prepared by the conventional method, the content of heterogeneous micron-sized inclusions determined by optical microscopy was $n \cdot 10^3$ pcs/cm^3. The content of submicron inclusions (0.1–0.9 μm) recorded by 3D laser ultramicroscopy reached $n \cdot 10^8$ pcs/cm^3. The samples prepared by the developed method had single micron inclusions (<10^2 pcs./cm^3). In the submicron region, there was only background scattering, i.e. intrinsic scattering on frozen fluctuations or on small (<100 nm) inclusions that did not contribute significantly to optical losses in the mid-infrared range.

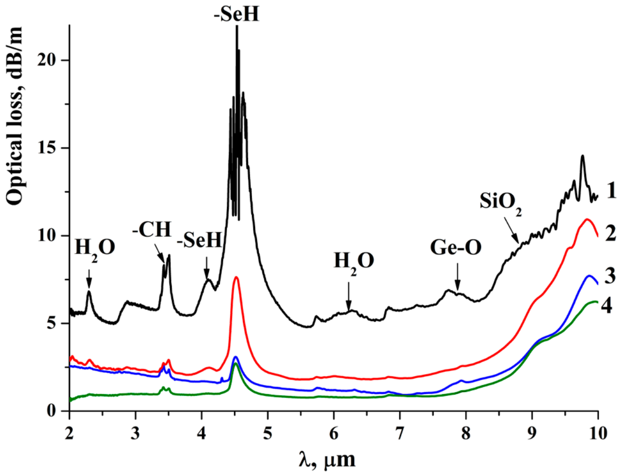

Fig. 4. Spectra of total optical losses of optical fibers without a reflective cladding, made of $Ge_{20}Se_{80}$ glasses prepared: from simple substances without additional purification (1); with the addition of aluminum to the batch and double distillation of the melt (2); by passing selenium vapor over germanium (3); by passing selenium vapor over a mixture of germanium and aluminum (4) [54]

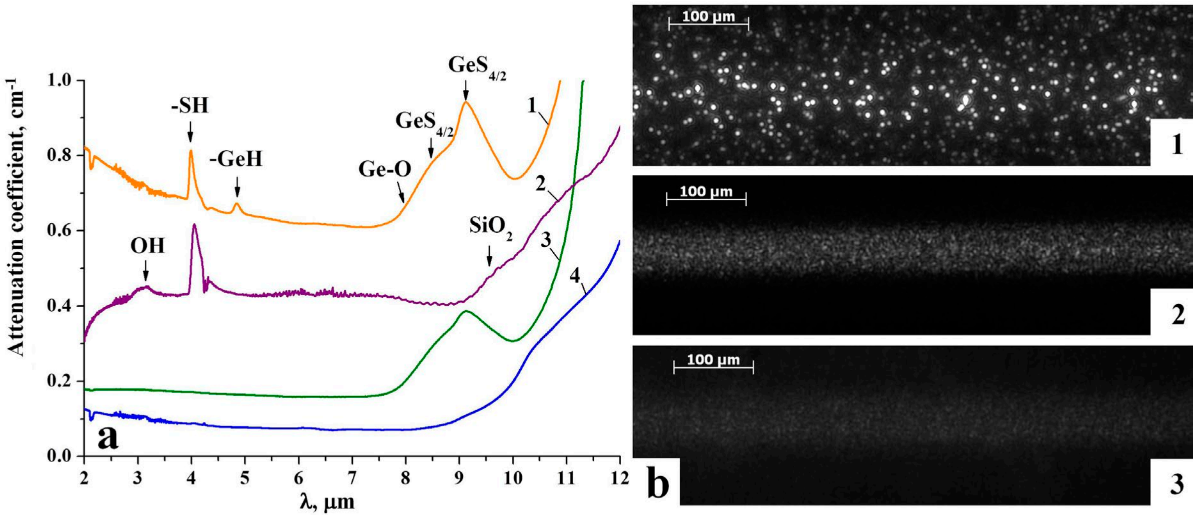

Fig. 5. Absorption spectra (a) and photographs of diffraction spots from submicron inclusions (b) of $Ga_5Ge_{35}S_{60}$ and $Ga_8Sb_{32}S_{60}$ glasses; $Ga_5Ge_{35}S_{60}$ samples prepared by the traditional method (a1, b1) and by the developed method (a3, b2); $Ga_8Sb_{32}S_{60}$ samples prepared by the traditional method (a2) and by the developed method (a4, b3) [53]

The developed method has the following key advantages as compared to the conventional distillation of the melt:

– Higher volatility of germanium monochalcogenides as compared to dichalcogenides allows reducing the temperature of the vacuum purification of the batch by 50–100 °C.

– The addition of the getter to the intermediate ampoule with germanium minimizes the products of its interaction with impurities and the silica-glass reactor entering the glass-forming melt.

– Passing chalcogen vapors over the mixture allows for preliminary chemical etching of germanium granules before the batch components are loaded into the reactor. This contributes to the removal of surface contamination from the granules (adsorbed gases, water, OH-groups, oxides, and heterogeneous inclusions) due to the capture of germanium monochalcogenide by the vapors or due to chemical reactions of type (15)–(17):

$$3S + GeO_2 \rightleftarrows GeS_2 + SO_2, \qquad (15)$$

$$3S + 2H_2O \rightleftarrows 2H_2S + SO_2, \qquad (16)$$

$$(y/2+2x)S + C_xH_y \rightleftarrows y/2H_2S + xCS_2. \qquad (17)$$

For this, the first portions of germanium monochalcogenide (50–100 mg), in which surface impurities can be concentrated, are removed from the system.

5.2. The Ge – Te system

Another limitation of the conventional vacuum distillation of the batch during the preparation of glasses based on the Ge-Te system (for example, $Ge_{20}Te_{80}$, $Ga_{10}Ge_{15}Te_{75}$) is the dissociative evaporation of germanium monotelluride [30].

$$(x+y+z)\mathrm{GeTe}_{(\text{кр.})} \rightleftarrows$$
$$\rightleftarrows x\mathrm{GeTe}_{(\text{г.})} + y/2\mathrm{Te}_2 + z/2\mathrm{GeTe}_{2(\text{г.})} + (y+z/2)\mathrm{Ge}_{(\text{кр.})}. \qquad (18)$$

The released germanium remains in the evaporator, which leads to a noticeable deviation of the glass composition from the specified value. According to the experimental results, after single, double and triple distillation of the melt, the deviations in the content of germanium in $Ge_{20}Te_{80}$ glasses reached 0.5, 0.9, and 2.1 at. % [55]. This corresponds to the degree of GeTe decomposition of 2.5, 4.5, and 10.5 %, respectively. In the developed method, the problem of preserving the chemical composition of the batch is solved due to the constant presence of tellurium vapors over GeTe, which shifts the equilibrium of reaction (18) to the left. However, re-distillation of the $(GeTe)_xTe_{100-x}$ batch aimed at further reduction in the content of impurities was accompanied by a noticeable decomposition of GeTe. This could be explained by the fact that at the initial stage of low-temperature distillation tellurium evaporates completely. Suppression of the germanium(II) telluride dissociation caused by excess chalcogen in the vapor phase is impossible during the final stages of purification.

To solve this problem, a novel method for purification of the $(GeTe)_xTe_{100-x}$ batch by distillation was developed [55]. The main idea of the proposed method is to provide for the separate condensation of tellurium and germanium(II) telluride during the purification of the glass-forming melt by distillation. The separation of the batch components allowed for its subsequent purification without GeTe dissociation. This was achieved by the possibility of sequential distillation of GeTe and tellurium from separate ampoules. During the final stages of the germanium(II) telluride evaporation, tellurium vapors were passed over it, which suppressed reaction (18) in the forward direction. In the case of partial decomposition of GeTe during distillation, tellurium vapors interacted with the released germanium and transferred it to the vapor phase. This eliminated the incomplete transition of germanium from the evaporator to the receiver during the purification of the $(GeTe)_xTe_{100-x}$ batch.

The deviations of the compositions of Ge_xTe_{100-x} glasses prepared by the developed method of purification did not exceed 0.2 at. % even after triple distillation of the melt. The corresponding degree of the GeTe decomposition was 1.0%. Such deviations do not have any noticeable effects on the key properties of chalcogenide glassy materials. This method is an integral part of comprehensive approaches to the production of especially pure glasses based on the Ge-Te system.

6. Conclusions

The developed methods allow significantly (by 1–2 orders of magnitude) reducing the content of impurities in glasses based on germanium and gallium chalcogenides. This is largely due to the fact that the methods implement the chemical principles of the deep purification of substances. As a rule, the efficiency of a single stage of purification from impurities using chemical reactions is higher than that using physicochemical methods (distillation, crystallization, etc.) [56]. In chemical methods, the partition coefficient is determined by the difference in the thermodynamic potentials of reactions with the participation of the main substance and impurity. This difference can significantly exceed the differences in the thermodynamic functions of the phase transitions of the impurity and the purified substance (melting, evaporation), on which the physicochemical methods of separation are based. In turn, these differences are determined by the fact that in chemical methods the purification effect is due to the re-distribution of intramolecular bonds, the energy of which, in general, is higher than that of intermolecular bonds. The efficiency of separation in chemical methods depends on the type of reaction. By selecting the appropriate reagent, it is possible to provide high values of the partition coefficients. A definitive advantage of chemical methods is their applicability in cases when the main substance is a non-volatile, high-melting or thermally unstable compound. Nonetheless, to prepare chalcogenide glasses with a low content of all types of impurities, it is necessary to use a set of methods with regard to the purification and loading of the batch components into the reactor, including vacuum distillation.

An important technique implemented in the developed methods is the transformation of the chemical form of the batch components in order to increase their volatility and meltability and to change (increase or decrease) their reactivity properties. This allows: 1) significantly reducing the temperature and duration of the synthesis; 2) reducing the interaction with the silica-glass reactor; 3) increasing the efficiency of the removal of impurities.

The main disadvantage of chemical methods of purification is the contamination of the main substance with the elements present in the reagents. In the developed methods, the key reagents are iodides. At moderate concentrations iodine does not have any noticeable negative effects on the target properties of chalcogenide glasses. Moreover, it is known that the addition of iodine increases the crystallization stability of glasses, increases their overall transparency and expands its range, and contributes to the dissolution of REE [57–60]. This makes iodides of *p*-elements one of the most suitable transport agents for the production of especially pure chalcogenide glasses.

Despite a significant increase in purity, the achieved content of impurities is still 2 orders of magnitude higher than the upper values, which do not affect the optical properties of chalcogenide glasses. This means that it is necessary to further improve the developed methods, their temperature and time regimes, and equipment. To reduce the contamination effect of the silica-glass reactor during chemical transport with the participation of iodides, individual elements or coatings can be developed for the zones of the highest temperature. These elements or coatings can be made of materials such as corundum, pyrolytic boron nitride, etc. The original silica-glass tubes should meet high quality standards in terms of the content of impurities of OH-groups and metals. Surface defects should be under strict control since they are the most chemically active centers when the reactor walls come into contact with the chalcogenide melt. It is necessary to develop methods for reducing the content of these impurities and defects in reactors for thermal, chemical, plasma-chemical, and other types of treatment [61, 62]. An important area for further research is the assessment of the minimum achievable optical losses in glasses based on germanium and gallium chalcogenides to determine the limits of the influence of impurities on this key property.

Author contributions

A. P. Velmuzhov: research concept, methodology development, conducting research, text writing, final conclusions. M. V. Sukhanov: research concept, methodology development, conducting research, editing. E. A. Tyurina: methodology development, conducting research, editing. V. S. Shiryaev: research concept, conducting research, editing.

Conflict of interests

The authors declare that they have no known competing financial interests or personal relationships that could have influenced the work reported in this paper.

References

1. Sanghera J. S. Optical properties of chalcogenide glasses and fibers. In: *Chalcogenide glasses: preparation, properties and applications*. J.-L. Adam, X. Zhang (eds.). Oxford Cambridge Philadelphia New Delhi: Woodhead Publishing Series in Electronic and Optical Materials; 2014;44: 113–138. https://doi.org/10.1533/9780857093561.1.113

2. Zakery A., Elliott S. R. Optical properties and applications of chalcogenide glasses: a review. *Journal of Non-Crystalline Solids*. 2003;330: 1–12. https://doi.org/10.1016/j.jnoncrysol.2003.08.064

3. Cao Z., Dai S., Liu Z., Liu C., Ding S., Lin C. Investigation of the acousto-optical properties of Ge–As–Te–(Se) chalcogenide glasses at 10.6 μm wavelength. *Journal of American Ceramic Society*. 2021;104: 3224–3234. https://doi.org/10.1111/jace.17767

4. Vinogradova G. Z. *Glass formation and phase equilibria in chalcogenide systems: binary and ternary systems**. Moscow: Nauka Publ.; 1984. 174 p. (In Russ.)

5. Felts A. *Amorphous and glassy inorganic solids**. Moscow: Mir Publ., 1986. 558 p. (In Russ.)

6. Yang A., Zhang M., Li L., ... Tang D. Ga – Sb – S chalcogenide glasses for mid-infrared applications. *Journal of the American Ceramic Society*. 2015;99(1): 12–15. https://doi.org/10.1111/jace.14025

7. Lecomte A., Nazabal V., Le Coq D., Calvez L. Ge-free chalcogenide glasses based on Ga-Sb-Se and their stabilization by iodine incorporation. *Journal of Non-Crystalline Solids*. 2018;481: 543–547. https://doi.org/10.1016/j.jnoncrysol.2017.11.046

8. Zhou T., Zhu Z., Liu X., Liang Z., Wang X. A Review of the precision glass molding of chalcogenide glass (ChG) for infrared optics. *Micromachines*. 2018;9: 337. https://doi.org/10.3390/mi9070337

9. Kumar M. B., Kumar P. R. A missile jamming design for aircraft defence using infrared automated counter measures. *Journal of Scientific Research*. 2022;66(02): 163–171. https://doi.org/10.37398/jsr.2022.660222

10. Boussard-Plédel C. Chalcogenide waveguides for infrared sensing. In.: *Chalcogenide glasses: preparation, properties and applications*. J.-L. Adam, X. Zhang (eds.). Oxford Cambridge Philadelphia New Delhi: Woodhead Publishing Series in Electronic and Optical Materials; 2014;44: 381–410. https://doi.org/10.1533/9780857093561.2.381

11. Hyot B. Chalcogenide for phase change optical and electrical memories. In.: *Chalcogenide glasses: preparation, properties and applications*. J.-L. Adam, X. Zhang (eds.). Oxford Cambridge Philadelphia New Delhi: Woodhead Publishing Series in Electronic and Optical Materials; 2014;44: 597–631. https://doi.org/10.1533/9780857093561.2.597

12. Saini T. S., Sinha R. K. Mid-infrared supercontinuum generation in soft-glass specialty optical fibers: a review. *Progress in Quantum Electronics*. 2021;78: 1000342. https://doi.org/10.1016/j.pquantelec.2021.100342

13. Lin C., Rüssel C., Dai S. Chalcogenide glass-ceramics: functional design and crystallization mechanism. *Progress in Materials Science*. 2017;93: 1–44. https://doi.org/10.1016/j.pmatsci.2017.11.001

14. Heo J., Chung W. J. Rare-earth-doped chalcogenide glass for lasers and amplifiers. In: *Chalcogenide glasses: preparation, properties and applications*. J.-L. Adam, X. Zhang (eds.). Oxford Cambridge Philadelphia New Delhi: Woodhead Publishing Series in Electronic and Optical Materials; 2014;44: 347–380. https://doi.org/10.1533/9780857093561.2.347

15. Jackson S. D., Jain R. K. Fiber-based sources of coherent MIR radiation: key advances and future prospects. *Optics Express*. 2020;28(21): 30964–31017. https://doi.org/10.1364/OE.400003

16. Snopatin G. E., Shiryaev V. S., Plotnichenko V. G., Dianov E. M., Churbanov M. F. High-purity chalcogenide glasses for fiber optics. *Inorganic Materials*. 2009;45(13): 1439–1460. https://doi.org/10.1134/S0020168509130019

17. Shiryaev V. S., Ketkova L. A., Churbanov M. F., ... Sibirkin A. A. Heterophase inclusions and dissolved impurities in $Ge_{25}Sb_{10}S_{65}$ glass. *Journal of Non-Crystalline Solids*. 2009;355(52–54): 2640–2646. https://doi.org/10.1016/j.jnoncrysol.2009.08.022

18. Nishii J., Yamashita T., Yamagishi T. Oxide impurity absorptions in Ge – Se – Te glass fibres. *Journal of Materials Science*. 1989;24: 4293–4297. https://doi.org/10.1007/BF00544501

19. He Y., Wang X., Nie Q., … Dai S. Optical properties of Ge–Te–Ga doping Al and $AlCl_3$ far infrared transmitting chalcogenide glasses. *Infrared Physics & Technology*. 2013;58: 1–4. https://doi.org/10.1016/j.infrared.2012.12.038

20. Ketkova L. A., Churbanov M. F. Heterophase inclusions as a source of non-selective optical losses in highpurity chalcogenide and tellurite glasses for fiber optics. *Journal of Non-Crystalline Solids*. 2017;480: 18–22. https://doi.org/10.1016/j.jnoncrysol.2017.09.018

21. Shiryaev V. S., Ketkova L. A., Churbanov M. F., … Sibirkin A. A. Preparation of optical fibers based on Ge – Sb – S glass system. *Optical Materials*. 2009;32: 362–367. https://doi.org/10.1016/j.optmat.2009.09.003

22. Churbanov M. F., Skripachev I. V., Snopatin G. E., Ketkova L. A., Plotnichenko V. G. The problems of optical loss reduction in arsenic sulfide glass IR fibers. *Optical Materials*. 2020;122: 109812. https://doi.org/10.1016/j.optmat.2020.109812

23. Dianov E. M., Petrov M. Yu., Plotnichenko V. G., Sysoev V. K. Estimate of the minimum optical losses in chalcogenide glasses. *Soviet Journal of Quantum Electronics*.1982;12(4): 498–499. https://doi.org/10.1070/QE1982v012n04ABEH012237

24. Churbanov M. F., Snopatin G. E., Shiryaev V. S., Plotnichenko V. G., Dianov E. M. Recent advances in preparation of high-purity glasses based on arsenic chalcogenides for fiber optics. *Journal of Non-Crystalline Solids*. 2011;357: 2352–2357. https://doi.org/10.1016/j.jnoncrysol.2010.11.057

25. Shiryaev V. S., Smetanin S. V., Ovchinnikov D. K., Churbanov M. F., Kryukova E. B., Plotnichenko V. G. Effects of oxygen and carbon impurities on the optical transmission of As_2Se_3 glass. *Inorganic Materials*. 2025;41(3): 308–314. https://doi.org/10.1007/s10789-005-0129-6

26. Shibata S., Terunuma Y., Manabe T. Ge – P – S chalcogenide glass fibers. *Japanese Journal of Applied Physics*. 1980;19(10): 603–605. https://doi.org/10.1143/JJAP.19.L603

27. Churbanov M. F., Shiryaev V. S. Preparation of high-purity chalcogenide glasses. In: *Chalcogenide glasses: preparation, properties and applications*. J.-L. Adam, X. Zhang (eds.). Oxford Cambridge Philadelphia New Delhi: Woodhead Publishing Series in Electronic and Optical Materials; 2014;44: 3–35. https://doi.org/10.1533/9780857093561.1.3

28. Troles J., Shiryaev V., Churbanov M., … Adam J. L. $GeSe_4$ glass fibres with low optical losses in the MID-IR. *Optical Materials*. 2009;32: 212–215. https://doi.org/10.1016/j.optmat.2009.07.024

29. Churbanov M. F., Velmuzhov A. P., Sukhanov M. V., Snopatin G. E., Scripachev I. V., Plotnichenko V. G. Arsenic-sulfide glasses with low content of hydrogen impurity for fiber optics. *Optical Materials*. 2018;77: 87–92. https://doi.org/10.1016/j.optmat.2018.01.023

30. Novoselova A. V., Zlomanov V. P., Karbanov S. G., Matveyev O. V., Gas'kov A. M. Physico-chemical study of the germanium, tin, lead chalcogenides. *Progress in Solid State Chemistry*. 1972;7: 85–115. https://doi.org/10.1016/0079-6786(72)90005-2

31. Speiser R., Johnston H. L. Vapor pressures of inorganic substances. IX. Gallium. *Journal of the American Chemical Society*. 1953;75(6): 1469–1470. https://doi.org/10.1021/ja01102a057

32. Greenberg H. Thermodynamic basis of crystal growth. *Phase P-T-X equilibrium and non-stoichiometry*. Springer Berlin Heidelberg: Springer series in materials science; 2002. 250 p. https://doi.org/10.1007/978-3-662-04876-4

33. Velmuzhov A. P., Sibirkin A. A., Shiryaev V. S., … Koltashev V. V. Preparation of Ge – Sb – S – I glass system via volatile iodides. *Journal of Optoelectronics & Advanced. Materials*. 2011;13(8): 936–939.

34. Velmuzhov A. P., Sibirkin A. A., Shiryaev V. S., … Plekhovich A. D. Preparation of Ge – Sb – Se – I glass system via volatile iodides. *Journal of Non-Crystalline Solids*. 2014;405: 100–103. https://doi.org/10.1016/j.jnoncrysol.2014.09.015

35. Churbanov M. F., Sibirkin A. A., Vel'muzhov A. P., Shirjaev V. S., Dianov E. M., Plotnichenko V. G. *Method of producing especially pure heat-resistant chalco-idide glass*. Patent RF: No. 2467962. Publ. 27.11.2012, bull. No. 33. (In Russ.). Available at: https://www.elibrary.ru/item.asp?id=37502753

36. Velmuzhov A. P., Sibirkin A. A., Shiryaev V. S., Churbanov M. F. Equilibrium in GeI_4 – S(Se) systems. *Journal of Optoelectronics & Advanced. Materials*. 2011;13(11–12): 1437–1441.

37. Velmuzhov A. P., Sukhanov M. V., Potapov A. M., Suchkov A. I., Churbanov M. F. Preparation of extrapure Ga_2S_3 by reacting GaI_3 with sulfur. *Inorganic Materials*. 2014;50(7): 656–660. https://doi.org/10.1134/S0020168514070152

38. Velmuzhov A. P., Sukhanov M. V., Suchkov A. I., Churbanov M. F., Turina E. A. Preparation of $ZnGa_2S_4$ by reacting GaI_3 and ZnI_2 with sulfur. *Inorganic Materials*. 2016;52(7): 650–654. https://doi.org/10.1134/S0020168516070141

39. Velmuzhov A. P., Tyurina E. A., Sukhanov M. V., Suchkov A. I. Preparation of $ZnGa_2Se_4$ by reacting GaI_3 and ZnI_2 with selenium. *Inorganic Materials*. 2024. (in press).

40. Churbanov M. F., Velmuzhov A. P., Sukhanov M. V. *Method of producing especially pure sulfides of p-elements of group III of the Periodic table*. Patent RF: No. 2513930. Publ. 20.04.2014, bull. No. 11. (In Russ.). Available at: https://patents.s3.yandex.net/RU2513930C1_20140420.pdf

41. PCPDFWIN – a Windows retrieval/display program for accessing the ICDD PDF-2 database, JSPDS – International Center for Diffraction Data, 1998.

42. Binnewies M., Glaum R., Schmidt M., Schmidt P. Chemical vapor transport reactions. Berlin/Boston: Walter de Gruyter GmbH & Co. KG; 2012. 628 p. https://doi.org/10.1515/9783110254655

43. Schlieper A., Feutelais Y., Fries S. G., Legendre B., Blachnik R. Thermodynamic evaluation of the Germanium – Tellurium system. *Calphad*. 1999;23(1): 1–18. https://doi.org/10.1016/S0364-5916(99)00012-7

44. Dembovsky S. A., Kirilenko V. V. Glass formation and chemical compounds in the systems A^{IV} – B^{VI} – C^{VII} (A^{IV} = Si, Ge; B^{VI} = S, Se; C^{VII} = Br, I)*. *Glass Physics and Chemistry*. 1975;3: 225–230. (In Russ.)

45. Pohl S., Seyer U., Krebs B. Sulfidhalogenide des Germaniums: Darstellung and Struktyruren von $Ge_4S_6Br_4$

und $Ge_4S_6I_4$. *Zeitschrift für Naturforschung B*. 1981;36(11): 1432–1436. https://doi.org/10.1515/znb-1981-1116

46. Velmuzhov A. P., Sukhanov M. V., Shiryaev V. S., Suchkov A. I., Plekhovich A. D. Thermal decomposition study of $GeSI_2$ and $Ge_2S_3I_2$ glassy alloys. *Journal of Non-Crystalline Solids*. 2015;411: 40–44. https://doi.org/10.1016/j.jnoncrysol.2014.09.018

47. Velmuzhov A. P., Sukhanov M. V., Plekhovich A. D., ... Churbanov M. F. New method for preparation of specially pure glasses in the Ge – S – I system by melting the products of thermal decomposition of $Ge_2S_3I_2$. *Journal of Non-Crystalline Solids*. 2015;429: 178–182. https://doi.org/10.1016/j.jnoncrysol.2015.09.006

48. Velmuzhov A. P., Sukhanov M. V., Churbanov M. F. *Method of obtaining portionally clear glasses of the system of germanium-sulfur-iodine*. Patent RF: No. 2618257. Publ. 03.05.2017, bull. No. 13. (In Russ.). Available at: https://patenton.ru/patent/RU2618257C1.pdf

49. Velmuzhov A. P., Sukhanov M. V., Shiryaev V. S., Kotereva T. V., Snopatin G. E., Churbanov M. F. Preparation of special purity Ge-S-I and Ge-Se-I glasses. *Optical Materials*. 2017;67: 59–63. https://doi.org/10.1016/j.optmat.2017.03.041

50. Blinov L. N. Modelling, synthesis, and study of new glassy chalcogenide materials. *Glass Physics and Chemistry*. 2015:41(1), 26–30. https://doi.org/10.1134/s108765961501006x

51. Velmuzhov A. P., Sukhanov M. V., Shiryaev V. S., ... Fadeeva D. A. Preparation of especially pure Ge-Se glasses via germanium monoselenide for Mid-IR fiber optics. *Optical Materials*. 2018;84: 888–892. https://doi.org/10.1016/j.optmat.2018.08.029

52. Velmuzhov A. P., Sukhanov M. V., Churbanov M. F. *Method for producing ultra-pure chalcogenide glasses in the germanium-selenium system*. Patent RF: No. 2648389. Publ. 26.03.2018, bull. No. 9. (In Russ.). Available at: https://patents.s3.yandex.net/RU2648389C1_20180326.pdf

53. Velmuzhov A. P., Tyurina E. A., Sukhanov M. V., ... Shiryaev V. S. Preparation of high-purity chalcogenide glasses containing gallium(III) sulfide. *Journal of Non-Crystalline Solids*. 2022;593: 121786. https://doi.org/10.1016/j.jnoncrysol.2022.121786

54. Velmuzhov A. P., Sukhanov M. V., Zernova N. S., ... Kurganova A. E. Preparation of $Ge_{20}Se_{80}$ glasses with low hydrogen and oxygen impurities content for middle IR fiber optics. *Journal of Non-Crystalline Solids*. 2019;521: 119505. https://doi.org/10.1016/j.jnoncrysol.2019.119505

55. Velmuzhov A. P., Tyurina E. A., Sukhanov M. V., ... Shiryaev V. S. Distillation with separate condensation of components as a new way to prepare especially pure Ge_xTe_{100-x} glasses with precisely desired composition. *Separation and Purification Technology*. 2023;324: 124532. https://doi.org/10.1016/j.seppur.2023.124532

56. Devyatykh G. G., Elliev Yu. E. *Introduction to the theory of deep purification of substances**. Moscow: Nauka Publ., 1981, 320 p. (In Russ.)]

57. Velmuzhov A. P., Sukhanov M. V., Plekhovich A. D., ... Shiryaev V. S. Preparation and investigation of Ge–S–I glasses for infrared fiber optics. *Optical Materials*. 2016;52: 87–91. https://doi.org/10.1016/j.optmat.2015.12.019

58. Velmuzhov A. P., Tyurina E. A., Sukhanov M. V., Plekhovich A. D., Shiryaev V. S. Effect of iodine on physicochemical and optical properties of $Ge_{20}Te_{77-x}Se_3I_x$ (x = 0–10) glasses. *Journal of Non-Crystalline Solids*. 2023;622: 122676. https://doi.org/10.1016/j.jnoncrysol.2023.122676

59. Wilhelm A. A., Boussard-Pledel C., Coulombier Q., Lucas J., Bureau B., Lucas P. Development of far-infrared-transmitting Te based glasses suitable for carbon dioxide detection and space optics. *Advanced Materials*. 2007;19: 3796–3800. https://doi.org/10.1002/adma.200700823

60. Galstyan A., Messaddeq S. H., Skripachev I., Galstian T., Messaddeq Y. Role of iodine in the solubility of Tm^{3+} ions in As_2S_3 glasses. *Optical Materials Express*. 2016;6(1): 230–243. https://doi.org/10.1364/OME.6.000230

61. Velmuzhov A. P., Sukhanov M. V., Churbanov M. F., Kotereva T. V., Shabarova L. V., Kirillov Yu. P. Behavior of hydroxyl groups in quartz glass during heat treatment in the range 750–950 °C. *Inorganic Materials*. 2018;54(9): 925–930. https://doi.org/10.1134/S0020168518090169

62. Lallement L., Gosse C., Cardinaud C., Peignon-Fernandez M.-C., Rhallabi A. Etching studies of silica glasses in inductively coupled plasmas: Implications for microfluidic devices fabrication. *Journal of Vacuum. Science & Technology A*. 2010;28: 277–286. https://doi.org/10.1116/1.3298875

** Translated by author of the article*

Information about the authors

Alexander P. Velmuzhov, Cand. Sci. (Chem.), Senior Research Fellow at the laboratory of High-purity chalcogenide glasses for Mid-IR photonics, G. G. Devyatykh Institute of Chemistry of High-Purity Substances of the Russian Academy of Science (Nizhny Novgorod, Russian Federation).

https://orcid.org/0000-0002-8739-3868
velmuzhov.ichps@mail.ru

Maxim V. Sukhanov, Cand. Sci. (Chem.), Senior Research Fellow at the Laboratory of High-purity Chalcogenide Glasses for Mid-IR Photonics, G. G. Devyatykh Institute of Chemistry of High-Purity Substances of the Russian Academy of Science (Nizhny Novgorod, Russian Federation).

https://orcid.org/0000-0003-0525-6286
sukhanov@ihps-nnov.ru

Elizaveta A. Tyurina, Junior Research Fellow at the laboratory of High-purity Chalcogenide Glasses for Mid-IR Photonics, G. G. Devyatykh Institute of Chemistry of High-Purity Substances of the Russian Academy of Science (Nizhny Novgorod, Russian Federation).

https://orcid.org/0000-0002-6107-9862
tyurina.ichps@mail.ru

Vladimir S. Shiryaev, Dr. Sci. (Chem.), Deputy Director for Research, G. G. Devyatykh Institute of Chemistry of High-Purity Substances of the Russian Academy of Science (Nizhny Novgorod, Russian Federation).

https://orcid.org/0000-0002-1726-7313
shiryaev@ihps-nnov.ru

Received 15.08.2024; approved after reviewing 26.08.2024; accepted for publication 16.09.2024; published online 15.01.2025.

Translated by Irina Charychanskaya

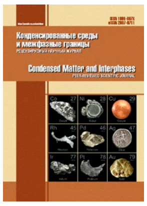

ISSN 1606-867X (Print)
ISSN 2687-0711 (Online)
Condensed Matter and Interphases
Kondensirovannye Sredy i Mezhfaznye Granitsy
https://journals.vsu.ru/kcmf/

Review

Review article
https://doi.org/10.17308/kcmf.2025.27/12484

Phases with layered (AB) and “defective” (A_2B_3) structures in A^{III}–B^{VI} systems. Part 2. Phase diagrams and approaches to some problems of reproducible synthesis in A^{III}– B^{VI} systems. Review

A. Yu. Zavraznov[1]✉, N. Yu. Brezhnev[2], I. N. Nekrylov[1], A. V. Kosyakov[1]

[1]*Voronezh State University,*
1 Universitetskaya pl., Voronezh 394018, Russian Federation

[2]*Voronezh State Agricultural University,*
1 Michurin st., Voronezh 394087, Russian Federation

Abstract

The paper analyzes phase diagrams of A^{III}–B^{VI} systems and phase equilibria involving crystalline compounds formed in these systems. The location of each solid binary phase mainly related to mono- and sesquisulfides families and selenides of aluminum, gallium, and indium on *T*-*x*-diagrams is discussed in detail. The homogeneity regions of these phases were also analyzed if the necessary data were available. For polymorphic (or close to them) transformations, the nature of the occurring structural transformations was described and the temperature stability of various modifications of similar composition was analyzed. Using examples of several systems, it was shown how, by changing the experimental conditions, it is possible to reproducibly obtain compounds with the required structure (even for different polytypes of structures with very similar structures of individual layers) and the required composition (including those within the regions of phase homogeneity). Various methods of reproducible inorganic synthesis were considered, taking into account the features of the phase diagram and phase equilibria. In conclusion, current and partially still unresolved issues concerning the characteristics of the $A_2^{III}B_3^{VI}$ and $A_1^{III}B_1^{VI}$ compounds were analyzed.

Keywords: Chalcogenides, *A*(III)*B*(VI), Stoichiometric vacancies, Phase diagrams, Phase equilibria

For citation: Zavrazhnov A. Y., Brezhnev N. Y., Nekrylov I. N., Kosyakov A. V. Phases with layered (AB) and “defective” (A_2B_3) structures in A^{III}- B^{VI} systems. Part 2. Phase diagrams and approaches to some problems of reproducible synthesis in A^{III}– B^{VI} systems. Review. *Condensed Matter and Interphases*. 2025;26(1): 29–47. https://doi.org/10.17308/kcmf.2025.27/12484

Для цитирования: Завражнов А. Ю., Брежнев Н. Ю., Некрылов И. Н., Косяков А. В. Кострюков В. Ф. Фазы со слоистыми (AB) и «дефектными» (A_2B_3) структурами в системах A^{III}–B^{VI}. Часть 2. Фазовые диаграммы и подходы к некоторым задачам воспроизводимого синтеза в системах A^{III}–B^{VI}. Обзор. *Конденсированные среды и межфазные границы*. 2025;26(1): 29–47. https://doi.org/10.17308/kcmf.2025.27/12484

✉ Alexander Y. Zavrazhnov, e-mail: alzavr08@rambler.ru
© Zavrazhnov A. Y., Brezhnev N. Y., Nekrylov I. N., Kosyakov A. V., 2025

The content is available under Creative Commons Attribution 4.0 License.

1. Introduction

This series of review articles is devoted to the description of two large groups of inorganic substances with very unusual structures and properties: mono- and sesqui-chalcogenides of Al, Ga, and In compounds. The first part of the study considers the structural features of phases of[*] $A_1^{III}B_1^{VI}$ and $A_2^{III}B_3^{VI}$ families and the possible areas of practical use of these compounds based on structural features. This second part of the study aimed to summarize and reconcile the data on phase diagrams and equilibria in $A^{III}–B^{VI}$ systems. The main attention was paid to the relationship between a specific phase diagram and the conditions of formation of certain modifications of crystalline phases of the families of mono- and sesquisulfides and selenides of aluminum, gallium, and indium. In this part of the study we also considered the basics of new methods for precision variation of both the phase and non-stoichiometric composition of already synthesized crystalline chalcogenides. The search for such methods is due to the fact that traditional methods of regulating the composition of the solid phase through vapor (for example, during directional crystallization with controlled vapor pressure) are almost unsuitable for $A^{III}B^{VI}$ chalcogenides due to the very low values of saturated vapor pressures above condensed phases even under conditions of contact with melts (S - L - V equilibrium) [1]. Both the previous and the present (second) parts of the review are based on the analysis of both third-party literary data and the results of the studies of authors of this review and other VSU employees.

2. Al-S and Al-Se systems

2.1. The T-x-diagram and phase equilibria in the Al-S system

When mentioning the aluminum-sulfur system, any chemist will immediately recall the existence of only one compound, Al_2S_3, which is easily obtained by direct synthesis (for example, by igniting a mixture of powdered Al + S). Until recently, this aluminum sulfide was considered unpromising for high-tech materials science. Indeed, Al_2S_3 is easily destroyed in air and liquid water (the latter interaction is a well-known convenient method for obtaining gaseous hydrogen sulfide). Despite the above, the example of the Al – S system clearly demonstrates how the phase diagram can become the basis for the creation of a new and possibly very promising chemical technology even in the case when solid intermediate phases cannot be obtained at room temperature (as AlS), or they quickly degrade in the atmosphere (as Al_2S_3).

The detailed analysis clearly demonstrates that the Al – S system is not so simple. Thus, back in 1940, Murakami and Shibata [2] showed that, along with Al_2S_3, there is also ***mono***-aluminum sulfide AlS, which can only be obtained at temperatures around 1000 °C. However, the region of existence of AlS (~50 °C) can be easily “skipped”, since when the upper limit of existence is exceeded, aluminum monosulfide decomposes according to a peritectic reaction (see Fig. 1):

$$AlS = L_2 + \gamma\text{-}Al_2S_3. \qquad (1)$$

As the temperature decreases, the AlS phase also decomposes. Moreover, it has not yet been possible to preserve aluminum monosulfide even with rapid quenching. The decomposition of AlS during cooling results in almost pure molten aluminum (L_1 liquid) and aluminum sesquisulfide [3]:

$$AlS = L_1 + \gamma\text{-}Al_2S_3. \qquad (2)$$

The authors of later studies [4-8] conducted a number of experiments using thermal and X-ray diffraction analysis (XRD), as well as optical metallography. The results of these studies demonstrated that aluminum monosulfide AlS melts peritectically at ~1058 °C (reaction 1) and Al_2S_3 sesquisulfide melts congruent at ~ 1073 °C. The general appearance of the diagram is shown in Fig. 1, and the most important data on phase equilibria are summarized in Table 1.

Among the features of the presented diagram, in addition to the already mentioned AlS, observed on T-x-diagram in a narrow temperature

---

[*] Various $A^{III}B^{VI}$ modifications, related by solid-phase transformations, are often characterized by similar but different compositions (for example, $\gamma Ga_{2+\delta}S_3$ and $\alpha' Ga_2S_3$). This contradicts the classical definition of polymorphism, according to which different structures must have the same composition. Taking into account the proximity of structural $A_2^{III}B_3^{VI}$ motifs we discussed phases of the sesqui-chalcogenide families (Ga_2S_3, Ga_2Se_3 etc.), trying to avoid using the term “polymorphism”. We also discussed phases of the monochalcogenide families.

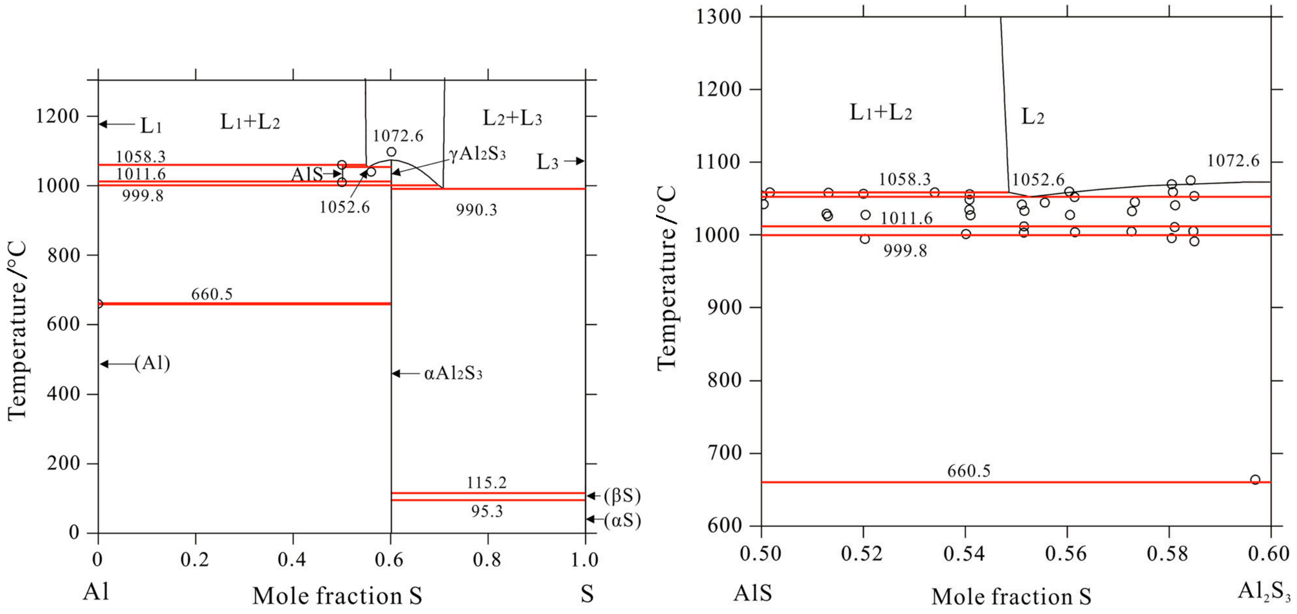

a b

Fig. 1. *T-x*-diagram for the Al – S system [3] (*a*) and an enlarged fragment of this diagram in the region for a sulfur content from 50 to 60 mol. % (*b*) [3] (*b*). The results of the CALPHAD calculation using the substitution solution model are given together with the experimental data

range, two modifications of Al_2S_3 should be noted (α and γ; the latter melts congruently), as well as three liquid phases separated by wide areas of stratification: L_1 - almost pure molten aluminum, L_3 – almost pure liquid sulfur and L_2 – a melt close in composition to the Al_2S_3. In addition, the authors of a new detailed analysis of the Al – S system [3] came to the conclusion that the upper limit of the existence of aluminum monosulfide is associated not with the peritectic (1), but with a very rare among phase equilibria synthetic transformation, in which a solid phase can be obtained by cooling two immiscible melts (shift to the right of equilibrium 3):

$$AlS = L_1 + L_2 \quad (3)$$

Structurally, AlS monosulfide has not yet been studied. The reason for this is the high aggressiveness of “low-valent” aluminum compounds in relation to almost any solid materials and the impossibility of hardening AlS without decomposition. Several polymorphic modifications have been identified for Al_2S_3, but, according to the data of [8] and [3], which have recently been confirmed by the results of experimental [9] and computational [10, 11] studies, only two modifications can be stable: the hexagonal form α-Al_2S_3 (SG $P6_1$, exists from room temperatures to ~1000 °C) and γ-Al_2S_3 phase with a trigonal structure of corundum (SG $R\bar{3}c$). The γ-phase exists at high temperatures: from ~1000 °C to the congruent melting point (~1070 °C). The α-modification, since it is the one that has a structure with stoichiometric vacancies, is of greatest interest. This structure is derived from the crystal lattice of “defective” wurtzite and was discussed in detail above in the analysis of “defective” gallium sesquisulfides of the α-Ga_2S_3 modification.

2.2. Physicochemical principles of using equilibria involving aluminum sulfides. Obtaining metallic aluminum using the carbosulfide method

Despite the apparent “academic nature” of the question of the existence of the AlS monosulfide on the phase diagram, which is formed only over a narrow temperature range and is not preserved upon hardening, the control of the processes of synthesis and decomposition of this substance seems very important for the development of a new scheme for the industrial production of metallic aluminum (see below). The search for new ways of obtaining metallic aluminum is connected with the fact that the traditional technology of smelting aluminum using electrolysis (the Hall-Héroult process) is accompanied by emissions of environmentally harmful carbon fluorides. These

Table 1. Three-phase equilibria of condensed phases in the Al – S system according to from a number of literary sources. In the columns "Compositions" the numerical values are given for the phases listed in accordance with the corresponding equations of phase reactions. All calculated (according to different models) data of the table refer to the work [3], the experimental values – to the sources [6–8]

Equation	Phase reaction type	*T*, °C	Compositions, mol. % S*			Source of information
$L_1 = Al_s + \alpha\text{-}Al_2S_3$	Eutectic (degenerate)	~ 660	–	0	60	Experiment, [6]
		660.5	0	0	60	Substitutional solution model (SSM)
		660.5	0	0	60	Associate model (AM)
$L_1 + L_2 = A1S$	Synthetic	1060.0	–	–51	50	Experiment, [6]
		1058.3	0	54.3	50	SSM
		1059.9	4.1	54.8	50	AM
$L_1 = AlS + \gamma\text{-}Al_2S_3$	Eutectic	1040.0	56.0	50.0	~ 59	Experiment, [6]
		1052.6	55.3	50.0	60	SSM
		1052.6	55.7	50.0	60	AM
$A1S = L_1 + \gamma\text{-}Al_2S_3$	Catatectic	1010.0	50.0	...	< 60	Experiment, [6]
		1011.6	50.0	0	60	SSM
		1011.5	50	2.6	60	AM
$L_2 = \gamma\text{-}A1_2S_3 + L_3$	Monotectic	973.0	–	...	...	Experiment, [7]
		990.3	70.7	60	100	SSM
		970.6	63.6	60	100	AM
$L_3 = \alpha\text{-}Al_2S_3 + \beta\text{-}S$	Eutectic (degenerate)	~ 115	~ 100	60	~ 100	Experiment, [8]
		115.2	100	60	100	SSM
		115.2	100	60	100	AM
$\beta\text{-}S = \alpha\text{-}Al_2S_3 + \alpha\text{-}S$	Eutectoid (degenerate)	~ 95.5	~ 100	60	~ 100	–
		95.3	100	60	100	SSM
		95.3	100	60	100	AM

fluorides (CF_4 with admixture of C_2F_6) are released as by-products at the sacrificial graphite anode, which is immersed in an $Al_2O_3 – Na_{3x}K_x[AlF_6]$ melt.

***Step* 1.** *Carbosulfidization of aluminum ore containing mostly* Al_2O_3 [12]

One of the most promising alternative methods of obtaining Al is based on the so-called carbosulfide method, which consists of the following three stages. The Loutfy method is based on the reaction of aluminum ore (Al_2O_3) with coal (graphite) and sulfur vapor at a temperature of 1027 – 1227 °C with the formation of an Al_2S_3 melt (4):

$$Al_2O_{3\,(s)} + 3C_{(s)} + 1.5S_{2\,(g)} = Al_2S_{3\,(l)} + 3CO_{\,(g)}. \quad (4)$$

A slightly different way of obtaining aluminum sesquisulfide was proposed by Sportel and Verstraten. According to this scheme $\gamma\text{-}Al_2O_3$ reacts with carbon disulfide vapors at a slightly lower temperature (⩾ 750 °C), but under pressure from 5 to 35 atm:

$$Al_2O_{3\,(g)} + 3CS_{2\,(g)} = Al_2S_{3\,(l)} + 3CO_{\,(g)} + 1.5S_{2\,(g)}. \quad (5)$$

Since CO and sulfur vapor react to form carbon monoxide sulfide, the latter equation is sometimes represented as:

$$Al_2O_{3\,(s)} + 3CS_{2\,(g)} = Al_2S_{3\,(l)} + 3COS_{\,(g)}. \quad (6)$$

The carbon disulfide used in this scheme can be obtained directly in the same reactor by reacting natural gas with sulfur vapor:

$$CH_{4\,(g)} + S_{2\,(g)} = CS_{2\,(g)} + 2H_{2\,(g)}. \quad (7)$$

***Step* 2.** *Incongruent sublimation of the Al_2S_3 melt.* The resulting melt is heated under reduced pressure to temperatures from ~1330 to ~1630 °C. This results in the removal of some of the sulfur from the melt and the composition of the liquid (L_2) shifts to a composition with a sulfur content of 53–54 mol. %:

$$Al_2S_{3\,(l)} \rightarrow L_{2\,(\sim AlS)} + S_{2\,(g)}. \quad (8)$$

***Step* 3.** *Release of* Al *during the catathetic decay* of AlS. Decrease in melt temperature of L_2, obtained in the previous step, causes crystallization of the AlS phase (Fig. 1). Further cooling to $t < 1010$ °C causes a disproportionation of aluminum monosulfide according to reaction (2). As a result, along with solid Al_2S_3, almost pure liquid aluminum is formed. The molten metal flows into the bottom of the reactor and the aluminum sesquisulfide is redirected for reheating for the removal of the sulfur.

Recently, other applications of aluminum sesqui-chalcogenides have been discovered. In particular, α-Al_2S_3 was used in promising chemical power sources (CPS) [13, 14]. Al-S batteries operate at relatively low temperatures (~85 °C) due to the transfer of electrons from the anode (metallic Al or Al alloy) to the cathode – sulfur (S^0). Free sulfur is intercalated into graphite-like boron nitride (α-BN) or distributed in an array of carbon nanotubes. When the battery discharges, sulfur turns into microcrystalline α-Al_2S_3. During charging, Al^{3+} ions are removed from the sulfide, and sulfur is converted to its original oxidized state S^0. It should be emphasized that the possibility of fast charging of Al-S batteries is probably associated with the structural features of α-Al_2S_3, which contains *stoichiometric vacancies* V_{Al}, which facilitates the diffusion of Al^{3+} ions in the solid phase. For the transfer of Al^{3+} ions in a liquid electrolyte, an ionic liquid is used in which the cations are represented by nitrogen-organic ions (for example, the cation of 1-ethyl-3-methylimidazolium), and the anions are $[AlCl_4]^-$ and $[Al_2Cl_7]^-$ ions. There are also reports on the high potential of such chemical power sources in which sulfur in the cathode material is partially or completely replaced by selenium [15], [16], and such CPS can be used even at room temperature.

2.3. The Al – Se system and aluminum selenide Al_2Se_3

In this part of the review, together with the Al – S system, we will also consider the corresponding selenium system. This is due to the fact that aluminum selenides have been less studied than sulfides, and the practical application of the only intermediate phase of this system, aluminum sesquiselenide (Al_2Se_3), is at the initial stage.

According to [3], a congruently melting narrowly homogeneous compound exists in this system at pressures close to atmospheric (Fig. 2), the monoclinic (Cc) structure of which is characterized by an ordered arrangement of vacancies and is considered in more detail in Chapter 2.1 (when considering the α'-Ga_2S_3 isostructural phase). At the same time, we note that the diagram presented in Fig. 2 is the result of calculations based on certain solution models and needs to be verified. The fact that this selenide was previously assigned the formula Al_3Se_4, may indicate a noticeable shift in the composition towards excess of aluminum relative to the ideal stoichiometry with a selenium content of 60 mol. % (compare with phase composition γ-$Ga_{2+\delta}S_3$ in the following described system).

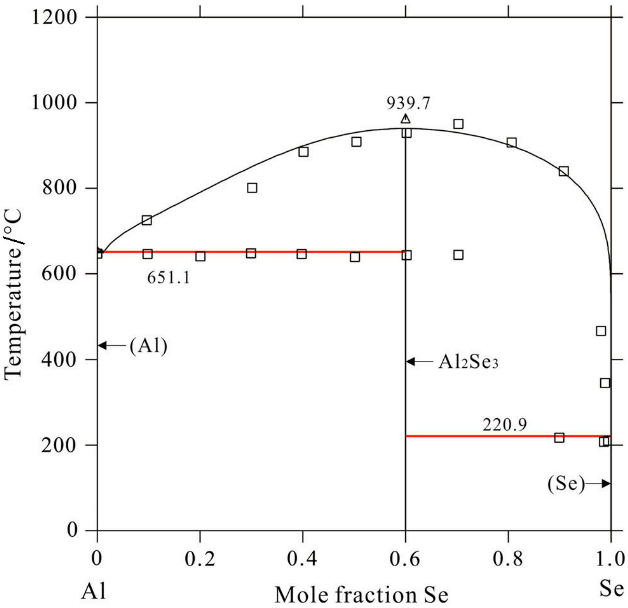

Fig. 2. *T*-*x*-diagram for the Al – Se system [3]. The results of the CALPHAD calculation using the substitution solution model are given together with the experimental data

3. The Ga – S system

When searching for ways of reproducibly synthesizing crystalline phases, especially in the case of the existence of many polymorphic modifications, it is highly desirable to find conditions under which these phases are stable relative to other compounds of this system*. In

---

* Definitely, synthesis can be performed in a way that allows immediately obtaining a metastable or even unstable (under reaction conditions) compound. However this approach has the risk of non-reproducibility of the method.

other words, when choosing such a strategy, the resulting modification must be present in the equilibrium phase diagram of the given system. In this case it is possible to obtain this phase under conditions close to equilibrium and then harden it. In our opinion, unsuccessful and mutually exclusive descriptions of the paths of formation of certain volumetric structures are associated with contradictory data on phase equilibria and on the phase diagram. The Ga – S system is an example of the need for a detailed study of the *P-T-x-* (or at least, *T-x-*) diagram.

Until now, the fact that this system contains solid congruently melting phases with the GaS and Ga_2S_3 stoichiometries, and also the fact that the latest stoichiometry corresponds to several modifications with “defective” crystal lattices, based on sphalerite or wurtzite structural types have not caused controversy [17], [18]. In addition, there was no question that the saturated vapor over gallium sulfides was represented by Ga_2S and S molecules. In this case, GaS sublimates incongruently with the formation of almost only Ga_2S, and for Ga_2S_3 in the homogeneity region there are congruently evaporating compositions [19, 20]. It should be noted that other chalcogenides of aluminum, gallium, and indium behave similarly during sublimation [1, 21].

However, until now, it has not been clear what other phases can be realized in this system and what is the structure of the corresponding diagram. In particular, in the studies of famous authors [20] and [19] GaS and Ga_2S_3 sulfides were considered as *the only* crystalline intermediates in this system (Fig. 3). However, the study [22] provides a completely different pattern, where in addition to gallium mono- and sesquisulfide, subsulfide (Ga_2S), as well as Ga_4S_5, both with an incongruent melting type, were indicated. In relatively modern reference studies [23] and [24] the Ga – S system is also presented in accordance with [22] (Fig. 4). In addition, the existence of Ga_2S and Ga_4S_5 phases was confirmed in an independent study [25].

However, in our latest detailed studies [26-31] we obtained a *T-x-* diagram of the Ga-S system (Fig. 5), significantly different from either of the two images shown above. Moreover, the diagram in Fig. 5 turned out to be close to the images published in little-known French-language studies [18, 32]. It should be emphasized that the ideas about the system and equilibria corresponding to Fig. 5 were obtained using various methods that confirm each other: X-ray diffraction analysis (XRD, HTXRD – up to 600 °C), *in situ* X-ray analysis using synchrotron X-ray radiation for high-temperature (up to ~

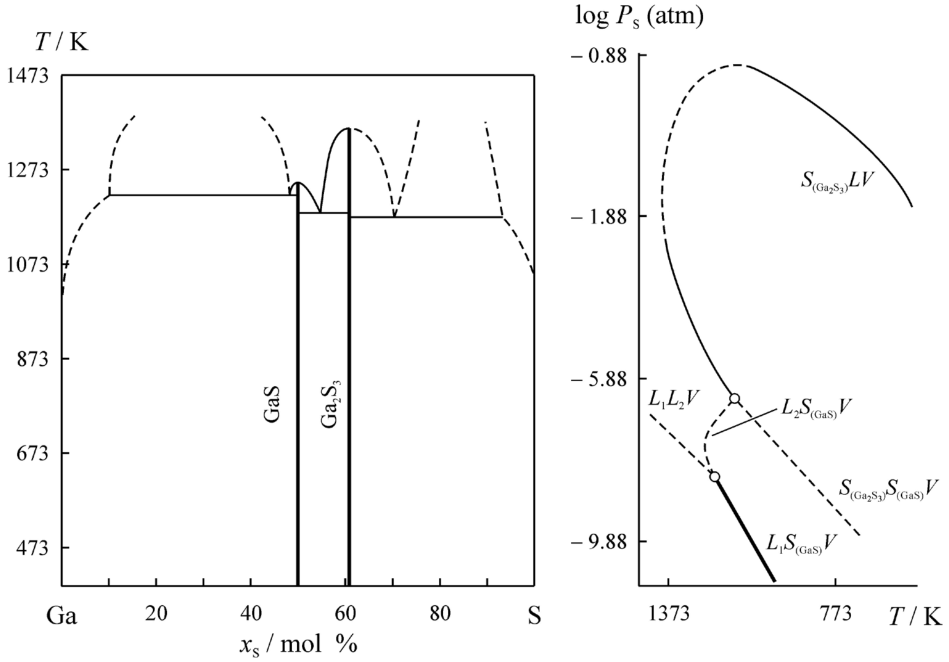

Fig. 3. *T-x* diagram for the Ga-S system according to the data of [19, 20]

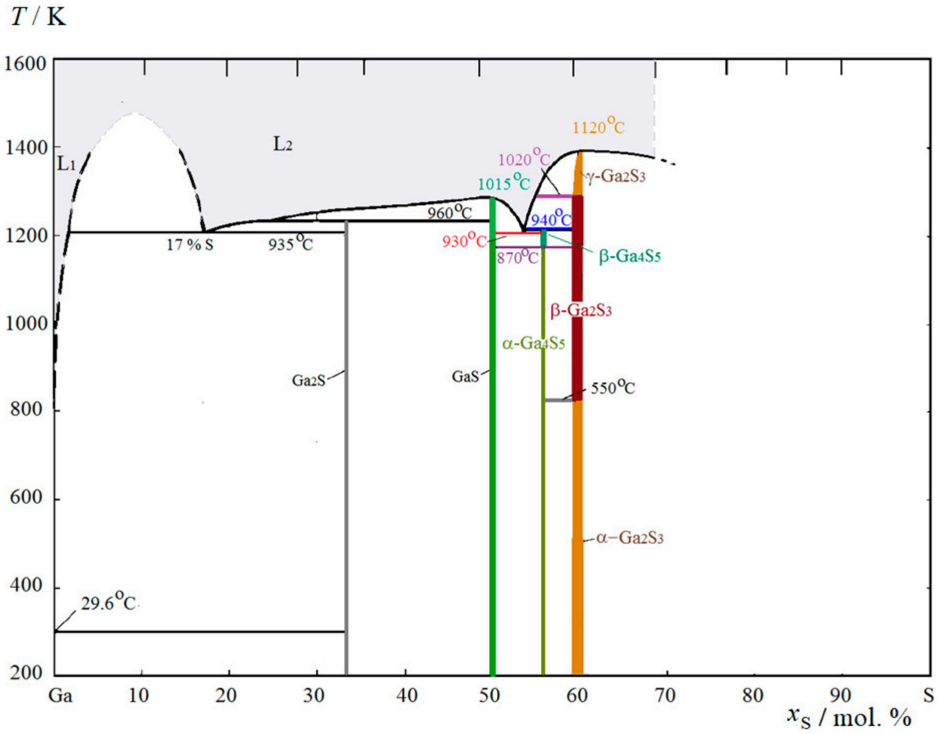

Fig. 4. *T-x* диаграмма системы Ga-S по данным [22]

1030 °C) studies of phase equilibria, differential thermal analysis (DTA) together with a new static method of thermal analysis [33], and methods of transmission electron microscopy (HRTEM, SAED). This diagram and the phases present in it are analyzed in detail in a recently published article [31]. We will not discuss this study in detail, just list the main features of the Ga – S system.

1. The existence of a Ga_2S solid phase was not confirmed experimentally. Moreover, there are no structural data on this substance in the literature. Most probably, the false ideas about solid gallium subsulfide arose from an analysis of the gross composition of the product of resublimation of gallium monosulfide from the hot zone to the cold zone. Indeed, the sublimation of GaS occurs incongruently with the predominant formation of Ga_2S vapor. However, upon condensation, the subsulfide vapors disproportionate, yielding a sample of Ga + GaS heterogeneous powder.

2. For the Ga_4S_5 phase found in [22], most likely, an error in the determination of the composition was made. Probably, in this study the authors obtained one of the phases of the Ga_2S family, namely, γ-$Ga_{2+\delta}S_3$ with a sulfur content of about 59.3 mol. %.

3. If gallium monosulfide is a practically completely stoichiometric compound, for gallium sesquisulfide there is a whole family of phases with “defective” structures of sphalerite or wurtzite. In this case, the phase with the highest ordering of stoichiometric vacancies during genesis from the wurtzite α′- Ga_2S_3 structure is, according to the ideas [18], the only phase that is stable at room temperature. Moreover, like GaS, it is narrowly homogeneous and almost completely stoichiometric. Other phases of this family can be stable (relative to other phases) only at high temperatures. In this case, it is mostly shifted towards gallium relative to the ideal composition – up to 0.7 mol. % – “defective-sphalerite” modification γ-$Ga_{2+\delta}S_3$, which is realized on the phase diagram in a narrow temperature region of about 900 °C. Higher temperature forms – α- and β-Ga_2S_3 are grouped closer to the composition of 60 mol. % S. All of them can be isolated individually and stored at room temperature after annealing under equilibrium conditions, followed by quenching.

4. Obtaining one or another modification of the Ga_2Se_3 family, probably, is very dependent on the presence of even small concentrations of impurities, as evidenced by the following facts.

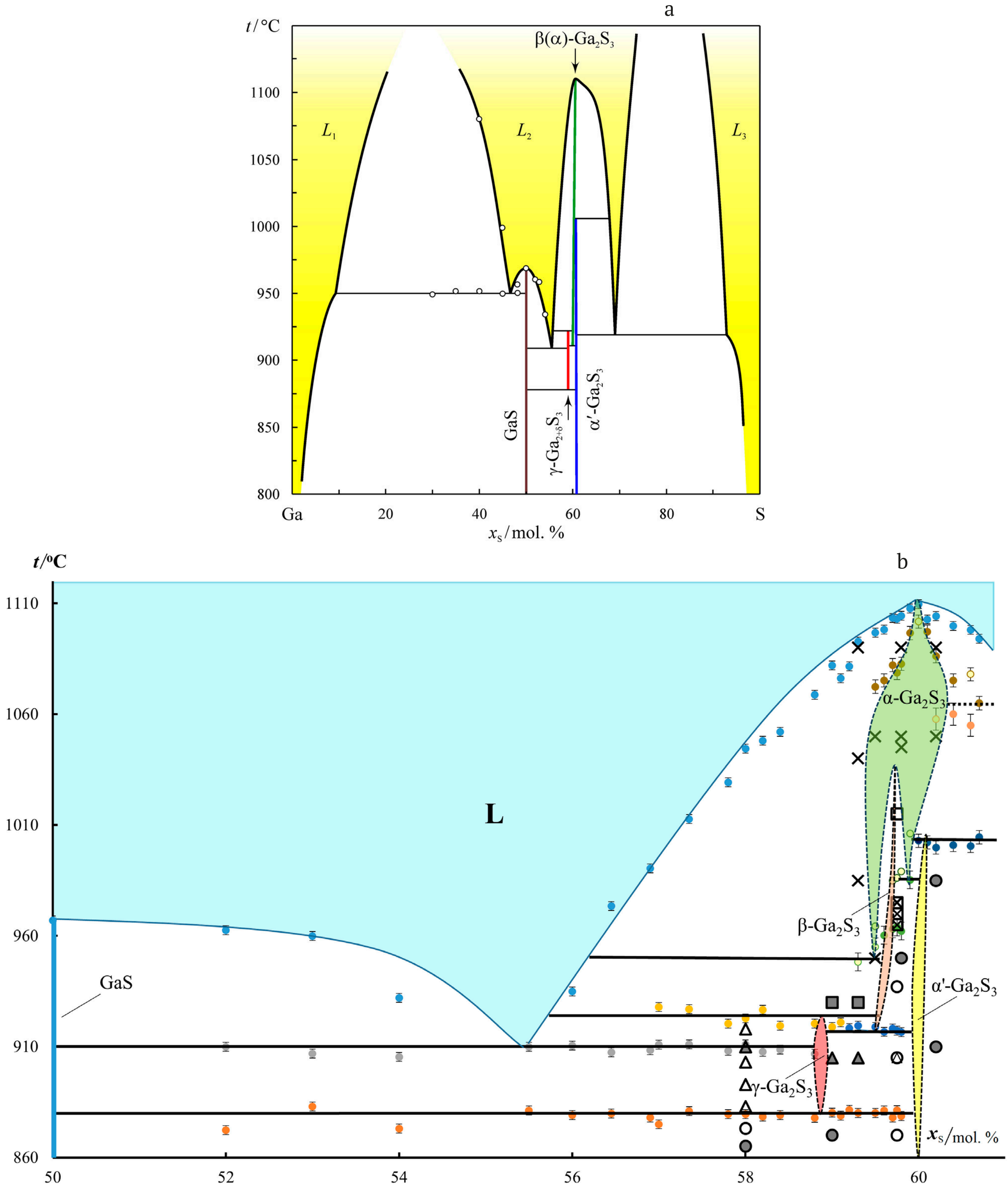

Fig. 5. New data on the *T*-*x* diagram of Ga – S: general view [29] (*a*) and a detailed fragment in which 4 “defective” modifications of the Ga_2S_3 family are realized [31] (*b*)

a). In particular, we observed stabilization of the cubic γ-$Ga_{2+\delta}S_3$ phase when introducing already 0.5 mol. % iron [34]. Hexagonal modifications, α- and β-Ga_2S_3, are stabilized by the addition of manganese [35]. These modifications were observed at temperatures much lower than those allowed for this system by the phase diagram of the Ga – S system, even taking into account a small possible supercooling.

b). The authors of [36] reported the isolation of a cubic form during crystallization from potassium iodide or lead chloride melts [36]. Moreover, in the latest study, the order of releasing of equilibrium phases of the Ga_2S_3 family at different temperatures turned out to be completely different than it follows from *T-x*-diagrams of the Ga – S system (compare Fig. 5 and Fig. 6).

c). A cubic γ-phase was also released during the crystallization of glasses of the Ga-Ge-S system (the Ga_2S_3 – GeS_2 section) at 750 °C. It should be noted that for pure gallium sesquisulfide the γ-$Ga_{2+\delta}S_3$ phase becomes metastable at temperatures below 878 °C and quickly turns into α'-Ga_2S_3 at *t* < 840 °C (with slow cooling or annealing) [37].

d). In the production of gallium sesquisulfide by the oxidation of molten gallium triiodide with elemental sulfur at 500 °C the γ-$Ga_{2+\delta}S_3$ cubic high-temperature modification was also released; with a slight increase in temperature (up to 650 °C) another phase with a hexagonal structure was released ($P6_1$) [38]. It should be noted that for *pure* gallium sesquisulfide both modifications should at the specified temperatures unambiguously transform into monoclinic α'-Ga_2S_3*.

Compounds from the gallium sesquisulfide family should be very promising for materials science (luminescent properties [39], [40], nonlinear optics [40], etc.). However, the incomplete reproducibility of the isolation of each individual modification significantly limits their use. We hope that a refined phase diagram of the Ga–S system, as well as detailed studies of the ternary diagrams Ga–S–X (X is an impurity), especially taking into account the extremely high sensitivity of the stability of various modifications to very small concentrations of impurities will contribute to the solution of the question of the use of phases of the Ga_2S_3 family in modern materials science.

4. The Ga – Se system

Currently, the Ga–Se system appears to be the poorest among A^{III} – B^{VI} based on the number of intermediate solid phases [3, 21]. The *T-x*-diagram of the discussed system contains two polymorphic modifications of layered gallium monoselenide [40] and two modifications of gallium sesquiselenide [41], [42] (Fig. 7).

“Defective” compounds of the Ga_2Se_3 family are represented by a high-temperature β-Ga_2Se_3 modification with a sphalerite structure (with disordered vacancies) and a low-temperature

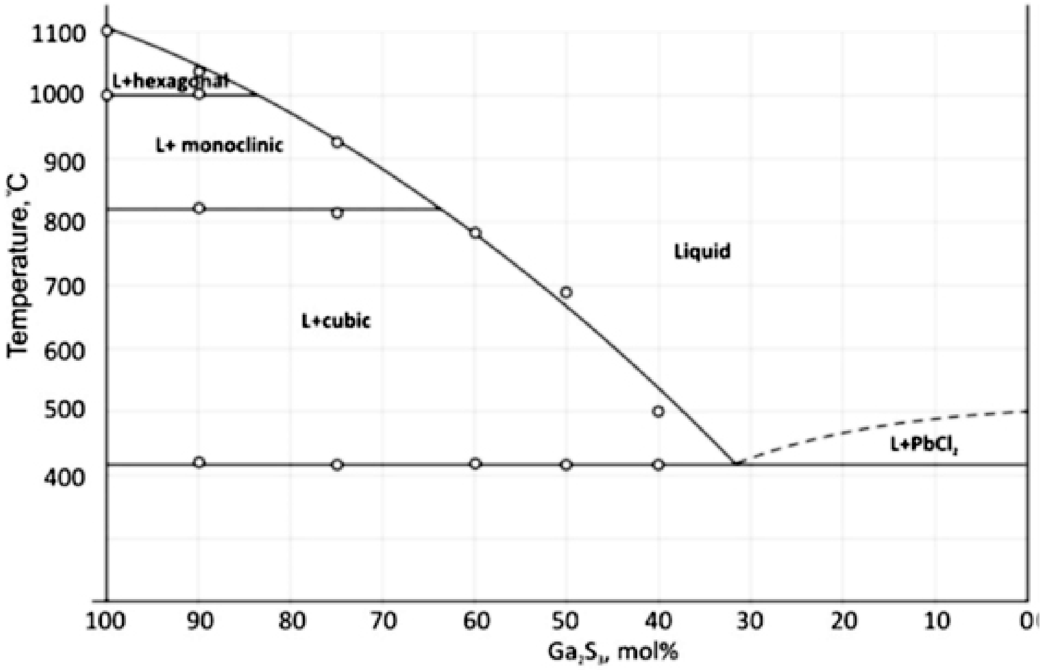

Fig. 6. *T-x* diagram for the Ga_2S_3 – $PbCl_2$ according to the data of [36]

---

* The authors [38] for the hexagonal modification with SG $P6_1$ used the name β-Ga_2S_3. In the majority of literary sources and in our studies this phase appears as α-Ga_2S_3, and the designation β-Ga_2S_3 was assigned to the wurtzite-like “defective” form with SG $P6_3mc$.

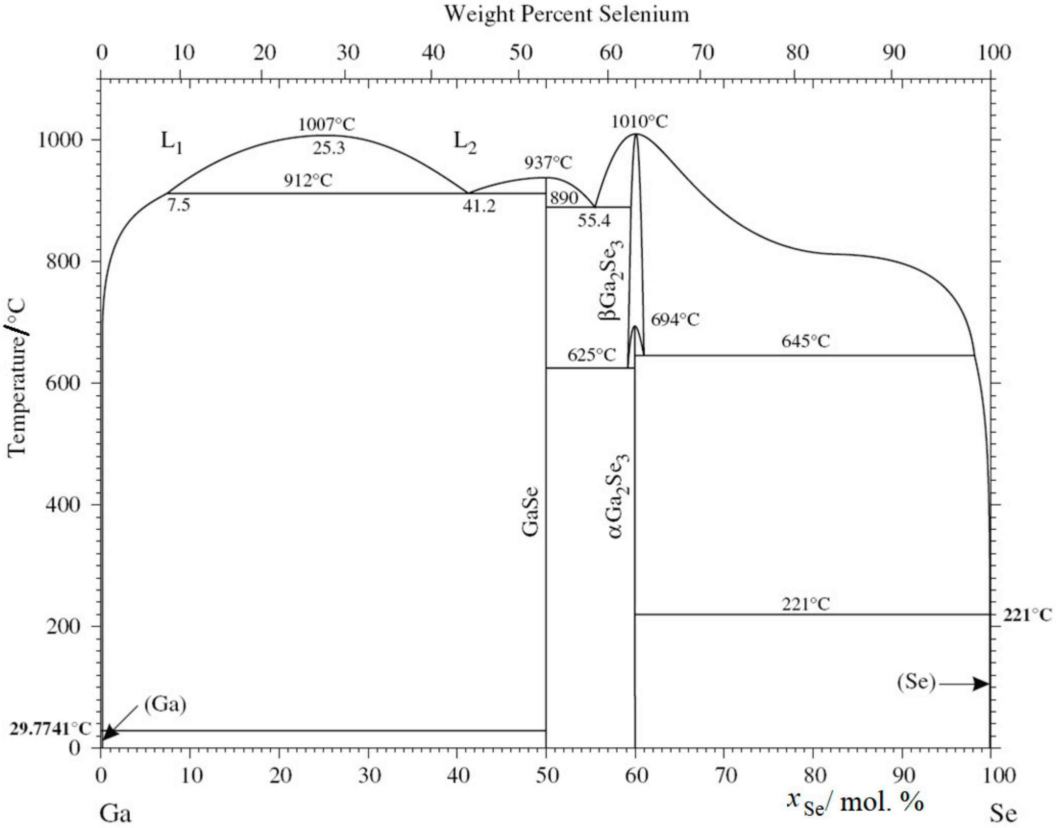

Fig. 7. *T-x* diagram for the Ga-Se system according to the data of [41, 42]

monoclinic α-Ga_2Se_3 form, which is isostructural to α′-Ga_2S_3 (with ordered vacancies) [41, 42]. At the same time, it should be noted that in our preliminary studies we have not yet been able to confirm the equilibrium existence of high-temperature α-phases, despite a fairly detailed study. In the latter, in addition to DTA, *in situ* X-ray powder analysis with X-ray synchrotron radiation was used. This allowed the Ga–Se system sample to be annealed under specific high-temperature conditions for several hours to establish equilibrium.

4.1. Regulation of the GaSe polytypic structure and composition by the SSCTR method

In our study, we were able to reproducibly obtain individual polytypes of layered gallium monoselenide [43–45]. For this purpose, a non-isothermal version of phase composition control (both phase and within the homogeneity region) was used using the method of selective chemical transport reactions (SSCTR).

The essence of the SSCTR is the introduction or removal of one of the components of the solid phase (in our case, Ga) during a selective gas transport reaction. In an experiment on regulating the phase composition using the SSCTR method, the initial sample is placed at one end of the ampoule, and the batch, which is the source of the transported component, is placed at the other end. Also, a certain amount of transport agent is introduced into the ampoule, which, under experimental conditions, produces unsaturated vapor. Then, after removing the air, the sealed ampoule is placed in an oven in a way that the higher temperature (T_2) corresponds to the sample, and the lower temperature (T_1) corresponds to the batch. In the system, selective transfer of only one component between the batch and the sample occurs. It should be emphasized that this transfer gradually ceases as the controlled sample reaches a certain phase composition (i.e. a certain structure) and a certain non-stoichiometry (i.e. a specific composition within the homogeneity region). As a result, a steady state without mass transfer is realized in the system, in which the sample can exist for an indefinite period of time at the fixed temperatures of the hot and cold zones (T_2, T_1) [46].

In our studies [43], [46], to regulate the composition and structure of gallium selenides, pure gallium was used as a batch and gallium triiodide was used as a transport agent. The chemistry of selective transfer was reduced to a reversible reaction (9):

$$2\mathrm{Ga}^{\text{in the composition of Ga selenides}} + \mathrm{GaI}_3^{\text{vapor}} \rightleftarrows 3\mathrm{GaI}^{\text{vapor}}. \quad (9)$$

It should be noted that at temperatures up to ~ 900 °C gallium selenides have only small values of saturated vapor (Ga_2Se, Se_2 pressure does not exceed several mm Hg [1, 21]). This fact, as well as the absence of stable forms of binary and ternary selenium iodides in the pair, lead to the fact that the role of selenium or its compounds in mass transfer is minimal. The latter allows the selective nature of iodide chemical mass transfer of gallium selenides.

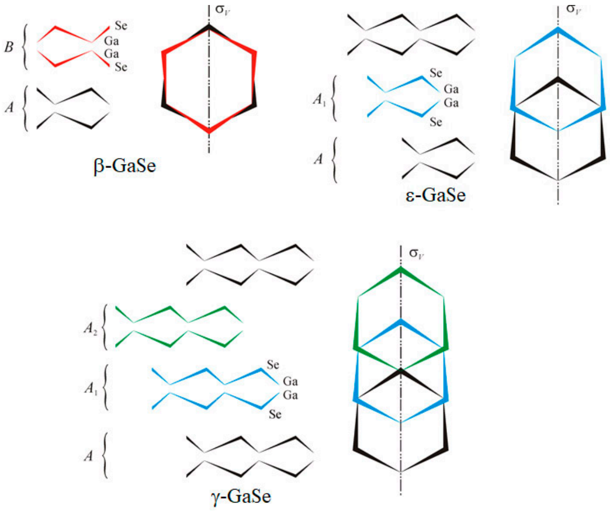

Fig. 8. Structures of some polytypes of GaSe (according to [44])

The results of the study showed that γ-modification of GaSe (alternating packets of the ...ABCABC...type, Fig. 8) exists on the phase diagram only with an excess of selenium and only at high temperatures close to the melting point. The ε-GaSe polytype (alternating packets of the ...ABAB-...type, Fig. 8) always turns out to be stable relative to other phases at low temperatures (up to ~700 °C), as well as at temperatures up to melting in the case of high gallium content within the homogeneity region [43, 44]. On the *T*-*x*-diagram these polytypes according to our research data are shown in Fig. 9.

Thus, it is possible to solve a rather complex problem of reproducible obtaining of a certain polytype. The deformation nature of the

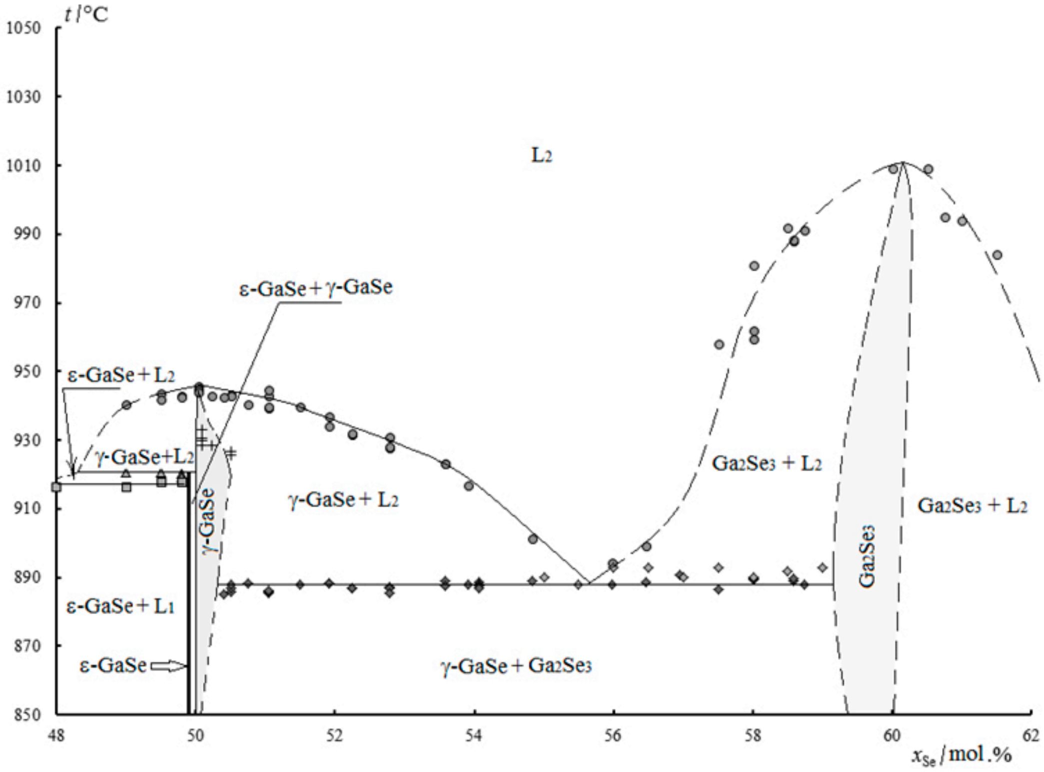

Fig. 9. High-temperature region of *T*-*x*-diagram for the Ga – Se system according to [45]

transformation of one polytype into another allows in this case to preserve single crystals of substances without their destruction. It also should be noticed that in [43], [44] the possibility of regulating not only the polytypic structure, but also the composition within the homogeneity regions of these phases is shown.

5. The In – S system

When moving to indium chalcogenides, a much greater variety of intermediate phases is observed. This is usually associated with the greater tendency of indium to form compounds with a larger proportion of the ionic component of the chemical bond (especially compared to gallium) with a variety of charge states (In^{+1}, In^{+3}, to a lesser extent In^{+2}). Thus, on the In – S phase diagram ([47–49], Fig. 10) there are InS phases (two modifications: the low-temperature form InS, which transforms via a distectoid path into the high-temperature form), In_6S_7, $In_{3-x}S_4$ (according to a number of sources, it is also α-In_2S_3), as well as polymorphic modifications of indium sesquisulfide: low-temperature β-In_2S_3 and high temperature γ-In_2S_3. The high temperature InS form, as well as n_6S_7 and $In_{3x}S_4$ melt incongruently. The γ-In_2S_3 is the most resistant to high temperatures and melts congruently at 1097 °C [49] (1090 °C according to [50]).

Taking into account the relatively low values of partial pressures over indium sulfides, their incongruent sublimation and the difficult kinetics of establishing equilibria between condensed phases and their own vapor, it is difficult to use classical tensimetric research methods for the In–S system, as well as classical methods for regulating the composition of these sulfides through the vapor phase. For this reason, the auxiliary component (AC) method seems to be promising both for a detailed analysis of the considered system and for tasks on the synthesis of indium sulfides.

The In–S system was studied by the AC method, primarily using hydrogen with the aid of a spectrophotometric technique [47], [48], [51]. The studied equilibrium in this case can be written as (10):

$$S^{\text{in the composition of In sulfides}} + H_2^{\text{gas}} \rightleftarrows H_2S^{\text{vapor}}. \qquad (10)$$

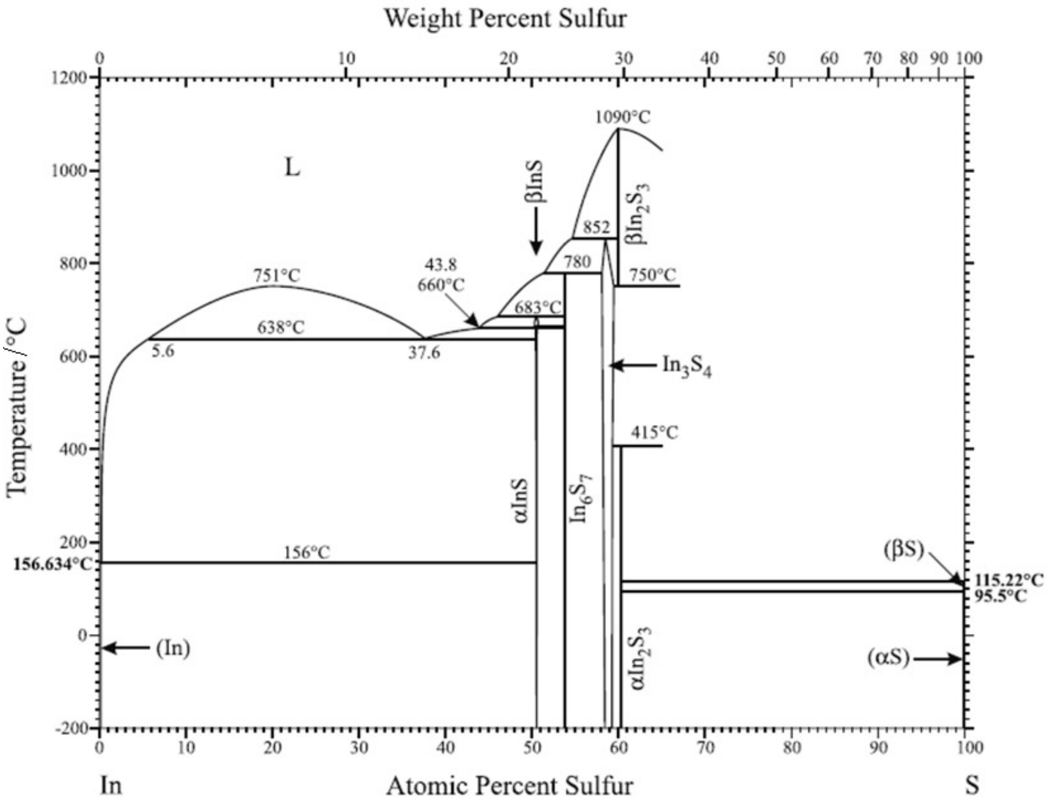

Fig. 10. *T-x* diagram for the In – S [50] system, based on the data of [49]

To achieve equilibrium, the studied sample of the In – S system was kept in contact with hydrogen at a temperature of 400 to 725 °C. After such annealing for many hours, the reactor with the substances (a sealed quartz cuvette) was quenched and the absorption spectrum in the region of hydrogen sulfide absorption was studied ().

In addition to the previously established set of intermediate phases of the In – S system (InS, In_6S_7, $In_{3-x}S_4$, In_2S_3 modifications) it was established that the $In_{3-x}S_4$* phase has a wide homogeneity range: from ~ 58.0 to 59.8 mol. % S. In this case, the behavior of the concentration dependences of the chemical potential of sulfur** in this area of homogeneity turned out to be very unusual. These dependences consisted of alternating almost horizontal and inclined sections, which, according to the authors [51], may indicate a tendency of this cubic phase to disintegrate into separate independent modifications with similar but different compositions.

The auxiliary component method was also used to solve problems related to the synthesis of substances with a given composition, both phase and within homogeneity regions. In these experiments, the goal was to specifically vary the composition of pre-synthesized indium sulfides, both fine-crystalline films and bulk samples [52-54]. For this purpose, chlorine in the form of indium chlorides was used as an auxiliary component (also known as a transport agent). In this case, transfer via a reversible reaction (11) was used, similar to (9):

$$2\mathrm{In}^{\text{in the composition of In sulfides}} + \mathrm{InCl}_3^{\text{vapor}} \rightleftarrows 3\mathrm{InCl}^{\text{vapor}}. \quad (11)$$

In this case, the sulfur atoms chemically bound in indium sulfide practically do not pass into vapor, which allows us to discuss the selectivity (11). However, the use of metallic indium as a control charge in such experiments turned out to be impossible because indium produces much more stable In^{+1} halides compared to similar gallium compounds. As a result, equilibrium (11) turns out to be extremely shifted to the right in the equilibria of the $InCl_3$ vapor with $In_{met.}$ To circumvent this difficulty, we used the dilution of indium in the batch with a chemically inert diluent. This allowed to reduce the activity of indium towards higher halides. Indeed, when using In–Au melt solutions, it was possible to change the direction of indium mass transfer between the sample and the batch and reproducibly obtain a sulfide of the required composition and structure depending on the gold content in the batch [44, 53]. In [54] the possibility of regulating the composition of indium sulfides using a batch of heterogeneous mixtures of indium sulfides (for example, In_6S_7 $In_{3-x}S_4$) instead of expensive gold was demonstrated.

6. The In – Se system

According to our latest studies [30, 55] and data of other authors [56, 57], the *T-x* diagram of the In – Se system is distinguished by a huge variety of phases even in comparison with the In – S system. Solid selenides are realized in a small concentration range (40–60 mol. % S) and demonstrate pronounced polymorphism (Fig. 11). These are In_4Se_3 selenides (however, there is no similar sulfide, or gallium chalcogenides with such a stoichiometry), InSe (a layered structure similar to ε-GaSe), In_6S_7 and In_2Se_3 (several modifications). In our latest studies, which were carried out using a new spectrophotometric technique with an auxiliary component ([58-60]), the following was discovered [30], [56].

1. It was shown that high temperature (650–890 °C) modification of δ-In_2Se_3, is wurtzite-like (SG $P6_3mc$; may contain stoichiometric vacancies), while in the literature it is classified as SG $P\bar{3}m1$.

2. Near the composition corresponding to the stoichiometry of In_6Se_7, there are two phases with similar but different structures and compositions. When this was revealed, alloys of the In – Se system with a selenium content of 54.0 and 57.5 mol. % Se were studied using X-ray phase analysis. Before the study, the alloys were homogenized in repeated long-term annealing

---

* The indium mono- and sesquisulfides differ from the structures of other $A^{III}B^{VI}$ mono- and sesquichalcogenide compounds (except γ-In_2S_3). In particular, the $In_{3-x}S_4$ phase (often not quite correctly called β-In_2S_3) has the structure of a “defective” inverted spinel (see Part 1 of this review).

** More precisely, we are discussing the value (let’s denote it $\ln(K_P^{\#})$, see [51]), which at a constant temperature T is linearly related to chemical potential μ_S in the solid phase [51]: $\ln(K_P^{\#}) = \dfrac{\mu_S}{RT} + Y$, where Y is a constant value (at T = const).

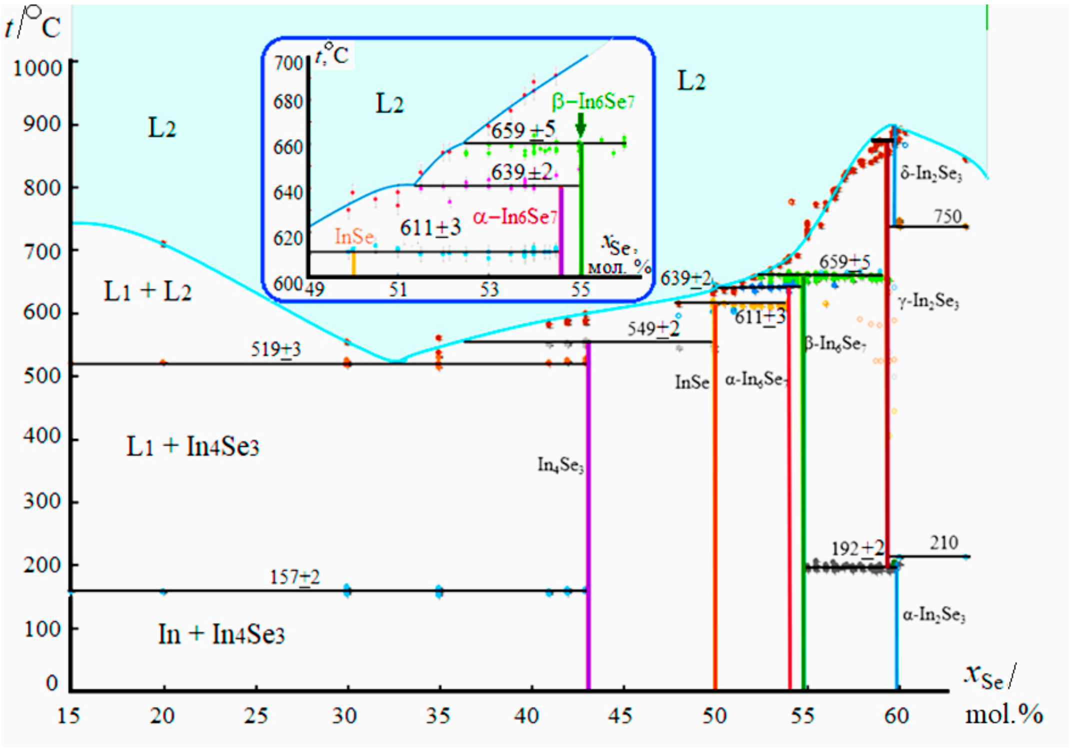

Fig. 11. *T-x*-diagram of the In – Se system in the composition range of 15.0 – 63.4 mol. % Se Se [30]

procedures (500 °C, 72 h) and grinding the powder (2 cycles in total). It was found that the first sample was represented by a monoclinic (SG $P2_1$) structure, and the second turned out to be a mixture of two phases and contained α-3R-In_2Se_3 as an impurity. The main phase of the sample with an increased selenium content (57.5 mol. %) compared to the stoichiometry of In_6Se_7 was identified as monoclinic and resembled the In_6Se_7 structure described above. However, it was well described by *another* space group ($P2_1/m$) and, therefore, was a *separate* phase. Both structures ($P2_1$ And $P2_1/m$) are mentioned in scientific papers, however, for the description of the In_6Se_7 structure [61-64] the second SG is used more often [61]. It is assumed that the crystal lattice of the compound with SG $P2_1/m$ corresponds to the phase with the stoichiometry In_9Se_{11} described in a number of studies [62, 63], but still not structurally characterized. The composition of this phase, which we designate as β-In_6Se_7 [30], was close to 55.0 mol. % Se. The composition of the modification with SG $P2_1$ is richer in indium (we denote it as β-In_6Se_7 [30]) better corresponds to the stoichiometry of In_6Se_7 (~54 mol. %Se).

3. In our study of this diagram, we did not find any structures that could correspond to the stoichiometries of In_5Se_7 and In_3Se_4. Phases with such compositions have not been confirmed either by X-ray powder diffraction studies or by thermographic or tensiometric experiments.

Thus, the main compounds of indium and selenium are In_4Se_3(P_{nnm}), InSe ($P6_3/mmc$), In_6Se_7 (two similar modifications, but differing in composition: $P2_1$ And $P2_1/m$) and In_2Se_3 (represented by at least three modifications, 3R-α-In_2Se_3, γ-In_2Se_3, as well as δ-In_2Se_3). Most of these phases decompose upon heating by peritectic reactions (except for congruently melting δ-In_2Se_3). Over the course of thermal analysis (DTA, chemiluminescence analysis [33]), we obtained the following quantitative data on the temperature stability of condensed phases of the In – Se system and equilibria involving these phases (Table 2).

Out of the issues that are not yet completely clear, we note that this system requires additional studies of samples with compositions close to 60 mol. % selenium content. In these studies, it is still necessary to determine in more detail the positions of the modifications of the In_2Se_3 family on the corresponding phase diagram. Today, only the exact position of the low-temperature 3R-α-In_2Se_3phase does not raise questions.

Table 2. Observed effects and phase equilibria in the In – Se system

No	Number of exp. points	Temperature at which the effect was observed, t, °C	The compound or range of compounds for which the effect was observed x_{Se}, mol. %	Corresponding phase equilibrium effect
1	9	156.5±2	30.0–43.01	$In_4Se_3 + In \Leftrightarrow L$, eutectic
2	9	519±2	30.0–43.01	$L_1 + In_4Se_3 \Leftrightarrow L_2$, monotectic
3	7	549±3.7	41.0–49.9	$In_4Se_3 \Leftrightarrow InSe + L$, peritectic
4	25	611±3.3	49.9–55.0(54.5)	$InSe \Leftrightarrow \alpha\text{-}In_6Se_7 + L$, peritectic
5	15	639±2.0	51.5–55.0	$\alpha\text{-}In_6Se_7 \Leftrightarrow \beta\text{-}In_6Se_7+L$, peritectic
6	30	659±4.5	53.5–59.5	$\beta\text{-}In_6Se_7 \Leftrightarrow \gamma\text{-}In_2Se_3+L$, peritectic
8	18	191±2.0	55.0–60.0	$\beta\text{-}In_6Se_7 + \alpha\text{-}In_2Se_3 \Leftrightarrow \gamma\text{-}In_2Se_3$, eutectoid
9	2	890±5.0	60.0	$\sigma\text{-}In_2Se_3 \Leftrightarrow L$, congr. melting
10	52	от ~520 до ~891	15.0–63.35	$S \Leftrightarrow L$ (liquidus)
11	3	211±2.0	60.0–63.5	$\alpha\text{-}In_2Se_3 \Leftrightarrow \gamma\text{-}In_2Se_{3\,+}$ L, peritectic

7. Conclusions

In conclusion of our review, we will summarize the most important results of the study. First of all, let’s analyze, *what do we know* about A^{III}–B^{VI} systems, as well as phases of families $A_1^{III}B_1^{VI}$ and $A_2^{III}B_3^{VI}$, to which this study is mainly devoted.

1. In all the discussed systems, non-molecular crystalline compounds with $A_1^{III}B_1^{VI}$ and $A_2^{III}B_3^{VI}$ stoichiometries are realized. A partial exception is aluminum monoselenide, but, as we already noted, this compound is also realized in the form of films.

2. $A_1^{III}B_1^{VI}$ **mono**chalcogenides form typical layered structures that have significant similarities with graphite (analogues of graphene, nanotubes and other nanoformations, intercalation reactions, including those during which there is partial damage to the structure of the intercalated crystal itself). Among the monosulfides and monoselenides of indium and gallium, the only partial exception is indium monosulfide, in which, despite the four-layer structure, the bonds between the individual layers can no longer be exclusively classified as van der Waals.

3. **Sesqui-chalcogenides** of aluminum, gallium and indium provide families of “defective” semiconductors, in which crystalline compounds with ordered and disordered stoichiometric vacancies based on wurtzite and sphalerite structures, containing stoichiometric vacancies as structural units, are realized. A partial exception is the In–S system: of the three modifications, close in stoichiometry to indium sesquisulfide, only the highest-temperature one can be classified as a “diamond-like defective” structure based on sphalerite or wurtzite. The other two forms, despite the fact that they also contain stoichiometric vacancies, are derivatives of defective spinel.

4. All intermediate solid compounds in A^{III} – B^{VI} systems are characterized by kinetic difficulties and “sticking” in metastable states. This is especially important when working with thermal analysis methods. In particular, in DTA experiments we observed the effect of “switching”

from one type of phase diagram to another when the heating rate threshold was exceeded by more than 13 K/min [49]. Sufficiently reproducible and clearly interpretable results appear only at the lowest heating rates (0.5–2 K/min). The static method of thermal analysis was developed for the elimination of this problem [33]. In addition, in order to circumvent the difficulties with kinetic difficulties, the auxiliary component method can be recommended [54], which can be used both in solving research problems and for the synthesis of substances with precisely specified compositions [46].

5. Phase equilibria in $A^{III}–B^{VI}$ systems, especially with the participation of “defective” phases of families are very sensitive even to small concentrations of impurities. Doping with even small concentrations of impurities can fundamentally change the pattern of phase equilibria and the appearance of phase diagrams of systems, which can no longer be considered binary, but must be considered as multi- (at least three-) component.

Let us now turn to the problems that remain open to the discussed systems and phases of $A_1^{III}B_1^{VI}$ ***and*** $A_2^{III}B_3^{VI}$ ***families.***

1. Now, the relationship between different defects in phases can be considered as an open problem. In particular, *a priori* it is assumed that in the γ-$Ga_{2+\delta}S_3$ cubic modification a noticeable phase deviation from ideal stoichiometry (59.3 instead of 60.0 mol. % S) occurs due to the “healing” of part of the stoichiometric vacancies by gallium atoms. However, this assumption has not yet been verified by anyone.

2. Another issue is related to finding a more adequate definition of what stoichiometric vacancies are. The point is that in some cases of ordering (for example, for α′-Ga_2S_3), it is no longer possible to discuss such vacancies, since a new type of crystal lattice is formed, in which the stoichiometry corresponds to a new structural type. At the same time, many properties (the possibility of creating interlayers during epitaxy, high diffusion coefficients, preserved radiation resistance, etc.) indicate the presence of such vacancies as independent structural units in crystal lattices.

3. For the monochalcogenides there is still no understanding of when, under what conditions and by what reagents intercalation interactions can be carried out, and when such reactions are impossible. This also includes the question of which areas are affected by intercalation if it occurs and which areas are not affected (and for what reason). There is currently no understanding of the question of how intercalation can be carried out, achieving equilibrium in a way, that this equilibrium can be controlled by changing the concentration of the guest substance in the layered crystal and its ordered or disordered arrangement in the van der Waals gaps.

These questions await answers in future studies.

Contribution of the authors

The authors contributed equally to this article.

Conflict of interests

The authors declare that they have no known competing financial interests or personal relationships that could have influenced the work reported in this paper.

References

1. Piacente V., Bardi G., Di Paolo V., Ferro D. The vapour pressure over Ga_2S_2 and Ga_2Se_2. *The Journal of Chemical Thermodynamics*. 1976;8(4): 391–401. https://doi.org/10.1016/0021-9614(76)90080-x

2. Murakami T., Shibata N. The action of sulfur against metals at high temperatures. 3-rd report. The action of sulfur against aluminum alloys. *Nippon Kinzoku Gakk*. 1940;4: 221–228. https://doi.org/10.2320/jinstmet1937.4.8_221

3. Shi C., Yang B., Hu B., Du Y., Yao S. Thermodynamic description of the Al–X (X = S, Se, Te) systems. *Journal of Phase Equilibria and Diffusion*. 2019;40: 392–402. https://doi.org/10.1007/s11669-019-00733-z

4. Kohlmeyer E. J., Retzlaff H. W. Aluminum sulfide, silicon sulfide and the Al – Si – S system. *Zeitschrift für anorganische Chemie*. 1950;261: 248–260. https://doi.org/10.1002/zaac.19502610314

5. Forland T., Gomez J., Ratkje S. K., Ostvold T. Measurements of phase equilibria in the aluminum-aluminum sulfide system. *Acta Chemica Scandinavica*. 1974;28a(2): 226–228. https://doi.org/10.3891/acta.chem.scand.28a-0226

6. Sharma R. C., Chang Y. A., The Al – S (aluminum-sulfur) system. *Journal of Phase Equilibria*. 1987;8(2): 128–131. https://doi.org/10.1007/BF02873197

7. Flahaut J. A variety of aluminum sulfide stable at high temperature. *Comp. Rend*. 1951;232: 2100–2102.

8. Flahaut. J. Contribution a l’e´tude du sulfure d’aluminium. *Annales de Chimie*. 1952;12: 632–696.

9. Huda N., Rhamdhani M. A., Brooks G. A., Monaghan B. J., Prentice L. Aluminium production route through carbosulfidation of alumina utilizing H_2S. In: *Light*

Metals. B. A. Sadler (ed.). 2013: 1299–1304. https://doi.org/10.1007/978-3-319-65136-1_219

10. Ramadhan M. R., Khansa S. A., Zulindra Q., Handayania D. P., Wardania N. A., Astuti F. Electronic structure calculation of α-Al_2X_3 system (X = O, S) based on r++scan functional. *East European Journal of Physics*. 2023;4: 210–215. https://doi.org/10.26565/2312-4334-2023-4-26

11. Shimomura Y., Ohno S., Hayashi K., Akamatsu H. Quadruple-well ferroelectricity and moderate switching barrier in defective wurtzite α-Al_2S_3: a first-principles study. *arXiv: Condensed Matter – Materials Science*. 2024;2406.04084: 1-35. https://doi.org/10.48550/arXiv.2406.04084

12. Rhamdhani M. A., Huda N., Khaliq A., … Prentice L. Novel multi-stage aluminium production: part 1 – thermodynamic assessment of car-bosulphidation of Al_2O_3/bauxite using H_2S and sodiothermic reduction of Al_2S_3. *Mineral Processing and Extractive Metallurgy*. 2017;127: 1–12. https://doi.org/10.1080/03719553.2017.1293352

13. Klimpel M., Kovalenko M. V., Kravchyk K. V. Advances and challenges of aluminum–sulfur batteries. *Communications Chemistry*. 2022;77(5): 1–12. https://doi.org/10.1038/s42004-022-00693-5

14. Meng J., Hong X., Xiao Z. Rapid-charging aluminium-sulfur batteries operated at 85 °C with a quaternary molten salt electrolyte. *Nature Communications*. 2024;15(596): 1–10. https://doi.org/10.1038/s41467-024-44691-8

15. Gordon L. W., Jay R., Jadhav A. L., Bhalekar S. S., Messinger R. J. Elucidating consequences of selenium crystallinity on its electrochemical reduction in aluminum–selenium batteries. *ACS Materials Letters*. 2024;6(7): 2577–2581. https://doi.org/10.1021/acsmaterialslett.4c00531

16. Wu S. C., Ai Y., Chen Y.-Z. High-performance rechargeable aluminum–selenium battery with a new deep eutectic solvent electrolyte: thiourea – $AlCl_3$. *ACS Materials Letters*. 2020;12: 27064–27073. https://doi.org/10.1021/acsmaterialslett.4c00531

17. Hahn H., Klingler W. Über die Kristallstrukturen von Ga_2S_3, Ga_2Se_3 und Ga_2Te_3. *Zeitschrift für anorganische Chemie*. 1949;259(1-4): 110–119. https://doi.org/10.1002/zaac.19492590111

18. Pardo M. P., Tomas A., Guittard M. Polymorphisme de Ga_2S_3 et diagramme de phase Ga-S. *Materials Research Bulletin*. 1987;22: 1677–1684. https://doi.org/10.1016/0025-5408(87)90011-0

19. Greenberg J. *Thermodynamic basis of crystal growth: P-T-X phase equilibrium and nonstoichiometry*. Springer-Vcrlag Berlin Heidelberg, Berlin; 2002. 247 p. https://doi.org/10.1007/978-3-662-04876-4

20. Zlomanov V. P., Novoselova A. V. *P-T-x-state diagrams of metal-chalcogen systems**. V. B. Lazarev (ed.). Moscow: Nauka Publ.; 1987. 187 p. (In Russ.). Available at: https://f.eruditor.link/file/1843241/

21. Ider M., Pankajavalli R., Zhuang W., Shen J. Y., Anderson T. J. Thermochemistry of the Ga-Se system. *ECS Journal of Solid State Science and Technology*. 2015;4(5): Q51–Q60. https://doi.org/10.1149/2.0011507jss

22. Rustamov P. G., Mardakhaev B. I., Safarov M. G. Study of the phase diagram of the gallium-sulphur system. *Izvestiya Akademii Nauk SSSR Neorganicheskie Materialy*. 1967;3(3): 479–484. (In Russ.)

23. Massalski T. *Binary alloy phase diagrams*. *Materials Information Soc*. 2-nd Ed., Volume. 2. Materials Park, Ohio; 1990. 1269 p.

24. Predel B., Ed.: O. Madelung. Ga-S (Gallium-Sulfur) System. In: *Phase equilibria, crystallographic and thermodynamic data of binary alloys*. Berlin: Springer; 1996;2(1-2): 2. https://doi.org/10.1007/10501684_1396

25. Spandau H., Klanberg F. Thermische Untersuchungen an Sulfiden. II. Das thermische Verhalten der Sulfide des Galliums. *Zeitschrift für anorganische und allgemeine Chemie*. 1958;295(5-6): 300–308. https://doi.org/10.1002/zaac.19582950504

26. Berezin S. S., Zavrazhnov A. Y., Naumov A. V., Nekrylov I. N., Brezhnev N. Y. The phase diagram of the Ga–S system in the concentration range from 48.0 to 60.7 mol % S. *Condensed Matter and Interphases*. 2017;19(3): 321–335. (In Russ., abstract in Eng.). https://doi.org/10.17308/kcmf.2017.19/208

27. Zavrazhnov A., Berezin S., Kosykov A., Naumov A., Berezina M., Brezhnev N. The phase diagram of the Ga–S system in the concentration range of 48.0–60.7 mol % S. *Journal of Thermal Analysis and Calorimetry*. 2018;134: 483–492. https://doi.org/10.1007/s10973-018-7124-z

28. Volkov V. V., Sidey V. I., Naumov A. V., Nekrylov I. N., Brezhnev N. Y., Malygina E. N., Zavrazhnov A. Y. The cubic high-temperture modification of gallium sulphide (xs = 59 mol %) and the *T*, *x*-diagram of the Ga – S system. *Condensed Matter and Interphases*. 2019;21(1): 37–50. (In Russ., abstract in Eng.). https://doi.org/10.17308/kcmf.2019.21/715

29. Volkov V. V., Sidey V. I., Naumov A. V., … Zavrazhnov A. Yu. Structural identification and stabilization of the new high-temperature phases in A(III) – B(VI) systems (A = Ga, In, B = S, Se). Part 1: high-temperature phases in the Ga – S system. *Journal of Alloys and Compounds*. 2022;899: 163264. https://doi.org/10.1016/j.jallcom.2021.163264

30. Brezhnev N. Yu. *Ga-S and In-Se systems: crystal structure of intermediate phases and T-x-diagrams**. Cand. chem. sci. diss. Voronezh; 2023. 28 p. (In Russ.). Available at: https://rusneb.ru/catalog/000199_000009_012131968/

31. Brezhnev N. Y., Dorokhin M. V., Zavrazhnov A. Y., Kolyshkin N. A., Nekrylov I. N., Trushin V. N. High-temperature gallium sesquisulfides and a fragment of the *T-x* diagram of the Ga – S system with these phases. *Condensed Matter and Interphases*. 2024;26(2): 225–237. https://doi.org/10.17308/kcmf.2024.26/11936

32. Pardo M., Guittard M., Chilouet A., Tomas A. Diagramme de phases gallium-soufre et études structurales des phases solides. *Journal of Solid State Chemistry*. 1993;102: 423–433. https://doi.org/10.1006/jssc.1993.1054

33. Berezin S. S., Berezina M. V., Zavrazhnov A. Yu., Kosyakov A. V., Sergeeva A. V., Sidei V. I. Phase transformations of indium mono- and sesquisulfides studied by a novel static thermal analysis technique. *Inorganic Materials*. 2013;49(6): 555–563. https://doi.org/10.1134/s0020168513060010

34. Zavrazhnov A. Yu., Nekrylov N. I., Berezina S. S., Zhuravlev I. A. Phases of the gallium sesquisulfide family stabilised by iron and manganese impurities. In: *Thermodynamics and Materials Science: Proc. XV Symposium with International Participation, 3–7 July 2023*. Novosibirsk: Nikolaev Institute of Inorganic Chemistry of the Siberian

Branch of the Russian Academy of Sciences; 2023. p. 35. https://doi.org/10.26902/THERM_2023_015

35. Zavrazhnov A. Yu., Nekrylov I. N., Berezin S. S., Brezhnev, N. Y. Zavaluev V. Y., Kosyakov A .V. Phase diagrams for the Ga – S and Mn – Ga – S systems. *XXIV International Conference on Chemical Thermodynamics in Russia (RCCT-2024), July 1-5, Ivanovo*. Ivanovo State University of Chemistry and Technology: 2024: 125. ISBN 978-5-6051371-2-2. Available at: https://rcct.isc-ras.ru/sites/default/files/collectionabstracts/56/rcct-2024.pdf

36. Kokh K. A., Huang Z. M., Huang J. G., Gao Y. Q., ... Andreev Yu. M. Study of Ga_2S_3 crystals grown from melt and $PbCl_2$ flux. *Materials Research Bulletin*. 2016;84: 462–467. https://doi.org/10.1016/j.materresbull.2016.08.046

37. Tyurina E. A., Velmuzhov A. P. Sukhanov M. V., ... Shiryaev V. S. Phase formation during crystallization of melts and glasses of the $Ga_xGe_{40-x}S_{60}$ system. *Journal of Non-Crystalline Solids*. 2023;622: 122686. https://doi.org/10.1016/j.jnoncrysol.2023.122686

38. Vel'muzhov A. P., Sukhanov M. V., Potapov A. M., Suchkov A. I., Churbanov M. F. Preparation of extrapure Ga2S3 by reacting GaI3 with sulfur. *Inorganic Materials*. 2014;50(7): 656–660. https://doi.org/10.1134/s0020168514070152

39. Lee J., Won Y. H., Kim H. N. Photoluminescence of Ga_2S_3 and Ga_2S_3:Mn single crystals. *Solid State Communications*. 1996;97(12): 1101–1104. https://doi.org/10.1016/0038-1098(95)00728-8

40. Kokh K., Lapin I. N., Svetlichnyi V., Galiyeva P., Bakhadur A., Andreev Y. Synthesis and bridgman growth of Ga_2S_3 crystals. *Key Engineering Materials*. 2016;683: 71–76. https://doi.org/10.4028/www.scientific.net/KEM.683.71

41. Kosyakov A. V., Nekrylov I. N., Brezhnev N. Y., Malygina E. N., Zavrazhnov A. Y. The *T-x* diagram of the Ga – Se system in the composition range from 48.0 to 61.5 mol % Se according to thermal analysis data. *Condensed Matter and Interphases*. 2019;21(4): 519–527. https://doi.org/10.17308/kcmf.2019.21/2363

42. Okamoto H. Ga-Se (Gallium-Selenium). *Journal of Phase Equilibria and Diffusion*. 2009;30: 659. https://doi.org/10.1007/s11669-009-9601-3

43. Zavrazhnov A. Yu., Naumov A. V., Kosyakov A. V., Ryazhskikh M. V. Ancillary component method: using in the research and synthesis of pure inorganic compounds. *Materials Science and Engineering B*. 2011:1(12): 906–912.

44. Zavrazhnov A.Yu., Naumov A. V., Pervov V. S., Riazhskikh M. V. Chemical vapor transport for the control of composition of low-volatile solids: II. The composition control of indium sulfides: Technique of the charge dilution *Thermochimica Acta*. 2012;532: 96–102. https://doi.org/10.1016/j.tca.2010.10.004

45. Zavrazhnov A. Yu., Naumov A. V., Turchen D. N., Zartsyn I. D., Zlomanov V. P. Chemical transport for controlling the composition of condensed bodies II. Control of the composition of gallium monoselenide within the homogeneity region and diagnostics of GaSe nonstoichiometry. *Condensed Matter and Interphases*. 2004;6 (4): 322–335. (In Russ., abstract in Eng.). Available at: https://www.elibrary.ru/item.asp?id=29833369

46. Zavrazhnov A. Yu., Zartsyn I. D., Naumov A. V., Zlomanov V. P., Davydov A. V. Composition control of low-volatility solids through chemical vapor transport reactions. I. Theory of selective chemical vapor transport. *Journal of Phase Equilibria and Diffusion*. 2007;28: 510–516. https://doi.org/10.1007/s11669-007-9200-0

47. Kosyakov A.V., Zavrazhnov A. Y., Naumov A. V. Refinement of the In-S phase diagram using spectrophotometric characterization of equilibria between hydrogen and indium sulfides. *Inorganic Materials*. 2010;46(4): 398-401. 343–345. https://doi.org/10.1134/s0020168510040035

48. Kosyakov A. V., Zavrazhnov A. Yu., Naumov A. V., Sergeeva A. S. Specification of the phase diagram of system In - S according to spectrophotometric researches ofbalance between sulfides of indium and hydrogen. *Proceedings of the Voronezh State University. Series: Chemistry. Biology. Pharmacy*. 2009;2: 28–39. (In Russ., abstract in Eng.). Available at: https://www.elibrary.ru/item.as-p?id=12992199

49. Zavrazhnov A. Yu., Naumov A. V., Anorov P. V., Goncharov E. G., Sidey V. I., Pervov V. S. *T*-x phase diagram of the In-S system. *Inorganic Materials*. 2006;42(12): 1294–1298. https://doi.org/10.1134/s0020168506120028

50. Okamoto H. In-S (Indium-Sulfur). *Journal of Phase Equilibria and Diffusion*. 2012;34(2): 149–150. https://doi.org/10.1007/s11669-012-0152-7

51. Zavrazhnov A., Kosyakov A., Naumov A., Sergeeva A., Riazhskikh M., Berezin S. Study of the In–S phase diagram using spectrophotometric characterization of equilibria between hydrogen and indium sulfides. *Thermochimica Acta*. 2013;566: 169–174. https://doi.org/10.1016/j.tca.2013.05.031

52. Naumov A. V., Sergeeva A. V., Semenov V. N. Oriented $In_{3-x}S_4$ films on the (100) surface of Si, GaAs, and InP single crystals. *Inorganic Materials*. 2017;53(6): 560–567. https://doi.org/10.1134/S0020168517060127

53. Zavrazhnov A. Yu., Naumov A. V., Sergeeva A. V., Sidey V. I. Selective chemical vapor transport as a means of varying the composition of nonstoichiometric indium sulfides. *Inorganic Materials*. 2007;43(11): 1167–1178. https://doi.org/10.1134/s0020168507110039

54. Zavrazhnov A., Naumov A., Kosyakov A., Riazhskikh M. Ancillary component method: using in the research and synthesis of pure inorganic compounds. *Materials Science and Engineering B*. 2011;1: 906–912. Available at: https://www.researchgate.net/publication/247931076_Ancillary_Component_Method_Using_in_the_Research_and_Synthesis_of_Pure_Inorganic_Compounds

55. Brezhnev N. Yu., Zavrazhnov A. Yu., Naumov A. V., Kosyakov A. V., Zavalyuev V. Yu. Refinement of the T-x diagram of the state of the In-Se system, as well as the structure of intermediate phases of this system. In: *Thermodynamics and Materials Science: Proc. XV Symposium with International Participation, 3–7 July 2023*. Novosibirsk: Nikolaev Institute of Inorganic Chemistry of the Siberian Branch of the Russian Academy of Sciences; 2023. p. 74. https://doi.org/10.26902/THERM_2023_054

56. Okamoto H. In-Se (Indium-Selenium). *Journal of Phase Equilibria and Diffusion*. 2004;25: 201. https://doi.org/10.1007/s11669-004-0031-y

57. Liu L., Dong J., Huang J, ... Liu Z. Atomically resolving polymorphs and crystal structures of In_2Se_3. *Chemistry of Materials*. 2019;31: 10143–10149 https://doi.org/10.1021/acs.chemmater.9b03499

58. Zavrazhnov A. Yu., Kosyakov A. V., Sergeeva A. V., Berezina S. S., Chernenko K. K. High-temperature in situ vapor spectrophotometry as a static variant of the tensimetric method equilibria in the Ga – I system. *Condensed Matter and Interphases*. 2015;17(4): 417–436. Available at: https://journals.vsu.ru/kcmf/article/view/87

59. Zavrazhnov A. Y., Naumov A. V., Malygina E. N., Kosyakov A. V. Indium monochloride vapor pressure: the vapor-gauge and spectrophotometric experimaental data. *Condensed Matter and Interphases*. 2019;21(1): 60–71. https://doi.org/10.17308/kcmf.2019.21/717

60. Brezhnev N. Y., Kosyakov A. V., Steich A. V., Zavrazhnov A. Y. High-temperature spectrophotometry of indium chloride vapours as a method of study of the In – Se system. *Condensed Matter and Interphases*. 2021;23(4): 482–495. https://doi.org/10.17308/kcmf.2021.23/3667

61. Walther R., Deiseroth J. Redetermination of the crystal structure of hexaindium heptaselenide, In_6Se_7. *Zeitschrift für Kristallographie – Crystalline Materials*. 1995;210: 359–365. https://doi.org/10.1524/zkri.1995.210.5.359

62. Gödecke T., Haalboom T., Sommer F. Stable and metastable phase equilibria of the In-Se system. *Journal of Phase Equilibria*. 1998;19(6): 572–576. https://doi.org/10.1007/BF02701021

63. Vassilev G. P. Infrared spectroscopy and X-ray diffraction data of In–Se compounds. *Int. International Journal of Materials Research*. 2007;98(1): 60–63 https://doi.org/10.3139/146.101428

64. Peng Y.-H., Muhimmah L. C., Ho C.-H. Phosphorus-doped multilayer In_6Se_7: the study of structural, electrical, and optical properties for junction device. *JACS Au*. 2023;4(1): 58–71. https://doi.org/10.1021/jacsau.3c00653

Information about the authors

Alexander Y. Zavrazhnov, Dr. Sci. (Chem.), Professor at the Department of General and Inorganic Chemistry, Voronezh State University (Voronezh, Russian Federation).

https://orcid.org/0000-0003-0241-834X
alexander.zavrazhnov@gmail.com

Nikolay Y. Brezhnev, Senior Lecturer at the Department of Chemistry, Voronezh State Agricultural University (Voronezh, Russian Federation).

https://orcid.org/0000-0002-3287-8614
brezhnevnick@gmail.com

Ivan N. Nekrylov, Department Assistant at the Department of General and Inorganic Chemistry, Voronezh State University (Voronezh, Russian Federation).

https://orcid.org/0000-0003-4491-4739
Icq492164858@gmail.com

Andrew V. Kosyakov, Cand. Sci. (Chem.), Assistant Professor, Department of General and Inorganic Chemistry, Voronezh State University (Voronezh, Russian Federation).

https://orcid.org/0000-0001-9662-7091
lavchukb@mail.ru

Received 28.07.2024; approved after reviewing 18.08.2024; accepted for publication 16.09.2024; published online 25.03.2025.

Translated by Valentina Mittova

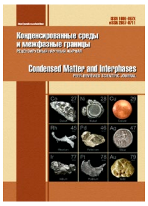

ISSN 1606-867X (Print)
ISSN 2687-0711 (Online)
Condensed Matter and Interphases
Kondensirovannye Sredy i Mezhfaznye Granitsy
https://journals.vsu.ru/kcmf/

Original articles

Research article
https://doi.org/10.17308/kcmf.2025.27/12485

Thermodynamic study of zinc antimonides by the electromotive force measurements

A. R. Aghayeva[1]✉, **S. H. Mammadova**[2], **D. M. Babanly**[1,3], **Ya. I. Jafarov**[4], **D. B. Tagiyev**[3]

[1]*French-Azerbaijani University, Azerbaijan State Oil and Industry University,*
Nizami 183, Baku, Azerbaijan

[2]*Institute of Charles Sadron of CNRS,*
Strasbourg 67200, France

[3]*Institute of Catalysis and Inorganic Chemistry,*
113 H. Javid ave., Baku, AZ-1143, Azerbaijan

[4]*Baku State University,*
23 Z.Khalilov, Baku Az-1048, Azerbaijan

Abstract

Zinc antimonides and phases based on them are of great interest as earth-abundant, low-cost, and environmentally friendly thermoelectric materials. The present work demonstrates the results of a thermodynamic study of the ZnSb and Zn_4Sb_3 compounds by a low-temperature electromotive force (emf) method with a glycerol electrolyte in the 300-430 K temperatures range.

Measurements were performed using equilibrium samples from the ZnSb+Sb and ZnSb+Zn_4Sb_3 two-phase regions of the Zn-Sb binary system. The phase compositions of prepared samples were controlled by means of the powder X-ray diffraction (PXRD) method. Using the least square method, the linear equations of temperature dependences of the emf data were obtained.

Based on these equations and relevant thermodynamic expressions, the partial molar Gibbs free energy, enthalpy, and entropy of zinc in alloys were calculated. Utilizing the phase diagram of the Zn-Sb system, the virtual-cell reactions for both binary compounds were determined, based on which their standard thermodynamic functions of formation and standard entropies were calculated. A comparative analysis of the obtained results with available literature data was carried out.

The results of the current work are highly accurate and can be considered a new contribution to the thermodynamics of zinc antimonides.

Keywords: ZnSb, Zn_4Sb_3, *emf* method, Electrochemical cells, Glycerol electrolyte, Thermodynamic functions

For citation: Aghayeva A. R., Mammadova S. H., Babanly D. M., Jafarov Ya. I., Tagiyev D. B. Thermodynamic study of zinc antimonides by the electromotive force measurements. *Condensed Matter and Interphases*. 2025;27(1): 48–56. https://doi.org/10.17308/kcmf.2025.27/12485

Для цитирования: Агаева А. Р., Мамедова С. Х., Бабанлы Д. М., Джафаров Я. И., Тагиев Д. Б. Термодинамическое исследование антимонидов цинка методом электродвижущих сил. *Конденсированные среды и межфазные границы*. 2025;27(1): 48–56. https://doi.org/10.17308/kcmf.2025.27/12485

✉ Aytekin R. Aghayeva, e-mail: aytekin_agayeva@mail.ru

© Aghayeva A. R., Mammadova S. H., Babanly D. M., Jafarov Ya. I., Tagiyev D. B. , 2025

The content is available under Creative Commons Attribution 4.0 License.

1. Introduction

Metal pnictides are a class of compounds which are intriguing due to their promising electronic, optical, magnetic, etc. properties, that have resulted in a wide range of applications in various fields of modern technology and industry. So that binary and more complex pnictides and phases based on them are considered promising materials for applications such as high-efficiency light-emitting diodes, solar cells, quantum transport, low-power high-speed electronics, mid- to long infrared wavelength optoelectronics, thermoelectric (TE) generation and so on [1–4]. Some of them have gained recognition in physics and materials science as 3D topological Dirac semimetals and have been suggested for use as Weyl semimetals, axion insulators, and topological superconductors, making them a unique parent compound for the study of these states and the phase transitions between them [5–8].

Among binary pnictides, Zn-Sb phases are the most investigated materials showing promising TE performance. In addition, they are earth-abundant, low-cost, environmentally friendly, and stable at high temperatures up to ~1000 K materials which make them one of the best choices for the TE industry since the discovery of the Seebeck effect [9–12].

Although zinc antimonides have glass-like thermal conductivity, which makes them attractive for TE applications, their poor carrier concentration compared with state-of-the-art TE materials [13] has inspired many scientists to try to improve their electrical properties by adding dopants such as In, Al, Sn, etc. [14–16].

The phase diagram of the Zn-Sb system has been extensively studied experimentally and theoretically by many authors [17–21]. The phase diagrams reported in these studies are very similar, although the topology is slightly different. The true equilibrium phase diagram determined by a careful study considering the differences among all the previous studies was reported by H. Okamoto [22]. According to [22], Zn-Sb phase diagram is characterized by the formation of 3 antimonides: ZnSb, Zn_4Sb_3, and Zn_3Sb_2. The first compound melts at 818 K by peritectic decomposition and is stable below its melting temperature. Zn_4Sb_3 and Zn_3Sb_2 compounds have distectic melting at accordingly 837 and 838 K temperatures. Zn_4Sb_3 has 3 modifications: stable below 768 K (α-Zn_4Sb_3), between 768 and 803 K (β-Zn_4Sb_3) and above 803 K (γ-Zn_4Sb_3), respectively. Zn_3Sb_2 appears in low- and high-temperature modifications and is metastable at room temperature [22].

In a recent study, an updated phase diagram of the system Zn–Sb provides new details about the composition, transformation, and stability temperatures for the four binary phases [23]. According to the results of [23], the Zn–Sb system contains two well-known thermoelectric materials: $Zn_{1-\delta}Sb$ and $Zn_{13-\delta}Sb_{10}$ ("Zn_4Sb_3"), and two other phases: $Zn_{9-\delta}Sb_7$ and $Zn_{3-\delta}Sb_2$, which are only stable at high temperatures. The chemical formula of the well-known $Zn_{4-\delta}Sb_3$ phase was suggested as $Zn_{13-\delta}Sb_{10}$ according to its structure and composition.

Thermodynamic properties of compounds are essential for forecasting the thermal behaviour and microstructure evolution of alloys as temperature changes. As scientists explore zinc antimonides for potential applications in electronic and optoelectronic devices, a precise comprehension of their thermodynamic properties becomes imperative, paving the way for optimized performance and leveraging their capabilities in technological advancements. The thermodynamic properties of zinc antimonides were studied by different authors and summarized in modern review papers and databases [24–27]. These works are mainly dedicated to the determination of their enthalpies and Gibbs free energies of formation with calorimetric and high-temperature *emf* methods, as well as by thermodynamic assessment. Later, in the discussions section of the paper, the results of these studies will be discussed, focusing on experimental methods and models that have been used to estimate related thermodynamic properties and will be compared with the ones obtained in the current study. Therefore, to obtain a more reliable set of thermodynamic functions, it is recommended to use experimental data obtained under conditions as close as possible to the standard.

Various modifications of the *emf* method are commonly employed for the thermodynamic analysis of binary and more complex inorganic systems. Depending on different factors such as measurement temperature, the composition of compounds, etc., different types of liquid and solid electrolytes can be applied for *emf* measurements [28-32].

Consequently, the present paper is dedicated to the thermodynamic study of zinc antimonides by low-temperature *emf* measurements.

2. Experimental part

The compositions of the prepared samples, as well as their synthesis and thermal annealing conditions were selected with respect to the phase diagram of the Zn–Sb system [22]. Alloys of different compositions from the ZnSb + Sb and ZnSb + Zn_4Sb_3 two-phase regions have been selected to study the thermodynamic properties of zinc antimonides stable at room temperature. Two samples with 52 and 70 at.% Sb composition from the ZnSb + Sb phase region and two samples with 43 and 47 at.% Sb composition from the ZnSb + Zn_4Sb_3 two-phase region of the system were selected for the thermodynamic study of the ZnSb and Zn_4Sb_3 compounds, respectively. High-purity elements (Zinc lumps - Sigma-Aldrich, CAS number 7440-66-6 and Antimony pieces - Alfa-Aesar, CAS number 7440-36-0) were used for sample preparation.

For synthesis, calculated amounts of zinc and antimony were weighed in an analytical balance and inserted into the quartz ampoules. Ampoules were evacuated up to ~ 10^{-2} Pa pressure and heated up to 900 K temperature. After 2-3 hours synthesis process, the temperature was gradually decreased to 600 K and the samples were kept at this temperature for ~500 hours.

The PXRD technique was used to confirm the phase composition of the prepared equilibrium samples. Data collection was performed at room temperature using the D2 Phaser diffractometer with Cu*K*α emission. Samples were scanned from ~ 5 to 75°. The Topas 4.2 profile modelling software was used to examine and analyse the recorder diffraction patterns.

PXRD spectrum of one sample from each phase region is given in Fig. 1. As can be seen, the PXRD spectrum of the sample with 47 at.% Sb composition (Fig. 1a) is composed of diffraction peaks of the ZnSb and Zn_4Sb_3 compounds, while the powder diffractogram of the sample with 70 at.% Sb composition (Fig. 1b) consists of diffraction lines of the ZnSb compound and an elemental antimony. Any signals belonging to other phases have not been detected in the diffraction patterns of samples, which confirms the complete synthesis and homogenization processes.

To start *emf* measurements, the following electrochemical cell was constructed:

$$(-)\ Zn(s)\ /\ glycerol + KCl + ZnCl_2\ /\ Zn\text{-}Sb\ alloy\ (s)\ (+) \quad (1)$$

The most active element of the system, namely zinc was used as the left electrode, while prepared equilibrium alloys of the Zn-Sb system were used as the right electrodes. To prepare the right electrodes, previously synthesized and annealed samples were powdered, pressed into tablets of 5-6 mm in diameter, and attached to the molybdenum rods. Molybdenum rods and electrodes were covered by glass coatings to prevent possible contact between them inside an electrolyte solution.

A liquid electrolyte of the constructed cell was a glycerol solution of KCl (Sigma Aldrich, 99.999%) with a small addition of anhydrous $ZnCl_2$ (Sigma Aldrich, 99.999%). Due to the presence of moisture and oxygen in the electrolyte, glycerol was thoroughly dehydrated and degassed at ~350 K under a dynamic vacuum. Preparation of the electrolyte and electrodes, as well as the assembly technique of the electrochemical cell (1) were put into practice as described in [33, 34].

A Keithley 2100 6 ½ The digital multimeter, having 1014 Ω input resistance and ±0.1 mV accuracy, was used to collect *emf* data in the 300- 430 K temperature interval. A chromel-alumel thermocouple and a mercury thermometer were used for temperature measurements. After keeping the cell at ~350 K for 40–60 hours, the first equilibrium values of the potential difference were obtained. Then subsequent measurements were taken every 3-4 h when a particular temperature was established. For equilibrium values of the *emf,* the difference between repeated measurements was not higher than 0.2 mV at the established temperature.

3. Results and discussions

According to experimental measurements' results, the *emf* values were constant within each

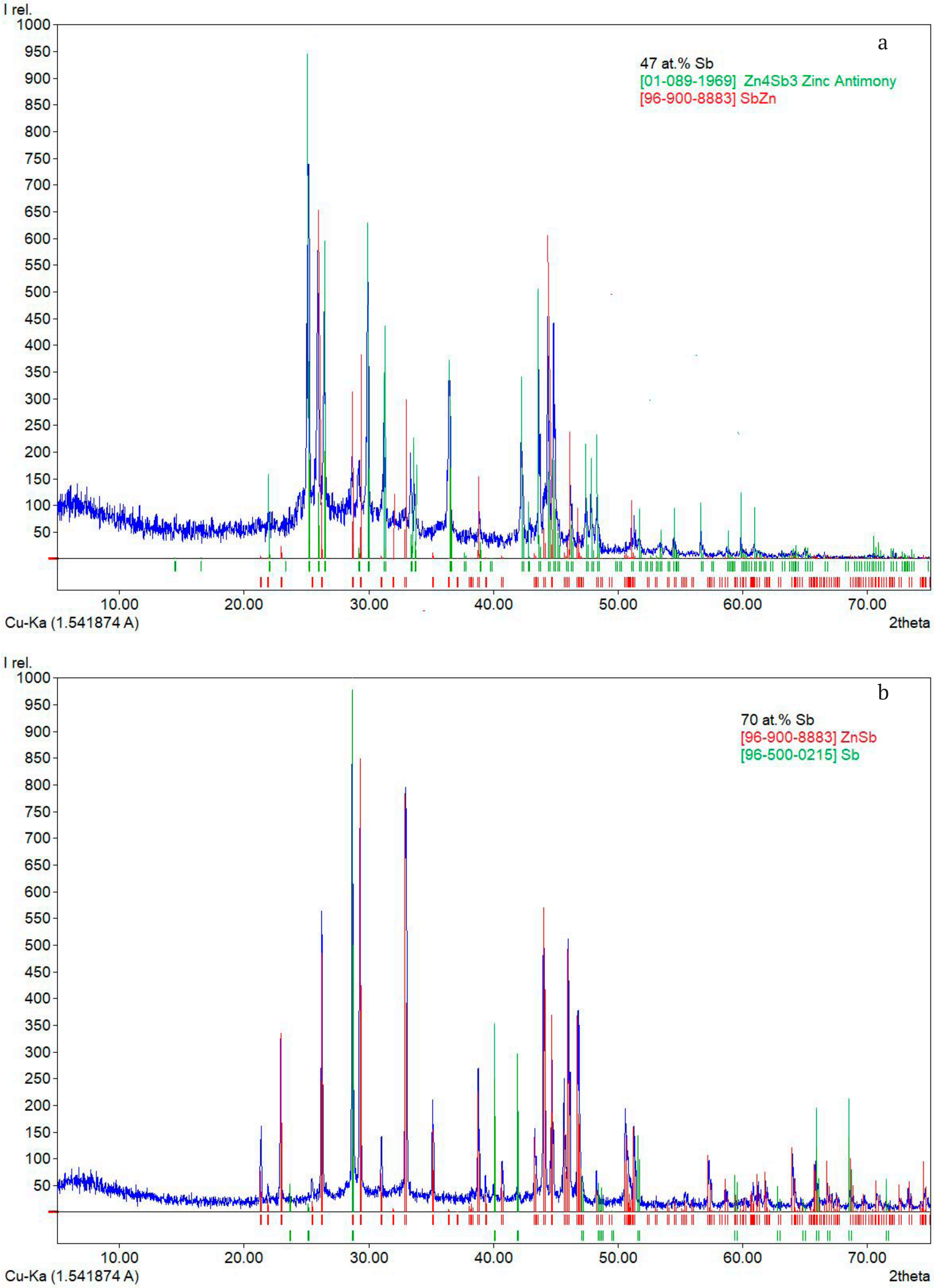

Fig. 1. PXRD spectrums of samples with a) 47 at. % Sb and b) 70 at. % Sb composition along the Zn-Sb binary system

of the ZnSb + Sb and Zn_4Sb_3+ZnSb two-phase fields, independent of the overall composition of electrode alloys. Temperature dependencies of the *emf* values for both samples are illustrated in Fig. 2. Analysis of the *E* ~ *f*(*T*) dependences of the alloys has shown that they are practically linear (Fig. 2). It confirms the stability of the compositions of coexisting phases in above mentioned heterogeneous phase areas in the temperature range under study and gives a base for estimations of the partial entropy and enthalpy from values of the temperature coefficients of the *emf* [35, 36].

Collected experimental data were processed using least squares fitting with the Microsoft Office Excel computer program to give linear equations

$$E = a + bT \pm t\left[\frac{\delta_E^2}{n} + \delta_b^2(T-\bar{T})^2\right]^{1/2}, \qquad (2)$$

where a and b are constant coefficients, n is the number of pairs of experimental E and T values; δ_E^2 and δ_b^2 are the error variances of the *emf* readings and b coefficient, respectively; $\bar{T}$ is the average of the absolute temperature; t is Student's test. With the number of experimental points $n = 30$, and the confidence level equal to 95%, the student's test is $t \leqslant 2$. Obtained linear equations of the type (2) are presented in Table 1. Based on these linear equations and using the thermodynamic expressions below given, the partial molar Gibbs free energy, enthalpy, and entropy of zinc in alloys have been calculated [33–36]:

$$\Delta\bar{G}_{Zn} = -zFE, \qquad (3)$$

$$\Delta\bar{S}_{Zn} = zF\left(\frac{\partial E}{\partial T}\right)_P = zFb, \qquad (4)$$

$$\Delta\bar{H}_{Zn} = -zF\left[E - T\left(\frac{\partial E}{\partial T}\right)_P\right] = -zFa. \qquad (5)$$

The obtained relative partial molar functions of zinc in the alloys are presented in Table 2.

According to the phase diagram of the Zn-Sb binary system [22], ZnSb compound is the richest in the antimony phase in the system and is in ZnSb + Sb equilibrium with it. Hence the partial molar functions of zinc in this region are thermodynamic functions of the following virtual-cell reaction:

$$\text{Zn(s)} + \text{Sb(s)} \rightarrow \text{ZnSb(s)}. \qquad (6)$$

This reaction is similar to the reaction of the formation of ZnSb compound from its elemental components. Therefore, the corresponding partial molar functions of zinc in the ZnSb + Sb phase area are standard thermodynamic functions of the formation of ZnSb.

The partial molar functions of zinc in the Zn_4Sb_3 + ZnSb two-phase field (Table 2) are thermodynamic functions of the following virtual-cell reaction:

$$\text{Zn(s)} + 3\text{ZnSb(s)} \rightarrow \text{Zn}_4\text{Sb}_3\text{(s)}. \qquad (7)$$

In accordance with the reaction (7), the following equations were used to calculate the standard Gibbs free energy, enthalpy, and entropy of the formation of the Zn_4Sb_3 intermediate compound:

$$\Delta_f Z^0(\text{Zn}_4\text{Sb}_3) = \Delta\bar{Z}_{Zn} + 3\Delta_f Z^0(\text{ZnSb}), \qquad (8)$$

where $Z \cong G, H,$ *or* S.

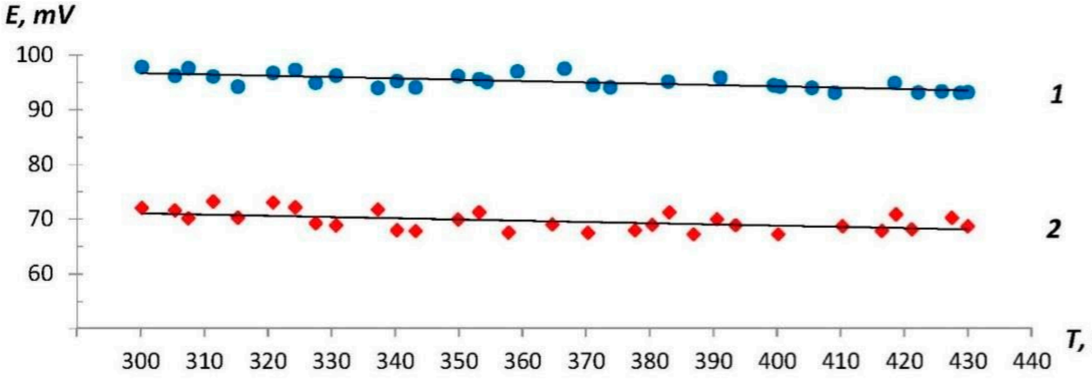

Fig. 2. *E* ~ *f*(*T*) plots for the samples along the system Zn-Sb: (a) ZnSb +Sb phase area; (b) ZnSb + Zn_4Sb_3 phase area

Table 1. Temperature dependencies of the *emf* for the cells of the type (1) in some phase areas of the Zn–Sb system at the 300–430 K temperature interval

Phase region	E, mV = $a + bT \pm 2S_E(T)$
ZnSb(s) + Sb(s)	$103.95 - 0.0243T \pm 2\left[\frac{1.04}{30} + 2.1\cdot10^{-5}(T-363.5)^2\right]^{1/2}$
Zn_4Sb_3(s) +ZnSb(s)	$77.78 + 0.0225T \pm 2\left[\frac{2.26}{30} + 4.7\cdot10^{-5}(T-363.2)^2\right]^{1/2}$

Table 2. Partial molar thermodynamic functions of zinc in the alloys of the Zn–Sb system at 298 K

Phase region	$-\Delta\bar{G}_{Zn}$, kJ/mol	$\Delta\bar{H}_{Zn}$, kJ/mol	$\Delta\bar{S}_{Zn}$, J/(mol·K)
ZnSb(s) + Sb(s)	18.66±0.14	20.06±0.64	−4.69±1.76
Zn_4Sb_3(s) + ZnSb(s)	13.71±0.20	15.01±0.98	−4.36±2.66

Absolute entropies of the ZnSb and Zn_4Sb_3 compounds have been calculated using the following equations:

$$S^0(\mathrm{ZnSb}) = \Delta\bar{S}_{\mathrm{Zn}} + S^0_{\mathrm{Zn}} + S^0_{\mathrm{Sb}} \tag{9}$$

$$S^0(\mathrm{Zn_4Sb_3}) = \overline{\Delta S}_{\mathrm{Zn}} + S^0{}_{\mathrm{Zn}} + 3S^0{}_{\mathrm{ZnSb}}. \tag{10}$$

Errors were calculated by the error accumulation method. Absolute entropies of the elementary zinc and antimony used for calculations were taken from [25]: S°(Zn) = 41.63±0.13 J/(mole·K); S°(Sb) = 45.69±0.63 J/(mole·K). Calculated standard integral thermodynamic functions of both compounds along with available literature data are tabulated in Table 3.

The $\Delta_f G$° values in the table related to the studies with the *emf* measurements [38-40, 46] were calculated by us for 298 K based on the results of those studies. Comparative analysis of the values in the table shows that the results of the current study for the ZnSb compound are in good agreement with the results of the *emf* measurements given in [37, 38], obtained by vapor pressure measurement method [41], as well as

Table 3. Standard integral thermodynamic functions of zinc antimonides

Compound	$-\Delta_f G$°	$-\Delta_f H$° kJ/mol	$\Delta_f S$° J/(mol·K)	S°	Reference, method
ZnSb	18.7±0.2	20.1±0.7	−4.7±1.8	82.6±2.5	This work, *emf*
	19.89	21.80			[37], *emf*
	17.75	19.10			[38], *emf*
	16.28	16.46			[39], *emf*
	16.53	17.15			[40], *emf*
	17.68	19.00			[41], vap. press.
		12.8			[42], calorimetry
		74.47			[43], calorimetry
	19.5	22.49			[17], optimization
	20.36	22.98			[44], optimization
		22.92			[45], optimization
		19.0±1.3		82.6±1.7	[24], recommend
	17.40	16.74		89.54±2.1	[25], recommend
	17.72	18.93		83.08	[26], recommend
Zn_4Sb_3	69.7±0.7	75.2±3.0	−18.5±7.9	285.1±10.4	This work, *emf*
	65.30	74.90			[37], *emf*
	55.48	37.24			[39], *emf*
	56.82	54.79			[46], *emf*
	61.31	65.57			[44], optimization
	65.02	65.65			[47], optimization

with the ones thermodynamically optimized in [17, 44, 45]. The results obtained from other *emf* studies are somewhat lower. Quantities obtained during two different calorimetric studies differ from each other by more than 5 times, and hence they are naturally insignificant. It should also be noted that for the ZnSb compound, the quantities provided in the reference books [24-26] are slightly different than our results. Among them, the results of [24] and [26] are in better agreement with the current study.

Thermodynamic properties of the Zn_4Sb_3 compound were experimentally studied only using the *emf* method [37, 39, 46] until our studies and their thermodynamic optimization were carried out by [44, 47]. As can be seen from Table 3, our results are closer to [37] and also agree with the optimized thermodynamic quantities.

Thus, the obtained standard thermodynamic functions have high accuracy and minimize existing contradictions, especially for the standard entropy and Gibbs free energy of formation for both compounds.

4. Conclusion

The present contribution shares the results of the thermodynamic study of the ZnSb and Zn_4Sb_3 compounds by a low-temperature *emf* method. Using samples from the ZnSb+Sb and Zn_4Sb_3+ZnSb phase areas of the system as a right electrode, the linear equations of temperature dependences of the *emf* have been obtained. From these linear equations, the partial molar thermodynamic functions of zinc in alloys have been calculated. Based on the *T-x* diagram of the Zn-Sb system, the potential generating reactions for both binary compounds have been defined and consequently, their standard integral thermodynamic functions have been determined. The set of obtained standard thermodynamic quantities is of high accuracy and a new contribution to the thermodynamics of zinc stibnites. These results allow us to minimize the contradictions between the existing literature data.

Contribution of the authors

The authors contributed equally to this article.

Conflict of interests

The authors declare that they have no known competing financial interests or personal relationships that could have influenced the work reported in this paper.

References

1. Assoud A., Kleinke H. *Metal pnictides: structures and thermoelectric properties*. *Handbook of Solid-State Chemistry*. 2017. https://doi.org/10.1002/9783527691036.hsscvol1012

2. Rasaki S. A., Thomas T., Yang M. Iron based chalcogenide and pnictide superconductors: from discovery to chemical ways forward. *Progress in Solid State Chemistry*. 2020;59: 100282. https://doi.org/10.1016/j.progsolidstchem.2020.100282

3. Kumar J., Gautam G. S. Study of pnictides for photovoltaic applications. *Physical Chemistry Chemical Physics*. 2023;25(13): 9626–9635. https://doi.org/10.1039/D2CP04453F

4. Marchand R., Jeitschko W. Ternary lanthanoid-transition metal pnictides with $ThCr_2Si_2$-type structure. *Journal of Solid-State Chemistry*. 1978;24(3-4): 351–357. https://doi.org/10.1016/0022-4596(78)90026-9

5. Liu Z. K., Jiang J., Zhou B., ...Chen Y. L. A stable three-dimensional topological Dirac semimetal Cd_3As_2. *Nature Materials*. 2014;13(7): 677–681. https://doi.org/10.1038/nmat3990

6. Liu Z. K., Zhou B., Zhang Y., ... Chen Y. L. Discovery of a three-dimensional topological Dirac semimetal, Na_3Bi. *Science*. 2014;343(6173): 864–867. https://doi.org/10.1126/science.1245085

7. Wang Z., Weng H., Wu Q., Dai X., Fang Z. Three-dimensional Dirac semimetal and quantum transport in Cd_3As_2. *Physical Review B – Condensed Matter and Materials Physics*. 2013;88(12): 125427. https://doi.org/10.1103/PhysRevB.88.125427

8. Crassee I., Sankar R., Lee W. L., Akrap A., Orlita M. 3D Dirac semimetal Cd_3As_2: a review of material properties. *Physical Review Materials*. 2018;2(12): 120302. https://doi.org/10.1103/PhysRevMaterials.2.120302

9. Song X., Finstad T. G. Review of research on the thermoelectric material ZnSb. *Thermoelectrics for power generation: a look at trends in the technology*. 2016. https://doi.org/10.5772/65661

10. Castellero A., Fanciulli C., Carlini R., ... Baricco M. Effect of processing routes on the synthesis and properties of Zn_4Sb_3 thermoelectric alloy. *Journal of Alloys and Compounds*. 2015;653: 54–60. https://doi.org/10.1016/j.jallcom.2015.08.251

11. Sreeparvathy P. C., Kanchana V., Vaitheeswaran G. Thermoelectric properties of zinc based pnictide semiconductors. *Journal of Applied Physics*. 2016;119(8): 085701. https://doi.org/10.1063/1.4942011

12. Bjerg L., Madsen G. K. H., Iversen B. B. Enhanced thermoelectric properties in zinc antimonides. *Chemistry of Materials*. 2011;23(17): 3907–3914. https://doi.org/10.1021/cm201271d

13. Snyder G. J., Toberer E. S. Complex thermoelectric materials. *Nature Materials*. 2008;7(2): 105–114. https://doi.org/10.1038/nmat2090

14. Ostovari Moghaddam A., Shokuhfar A., Zhang Y., … Cabot A. Ge-doped ZnSb/β-Zn_4Sb_3 nanocomposites with high thermoelectric performance. *Advanced Materials Interfaces*. 2019;6(18): 1900467. https://doi.org/10.1002/admi.201900467

15. Carlini R., Marré D., Pallecchi I., Ricciardi R., Zanicchi G. Thermoelectric properties of Zn_4Sb_3 intermetallic compound doped with aluminum and silver. *Intermetallics*. 2014;45: 60–64. https://doi.org/10.1016/j.intermet.2013.10.002

16. Gau H. J., Yu J. L., Wu C. C., Kuo Y. K., Ho C. H. Thermoelectric properties of Zn–Sb alloys doped with In. *Journal of Alloys and Compounds*. 2009;480(1): 73–75. https://doi.org/10.1016/j.jallcom.2008.09.202

17. Liu X. J., Wang C. P., Ohnuma I., Kainuma R., Ishida K. Thermodynamic assessment of the phase diagrams of the Cu-Sb and Sb-Zn systems. *Journal of Phase Equilibria*. 2000;21: 432–442. https://doi.org/10.1361/105497100770339608

18. Izard V., Record M. C., Tedenac J. C., Fries S. G. Discussion on the stability of the antimony zinc binary phases. *Calphad*. 2001;25(4): 567–581. https://doi.org/10.1016/S0364-5916(02)00008-1

19. Adjadj F., Belbacha E. D., Bouharkat M., Kerboub A. Crystallographic study of the intermediate compounds SbZn, Sb_3Zn_4 and Sb_2Zn_3. *Journal of Alloys and Compounds*. 2006;419(1-2): 267–270. https://doi.org/10.1016/j.jallcom.2005.09.068

20. Adjadj F., Belbacha E. D., Bouharkat M. Differential calorimetric analysis of the binary system Sb–Zn. *Journal of alloys and compounds*. 2007;430(1-2): 85–91. https://doi.org/10.1016/j.jallcom.2006.04.051

21. Li J. B., Record M. C., Tedenac J. C. A thermodynamic assessment of the Sb–Zn system. *Journal of Alloys and Compounds*. 2007;438(1-2): 171–177. https://doi.org/10.1016/j.jallcom.2006.08.035

22. Okamoto H. Sb-Zn (Antimony-Zinc). *Journal of Phase Equilibria and Diffusion*. 2008;29: 290–290. https://doi.org/10.1007/s11669-008-9315-y

23. Lo C. W. T., Svitlyk V., Chernyshov D., Mozharivskyj Y. The updated Zn–Sb phase diagram. How to make pure $Zn_{13}Sb_{10}$ ("Zn_4Sb_3"). *Dalton Transactions*. 2018;47(33): 11512–11520. https://doi.org/10.1039/C8DT02521E

24. Kubaschewski O., Alcock C. B., Spenser P. *Materials Thermochemistry*. Oxford: Pergamon Press; 1993. 6th edn. 363 p.

25. Iorish V. S., Yungman V. S. (eds.). *Thermal constants of substances: database, 2006. Version 2.*

26. Barin I. *Thermochemical data of pure substances*. New York: Wiley-VCH; 2008. 3rd edn. 2003 p.

27. Schlesinger M. E. Thermodynamic properties of solid binary antimonides. *Chemical Reviews*. 2013;113(10): 8066–8092. https://doi.org/10.1021/cr400050e

28. Aliev Z. S., Babanly M. B., Shevelkov A. V., Babanly D. M., Tedenac J. C. Phase diagram of the Sb–Te–I system and thermodynamic properties of SbTeI. *International journal of materials research*. 2012;103(3): 290–295. https://doi.org/10.3139/146.110646

29. Imamaliyeva S. Z., Musayeva S. S., Babanly D. M., Jafarov Y. I., Taghiyev D. B., Babanly M. B. Determination of the thermodynamic functions of bismuth chalcoiodides by EMF method with morpholinium formate as electrolyte. *Thermochimica Acta*. 2019;679: 178319. https://doi.org/10.1016/j.tca.2019.178319

30. Aliev Z. S., Musayeva S. S., Imamaliyeva S. Z., Babanly M. B. Thermodynamic study of antimony chalcoiodides by EMF method with an ionic liquid. *Journal of Thermal Analysis and Calorimetry*. 2018;133: 1115–1120. https://doi.org/10.1007/s10973-017-6812-4

31. Alverdiyev I. J., Aliev Z. S., Bagheri S. M., Mashadiyeva L. F., Yusibov Y. A., Babanly M. B. Study of the $2Cu_2S$+ $GeSe_2 \leftrightarrow 2Cu_2Se$+ GeS_2 reciprocal system and thermodynamic properties of the $Cu_8GeS_{6-x}Se_x$ solid solutions. *Journal of Alloys and Compounds*. 2017;691: 255–262. https://doi.org/10.1016/j.jallcom.2016.08.251

32. Mashadiyeva L. F., Mammadli P. R., Babanly D. M., Ashirov G. M., Shevelkov A. V., Yusibov Y. A. Solid-phase equilibria in the Cu-Sb-S system and thermodynamic properties of copper-antimony sulfides. *JOM*. 2021;73: 1522–1530. https://doi.org/10.1007/s11837-021-04624-y

33. Babanly M. B., Yusibov Y. A. *Electrochemical methods in thermodynamics of inorganic systems*. Baku: BSU Publ.; 2011. 306 p.

34. Morachevsky A. G., Voronin G. F., Heiderich V. A., Kutsenok I. B. *Electrochemical methods of research in the thermodynamics of metallic systems*. ICC "Akademkniga" Publ.; 2003. 334 p.

35. Babanly M. B., Yusibov Y. A., Babanly N. B. In: *Electromotive force and measurement in several systems.* S. Kara (ed.). London: Intechweb. Org; 2011. p. 57. https://doi.org/10.5772/28934

36. Shao Y. (ed.). *Electrochemical cells – new advances in fundamental research and applications*. London: InTech; 2012. 252 p. https://doi.org/10.5772/1890

37. Goryacheva V. I., Geiderikh V. A. The thermodynamic properties of phases in the zinc-antimony system. *Russian Journal of Physical Chemistry A*. 1997;71(4): 526–529.

38. Goncharuk L. V, Lukashenko G. M. Thermodynamic properties of zinc antimonides. *Journal of Applied Chemistry. USSR (Engl. Transl.)*. 1988;62(8): 10.

39. Zabdyr L. A. Thermodynamic properties of zinc antimonides. *Canadian Metallurgical Quarterly*. 1980;19(4): 359–362. https://doi.org/10.1179/cmq.1980.19.4.359

40. Eremenko V. N., Lukashenko G. M. Thermodynamic properties of higher zinc antimonide. *Russian Journal of Inorganic Chemistry. (Engl. Transl.)*. 1963;8(3).

41. Hirayama C. The dissociation pressure of zinc antimonide. *Journal of The Electrochemical Society*. 1963;110(1): 88. https://doi.org/10.1149/1.2425680

42. Stolyarova T. A. Enthalpy of formation of zinc antimonite ZnSb. *Russian Metallurgy (Metally). (Engl. Transl.)*. 1979;6: 61.

43. Shchukarev S. A., Morozova M. P., Sapozhnikov Yu. P. Enthalpy of formation of compounds of zinc with antimony. *Journal of General Chemistry of the USSR (Engl. Transl.)*. 1956;26: 321.

44. Liu Y., Tedenac J. C. Thermodynamic modeling of the Cd–Sb–Zn ternary system. *Calphad*. 2009;33(4): 684–694. https://doi.org/10.1016/j.calphad.2009.08.006

45. Li J. B., Record M. C., Tedenac J. C. A thermodynamic assessment of the Sb–Zn system. *Journal of Alloys and Compounds*. 2007;438(1-2): 171–177. https://doi.org/10.1016/j.jallcom.2006.08.035

46. Seltz H., DeWitt B. J. A thermodynamic study of the lead-antimony system. *Journal of the American Chemical Society*. 1939;61(10): 2594–2597. https://doi.org/10.1021/ja01265a007

47. Zabdyr L. A. Equilibrium diagram and thermodynamic properties of cadmium—antimony binary alloys. Critical assessment. *Calphad*. 1993;17(2): 125–132. https://doi.org/10.1016/0364-5916(93)90012-Z

Information about the authors

Aytekin R. Aghayeva, PhD student in physical chemistry, Laboratory assistant, Physics Department, French-Azerbaijani University, (Baku, Azerbaijan).

https://orcid.org/0000-0001-8184-0762
aytekin_agayeva@mail.ru

Sakina H. Mammadova, PhD student in polymer chemistry, Institute of Charles Sadron of CNRS (Strasbourg, France).

https://orcid.org/0009-0000-5731-9993
sakina.mammadova@ufaz.az

Dunya M. Babanly, Dr. Sci. (Chem.), Assoc. Professor, Head of the Chemistry Department, researcher-teacher, French-Azerbaijani University (Baku, Azerbaijan).

https://orcid.org/0000-0002-8330-7854
dunya.babanly@ufaz.az

Yasin I. Jafarov, Dr. Sci. (Chem.), Professor, Head of the General and Inorganic Chemistry Department, Baku State University (Baku, Azerbaijan).

https://orcid.org/0000-0002-3968-8725
yasin.cafarov@hotmail.com

Dilgam B. Tagiyev, Professor (Chem.), Academician, Vice-President of the National Academy of Sciences of Azerbaijan, General Director of the “Institute of Catalysis and Inorganic Chemistry” (Baku, Azerbaijan).

https://orcid.org/0000-0002-8312-2980
dtagiyev@rambler.ru

Translation by the author

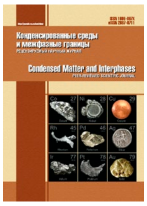

ISSN 1606-867X (Print)
ISSN 2687-0711 (Online)
Condensed Matter and Interphases
Kondensirovannye Sredy i Mezhfaznye Granitsy
https://journals.vsu.ru/kcmf/

Original articles

Research article
https://doi.org/10.17308/kcmf.2025.27/12487

Refinement of the phase diagram of the MnSe–In_2Se_3 system and the crystal structures of $MnIn_2Se_4$ and $Mn_2In_2Se_5$ compounds

F. M. Mammadov[1,2]✉, S. Z. Imamaliyeva[1], E. N. Ismailova[1], I. R. Amiraslanov[3], E. I. Akhmedov[4], M. B. Babanly[1.4]

[1]*Institute of Catalysis and Inorganic Chemistry,*
113 H. Javid av., Baku AZ-1143, Azerbaijan

[2]*Pedagogical University,*
68 Uzeyir Hajibeyov st., Baku AZ-1000, Azerbaijan

[3]*Institute of Physics of Azerbaijan National Academy of Sciences,*
131 G. Javid ave., Baku AZ-1143, Azerbaijan

[4]*Baku State University,*
23 Z. Khalilov st., Baku AZ-1148, Azerbaijan

Abstract

Complex chalcogenides based on transition elements, in particular ternary compounds of the AB_2X_4 type (M = Mn, Fe, Co, Ni; B = Ga, In, Sb, Bi; X = S, Se, Te) are among the important functional materials. Compounds of this class exhibit the phenomena of electronically or optically controlled magnetism and are very promising for the creation of lasers, light modulators, photodetectors, and other functional devices controlled by a magnetic field. Recent studies demonstrated that these compounds can also find application in photocatalysis, photovoltaics, and thermoelectric converters.

The study presents new data on phase equilibria in the MnSe–In_2Se_3 system, obtained by differential thermal analysis, X-ray phase analysis, and scanning electron microscopy. Two ternary compounds, $MnIn_2Se_4$ with congruent melting at 1193 K and $Mn_2In_2Se_5$, melting incongruently at 1196 K, were formed in the system. The first is a phase of variable composition and has a 5–6 mol. % homogeneity region towards an excess of In_2Se_3. Based on powder diffraction data, the Rietveld method was used to refine the crystal structures and lattice parameters of both ternary compounds.

Keywords: Manganese-indium selenides, Phase equilibria, Homogeneity region, Crystal structure, Rietveld method

Funding: This work is supported by the Azerbaijan Science Foundation – Grant No AEF-MCG-2022-1(42)-12/10/4-M-10.

For citation: Mammadov F. M., Imamaliyeva S. Z., Ismailova E. N., Amiraslanov I. R., Akhmedov E. I., Babanly M. B. Refinement of the phase diagram of the MnSe–In_2Se_3 system and the crystal structures of $MnIn_2Se_4$ and $Mn_2In_2Se_5$ compounds. *Condensed Matter and Interphases.* 2025;27(1): 57–66. https://doi.org/10.17308/kcmf.2025.27/12487

Для цитирования: Мамедов Ф. М., Имамалиева С. З., Исмаилова Э. Н., Амирасланов И. Р., Ахмедов Э. И., Бабанлы М. Б. Уточнение фазовой диаграммы системы MnSe–In_2Se_3 и кристаллических структур соединений $MnIn_2Se_4$ и $Mn_2In_2Se_5$. *Конденсированные среды и межфазные границы.* 2025;27(1): 57–66. https://doi.org/10.17308/kcmf.2025.27/12487

✉ Faik M. Mammadov, e-mail: faikmamadov@mail.ru

© Mammadov F. M., Imamaliyeva S. Z., Ismailova E. N., Amiraslanov I. R., Akhmedov E. I., Babanly M. B., 2025

The content is available under Creative Commons Attribution 4.0 License.

1. Introduction

Complex transition metal chalcogenides, in particular compounds of the AB_2X_4 and $A_2B_2X_5$ types (A = Fe, Mn, Co; B = Al, Ga, In, Sb, Bi; X = S, Se, Te) with a layered structure are among the important materials possessing thermoelectric [1, 2], magnetic [3–9], optical, and other functional properties [10–13]. This makes them very promising for use in the creation of lasers, light modulators, photodetectors, thermoelectric, and other functional devices. In addition, they are objects of intensive research as magnetic topological insulators, combining the properties of an antiferromagnet and a topological insulator, and are extremely promising for use in spintronics, quantum computing, and information processing devices [14–22].

A number of recent studies have shown that some compounds of the AB_2X_4 type and heterojunctions based on them can find application in photocatalysis and photovoltaics, in particular, in photocatalytic water splitting [23–27]. According to the results of [28–30], some compounds of the above type with a spinel structure are good candidates for use as a new type of anode materials for the stable storage of ions in lithium (sodium) ion batteries.

The results described above show the relevance of research aimed at obtaining and studying the properties of new complex layered chalcogenides of transition elements. Modification of such compounds by alloying and obtaining solid solutions can be used to optimize their functional properties [31–36].

The development of methods for the targeted synthesis of complex chalcogenide compounds and phases of variable composition is based on data of phase equilibria in the corresponding systems. Phase diagrams provide valuable information on the nature of formation, thermal stability, phase transformations, primary crystallization regions, and the homogeneity of intermediate phases [37–43].

Previously, studies of phase equilibria in a number of quasi-ternary MX–Ga_2X_3–In_2X_3 systems (M = Mn, Fe; X = S, Se, Te) were performed, in search of the physicochemical foundations for creating new magnetic semiconductors [44–50]. In the indicated systems, new phases of variable composition based on ternary AB_2X_4 compounds have been identified, their primary crystallization fields and homogeneity regions were determined.

Preliminary experimental results in the study of the MnSe–Ga_2Se_3–In_2Se_3 system, revealed their discrepancy with the known [51] phase diagram of the MnSe–In_2Se_3 boundary system. Taking this into account these findings, in this study we have undertaken a repeated study of phase equilibria in the MnSe–In_2Se_3system.

The initial compounds of the studied system were investigated in detail. The MnSe compound melts congruently at 1875 K and has three modifications: a stable low-temperature α-MnSe crystallizes in a cubic NaCl-type structure. The β-MnSe and γ-MnSe phases are unstable. The first phase crystallizes in a cubic structure of the sphalerite type, and the second crystallizes in a hexagonal structure of the wurtzite type [52–55], (Table 1).

The In_2Se_3 compound melts with an open maximum at 1158 K and undergoes three polymorphic transformations (473, 920, and 1023 K) [52, 53]. The types and parameters of crystal lattices of all four crystalline modifications of In_2Se_3 are described in detail in [56], (Table 1).

Table. 1. Crystallographic data of MnSe and In_2Se_3

Соединение	Type and parameters of the crystal lattice, nm	Ref.
MnSe-rt	Kubik, Sp.Gr. $Fm\bar{3}m$; $a = 0.5456$	[54]
MnSe-ht1	Kubik, Sp.Gr. $F\bar{4}3m$; $a = 0.583$	[55]
MnSe-ht2	Heksaqonal, Sp.Gr. $P63mc$; $a = 0.413$, $c = 0.673$	[55]
In_2Se_3-rt	Heksaqonal, Sp.Gr. $R3m$; $a = 0.405$, $c = 2.877$	[56]
In_2Se_3-ht1	Heksaqonal, Sp.Gr. $P6_5$; $a = 0.711$, $c = 1.930$	[56]
In_2Se_3-ht2	Heksaqonal, Sp.Gr. $P6_1$; $a = 0.7133$, $c = 1.934$	[56]
In_2Se_3- ht3	Heksaqonal, Sp.Gr. $P6_1$; $a = 0.4014$, $c = 0.964$	[56]

2. Experimental

2.1. Synthesis

The MnSe and In_2Se_3 compounds were synthesized by the direct interaction of stoichiometric quantities of high-purity elemental components (manganese – 99.95%, indium – 99.999% and selenium – 99.99% from Alfa Aesar) in sealed quartz glass ampoules evacuated to ~ 10^{-2} Pa. The syntheses were carried out in a two-zone inclined furnace. The lower "hot" zone was heated to 1200 K, and the upper "cold" zone was heated to 900 K, which is slightly lower than the boiling point (958 K) of elemental selenium [57]. In order to avoid the interaction of quartz with manganese, MnSe synthesis was carried out in a graphitized ampoule.

The individuality of the synthesized compounds was controlled by differential thermal analysis (DTA) and X-ray diffraction (XRD) methods. Temperatures of polymorphic transitions and melting of In_2Se_3, determined based on the DTA heating curves, coincided with the available literature data [52, 53]. The following crystallographic parameters were obtained by interpretation of the powder X-ray diffraction patterns: MnSe – cubic, sp. gr. $Fm\bar{3}m$, a = 0.54542(4) nm, RT-In_2Se_3 – hexagonal, sp.gr. $R\bar{3}m$, a = 0.40804(5), c = 2.8712(14) nm, which are in good agreement with the literature data [54–56], (Table 1).

Alloys of the MnSe– In_2Se_3 system were prepared by fusing the initial binary compounds in various ratios in evacuated quartz ampoules at 1200–1300 K, followed by thermal annealing at 800 K for 500 hours and cooling in a switched-off furnace.

2.2. Research methods

The studies were carried out using DTA, X-ray diffraction and scanning electron microscopy (SEM) methods. The DTA of samples weighing 0.1–0.3 g in evacuated quartz ampoules was carried out using a Netzsch STA 449 F3 unit (platinum – platinum/rhodium thermocouples) in the temperature range from room temperature to ~ 1450 K with a heating rate of 10 K·min^{-1}. The temperature measurement accuracy was within ±2 K.

The X-ray powder diffraction analysis of powder samples was performed using a D2 Phaser diffractometer (Bruker, Germany; Cu$K\alpha$-radiation, angle range $5° \leqslant 2\theta \leqslant 80°$, scanning rate of 0.03°×0.2 min). The crystal lattice parameters of ternary compounds were refined by the Rietveld method using the EVA and TOPAS 4.2 programs. The SEM analysis was performed using the Tescan Vega 3 SBH scanning electron microscope.

3. Results and discussion

The joint processing of DTA, X-ray diffraction, and SEM data for synthesized and annealed alloys allowed us to obtain a new, more precise pattern of phase equilibria in the MnSe – In_2Se_3 system. Below in the text, in the figures and in the tables the following phase designations are used: α and γ-solid solutions based on the MnSe and $MnIn_2Se_4$; β_1, β_2, β_3 and β_4-solid solutions based on high-temperature, two intermediate and low-temperature modifications of the In_2Se_3 compound, respectively.

The X-ray diffraction method showed that alloys of composition 33.3 ($Mn_2In_2Se_5$) and 50 mol. % In_2Se_3 ($MnIn_2Se_4$) have individual diffraction patterns that differ from those of the original compounds. Diffraction patterns of other intermediate alloys consisted of two-phase mixtures α + $Mn_2In_2Se_5$, $Mn_2In_2Se_5$ + $MnIn_2Se_4$ (γ) and γ + β_4 respectively (Fig. 1).

Based on powder diffraction patterns, the Rietveld method was used to refine the crystal structures of both ternary compounds. The experimental and calculated diffraction patterns, as well as the differences in their intensities are shown in Fig. 2 and 3. The refined parameters of the elementary cells are shown in Table 2, and the atomic positional parameters are shown in Tables 3 and 4. The crystal structures of the $MnIn_2Se_4$ and $Mn_2In_2Se_5$ compounds are shown in Fig. 4. Both compounds are layered phases of the van der Waals type. Their structural blocks are fragments consisting of 7 and 9 atomic layers, in which the atoms alternate as Se-In-Se-Mn-Se-In-Se and Se-In-Se-Mn-Se-Mn-Se-In-Se respectively. In both structures, Mn atoms are located at the centers of octahedra, and In atoms are located at the centers of tetrahedra formed by Se atoms. These blocks are bound together by van der Waals bonds. The results obtained for polycrystalline samples using the Rietveld method are in good agreement with the data of studies [58, 59], obtained based on diffraction data of single crystals.

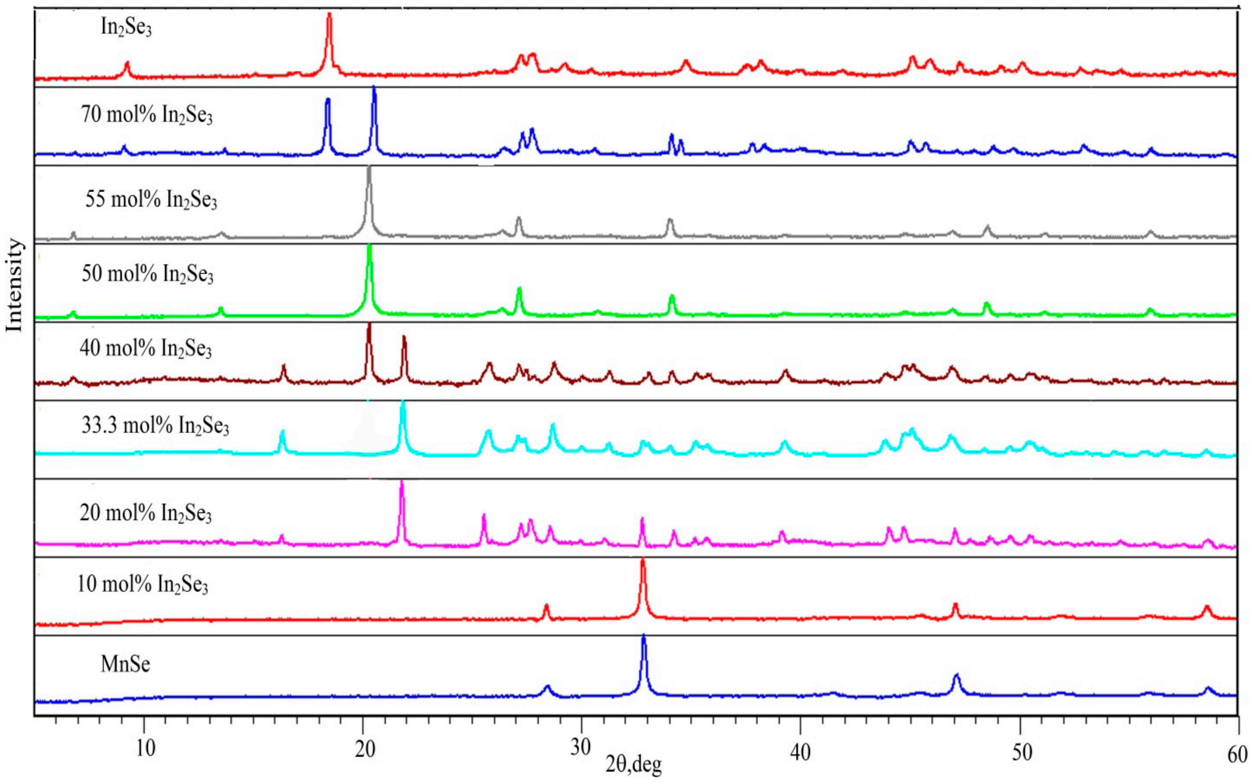

Fig. 1. The XRD patterns of alloys of the MnSe-In_2Se_3 system

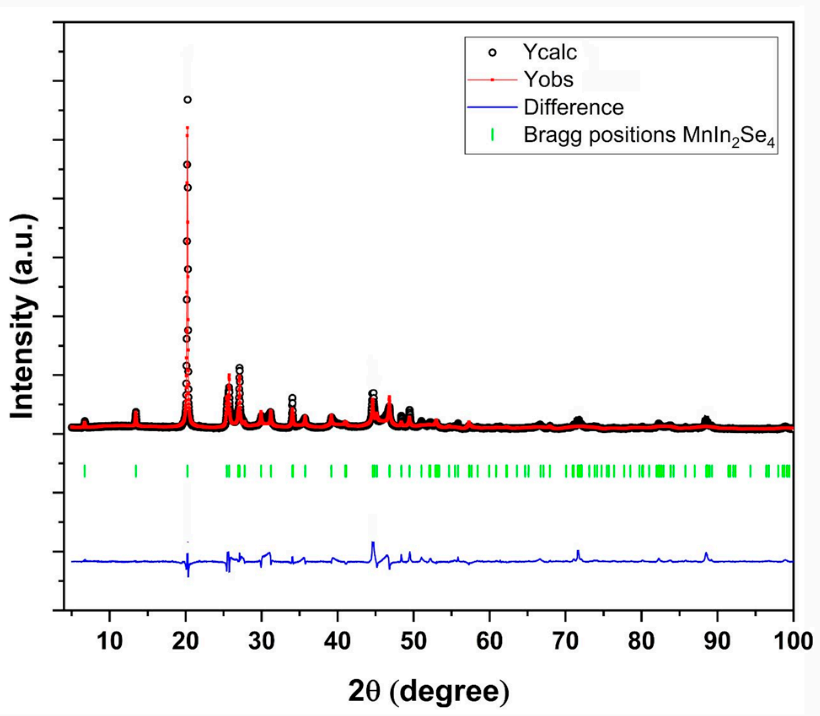

Fig. 2. Experimental and calculated diffraction lines of $MnIn_2Se_4$, as well as the differences in their intensities

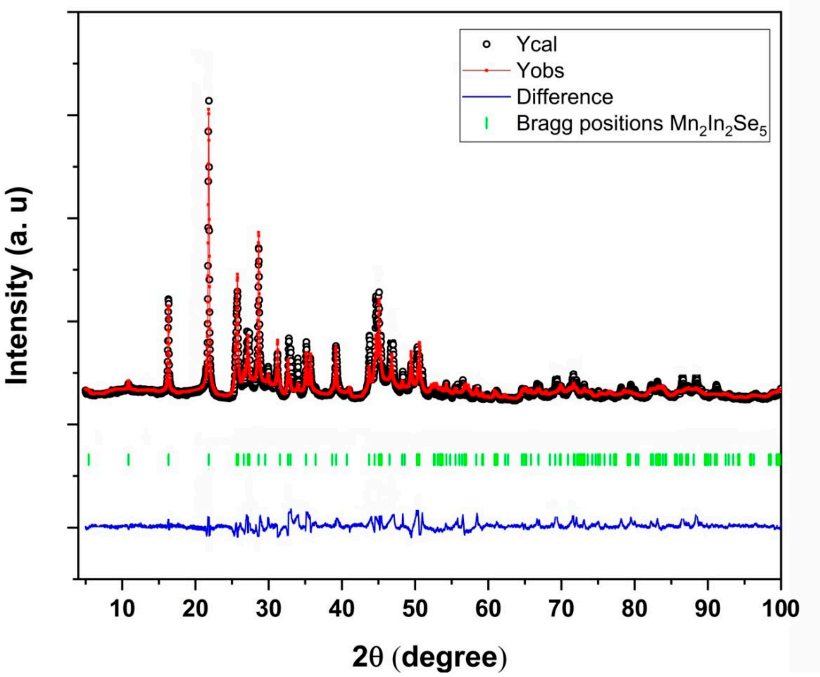

Fig. 3. Experimental and calculated diffraction lines of $Mn_2In_2Se_5$, as well as the differences in their intensities

Table. 2. Refined parameters of the structure of $MnIn_2Se_4$ and $Mn_2In_2Se_5$

Structure parameters	$MnIn_2Se_4$	$Mn_2In_2Se_5$
Space group	$R\bar{3}m$	$R\bar{3}m$
Cell parameters: *a* (nm) *c* (nm)	 0.405289(45) 3.94594(44)	 0. 402240(57) 4.87486(79)
The cell volume (nm^3)	0.56243(17)	0.68307(22)
Density (g/cm^3)	5.318(91)	5.36014(50)
R-Bragg (%)	0.873	0.428

Table. 3. Atomic positional parameters in $MnIn_2Se_4$

Atoms	Multiplicity of positions	*x*	*y*	*z*	Atom type	Relative occupation
In1	6	0.00000	0.00000	0.76964(31)	In^{+3}	1.000(42)
Se2	6	0.00000	0.00000	0.70467(46)	Se	1
Se1	6	0.00000	0.00000	0.12160(56)	Se	1
Mn	3	0.00000	0.00000	0.00000	Mn^{+2}	1.001(68)

Table.4. Atomic positional parameters in $Mn_2In_2Se_5$

Atoms	Multiplicity of positions	*x*	*y*	*z*	Atom type	Relative occupation
Se2	6	0.00000	0.00000	0.39354(22)	Se	1
Mn1	6	0.00000	0.00000	0.70092(31)	Mn^{+2}	1
Se1	6	0.00000	0.00000	0.13546(20)	Se	1
In2	6	0.00000	0.00000	0.55513(13)	In^{+3}	1
Se3	3	0.00000	0.00000	0.00000	Se	1

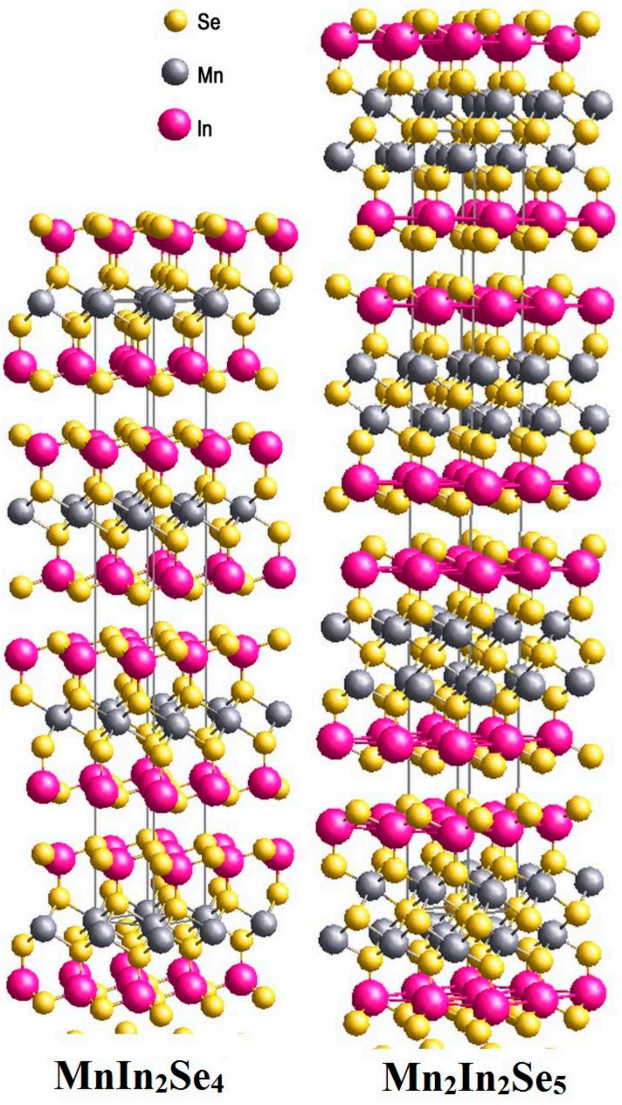

Fig. 4. Three-dimensional view of the structures of $MnIn_2Se_4$ and $Mn_2In_2Se_5$

It should be noted that the $MgIn_2Se_4$ and $ZnIn_2S_4$ compounds are also characterized by a similar structure, however, the authors [60] chose an asymmetric space group $R\bar{3}m$ to describe the structure of $MgIn_2Se_4$.

Interpretation of DTA data on the heating of annealed alloys of $MnSe–In_2Se_3$ system (Table 5), taking into account the above presented XRD results, allowed us to construct a *T-X* phase diagram (Fig. 5). According to our data, the $MnSe–In_2Se_3$ system can be considered quasi-binary, since the compositions of all phases in equilibrium are on its *T-X* planes. The system is characterized by the formation of two intermediate compounds: the $MnIn_2Se_4$ compound melts congruently at 1195 K and has a wide homogeneity region

Table. 5. DTA results of alloys of the $MnSe–In_2Se_3$ system

Composition, mol. % In_2Se_3	Thermal effects, K
10	–
20	1195
30	1197; 1197–1440
33.3	1196; 1196–1390
35	1188–1196; 1196–1360
40	1188 –1196; 1196-1285
45	1188
50	1195
55	1180–1193
60	1150–1190
70	462; 1148; 1148–1185
80	460; 1148; 1148–1176
90	463; 910; 1005; 1150
95	465; 910; 1005;1148–1155
100	475; 920 ; 1023; 1163

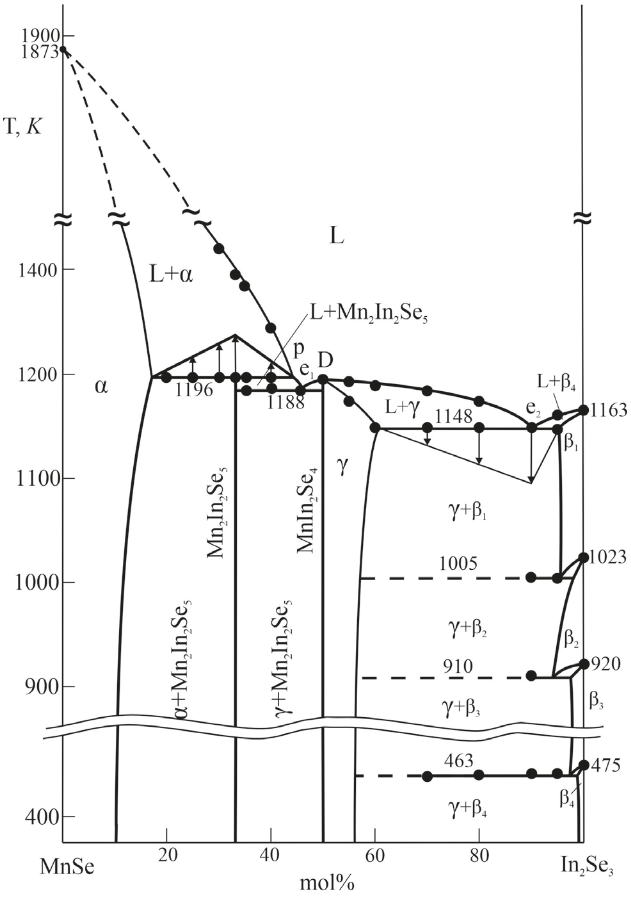

Fig. 5. Phase diagram of the $MnSe-In_2Se_3$ system

(γ-phase) towards an excess of the In_2Se_3. The second compound of the composition $Mn_2In_2Se_5$ melts with decomposition according to the peritectic reaction L + a ↔ $Mn_2In_2Se_5$ at 1196 K. The peritectic point has a composition of 42 mol. % In_2Se_3, the γ-phase is in eutectic equilibrium with the neighboring phases:

$L \leftrightarrow Mn_2In_2Se_5 + \gamma$
(point e_1, 45 mol. % In_2Se_3, 1188 K)
$L \leftrightarrow \beta_1 + \gamma$ (point e_2, 90 mol. % In_2Se_3, 1148 K).

The compositions of the peritectic and eutectic points, as well as the homogeneity regions of the phases, were refined by the plotting of the Tamman's triangle (Fig. 5). It has been established that the homogeneity region of the α-phase at the peritectic temperature is 15 mol. %, and at eutectic temperature e_2 homogeneity regions of γ- and β_1-phases reach 10 and 5 mol. %, respectively. With a decreasing temperature of the homogeneity region the α- and γ-phases were somewhat narrowed and, according to X-ray diffraction data (Fig. 1), at room temperature, they were ~10 and 5 mol. %.

The phase compositions of the alloys, in particular the areas of phase homogeneity, were confirmed by SEM results (Fig. 6). As can be seen, the SEM images are in accordance with the phase diagram: the alloy with the composition 55 mol. % In_2Se_3, as well as the alloy with the stoichiometric composition $MnIn_2Se_4$ are single-phase, and the other three samples from different two-phase regions of the phase diagram are two-phase.

The obtained pattern of phase equilibria in the MnSe– In_2Se_3 system differed significantly from the data obtained in [51]. The phase diagram presented in [51] reflected only one ternary compound: $MnIn_2Se_4$ with congruent melting at ~1200 K. In

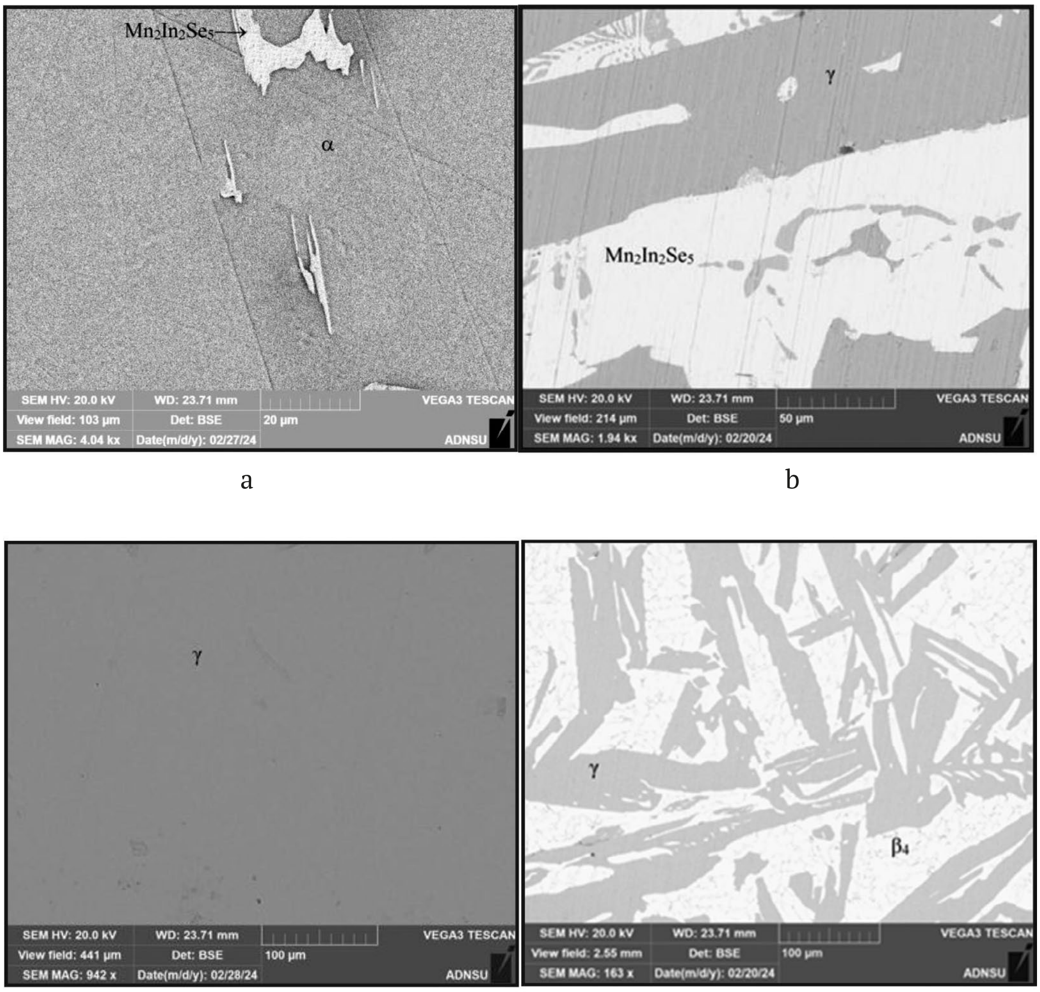

a b

c d

Fig. 6. SEM images of some single- and two-phase alloys of the MnSe-In_2Se_3 system: a) 15; b) 40; c) 55 and d) 70 mol. % In_2Se_3

addition, according to data [51], solubility based on MnSe was practically absent, and homogeneity regions based on various modifications of In_2Se_3 ranged from 5 (low temperature) to 25 mol. % (high temperature). Our data also differ significantly from data of [51] for the coordinates of eutectic and eutectoid equilibria.

4. Conclusions

Thus, we present a new refined version of the phase diagram of the MnSe-In_2Se_3 system, on which, in contrast to the data [51], in addition to $MnIn_2Se_4$, a ternary compound of the $Mn_2In_2Se_5$composition, melting with decomposition according to a peritectic reaction at 1196 K, was also formed. According to our data, $MnIn_2Se_4$ melts congruently at 1193 K and is a phase of variable composition, the homogeneity region at room temperature is ~5 mol. %. The crystal structures and lattice parameters of the $MnIn_2Se_4$ and $Mn_2In_2Se_5$ compounds were refined based on the XRD data, using the Rietveld method. Both ternary compounds were shown to have a layered structure and crystallize in the $R\bar{3}m$ space group.

Author contributions

F. M. Mammadov – research concept, discussion of results, writing the article; S. Z. Imamaliyeva – processing of the obtained results and participation in writing the article; E. N. Ismailova – literature search and participation in experiments; I. R. Amiraslanov – conducting structural studies; E. I. Akhmedov – processing the obtained results and writing the article; M. B. Babanly – scientific leadership, scientific editing.

Conflict of interests

The authors declare that they have no known competing financial interests or personal relationships that could have influenced the work reported in this paper.

References

1. Wyżga P., Veremchuk I., Bobnar M., Hennig C., Jasper A. L., Gumeniuk R. Ternary MIn_2S_4 (M = Mn, Fe, Co, Ni) thiospinels – crystal structure and thermoelectric properties. *Zeitschrift für anorganische und allgemeine Chemie*. 2020;646(14): 1091. https://doi.org/10.1002/zaac.202000014

2. Karthikeyan N., Aravindsamy G., Balamurugan P., Sivakumar K. Thermoelectric properties of layered type $FeIn_2Se_4$ chalcogenide compound. *Materials Research Innovations*. 2018;22(5): 278. https://doi.org/10.1080/14328917.2017.1314882

3. Hyunjung K., Tiwari A. P., Hwang E., … Hyoyoung L. $FeIn_2S_4$ nanocrystals: a ternary metal chalcogenide material for ambipolar field-effect transistors. *Advanced Science*. 2018;5(7): 1800068. https://doi.org/10.1002/advs.201800068

4. Yang J., Zhou Z., Fang J., … Wei Z. Magnetic and transport properties of a ferromagnetic layered semiconductor $MnIn_2Se_4$. *Applied Physics Letters*. 2019;115(22): 222101. https://doi.org/10.1063/1.5126233

5. Myoung B. R., Lim J. T., Kim C. S. Investigation of magnetic properties on spin-ordering effects of $FeGa_2S_4$ and $FeIn_2S_4$. *Journals of Magnetism and Magnetic Materials*. 2017;438: 121. https://doi.org/10.1016/j.jmmm.2017.04.056

6. Ranmohotti K. G. S., Djieutedjeu H., Lopez J., … Poudeu P. F. P. Coexistence of high-T c herromagnetism and n-type electrical conductivity in $FeBi_2Se_4$. *Journal of the American Chemical Society*. 2015;137(2): 691–698. https://doi.org/10.1021/ja5084255

7. Guratinder K., Schmidt M., Walker H. C., … Zaharko O. Magnetic correlations in the triangular antiferromagnet $FeGa_2S_4$. Physical Review B. 2021;104: 064412. https://doi.org/10.1103/PhysRevB.104.064412

8. Romero L., Pacheco J., Cadenas R. Calculation of the lattice energy and the energy gap of the magnetic semiconductor $MnGa_2Se_4$ using Hartree-Fock and density functional theory methods. *Revista Mexicana de F´ısica*. 2016;62(6): 526–529. Режим доступа: https://www.scielo.org.mx/scielo.php?script=sci_arttext&pid=S0035-001X2016000600526

9. Verchenko V. Yu., Kanibolotskiy A.V., Bogach A. V., Znamenkova K. O., Shevelkov A. V. Ferromagnetic correlations in the layered van der Waals sulfide $FeAl_2S_4$. *Dalton Transactions*. 2022;51(21): 8454–8460. https://doi.org/10.1039/d2dt00671e

10. Hwang Y., Choi J., Ha Y., Cho S., Park H. Electronic and optical properties of layered chalcogenide $FeIn_2Se_4$. *Current Applied Physics*. 2020;20(1): 212–218. https://doi.org/10.1016/j.cap.2019.11.005

11. Pauliukavets S. A., Bychek I. V., Patapovich M. P. Specific features of the growth, structure, and main physicochemical properties of $FeGa_2Se_4$ single crystals. *Inorganic Materials: Applied Research*. 2018;9(2): 207–211. https://doi.org/10.1134/S2075113318020223

12. Chernoukhov I. V., Bogach A. V., Cherednichenko K. A., Gashigullin R. A., Shevelkov A. V., Verchenko V. Yu. $Mn_2Ga_2S_5$ and $Mn_2Al_2Se_5$ van der Waals chalcogenides: a source of atomically thin nanomaterials. *Molecules*. 2024;29(9): 12. https://doi.org/10.3390/molecules29092026

13. Verchenko Yu. V., Kanibolotskiy A.V., Chernoukhov I. V., … Shevelkov A. V. Layered van der Waals chalcogenides $FeAl_2Se_4$, $MnAl_2S_4$, and $MnAl_2Se_4$: atomically thin triangular arrangement of transition-metal atoms. *Inorganic Chemistry*. 2023;62(19): 7557–7565. https://doi.org/10.1021/acs.inorgchem.3c00912

14. Otrokov M. M., Klimovskikh I. I., Bentmann H., … Chulkov E. V. Prediction and observation of an antiferromagnetic topological insulator. *Nature*. 2019;576: 416–422. https://doi.org/10.1038/s41586-019-1840-9

15. Estyunin D. A., Klimovskikh I. I., Shikin A. M., … Chulkov E. V. Signatures of temperature driven antiferromagnetic transition in the electronic structure of topological insulator $MnBi_2Te_4$. *Materials*. 2020;8(2): 021105(1-7). https://doi.org/10.1063/1.5142846

16. Jahangirli Z. A., Alizade E. H., Aliev Z. S., ... Chulkov E. V. Electronic structure and dielectric function of Mn-Bi-Te layered compounds. *Journal of Vacuum Science and Technology B*. 2019;37(6): 062910. https://doi.org/10.1116/1.5122702

17. Garnica M., Otrokov M., Aguilar P. C., ... Miranda R. Native point defects and their implications for the Dirac point gap at $MnBi_2Te_4$(0001). *npj Quantum Materials*. 2022;7(7): 1. https://doi.org/10.1038/s41535-021-00414-6

18. Yonghao Y., Xintong W., Hao L., ... Qi-Kun X. Electronic states and magnetic response of $MnBi_2Te_4$ by scanning tunneling microscopy and spectroscopy. *Nano Letters*. 2020;20: 3271–3277. https://doi.org/10.1021/acs.nanolett.0c00031

19. Zhou L., Tan Z., Yan D., Fang Z., Shi Y., Weng H. Topological phase transition in the layered magnetic compound $MnSb_2Te_4$: spin-orbit coupling and interlayer coupling dependence. *Physical Review B*. 2020;102: 085114(1-8). https://doi.org/10.1103/PhysRevB.102.085114

20. Zhu T., Bishop A. J., Zhou T. Synthesis, magnetic properties, and electronic structure of magnetic topological insulator $MnBi_2Se_4$. *Nano Leterst*. 2021;21(12): 5083–5090. https://doi.org/10.1021/acs.nanolett.1c00141

21. Swatek P., Wu Y., Wang L. L. Gapless Dirac surface states in the antiferromagnetic topological insulator $MnBi_2Te_4$. *Physical Review B: Condensed Matter and Materials Physics*. 2020;101(16): 161109. https://doi.org/10.1103/PhysRevB.101.161109

22. Ovchinnikov D., Huang X., Lin Z., ... Xu X. Intertwined topological and magnetic orders in atomically thin chern insulator $MnBi_2Te_4$. *Nano Letters*. 2021;21(6): 2544. https://doi.org/10.1021/acs.nanolett.0c05117

23. Liang H., Feng T., Tan S., ... Cao L. Two-dimensional (2D) $MnIn_2Se_4$ nanosheets with porous structure: a novel photocatalyst for water splitting without sacrificial agents. *Chemical Communications*. 2019;55: 15061. https://doi.org/10.1039/C9CC08145C

24. Chen W., He Z. C., Huang G. B., Wu C.-L., Chen W.-F., Liu X.-H. Direct Z-scheme 2D/2D $MnIn_2S_4$/g-C_3N_4 architectures with highly efficient photocatalytic activities towards treatment of pharmaceutical wastewater and hydrogen evolution. *Chemical Engineering Journal*. 2019;359: 244. https://doi.org/10.1016/j.cej.2018.11.141

25. Song Y., Guo Y., Qi S., ... Lou Y. Cu_7S_4/$MnIn_2S_4$ heterojunction for efficient photocatalytic hydrogen generation. *Journal of Alloys and Compounds*. 2021;884: 161035. https://doi.org/10.1016/j.jallcom.2021.161035

26. Zhang B., Liu Y., Zhu H., Gu D., Zhou K., Hao J. Enhanced visible light photocatalytic performance of a novel $FeIn_2S_4$ microsphere/BiOBr nanoplate heterojunction with a Z-scheme configuration. *Environmental Science and Pollution Research*. 2023;30: 13438–13448 . https://doi.org/10.1007/s11356-022-22929-6

27. Sharan A., Sajjad M., Singh D. J., Singh N. Two-dimensional ternary chalcogenides FeX2Y4 (X = Ga, In; Y = S, Se, Te): Promising materials for sustainable energy. *Physical Review Materials*. 2022;6: 094005. https://doi.org/10.1103/PhysRevMaterials.6.094005

28. Muruganantham R., Chen J.-A., Yang C.-C. Spinel phase $MnIn_2S_4$ enfolded with reduced graphene oxide as composite anode material for lithium-ion storage. *Materials Today Sustainability*. 2023;21: 100278. https://doi.org/10.1016/j.mtsust.2022.100278

29. Wu P., Huang Ch., Hsieh Ch., Liu W. Synthesis and characterization of $MnIn_2S_4$/single-walled carbon nanotube composites as an anode material for lithium-ion batteries. *Nanomaterials*. 2024;14(18): 716. https://doi.org/10.3390/nano14080716

30. Yan D., Li K., Yan Y., ... Yang H. Y. Cubic spinel XIn_2S_4 (X = Fe, Co, Mn): a new type of anode material for superfast and ultrastable Na-ion storage. *Advanced Energy Materials*. 2021;11: 2102137. https://doi.org/10.1002/aenm.202102137

31. Tarasov A. V., Makarova T. P., Estyunin D. A., ... Shikin A. M. Topological phase transitions driven by Sn doping in $(Mn_{1-x}Sn_x)Bi_2Te_4$. *Symmetry*. 2023;15(2): 469. https://doi.org/10.3390/sym15020469

32. Djieutedjeu H., Lopez J. S., Lu R., ... Poudeu P. F. P. Charge disproportionation triggers bipolar doping in $FeSb_{2-x}Sn_xSe_4$ ferromagnetic semiconductors, enabling a temperature-induced lifshitz transition. *Journal of the American Chemical Society*. 2019;141(23): 9249. https://doi.org/10.1021/jacs.9b01884

33. Levy I., Forrester C., Ding X., Testelin C., Krusin-Elbaum L., Tamargo M. C. High Curie temperature ferromagnetic structures of $(Sb_2Te_3)_{1-x}(MnSb_2Te_4)_x$ with $x = 0.7–0.8$. *Scientific Reports*. 2023;13: 7381. https://doi.org/10.1038/s41598-023-34585-y

34. Moroz N. A., Lopez J. S., Djieutedjeu H., ... Poudeu P. F. P. Indium preferential distribution enables electronic engineering of magnetism in $FeSb_{2-x}In_xSe_4$ *p*-type high-Tc ferromagnetic semiconductors. *Chemistry of Materials*. 2016;28(23): 8570. https://doi.org/10.1021/acs.chemmater.6b03293

35. Levy I., Forrester C., Deng H., ... Tamargo M. C. Compositional control and optimization of molecular beam epitaxial growth of $(Sb_2Te_3)_{1-x}(MnSb_2Te_4)_x$ magnetic topological insulators. *Crystal Growth and Design*. 2022;22(5): 3007. https://doi.org/10.1021/acs.cgd.1c01453

36. Liu Y., Kang Ch., Stavitski E., Attenkofer K., Kotliar G., Petrovic C. Polaronic transport and thermoelectricity in $Fe_{1-x}Co_xSb_2S_4$ (x = 0, 0.1, and 0.2). *Physical Review B*. 2018;97(15): 155202. https://doi.org/10.1103/PhysRevB.97.155202

37. Babanly M. B., Yusibov Y. A., Imamaliyeva S. Z., Babanly D. M., Alverdiyev I. J. Phase diagrams in the development of the argyrodite family compounds and solid solutions based on them. *Journal of Phase Equilibria and Diffusion*. 2024;45: 228–255 https://doi.org/10.1007/s11669-024-01088-w

38. Babanly M. B., Mashadiyeva L. F., Imamaliyeva S. Z., Tagiev D. B., Babanly D. M., Yusibov Yu. A. Thermodynamic properties of complex copper chalcogenides (review). *Chemical Problems*. 2024;3(22): 243-280. https://doi.org/10.32737/2221-8688-2024-3-243-280

39. Imamaliyeva S. Z., Mekhdiyeva I. F., Babanly D. M., Zlomanov V. P., Tagiyev D. B., Babanly M. B. Solid-phase equilibria in the $Tl_2Te–Tl_2Te_3–TlErTe_2$ system and the thermodynamic properties of the Tl_9ErTe_6 and $TlErTe_2$ compounds. *Russian Journal of Inorganic Chemistry*. 2020;65: 1762–1769. https://doi.org/10.1134/S0036023620110066

40. Orujlu E. N., Aliev Z. S., Babanly M. B. The phase diagram of the MnTe–SnTe–Sb_2Te_3 ternary system and synthesis of the iso- and aliovalent cation-substituted solid solutions. *Calphad*. 2022;76: 102398. https://doi.org/10.1016/j.calphad.2022.102398

41. Aghazade A. I., Babanly D. M., Zeynalova G. S., Gasymov V. A., Imamaliyeva S. Z. Phase relations in the Bi$_2$-Bi$_2$Se$_3$-Bi$_2$Te$_3$ system and characterization of solid solutions. *Azerbaijan Chemical Journal*. 2024;1: 76–88. https://doi.org/10.32737/0005-2531-2024-76-88

42. Ismailova E.N., Mashadiyeva L.F., Bakhtiyarly I.B., Babanly M.B. Phase equilibria in the Cu2SnSe3–Sb2Se3–Se system. *Condensed Matter and Interphases*. 2023; 25(1): 47–54 https://doi.org/10.17308/kcmf.2023.25/10973

43. Mammadov S. H. The study of the quasi-triple system FeS-Ga$_2$S$_3$-Ag$_2$S by a FeGa$_2$S$_4$-AgGaS$_2$ section. *Condensed Matter and Interphases*. 2020;22(2): 232–237.

44. Mammadov F. M., Imamaliyeva S. Z., Jafarov Ya. I., Bakhtiyarly I. B., Babanly M. B. Phase equilibria in the MnTe–MnGa$_2$Te$_4$–MnIn$_2$Te$_4$ system. *Condensed Matter and Interphases*. 2022;24(3): 335–344. https://doi.org/10.17308/kcmf.2022.24/9856

45. Mammadov F. M., Amiraslanov I. R., Imamaliyeva S. Z., Babanly M. B. Phase relations in the FeSe–FeGa$_2$Se$_4$–FeIn$_2$Se$_4$ system: refinement of the crystal structures of FeIn$_2$Se$_4$ and FeGaInSe$_4$. *Journal of Phase Equilibria and Diffusion*. 2019;40(6): 787–796. https://doi.org/10.1007/s11669-019-00768-2

46. Mammadov F. M., Agayeva R. M., Amiraslanov I. R., Babanly M. B. Revised phase diagram of the MnSe–Ga$_2$Se$_3$ system. *Russian Journal of Inorganic Chemistry*. 2024. https://doi.org/10.1134/S0036023623602611

47. Mamedov F. M., Babanly D. M., Amiraslanov I. R., Tagiev D. B., Babanly M. B. Physicochemical analysis of the FeSe–Ga2Se3–In2Se3 system. *Russian Journal of Inorganic Chemistry*. 2020;65(11): 1747–1755. https://doi.org/10.1134/s0036023620110121

48. Mammadov F. M., Amiraslanov I. R., Aliyeva Y. R., Ragimov S. S., Mashadiyeva L. F., Babanly M. B. Phase equilibria in the MnGa$_2$Te$_4$-MnIn$_2$Te$_4$ system, crystal structure and physical properties of MnGaInTe$_4$. *Acta Chimica Slovenica*. 2019;66: 466. https://doi.org/10.17344/acsi.2019.4988

49. Mammadov F. M., Babanly D. M., Amiraslanov I. R., Tagiev D. B., Babanly M. B. FeS–Ga$_2$S$_3$–In$_2$S$_3$ system. *Russian Journal of Inorganic Chemistry*. 2021;66(10): 1533. https://doi.org/10.1134/s0036023621100090

50. Mammadov F. M., Niftiev N. N., Jafarov Ya. I., Babanly D. M., Bakhtiyarly I. B., Babanly M. B. Physicochemical analysis of the MnTe–Ga$_2$Te$_3$–In$_2$Te$_3$ system and AC electrical conductivity of MnGaInTe$_4$. *Russian Journal of Inorganic Chemistry*. 2022;67(10): 1623–1633. https://doi.org/10.1134/S0036023622600769

51. Babaeva P. K., Allazov M. R. *Research in the field of inorganic and physical chemistry**. Collection of works / Z. G. Zulfugarov et al. (eds.). Institute of Inorganic and Physical Chemistry of the USSR Academy of Sciences. Baku: Elm, 1974. 318 p. (In Russ.)

52. *Phase diagrams of binary metallic systems** / N. R. Lyakishev (rd.). Moscow: Mashinostroenie Publ.; 2001. Vol. 3. Book 1. p. 382.

53. Massalski T. B. *Binary alloy phase diagrams - second edition*.,Ohio: ASM International Materials Park; 1990. 3875 p.

54. Hussain R. A., Hussain I. Manganese selenide: synthetic aspects and applications. *Journal of Alloys and Compounds*. 2020;842(25): 155800. https://doi.org/10.1016/j.jallcom.2020.155800

55. Hyunjung K.,Vogelgesang R., Ramdas A. K., Peiris F. C., Bindley U., Furdyna J. K. MnSe: rocksalt versus zinc-blende structure. *Physical Review B*. 1998;58(11): 6700–6703. https://doi.org/10.1103/physrevb.58.6700

56. Jiping Ye J. Y., Sigeo Soeda S. S., Yoshio Nakamura Y. N., Osamu Nittono O. N. Crystal structures and phase transformation in In$_2$Se$_3$ compound semiconductor. *Japanese Journal of Applied Physics*. 1998; 37(8R): 4264. https://doi.org/10.1143/JJAP.37.4264

57. Emsley J. *The elements*. Oxford University Press; 1998. 300 p.

58. Range K.-J., Klement U., Döll G. Notizen: The crystal structure of MnIn$_2$Se$_4$, a ternary layered semiconductor. *Zeitschrift Für Naturforschung B*. 1991;46(8): 1122. https://doi.org/10.1515/znb-1991-0825

59. Range K.-J., Klemnt U., Döll G. Dimanganese diindium pentaselenide, Mn$_2$In$_2$Se$_5$. *Acta Crystallographica Section C Crystal Structure Communications*. 1992;48(2): 355 https://doi.org/10.1107/S0108270191008521

60. Dotzel P., Schäfer H., Schön G. Zur Darstellung und Strukturchemie Ternärer Selenide des Magnesiums mit Indium und Aluminium. *Zeitschrift für anorganische und allgemeine Chemie*. 1976;426: 260-268. https://doi.org/10.1002/zaac.19764260305

** Translated by author of the article*

Information about the authors

Faik M. Mammadov, PhD (Chem.), Assistance Professor, Leading Researcher, Institute of Catalysis and Inorganic Chemistry (Baku, Azerbaijan).

https://orcid.org/0000-0003-3317-7438
faikmamadov@mail.ru

Samira Z. Imamaliyeva, Dr. Sci. (Chem.), Assistance Professor, Institute of Catalysis and Inorganic Chemistry (Baku, Azerbaijan).

https://orcid.org/0000-0001-8193-2122
samira9597a@gmail.com

Elnara N. Ismailova, PhD student, Researcher, Institute of Catalysis and Inorganic Chemistry (Baku, Azerbaijan).

https://orcid.org/0000-0002-1327-1753
ismayilova818@mail.ru

Imamaddin R. Amiraslanov, Dr. Sci. (Phys.), Professor, Head of Laboratory, Institute of Physics (Baku, Azerbaijan).

https://orcid.org/0000-0001-7975-614X
iamiraslan@gmail.com

Eldar I. Ahmadov, Dr. Sci. (Chem.), Professor, Baku State University (Baku, Azerbaijan).

eldar_akhmedov@mail.ru

Mahammad B. Babanly, Dr. Sci. (Chem.), Professor, Associate Member of the Azerbaijan National Academy of Sciences, Deputy-director of the Institute of Catalysis and Inorganic Chemistry (Baku, Azerbaijan).

https://orcid.org/0000-0001-5962-3710
babanlymb@gmail.com

Received 05.09.2024; approved after reviewing 18.09.2024; accepted for publication 15.10.2024; published online 25.03.2025.

Translated by Valentina Mittova

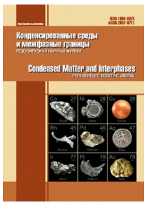

ISSN 1606-867X (Print)
ISSN 2687-0711 (Online)
Condensed Matter and Interphases
Kondensirovannye Sredy i Mezhfaznye Granitsy
https://journals.vsu.ru/kcmf/

Original articles

Research article
https://doi.org/10.17308/kcmf.2025.27/12491

A universal algorithm for the calculation of vapor-liquid equilibrium diagrams in quasi-simple multicomponent systems

N. A. Charykov[1,2,3], A. V. Rumyantsev[1], V. A. Keskinov[2]✉, K. N. Semenov[1,4,5], V. P. German[1], N. A. Kulenova[2], M. V. Charykova[4], M. V. Keskinova[1], M. Yu. Arshinov[1]

*[1]St. Petersburg State Institute of Technology,
26 Moskovsky pr., Saint Petersburg 190013, Russian Federation*

*[2]D. Serikbayev East Kazakhstan Technical University, Center of Excellence "VERITAS",
69. A. K. Protosanova ul., Ust-Kamenogorsk 070004, Republic of Kazakhstan*

*[3]St. Petersburg Electrotechnical University "LETI",
5 Professora Popova ul., Saint Petersburg 197022, Russian Federation*

*[4]St. Petersburg State University,
7/9 Universitetskaya Embankment, Saint Petersburg 199034, Russian Federation*

*[5]Pavlov First Saint Petersburg State Medical University,
6 - 8 L'va Tolstogo st., Saint Petersburg 197022, Russian Federation*

Abstract

The purpose of the study was to consider isothermal vapor-liquid diagrams of quasi-simple systems and to develop a universal algorithm for the calculation of isothermal vapor-liquid diagrams of these systems independent of the type of valence of the electrolyte, the number of components in the system, and the types of solid solutions. The suggested analogues of the three Gibbs–Konovalov and Gibbs–Roozeboom laws are true when moving along the univariant equilibrium lines on the solubility diagrams of systems with a random number of components.

The study did not involve any experiments. The suggested algorithm was applied for the description of solubility (solid-liquid) diagrams and vapor-liquid equilibrium diagrams of three- and four-component systems with one, two, or three volatile components. In all the cases, the results of thermodynamic first-principles calculations agreed well with the experimental data presented in the literature.

Both the experimental data presented in the literature and the results of the thermodynamic first-principles calculation performed by the authors are also in good agreement with the suggested analogues of the Gibbs–Konovalov and Gibbs–Roozeboom laws.

Keywords: Zdanovskii's rule, Quasi-simple systems, Vapor-liquid equilibrium diagrams, Partial molar Gibbs energy, Analogues, Gibbs–Konovalov's laws, Gibbs–Roozeboom rules

Funding: The study was supported by the Russian Science Foundation, project No. 23-23-00064 (https://rscf.ru/project/23-23-00064).

For citation: Charykov N. A., Rumyantsev A. V., Keskinov V. A., Semenov K. N., German V. P., Kulenova N. A., Charykova M. V., Keskinova M. V., Arshinov M. Yu. A universal algorithm for the calculation of vapor-liquid equilibrium diagrams in quasi-simple multicomponent systems. *Condensed Matter and Interphases.* 2025;27(1): 67–85. https://doi.org/10.17308/kcmf.2025.27/12491

✉ Viktor A. Keskinov, e-mail: keskinov@mail.ru

© Charykov N. A., Rumyantsev A. V., Keskinov V. A., Semenov K. N., German V. P., Kulenova N. A., Charykova M. V., Keskinova M. V., Arshinov M. Yu., 2025

The content is available under Creative Commons Attribution 4.0 License.

Для цитирования: Чарыков Н. А., Румянцев А. В., Кескинов В. А., Семенов К. Н., Герман В. П., Куленова Н. А., Чарыкова М. В., Кескинова М. В., Аршинов М. Ю. Универсальный алгоритм расчета фазовых равновесий жидкость – пар в квазипростых многокомпонентных системах. *Конденсированные среды и межфазные границы*. 2025;27(1): 67–85. https://doi.org/10.17308/kcmf.2025.27/12491

1. Introduction

1.1. Main thermodynamic properties of quasi-simple systems

We shall start by introducing the main definitions. Water-salt systems with three or more components (or, in the general case, solvent-solute systems) comply with the so-called Zdanovskii's rule, if isoactivates of the solvent (hereinafter, water – *W*) are line segments (n = 3), plane sections (n = 4), or hyperplane sections ($n \geqslant 5$) [1–6]. Section 1.1 of the article is largely based on the terms used in [6]. The article considers isothermal–isobaric conditions (T, P = const). Water isoactivates (a_w = const) are isopotentials (μ_w = const; μ_w is the chemical potential), isobars of partial pressures of water (P_w = const), and isotherm-isobars of a two-phase vapor-liquid equilibrium (l–*v*) in the region of homogeneous liquid solutions at the same time [1-6]. The equation of the isoactive line divided into segments for a ternary system complying to Zdanovskii's rule is mathematically expressed by the following relation [1, 3, 4, 6]:

$$m_1 / m_1^0 + m_2 / m_2^0 = 1, \quad (1)$$

where: m_i и m_i^0 is the molality of the i-th component of a ternary and a binary system with the same value of μ_W, respectively. When dealing with a random n-component system, the equation of the isoactive hyperplane is presented as follows:

$$\sum_{i=1, i\neq W}^{n-1} m_i / m_i^0 = 1\,; \tag{2}$$

or:

$$\sum_{i=1, i\neq W}^{n-1} Y_i = 1; \;\; Y_i = m_i / m_i^0\,. \tag{3}$$

It is important that the isopotentials of other (i.e. salt) components are not line segments or hyperplane sections. In particular, they are crystallization curves of these anhydrous components on the solubility diagrams of ternary systems and cannot be linear by nature.

Hereinafter, in order to avoid ambiguity, we will refer to systems as being **quasi-simple** if the **isoactivates** of at least one component are **linear**. In this case, the properties of systems with three or more components are determined by the properties of their binary subsystems. This is accounted for by the Gibbs-Duhem equation and the conditions of cross product derivation for the liquid phase under isothermal–isobaric conditions [4, 7-9]:

$$SdT - VdP + \sum_{i=1}^{n} n_i d\mu_i = 0 \tag{4}$$

or when $T, P = const$:

$$\sum_{i=1}^{n} n_i d\mu_i = 0\,, \tag{5}$$

$$\frac{\partial^2 G}{\partial n_i \partial n_j} = \frac{\partial^2 G}{\partial n_j \partial n_i} \tag{6}$$

or when $T, P = const$:

$$\partial\mu_i / \partial n_j = \partial\mu_j / \partial n_i\,. \quad (7)$$

Thus, in particular, excess thermodynamic functions of multi-component liquid phases (activity of the components – a_i, activity coefficients – γ_i, water osmotic coefficients – ϕ), as well as equilibrium diagrams (*l*–*v*) and (*s*–*l*) of multi-component systems should be calculated based on the data regarding the thermodynamic functions of their binary subsystems. The main question can be formulated as follows: "Which unique properties of thermodynamic potentials of a phase of variable composition, i.e. a liquid (in our case, they are the Gibbs energy – G or partial potentials – Korzhinsky's potentials [4, 10] – $G^{[W]}$), make a system quasi-simple?". This question can be answered by determining the type of functional dependence of excess thermodynamic functions on the composition of multi-component systems.

Let's briefly review the main points presented in [6]. Let's consider an n-component system: 1–2–3... n–1–W (W is a solvent (water), components 1, 2, 3... n-1 are dissolved electrolytes (salts)) with T, P = const. Let's introduce the partial Gibbs energy [4, 10–12]:

$$G^{[W]} = G - n_W\mu_W = \sum_{i=1, i\neq W}^{n-1} n_i\mu_i, \tag{8}$$

where $G^{[W]}$ is the partial Gibbs energy, μ_i is the chemical potential of the *i*-th solute; μ_w is the chemical potential of water. $G^{[W]}$ is characteristic for the set of variables (T, P, n_i ($i \leqslant n-1$), μ_W). Let's now consider the quasi-average partial molar Gibbs energy calculated for 1 mole of solutes – $G^{(W)}$:

$$G^{(W)} = \sum_{i=1, i\neq W}^{n-1} Z_i\mu_i, \tag{9}$$

where: Z_i is the mole fraction of the *i*-th solute in the concentration space without solvents:

$$Z_j = \frac{n_j}{\sum_{i=1, i\neq W}^{n-1} n_i}; \quad \sum_{i=1, i\neq W}^{n-1} Z_i = 1 \ . \tag{10}$$

When T, P = const, $G^{(W)}$ is characteristic for the set of variables ($Z_1, Z_2, \ldots, Z_{n-2}$, μ_W).

Let's introduce the function $\Delta G_{mix}^{(W)}$, which reflects changes in the average partial molar Gibbs energy when mixing ($n-1$) binary solutions ($i-W$), each of which contains Z_i moles of the *i*-th component [6]. Let all the mixed binary solutions have the same chemical potential of the solvent (i.e. are isopiestic), $\mu_W^{(1-W)} = \mu_W^{(2-W)} = \ldots = \mu_W^{(n-1-W)} = const$. Let's assume that after mixing, the chemical potential of the solvent in the resulting multi-component system remains the same, $\mu_W^{(mult)} = const$ i.e. the system complies with Zdanovskii's rule. Then function $\Delta G_{mix}^{(W)}$ no longer depends on μ_w but rather on the variables of the composition – Z_i: $\Delta G_{mix}^{(W)}(Z_1, Z_2 \ldots Z_{n-2})$ [6]. Obviously, in the general case:

$$\frac{\Delta G_{mix}^{(W)}}{RT} = \sum_{i=1}^{n-1} Z_i\left(\ln a_i^{(mult)} - \ln a_i^0\right), \tag{11}$$

where: $a_i^{(mult)}$ is the activity of the *i*-th solute after mixing; a_i^0 is the activity of the *i*-th solute in the binary system ($i-W$) with the same value of μ_w before mixing [6].

Let's assume that **in quasi-simple systems, the function $\Delta G_{mix}^{(W)}$, corresponding to the mixing of binary solutions (*i*-*W*) with the same μ_W, provided that μ_W remains unchanged after mixing, is only determined by the entropy of ideal mixing of binary solutions** or [6]:

$$\frac{\Delta G_{mix}^{(W)}}{RT} = \sum_{i=1}^{n-1} Z_i \ln Z_i. \tag{12.1}$$

In other words, the excess partial Gibbs free energy of the mixed isopiestic binary solutions ($\Delta G_{mix}^{(W)-ex}$) should be zero:

$$\frac{\Delta G_{mix}^{(W)-ex}}{RT} = 0. \tag{12.2}$$

By comparing equations (11) and (12.1) we obtain:

$$\ln a_i^0 + \ln Z_i = \ln a_i^{(mult)} \ (\text{при } \mu_W = const), \tag{12.3}$$

$$\ln m_i = \ln Z_i + \ln m_i^0, \tag{13}$$

where: m_i^0 is the molality of the *i*-th component in the binary solution (before mixing) with constant μ_w; m_i is the molality of the *i*-th component in the multi-component solution (after mixing) with the same value of μ_w.

In [6], the main equations (12.1) – (12.3) are substantiated in a different way. Let's accept the classical definition of the number of components in a system (n) as a number of ion and molecular forms in the system, whose masses can change independently [4, 6, 9]. Let's assume that the studied system is quasi-simple. Let the chemical potential of the solvent be $\mu_w = const$. Then binary solutions ($i-W$) with identical μ_w can be considered to be **new individual components.** If, with the same μ_w, these components are mixed as components of an ideal solution, then equations (12.1)–(12.3) are true.

[6] presents the results of the first-principles calculation of equations (12, 13) based on the data regarding the corresponding binary subsystems of the solubility diagrams of three- and four-component systems with crystallization of anhydrous salt components, their crystalline hydrates, ternary compounds of constant compositions, and solid solutions with isovalent substitutions. In all the cases, the calculations agreed well with the experimental data presented in the literature.

1.2. Calculation of vapor-liquid equilibria of quasi-simple systems

The article focuses on first-principles calculation of vapor-liquid equilibrium diagrams of three- and more component systems with volatile components based on equations (12, 13) and the data regarding their binary subsystems.

Let the chemical potential or activity of water be constant ($\mu_w = const$; $\ln a_w = const$).

According to Henry's law, for the partial vapor pressure of a volatile component of a multi-component system (hereinafter, assuming that the vapor phase is ideal) the following is true [7, 9, 13]:

$$\ln P_i = \ln a_i^{(mult)} + \ln K_{H,i}^m, \quad (14.1)$$

where: P_i is the partial pressure of the *i*-th volatile component (mm Hg), $a_i^{(mult)}$ is the activity of the *i*-th component on the molality scale, and $K_{H,i}^m$ is the Henry's law constant of the *i*-th component on the molality scale. Or, taking into account (12.3):

$$\ln P_i = \ln a_i^0 + \ln Z_i + \ln K_{H,i}^m \ (\text{при } \mu_W = const), \quad (14.2)$$

where: a_i^0 is the activity of the *i*-th solute in the binary system (*i*–*W*) with the same μ_w before mixing [6].

The partial pressure of the solvent P_w is determined according to Raoult's law [7, 9, 13]:

$$\ln P_W = \ln a_W + \ln P_W^{(0)}, \quad (14.3)$$

where $P_W^{(0)}$ is the vapor pressure above the pure solvent under specific conditions (mm Hg). For instance, with water being the solvent, at 25 °C $P_W^{(0)} = = 23.76$ mm Hg.

Thus, according to Dalton's law, the total vapor pressure above the solution is P_{sum}, [7, 9, 13]:

$$P_{sum} = \sum_{i=vc} a_i^0 Z_i K_{H,i}^m + a_W P_W^{(0)}, \quad (14.4)$$

where all the volatile components except for the solvent are summarized. The composition of the solution (m_i) is set by equation (13), based on the data regarding binary isopiestic concentrations (m_i).

2. Binary systems HCl – H_2O and HBr – H_2O at 25 °C

This section, though not entirely within the scope of the study, is still important, because it demonstrates the accuracy of the calculation of partial pressures of the components performed by means of a classical model of electrolyte solutions used to describe binary systems, namely the Pitzer model [14, 15] with three and four parameters. As a result, we selected two binary systems with two volatile components: a solvent ($W = H_2O$) and a volatile acid, HCl – H_2O, HBr – H_2O at 25 °C. The data regarding the binary Pitzer parameters is presented in Table 1. We should note that the said parameters quite accurately describe the concentration dependence of the water osmotic coefficients on the molality of the binary solutions φ(*m*) almost over the whole concentration range m = 0÷16 mol/kg H_2O, including the region of azeotropes (*Az*), where the vapor pressure is low ($P_T^{Az} = \min$). The corresponding Henry constants ($K_{\text{H,HCl}}^m; K_{\text{H,HBr}}^m$) are given in Table 2. Fig. 1 and 2 present the results of calculations and the experimental data regarding the partial pressures of halogen hydracids and water and the total vapor pressure above the solutions studied in [16, 17]. The figures show that the experimental and calculated data are in good agreement, including in the region of binary azeotropes – Az_i.

Table 1. Binary Pitzer parameters at 25 °C

System	Binary parameters (r.u.)					
	$\beta^{(0)}$	$\beta^{(1)}$	$\beta^{(2)}$	C^{φ}	α_1	α_2
NaCl–H_2O	0.0765	0.2664	0	0.00124	2.0	–
KCl–H_2O	0.0484	0.2122	0	-0.00084	2.0	–
LiCl–H_2O	0.27909	1.5093	−0.78110	-0.00765	2.0	1.0
$LiNO_3$–H_2O	0.09642	0.03872	0.02704	-0.01010	2.0	−0.4
HCl–H_2O	0.1769	0.2972	0	0.00072	2.0	–
HBr–H_2O	0.2259	0.1372	0.0289	-0.00167	2.0	1.0

Table 2. Henry constants (on molality scale) for systems HCl – H_2O, HBr – H_2O at 25 °C

System	HCl–H_2O	HBr–H_2O
K_H^m (mm Hg)	$1.99{\cdot}10^{-4}$	$4.04{\cdot}10^{-6}$

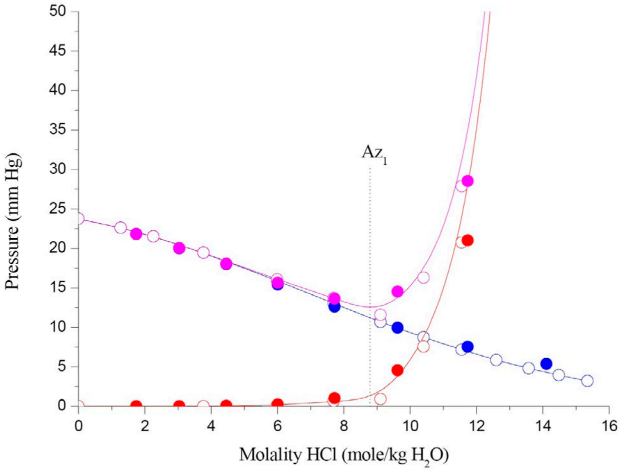

Fig. 1. The data calculated based on the Pitzer equations (lines and open circles) and the experimental data [16] (solid circles) regarding the concentration dependence of the pressures: H_2O (blue), HCl (red), and total (violet). Az$_1$ – azeotrope

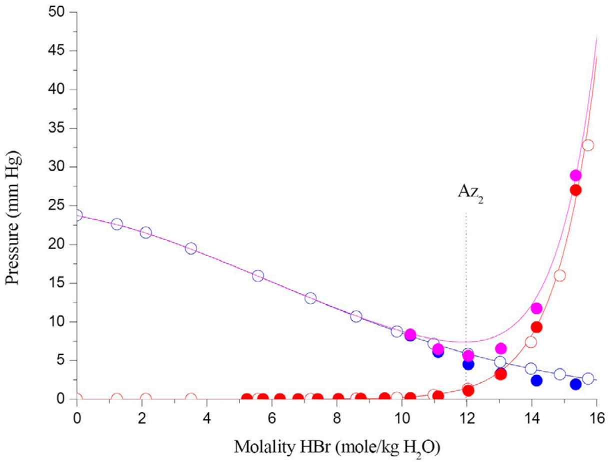

Fig. 2. The data calculated based on the Pitzer equations (lines and open circles) and the experimental data [17] (solid circles) regarding the concentration dependence of the pressures: H_2O (blue), HBr (red), and total (violet). Az$_2$ – azeotrope

3. Ternary systems with one volatile component – the solvent (for instance, the LiCl – $LiNO_3$ system) at 25 °C

This section considers a system with one volatile component, namely the LiCl – $LiNO_3$ system at 25 °C. The system is quite trivial. Its equilibrium diagram is represented by a set of linear isoactivates of water. Therefore, we assume that the system complies with Zdanovskii's rule over the whole concentration range. The calculated and experimental isoactivates of water in the studied system are presented in Table 3 and Fig. 3. The experimental data regarding the water activity was obtained by means of the isopiestic method using a variation of Resnik's measurement unit [18]. Binary solutions of the LiCl – H_2O system were used as reference solutions. The solubility was calculated based on the data regarding the binary subsystems using an algorithm of calculation of solubility diagrams suggested in [6]. Fig. 3 shows that the calculated data on the isoactivates of water agrees well with the experimental data. In order to determine the degree of compliance of the LiCl – $LiNO_3$ – H_2O system at 25 °C with Zdanovskii's rule, we

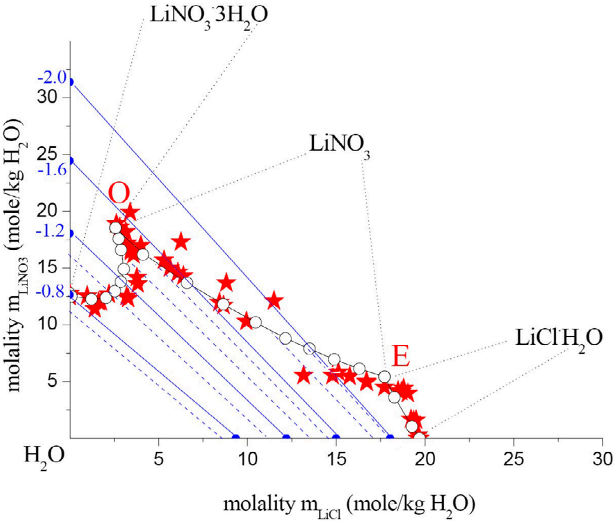

Fig. 3. Solubility diagram of the LiCl – $LiNO_3$ – H_2O system at 25 °C (open circles and lines – calculation results, red stars – experimental data [19], blue solid lines – calculated water isoactivates, lna_W values are shown in blue, blue dotted lines – experimental data obtained by the authors). According to the general classification of invariant points [20, 21], point O is a so–called through point, corresponding to the saturation with two different crystalline hydrates of one salt component, and point E is eutonic

Table 3. Dependence of osmotic coefficients on the solution composition in the LiCl – $LiNO_3$ – H_2O system at 25 °C

m_{LiNO_3} (mol/kg H_2O)	m_{LiCl} (mol/kg H_2O)	φ_{H_2O}	m_{LiNO_3} (mol/kg H_2O)	m_{LiCl} (mol/kg H_2O)	φ_{H_2O}
$\ln a_W = -0.6999$			$\ln a_W = -1.0674$		
11.36	0.00	1.71	16.55	0.00	1.79
9.50	1.39	1.78	13.62	1.99	1.90
8.02	2.51	1.84	11.34	3.56	1.99
6.65	3.55	1.90	9.28	4.95	2.08
5.34	4.54	1.96	7.37	6.27	2.17
4.30	5.33	2.01	5.89	7.36	2.14
3.26	6.13	2.06	4.43	8.31	2.33
2.39	6.78	2.11	3.21	9.11	2.41
1.48	7.47	2.17	1.98	9.95	2.49
0.65	8.10	2.22	1.71	10.11	2.56
0.00	8.59	2.26	0.00	11.29	2.60
$\ln a_W = -1.3490$			$\ln a_W = -1.5055$		
16.88	2.47	1.93	18.75	2.74	1.94
13.90	4.36	2.05	15.39	4.83	2.06
11.28	6.03	2.16	12.42	6.64	2.19
8.88	7.57	2.28	9.76	8.31	2.31
7.05	8.73	2.37	7.71	9.59	2.41
5.26	9.87	2.47	4.14	11.75	2.63
3.81	10.80	2.56	2.53	12.76	2.73
2.33	11.73	2.66	0.00	14.31	2.92
0.00	13.23	2.83	$\ln a_W = -1.8461$		
$\ln a_W = -1.6741$			7.18	12.45	2.61
8.64	10.14	2.47	4.84	13.84	2.68
6.59	11.43	2.58	4.29	14.18	2.77
5.37	12.18	2.65	2.93	15.05	2.85
3.95	13.06	2.73	1.45	15.91	2.95
2.70	13.84	2.81	0.00	16.80	3.05
1.34	14.70	2.90			
0.00	15.54	2.99			
$\ln a_W = -1.9976$					
4.63	15.31	2.78			
3.16	16.18	2.87			
1.56	17.13	2.97			
0.00	18.06	3.07			

presented the deviations of the water isoactivates from linearity $\Delta_{Zd} = 1 - m_{LiNO_3} / m^0_{LiNO_3} - m_{LiCl} / m^0_{LiCl}$ as a function of the Janecke index of $LiNO_3$ – $Y_{LiNO_3} = m_{LiNO_3} / (m_{LiNO_3} + m_{LiCl})$ over the whole array of experimental data (Fig. 4). Fig. 4 shows that for all the 55 experimental points, except for one, deviations from Zdanovskii's rule are very insignificant ($\leqslant 0.002$), which demonstrates the accuracy of the isopiestic experiment. The thermodynamic potentials of the solid phases required for the calculation of the solubility diagrams of the LiCl – $LiNO_3$ – H_2O system at 25 °C are presented in Table 4. The table also demonstrates the thermodynamic potentials – $\ln SP$ (*SP* – solubility product of the solid phase) of all the other solid phases in the subsequent

Table 4. Thermodynamic potentials of solid phases (ln *SP*) at 25 °C

Solid phase	ln *SP*	Solid phase	ln *SP*	Solid phase	ln *SP*
NaCl	3.65	$LiCl \cdot H_2O$	12.13	KCl	2.09
$LiNO_3$	9.08	$LiNO_3 \cdot 3H_2O$	4.73		

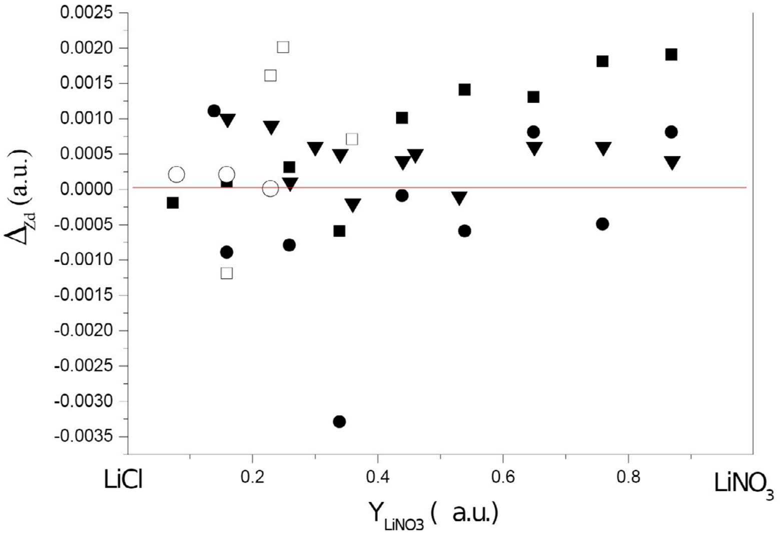

Fig. 4. Deviations from Zdanovskii's rule in the LiCl – $LiNO_3$ – H_2O system at 25 °C: $Y_{LiNO_3} = m_{LiNO_3} / (m_{LiNO_3} + m_{LiCl})$; $\Delta_{Zd} = 1 - m_{LiNO_3} / m^0_{LiNO_3} - m_{LiCl} / m^0_{LiCl}$. Designations: solid squares – ln a_W = –0.6999; solid circles – ln a_W = –1.0674; up triangles – ln a_W = –1.3490; down triangles – ln a_W = –1.5055; rhombi – ln a_W = –1.6741; open squares – ln a_W = –1.8461; open circles – ln a_W = –1.9976

systems. The values of ln *SP* are calculated based on the solubility in the binary systems.

4. Ternary systems with two volatile components (HCl – KCl – H_2O, HCl – NaCl – H_2O) at 25 °C

The ternary systems with two volatile components considered in our study were HCl – KCl – H_2O and HCl – NaCl – H_2O at 25 °C. The existing literature presents a lot of experimental data regarding these systems [19–23]. The process of plotting of solubility diagrams (in our case, univariant crystallization curves of NaCl and KCl) is quite clear.

4.1. An algorithm for the calculation of solubility diagrams

A1) Define a_W.

A2) Find m_1^0, m_2^0 in the binary subsystems corresponding to a_W. This can be done based on the experimental data or an accurate thermodynamic model, for instance the Pitzer model. Values m_1^0, m_2^0 can correspond to both stable homogeneous solutions and supersaturated solutions. In the latter case, it is necessary to extrapolate the model for supersaturated solutions.

A3) Determine the activity of salt components in binary solutions – a_1^0, a_2^0 based on the experimental data or a thermodynamic model.

A4) Determine the thermodynamic potential of the solid phase $M_{\nu_{M1}}X_{\nu_X}$ based on the solubility of the salt – m_1^s:

$$\ln SP\left(M_{\nu_{M1}}X_{\nu_X}\right) = \ln a_1^s = \nu_{M1}\ln\left(\nu_{M1}m_1^s\right) + \\ +\nu_X\ln\left(\nu_X m_1^s\right) + \left(\nu_{M1}+\nu_X\right)\ln\gamma_1^s, \quad (15.1)$$

where a_1^s and γ_1^s are the activity and activity coefficient of $M_{\nu_{M1}}X_{\nu_X}$ in the saturated solution.

A5) Use equation (12.3), taking into account that $a_i^{(mult)} \equiv a_i^s$:

$$\ln Z_1 = \ln SP\left(M_{\nu_{M1}}X_{\nu_X}\right) - \ln a_1^0 \quad (15.2)$$

and find Z_1 and $Z_2 = 1 - Z_1$.

A6) Find a point on the crystallization curve $M_{\nu_{M1}}X_{\nu_X}$:

$$\ln m_i = \ln Z_i + \ln m_i^0 \quad (i = 1, 2). \quad (15.3)$$

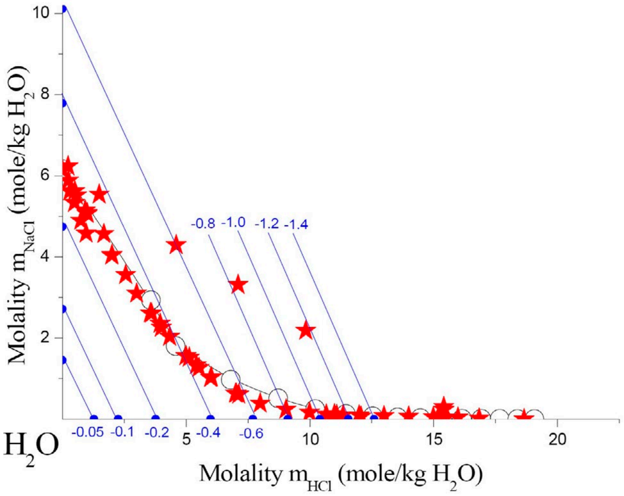

Fig. 5.1. Solubility diagram of the NaCl – HCl – H_2O system at 25 °C (open circles and lines – calculation results, red stars – experimental data [19, 20], blue lines – calculated water isoactivates, $\ln a_W$ values are shown in blue

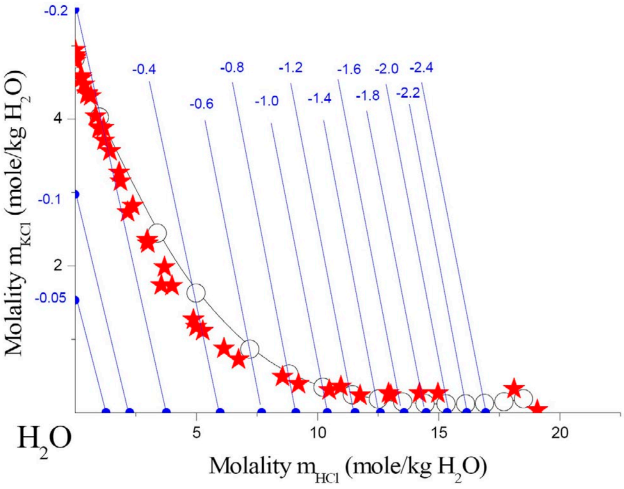

Fig. 5.2. Solubility diagram of the KCl – HCl – H_2O system at 25 °C (open circles and lines – calculation results, red stars – experimental data [19, 23, 24], blue lines – calculated water isoactivates, $\ln a_W$ values are shown in blue

The results of the calculation are presented in Fig. 5.1 and 5.2. The figures also demonstrate the isoactivates of water calculated based on Zdanovskii's rule and extrapolated to the region of metastable supersaturated solutions. Fig. 5 demonstrates that the experimental data is in good agreement with the results of the calculation based on the binary subsystems.

4.2. An algorithm for the calculation of solid-vapor-liquid equilibrium diagrams

Let's calculate the partial pressures of volatile components, i.e. the solvent (*W*) and HCl, above saturated solutions in both systems using the following algorithm.

B1) Define a_W and calculate $\ln P_W = \ln a_W + \ln P_W^{(0)}$.

B2) Calculate $\ln a^0_{\text{HCl}}$, Z_{HCl} (see algorithm 4.1) and $P_{\text{HCl}} = a^0_{\text{HCl}} Z_{\text{HCl}} K^m_{\text{H,HCl}}$.

B3) Calculate the total pressure of volatile components in the system: $P_{sum} = P_W + P_{\text{HCl}}$.

B4) The composition of the solution is still described by the equation (15.3):

$$\ln m_{\text{HCl}} = \ln Z_{\text{HCl}} + \ln m^0_{\text{HCl}};$$
$$\ln m_{\text{NaCl}} = \ln Z_{\text{NaCl}} + \ln m^0_{\text{NaCl}}. \tag{16}$$

The calculated pressures above saturated solutions in both systems are given in Fig. 6.1, 6.2 and Tables 5.1, 5.2. The figures demonstrate that in both systems a pseudo-azeotrope negative with regard to P_T is implemented with a minimum total pressure – P_{Azi}. The calculation based on the binary subsystems of the ternary HCl – KCl – H_2O system at 25 °C are in good agreement with the only experimental data that we managed to find [24].

4.3. An algorithm for the calculation of vapor-liquid equilibrium diagrams in unsaturated solutions

C1) Obtain linear water isoactivates with $P_W = const$, using trivial methods (see Fig. 5.1, 5.2), including in the metastable region of supersaturated solutions.

C2) Curvilinear isoactivates or isobars of partial pressures $P_{\text{HCl}} = const$ are obtained by solving equations of the following type: $a^0_{\text{HCl}} Z_{\text{HCl}} K^m_{\text{H,HCl}} = const$ with various a_W, finding Z_{HCl} and the corresponding compositions of solutions (m_{HCl}, m_{KCl}), followed by combining the solutions to the equations in a continuous smooth curve.

C3) The curvilinear isobars of the total pressures of volatile components $P_{sum} = const$ are also obtained by solving equations of type $a^0_{\text{HCl}} Z_{\text{HCl}} K^m_{\text{H,HCl}} + P_W = const$ with various a_W and finding the corresponding Z_{HCl} and the corresponding compositions of solutions (m_{HCl}, m_{KCl}), followed by combining the solutions to the equations in a continuous smooth curve. The latter curves, i.e. isobars of the total pressure in both ternary systems, are given in Fig 7.1 and 7.2. In both figures, some of the vapor-liquid

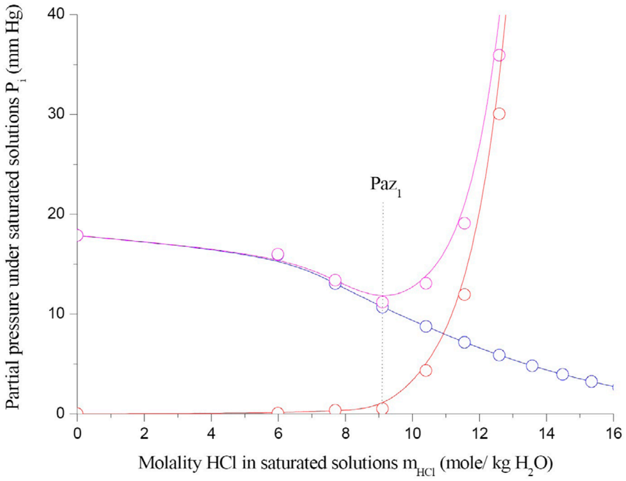

Fig. 6.1. Dependence of partial pressures P_{H_2O} (blue lines and circles), P_{HCl} (red lines and circles), and the total pressure P_{sum} (violet lines and circles) in the NaCl – HCl – H_2O system at 25 °C – calculation based on binary subsystems

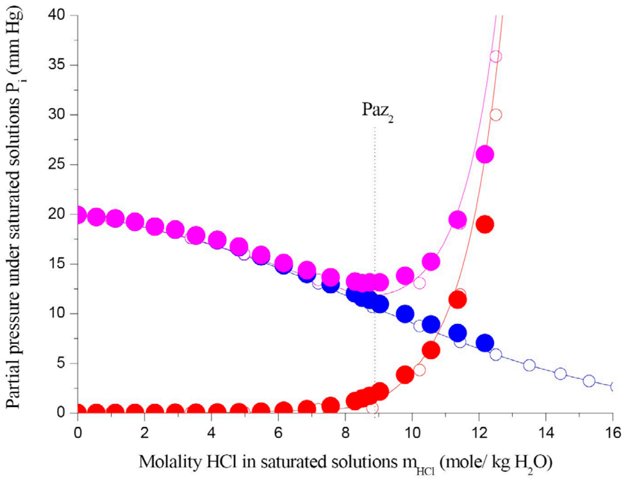

Fig. 6.2. Dependence of partial pressures P_{H_2O} (blue lines and circles), P_{HCl} (red lines and circles), and the total pressure P_{sum} (violet lines and circles) in the KCl – HCl – H_2O system at 25 °C – calculation based on binary subsystems, solid circles – experimental data [24]

Table 5.1 Solubility, partial, and total pressures in saturated solutions in the HCl – NaCl – H_2O system at 25 °C

$\ln a_W$ r.u.	m^0_{HCl}	m^0_{NaCl}	$\ln a^0_{HCl}$	$\ln a^0_{NaCl}$	Z_{NaCl}	Z_{HCl}	m_{NaCl}	m_{HCl}
	mol/kg H_2O		r.u.		r.u.		mol/kg H_2O	
0.00	0.00	0.00	–	3.65	1.00	0.00	6.16	0.00
–0.05	1.28	1.45	0.19	–0.10	–	–	–	–
–0.1	2.26	2.71	1.78	1.27	–	–	–	–
–0.2	3.77	4.74	3.64	2.78	–	–	–	–
–0.4	5.99	7.78	5.93	4.56	0.4025	0.597	3.131	3.57
−0.6	7.70	10.11	7.55	5.80	0.1164	0.883	1.177	6.80
−0.8	9.11	12.05	7.87	6.81	0.0424	0.957	0.511	8.72
−1.0	10.41	13.74	10.00	7.67	0.0179	0.982	0.246	10.22
−1.2	11.56	15.24	11.01	8.43	0.0084	0.991	0.127	11.46
−1.4	12.60	16.50	11.93	9.13	0.0041	0.995	0.068	12.54
−1.6	13.58	17.85	12.78	9.78	0.0022	0.997	0.038	13.55
−1.8	14.49	19,01	13.57	10,38	0.0012	0.998	0.022	14.47
−2.0	15.35	20,09	14.32	10,95	$6.75 \cdot 10^{-4}$	0.999	0.013	15.33
−2.2	16.16	21,11	15.02	11,48	$3.97 \cdot 10^{-4}$	0.9996	0.0083	16.15

$\ln a_W$ r.u.	P_W	P_{HCl}	P_{sum}
	mm Hg		
−0.2850	17.86	0.000	17.86
−0.4	15.92	0.044	15.97
.6	13.03	0.333	13.37
−0.8	10.67	0.498	11.17
−1.0	8.74	4.30	13.04
−1.2	7.15	11.92	19.08
−1.4	5.85	30.04	35.90
−1.6	4.79	70.44	75.23
−1.8	3.92	155.3	159.2
−2.0	3.21	329.2	332.4
−2.2	2.63	663.4	666.0

Table 5.2. Solubility, partial, and total pressures in saturated solutions in the HCl – KCl – H_2O system at 25 °C

ln a_W r.u.	m^0_{HCl}	m^0_{KCl}	$\ln a^0_{\text{HCl}}$	$\ln a^0_{\text{KCl}}$	Z_{KCl}	Z_{HCl}	m_{KCl}	n_{HCl}
	mol/kg H_2O		r.u.		r.u.		mol/kg H_2O	
0.00	0.00	0.00	0.00	2.08	1.000	0.000	4.82	0.00
−0.05	1.28	1.53	0.19	−0.23	–	–	–	–
−0.1	2.26	2.97	1.78	1.04	–	–	–	–
−0.2	3.77	5.49	3.64	2.39	0.733	0.266	4,02	1.00
−0.3	4.97	7.72	4.91	3.23	0.316	0.683	2,44	3.39
−0.4	5.99	9.75	5.93	3.87	0.166	0.833	1.62	4.98
−0.6	7.70	13.49	7.55	4.83	0.063	0.936	0.86	7.20
−0.8	9.11	16.97	7.87	5.56	0.030	0.969	0.52	8.82
−1.0	10.41	20.38	10.00	6.16	0.016	0.983	0.34	10.23
−1.2	11.56	23.83	11.01	6.67	0.010	0.989	0.24	11.44
−1.4	12.60	27.48	11.93	7.10	0.0066	0.993	0.18	12.51
−1.6	13.58	31.57	12.78	7.47	0.0045	0.995	0.14	13.51
−1.8	14.49	36.85	13.57	7.80	0.0032	0.996	0.12	14.44
−2.0	15.35	41.83	14.31	7.96	0.0027	0.997	0.12	15.30
−2.2	16.16	47.43	15.02	8.09	0.0024	0.997	0.12	16.12

ln a_W r.u.	P_W	P_{HCl}	P_{sum}
	mm Hg		
−0.1720	19.90	0.00000	19.90
−0.2	19.45	0.00202	19.45
−0.3	17.60	0.0184	17.62
−0.4	15.92	0.0625	15.98
−0.6	13.03	0.354	13.39
−0.8	10.67	0.504	11.18
−1.0	8.74	4.308	13.04
−1.2	7.15	11.90	19.05
−1.4	5.85	29.98	35.84
−1.6	4.79	70.30	75.09
−1.8	3.92	155.0	158.9
−2.0	3.21	325.3	328.5
−2.2	2.63	661.6	664.3

diagrams correspond to stable solutions, and some (with high salt concentrations) correspond to metastable solutions supersaturated with respect to salts. Both figures demonstrate a univariant line of local extrema of function P_{sum} (in our case, local minimums), i.e. a negative fold on the surface of $P_{sum}(m_{\text{HCl}}, m_{salt})$ [7, 25, 26]. This fold lies between the binary azeotrope – Az_1 and the salt-water binary subsystem, where it degrades, because in binary systems dependence $P_{sum}(m_{salt})$ is strictly monotonous $\frac{dP_{sum}}{dm_{salt}} < 0$ and cannot have extrema, according to the criteria of diffusion resistance: [7–9].

5. Quaternary systems with two volatile components (HCl – NaCl – KCl – H_2O) at 25 °C

The calculation of phase equilibria in quaternary systems with two volatile components was performed using the HCl(1) – NaCl(2) – KCl(3) – H_2O) system at 25 °C.

5.1. An algorithm for the calculation of solubility diagrams

D1) Define value a_W.

D2) Find m_1^0, m_2^0, m_3^0 in the binary subsystems corresponding to a_W. This can be done based on the experimental data or an accurate thermodynamic

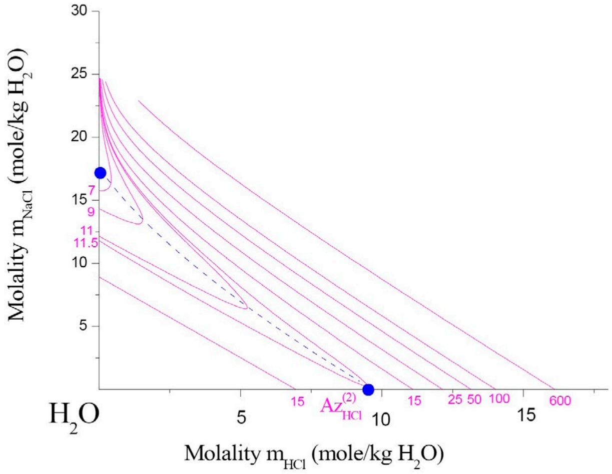

Fig. 7.1. Dependence of the total pressure of volatile components in the NaCl – HCl – H_2O system at 25 °C: solid violet lines – calculation based on binary subsystems; P_{sum} values are represented by digits of the same color. The dotted blue line is the line of local extrema of the P_{sum} function (in our case, local minima), i.e. a negative fold on the surface of $P_{\text{sum}}(m_{\text{HCl}}, m_{\text{NaCl}})$ [7, 8]. The blue dots of the binary azeotrope in the HCl – H_2O subsystem are below and the point of degeneration of the fold is on the left

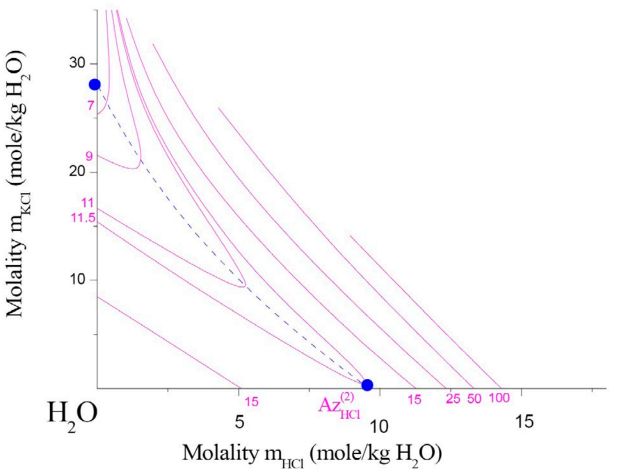

Fig. 7.2. Dependence of the total pressure of volatile components in the KCl – HCl – H_2O system at 25 °C: solid violet lines – calculation based on binary subsystems; P_{sum} values are represented by digits of the same color. The dotted blue line is the line of local extrema of the P_{sum} function (in our case, local minima), i.e. a negative fold on the surface of P_{sum} $(m_{\text{HCl}}, m_{\text{KCl}})$ [7, 8]. The blue dots of the binary azeotrope in the HCl – H_2O subsystem are below and the point of degeneration of the fold is on the left

model for instance the Pitzer model. Values m_1^0, m_2^0, m_3^0 can correspond to both stable homogeneous solutions and supersaturated solutions. In the latter case, it is necessary to extrapolate the model for supersaturated solutions.

D3) Determine the activity of salt components in binary solutions – a_1^0, a_2^0, a_3^0 based on the experimental data or a thermodynamic model.

D4) Determine the thermodynamic potentials of two solid phases $i = 2, 3$ (NaCl, KCl) crystallized on a single crystallization curve on the solubility diagram of the quaternary system based on the solubility of the salts – $m_i^s : \ln SP_i$.

D5) Use equation (12.3), taking into account that $a_i^{(mult)} \equiv a_i^s$:

$$\ln Z_i = \ln SP_i - \ln a_i^0 \tag{17.1}$$

and find Z_i (i = 2, 3) and $Z_1 = 1 - Z_2 - Z_3$.

D6) Find a point on the univariant crystallization curve of phases 2 and 3:

$$\ln m_i = \ln Z_i + \ln m_i^0 \quad (i = 1,\ 2,\ 3). \tag{17.2}$$

The results of the calculation of the solubility diagram of the quaternary system are given in Fig. 8.1 and Table 6. The results are presented in comparison with the experimental data provided in [24], which are in good agreement.

5.2. An algorithm for the calculation of solid$_1$-solid$_2$-liquid-vapor equilibrium diagrams

Let's calculate the partial pressures of volatile components, i.e. the solvent (*W*) and HCl, above saturated solutions in the HCl – NaCl – KCl – H_2O system at 25 °C. The following algorithm can be used.

E1) Define a_W and calculate $\ln P_W = \ln a_W + \ln P_W^{(0)}$.

E2) Calculate $\ln a^0_{\text{HCl}}$, Z_{HCl} (see algorithm 5.1) and $P_{\text{HCl}} = a^0_{\text{HCl}} Z_{\text{HCl}}\, K^m_{\text{H,HCl}}$.

E3) Calculate the total pressure of volatile components in the system: $P_{sum} = P_W + P_{\text{HCl}}$.

E4) The composition of the solution is still described by the equation (17.2):

The calculated pressures above saturated solutions in both systems are given in Fig. 8.2 and Table 6. Fig. 8.2 demonstrates that a pseudo-azeotrope negative with respect to P_T is implemented with a minimum total pressure – P_{Az3}.

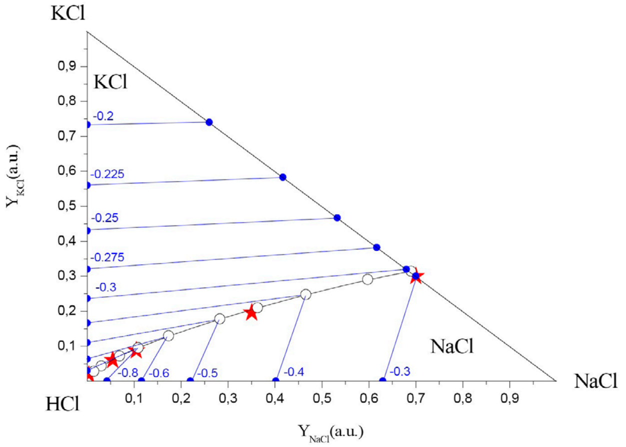

Fig. 8.1. Solubility diagram of the KCl – NaCl – HCl – H_2O system at 25 °C (open circles and lines – calculation results, red stars – experimental data [38], blue lines – calculated water isoactivates, $\ln a_W$ values are shown in blue

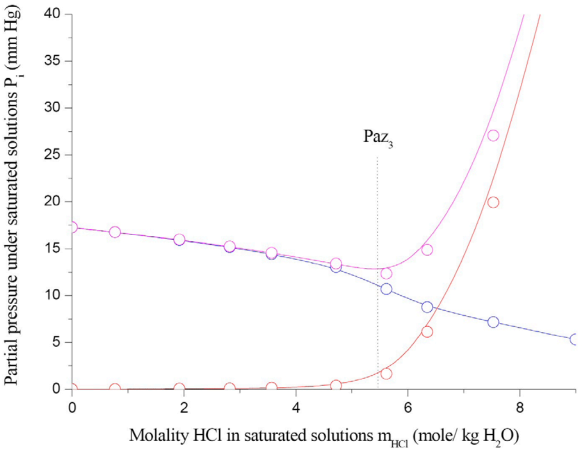

Fig. 8.2. Dependence of partial pressures P_{H_2O} (blue lines and circles), P_{HCl} (red lines and circles), and the total pressure P_{sum} (violet lines and circles) in the KCl – NaCl – HCl – H_2O system at 25 °C – calculation based on binary subsystems

Table 6. Solubility, partial, and total pressures in saturated solutions in the NaCl – KCl – HCl – H_2O system at 25 °C

$\ln a_W$ r.u.	m^0_{NaCl}	m^0_{KCl}	m^0_{HCl}	$\ln a^0_{NaCl}$	$\ln a^0_{KCl}$	Z_{NaCl}	Z_{KCl}	Z_{HCl}	m_{NaCl}	m_{KCl}	m_{HCl}
	mol/kg H_2O			r.u.					mol/kg H_2O		
−0.32	6.69	8.14	5.18	3.94	3.37	0.728	0.272	0.000	5.00	2.28	0,00
−0.35	7.11	8.76	5.49	4.19	3.57	0.582	0.229	0.187	414	2.01	0.77
−0.40	7.78	9.75	5.99	4.56	3.87	0.402	0.170	0.427	3.13	1.66	1.92
−0.45	8.41	10.72	6.45	4.90	4.14	0.286	0.130	0.583	2.40	1.39	2.82
−0.50	9.01	11.66	6.89	5.22	4.39	0.208	0.101	0.690	1.87	1.18	3.57
−0.60	10.12	13.48	7.70	5.80	4.83	0.116	0.065	0.818	1.17	0.87	4.72
−0.80	11.12	15.24	9.14	6.32	5.22	0.069	0.044	0.886	0.77	0.67	5.62
−1.00	12.05	16.97	10.41	6.81	5.56	0.042	0.031	0.926	0.51	0.53	6.35
−1.20	13.74	20.37	11.55	7.67	6.16	0.017	0.017	0.964	0.24	0.35	7.53

$\ln a_W$ r.u.	P_W	P_{HCl}	P_{sum}
	mm Hg		
−0.32	17.25	0.000	17.25
−0.35	16.74	0.0090	16.75
−0.40	15.92	0.033	15.96
−0.45	15.15	0.073	15.22
−0.50	14.41	0.134	14.54
−0.60	13.03	0.359	13.39
−0.80	10.66	1.64	12.31
−1.00	8.74	6.11	14.85
−1.20	7.15	19.90	27.06

6. Topological isomorphism of *n*-phase equilibrium diagrams of *n*-component systems with two volatile components in decreased concentration spaces

This section focuses on the topological isomorphism of equilibrium diagrams of multicomponent multiphase systems containing two volatile components in univariant multicomponent multiphase systems. Earlier studies considered some particular systems of the same or similar types (for instance, [27]).

6.1. Topological isomorphism of three-phase equilibrium diagrams of ternary systems with two volatile components

Let's consider a three-phase equilibrium (solid phase – non-volatile component 3 (*s*) – vapor, consisting of two volatile components 1 – volatile acid 2 – solvent (*v*) – liquid solution, consisting of all the three components of the ternary system) at a constant temperature *T* = const. For instance, let's consider the following system: HCl(1) – H_2O(2) – NaCl(3). Let's introduce the partial Gibbs energy:

$$G^{[3]} = G - \mu_3 n_3 = \sum_{i=1}^{2} \mu_i n_i, \tag{18}$$

where μ_i and n_i are the chemical potential and the number of moles of the *i*-th volatile component.

Let's consider a heterogeneous ternary system and introduce a scalar quantity $y_1^{(i)}$, where $y_1^{(i)}$ is the mole fraction of the 1st component (in the *i*-th phase) in the concentration space reduced with respect to the 3rd component. These are the so-called Janecke indices:

$$y_1 = n_1 / \sum_{j=1}^{2} n_j. \tag{19}$$

The independent characteristic parameters of the partial molar Gibbs energy (18) are as follows: temperature – *T*, pressure – *P*, the Janecke index – y_1, and the chemical potential of the 3rd component in the solid phase – μ_3. The equation of the two-phase (α–β) equilibrium shift can be described by the following system of generalized differential van der Waals equations:

$$\begin{aligned}&(y_1^{(\alpha)} - y_1^{(\beta)}) G_{11}^{[3](\alpha)} dy_1^{(\alpha)} = \\ &= S^{[3](\alpha\to\beta)} dT - V^{[3](\alpha\to\beta)} dP + n_3^{[3](\alpha\to\beta)} d\mu_3,\end{aligned} \tag{20}$$

$$\begin{aligned}&(y_1^{(\beta)} - y_1^{(\alpha)}) G_{11}^{[3](\beta)} dy_1^{(\beta)} = \\ &= S^{[3](\beta\to\alpha)} dT - V^{[3](\beta\to\alpha)} dP + n_3^{[3](\beta\to\alpha)} d\mu_3,\end{aligned} \tag{21}$$

where:

$$\begin{aligned}
S^{[3](\alpha\to\beta)} &= \left[S^{[3](\beta)} - S^{[w](\alpha)} + (y_1^{(\beta)} - y_1^{(\alpha)}) \nabla S^{[3](\alpha)} \right] \\
S^{[3](\beta\to\alpha)} &= \left[S^{[3](\alpha)} - S^{[3](\beta)} + (y_1^{(\alpha)} - y_1^{(\beta)}) \nabla S^{[3](\beta)} \right] \\
V^{[3](\alpha\to\beta)} &= \left[V^{[3](\beta)} - V^{[3](\alpha)} + (y_1^{(\beta)} - y_1^{(\alpha)}) \nabla V^{[3](\alpha)} \right] \\
V^{[3](\beta\to\alpha)} &= \left[V^{[3](\alpha)} - V^{[3](\beta)} + (y_1^{(\alpha)} - y_1^{(\beta)}) \nabla V^{[3](\beta)} \right] \\
n_w^{[3](\alpha\to\beta)} &= \left[n_w^{[3](\beta)} - n_w^{[3](\alpha)} + (y_1^{(\beta)} - y_1^{(\alpha)}) \nabla n_3{}^{(3)(\alpha)} \right] \\
n_w^{[3](\beta\to\alpha)} &= \left[n_w^{[3](\alpha)} - n_w^{[3](\beta)} + (y_1^{(\alpha)} - y_1^{(\beta)}) \nabla n_W{}^{(3)(\beta)} \right],
\end{aligned} \tag{22}$$

where $V^{[3](\tau)}$, $S^{[3](\tau)}$ and $n_w^{[3](\tau)}$ are the molar volume, entropies, and numbers of moles of the 3rd component of phase τ, calculated without taking into account the number of moles of the salt (per 1 mole of volatile components). The $\nabla V^{[3](\tau)}$, $\nabla S^{[3](\tau)}$, $\nabla n_w^{[3](\tau)}$ functions are gradients of concentration of the corresponding functions in the reduced concentration space, $\left(\partial V^{[3](\tau)} / \partial y_1^{(\tau)}\right)_{T,P,\mu_3^{(\tau)}}$, $\left(\partial S^{[3](\tau)} / \partial y_1^{(\tau)}\right)_{T,P,\mu_3^{(\tau)}}$, and $\left(n_w^{[3](\tau)} / \partial y_1^{(\tau)}\right)_{T,P,\mu_3^{(\tau)}}$, respectively; $y_1^{(\tau)}$ is the parameter, characterizing the state of the figurative point of phase τ in the reduced concentration space; $dy_1^{(\tau)}$ characterizes the displacement of $y_1^{(\tau)}$ according to the displacement of the two-phase equilibrium; $G_{11}^{[3](\tau)}$ is determined as:

$$G_{11}^{[3](\alpha)} = \left(\frac{\partial^2 G^{[1](\alpha)}}{\partial y_1^{(\alpha)2}} \right)_{T,P,\mu_3^{(\alpha)}} \tag{23}$$

and

$$G_{11}^{[3](\beta)} = \left(\frac{\partial^2 G^{[1](\beta)}}{\partial y_1^{(\beta)2}} \right)_{T,P,\mu_3^{(\beta)}}. \tag{24}$$

According to the diffusion resistance criteria and Sylvester's criterion, for the positive definite quadric forms, the following is true:

$$G_{11}^{[3](\tau)} > 0\ . \tag{25}$$

The $S^{[3](\alpha\to\beta)}, S^{[3](\beta\to\alpha)}, V^{[3](\alpha\to\beta)}, V^{[3](\beta\to\alpha)}, n_w^{[3](\beta\to\alpha)}$ parameters have the physical senses of entropy, the volume and the number of moles of the 3rd component in the isotherm–isobar–isopotential (with respect to the 3rd component) process of formation of one mole of phase β from an infinitely large.

Let's assume that the α phase is a liquid solution (l), the β phase is vapor (v), and the α → β equilibrium is (l)–(v), $dT = 0$, $d\mu_3 = 0$. The latter is true because the standard chemical potential of the solid phase (s), μ_3, depends on the temperature only. Therefore, we are dealing with a three-phase equilibrium (l)–(v)–(s). Let's rewrite the system of differential equations (20, 21):

$$(y_1^{(l)} - y_1^{(v)})G_{11}^{[3](l)}dy_1^{(l)} = -V^{[3](l\to v)}dP \qquad (26)$$

$$(y_1^{(v)} - y_1^{(l)})G_{11}^{[3](v)}dy_1^{(v)} = -V^{[3](v\to l)}dP\ . \qquad (27)$$

Naturally, the equation cannot be used with $dP = 0$, $dT \neq 0$, because then $d\mu_3 \neq 0$, and the corresponding term should be added to equations (26, 27).

Based on the physical sense, $V^{[3](l\to v)} > 0$, $V^{[3](v\to l)} < 0$, and therefore we can formulate three analogues of the three Gibbs–Konovalov and Gibbs–Roozeboom rules.

First rule.

When moving along the crystallization curve of the non-volatile component on the isothermal solubility diagram of a ternary system, the total pressure of vapors above saturated solutions increases (decreases) following an increase in the Janecke index of the volatile component (excluding the non-volatile component), whose concentration in the ternary system of vapor is larger (smaller) than in the solution:

$$\left[dP / dy_1^{(l)}\right]_{T,\mu_3^{(\tau)}} > (<) 0\ , \text{ if } \ y_1^{(v)} > (<) y_1^{(l)}\ . \qquad (28.1)$$

Second rule.

When moving along the crystallization curve of the non-volatile component on the isothermal solubility diagram of a ternary system in a reduced (excluding the non-volatile component) concentration space, the total pressure of the volatile components passes through the extremum, if the compositions of the existing phases in the reduced concentration space, i.e. the Janecke indices, coincide. These points will be called pseudo-azeotropes - P_{Az}.

$$\left[dP / dy_1^{(l)}\right]_{T,\mu_3^{(\tau)}} = 0,\ \text{ if } \ y_1^{(v)} = y_1^{(l)}\ . \qquad (28.2)$$

Third rule.

Dividing equation (26) by equation (27) we obtain:

$$\left[dy_1^{(l)} / dy_1^{(v)}\right]_{T,\mu_3^{(\tau)}} = \\ = -\left[G_{11}^{[3](v)} / G_{11}^{[3](v)}\right]\left[V^{[3](l\to v)} / V^{[3](v\to l)}\right] > 0. \quad . \ (28.3)$$

When moving along the crystallization curve of the non-volatile component on the isothermal solubility diagram of a ternary system in a reduced (excluding the non-volatile component) concentration space, the Janecke indices of the equilibrium liquid and vapor phases change simbatically.

6.2. Topological isomorphism of four-phase equilibrium diagrams of four-component systems with two volatile components

Let's consider a four-phase equilibrium (solid non-volatile component 3 (s_1) – solid non-volatile component 4 (s_2) – vapor, consisting of two volatile components 1 – volatile acid 2 and solvent (v) – liquid solution, consisting of all the four components of the four-component system) at a constant temperature T = const. For instance, let's consider the following system: HCl(1) – H_2O(2) – NaCl(3) – KCl(4). Let's introduce the partial Gibbs energy:

$$G^{[3,4]} = G - \mu_3 n_3 - \mu_4 n_4 = \sum_{i=1}^{2} \mu_i n_i\ . \qquad (29)$$

Let's consider a heterogeneous four-component system and introduce a scalar quantity in the twice reduced concentration space $y_1^{(i)}$, where $y_1^{(i)}$ is the molar fraction of the 1-st component (in the i-th phase) in the twice reduced concentration space (excluding components 3 and 4). In this case, the Janecke indices are set by the following relation:

$$y_1 = n_1 \Big/ \sum_{j=1}^{2} n_j\ . \qquad (30)$$

The characteristic parameters of the partial molar Gibbs energy (29) are the following: temperature – T, pressure – P, the Janecke index – y_1, and the chemical potentials of salts – μ_3, μ_4. The equation of the two-phase (α–β) equilibrium shift can be described by the following system of differential van der Waals equations:

$$(y_1^{(\alpha)} - y_1^{(\beta)})G_{11}^{[3,4](\alpha)}dy_1^{(\alpha)} = S^{[3,4](\alpha\to\beta)}dT - \\ -V^{[3,4](\alpha\to\beta)}dP + n_3^{[3,4](\alpha\to\beta)}d\mu_3 + n_4^{[3,4](\alpha\to\beta)}d\mu_4, \qquad (31)$$

$$(y_1^{(\beta)} - y_1^{(\alpha)})G_{11}^{[3,4](\beta)}dy_1^{(\beta)} = S^{[3,4](\beta\to\alpha)}dT - \\ -V^{[3,4](\beta\to\alpha)}dP + n_3^{[3,4](\beta\to\alpha)}d\mu_3 + n_4^{[3,4](\beta\to\alpha)}d\mu_4, \qquad (32)$$

where parameters $G_{11}^{[3,4](\tau)}$, $S^{[3,4](\alpha\to\beta)}$, $S^{[3,4](\beta\to\alpha)}$, $V^{[3,4](\alpha\to\beta)}$, $V^{[3,4](\beta\to\alpha)}$, $n_3^{[3,4](\alpha\to\beta)}$, $n_4^{[3,4](\alpha\to\beta)}$, $n_3^{[3,4](\beta\to\alpha)}$, and $n_4^{[3,4](\beta\to\alpha)}$ have the same sense as the parameters in equations (22) with the only addition – $\mu_4^{(\tau)}$ should be constant for the corresponding derivatives:

$$\left(\partial V^{[3](\tau)} / \partial y_1^{(\tau)}\right)_{T,P,\mu_3^{(\tau)},\mu_4^{(\tau)}}, \left(\partial S^{[3](\tau)} / \partial y_1^{(\tau)}\right)_{T,P,\mu_3^{(\tau)},\mu_4^{(\tau)}},$$

$$\left(n_w^{[3](\tau)} / \partial y_1^{(\tau)}\right)_{T,P,\mu_3^{(\tau)},\mu_4^{(\tau)}}, G_{11}^{[3](\tau)} = \left(\frac{\partial^2 G^{[1](\tau)}}{\partial y_1^{(\tau)2}}\right)_{T,P,\mu_3^{(\tau)},\mu_4^{(\tau)}}.$$

Parameters $S^{[3](\alpha\to\beta)}$, $S^{[3](\beta\to\alpha)}$, $V^{[3](\alpha\to\beta)}$, $n_w^{[3](\alpha\to\beta)}$, and $n_w^{[3](\alpha\to\beta)}$ reflect the changes in the entropy, volume, and the number of moles of the components (3, 4) during the isotherm–isobar–isopotential (with regard to the 3rd and 4th components) process of formation of one mole of phase β from an infinitely large mass of phase α, and vice versa in the concentration space, reduced with respect to the 3rd and 4th components.

Let's assume that the α phase is a liquid solution (l), the β phase is vapor (v), and the α → β equilibrium is (l)–(v), dT = 0, $d\mu_3 = d\mu_4 = 0$. The latter is true because the standard chemical potentials of the components in the solid phase (s_1, s_2) μ_3 and μ_4 depend on the temperature only. Therefore, we are dealing with a four-phase equilibrium (l)–(v)–(s_1)–(s_2). Let's rewrite equations (31, 32) for the set conditions. Then we can easily derive equations (26, 27).

Therefore, we can formulate three analogues of the Gibbs–Konovalov and Gibbs–Roozeboom rules, which will be true for the twice reduced concentration space:

$$\left[dP / dy_1^{(l)}\right]_{T,\mu_3^{(\tau)},\mu_4^{(\tau)}} > (<) 0, \text{ if } y_1^{(v)} > (<) y_1^{(l)}; \qquad (33.1)$$

$$\left[dP / dy_1^{(l)}\right]_{T,\mu_3^{(\tau)},\mu_4^{(\tau)}} = 0, \text{ if } y_1^{(v)} = y_1^{(l)}; \qquad (33.2)$$

$$\left[dP / dy_1^{(l)}\right]_{T,\mu_3^{(\tau)},\mu_4^{(\tau)}} = \\ = -\left[G_{11}^{[3](v)} / G_{11}^{[3](v)}\right]\left[V^{[3](l\to v)} / V^{[3](v\to l)}\right] > 0. \qquad (33.3)$$

The wording of the analogues is the same as that of the ones presented in section 6.1, the only difference being the following: "When moving along the **co-crystallization** curve of the **two** non-volatile components on the isothermal solubility diagram of a **four-component** system in a **twice** reduced (excluding both non-volatile components) concentration space...".

6.3. Topological isomorphism of n-phase equilibrium diagrams of n-component systems with two volatile components

Naturally, the suggested analogues of the three Gibbs–Konovalov and Gibbs–Roozeboom rules can be applied to *n*-phase heterogeneous systems within *n*-component systems with two volatile components. Let's consider a phase equilibrium (solid pure non-volatile component 3 (s_1) – solid pure non-volatile component 4 (s_2) – solid pure non-volatile component *n* (s_{n-2}) – vapor, consisting of two volatile components 1 – volatile acid and 2 – solvent (*v*) – liquid solution, consisting of 1, 2, 3...*n* components) at a constant temperature *T* = const. In this case, we are dealing with an (*n*-2)-time reduced concentration space and can formulate another three analogues of the Gibbs–Konovalov and Gibbs–Roozeboom rules, which will be true for an (*n*-2)-time reduced concentration space:

$$\left[dP / dy_1^{(l)}\right]_{T,\mu_3^{(\tau)},\mu_4^{(\tau)},\ldots,\mu_n^{(\tau)}} > (<) 0, \text{ if } y_1^{(v)} > (<) y_1^{(l)}; \qquad (34.1)$$

$$\left[dP / dy_1^{(l)}\right]_{T,\mu_3^{(\tau)},\mu_4^{(\tau)},\ldots,\mu_n^{(\tau)}} = 0, \text{ if } y_1^{(v)} = y_1^{(l)}; \qquad (34.2)$$

$$\left[dP / dy_1^{(l)}\right]_{T,\mu_3^{(\tau)},\mu_4^{(\tau)},\ldots,\mu_n^{(\tau)}} = \\ = -\left[G_{11}^{[3](v)} / G_{11}^{[3](v)}\right]\left[V^{[3](l\to v)} / V^{[3](v\to l)}\right] > 0. \qquad (34.3)$$

The wording of the analogues is the same as that of the ones presented in section 6.1, the only difference being the following: "When moving along the **co-crystallization** curve of **(*n*–2)** non-volatile components on the isothermal solubility diagram of an **n-component** system in an **(*n*–2)-time** reduced (excluding **(*n*–2)** non-volatile components) concentration space...".

6.4. Topological isomorphism of n-phase equilibrium diagrams of n-component systems with two volatile components with crystal solvates (crystalline hydrates) of solid components of constant composition

Until now, we assumed that all solid phases of constant composition that are in equilibrium with vapor and liquid solution are pure salt-type components. Let's assume that crystal solvates (crystalline hydrates) of solid solutions of constant compositions are crystallized in the system. Are they then the true analogues of the three Gibbs–Konovalov and Gibbs–Roozeboom rules presented in (34.1–34.3)? The answer to this question is positive provided that we consider crystalline hydrates or compounds of constant compositions rather than particular salts as independent components of the system. This can be done, because the independent components, or variables of the composition of a multicomponent system, are random, with only the number of independent components being constant. Therefore, the laws will be true in the concentration space reduced with respect to the new components. For instance, on the crystallization curve of crystalline hydrate $LiCl\cdot H_2O$ in the $HCl(1) – H_2O(2) – LiCl(3)$ system, all the analogues of the Gibbs–Konovalov and Gibbs–Roozeboom rules are true (28.1–28.3), if we recalculate the Janecke indices for the new components of the system: $HCl(1) – H_2O(2) – LiCl\cdot H_2O(3)$. In this case, the molar fractions in the new set of variables $n_i^{(new)}$ are easily calculated based on the molar fractions in the previous set of variables $n_i^{(old)}$: $n^{(new)}_{LiCl\cdot H_2O}=n^{(old)}_{LiCl}$, $n^{(new)}_{HCl}=n^{(old)}_{HCl}$, $n^{(new)}_{H_2O}=n^{(old)}_{H_2O}-n^{(old)}_{LiCl}$. Let's consider another example: for the co-crystallization curve of $MgCl_2\cdot CaCl_2\cdot 12H_2O$ and crystalline hydrate $MgCl_2\cdot 6H_2O$ in the $HCl(1) – H_2O(2) – MgCl_2(3) – CaCl_2(4)$ system the analogues of the said laws (28.1–28.3) are true, if we recalculate the molar fractions of the components with respect to $HCl(1) – H_2O(2) – MgCl_2\cdot 6H_2O(3) – MgCl_2\cdot CaCl_2\cdot 12H_2O(4)$. The recalculation is performed based on the relations:

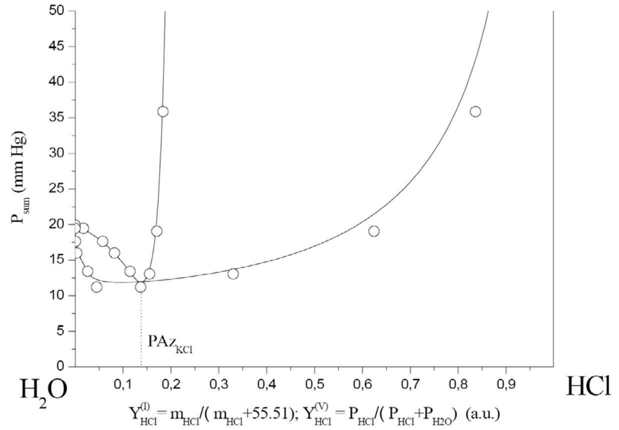

Fig. 9.2. Liquid-vapor phase diagram in the KCl – HCl – H_2O system at 25 °C in variables: the total vapor pressure of volatile components is the Yanecke HCl index; P_{AzKCl} is a pseudo-azeotrope when moving along the NaCl crystallization curve

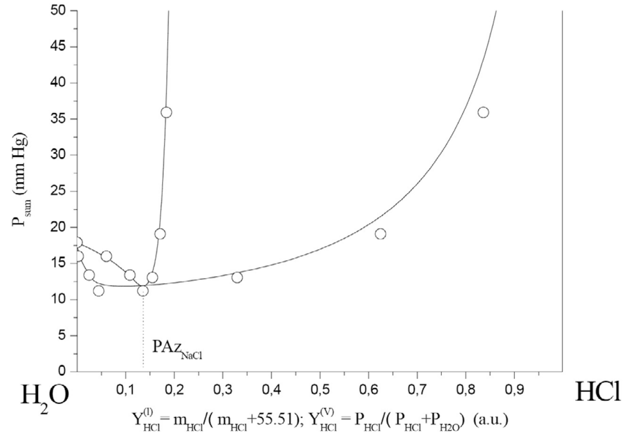

Fig. 9.1. Liquid-vapor phase diagram in the NaCl – HCl – H_2O system at 25 °C in variables: the total vapor pressure of volatile components is the Yanecke HCl index; P_{AzNaCl} is a pseudo-azeotrope when moving along the NaCl crystallization curve

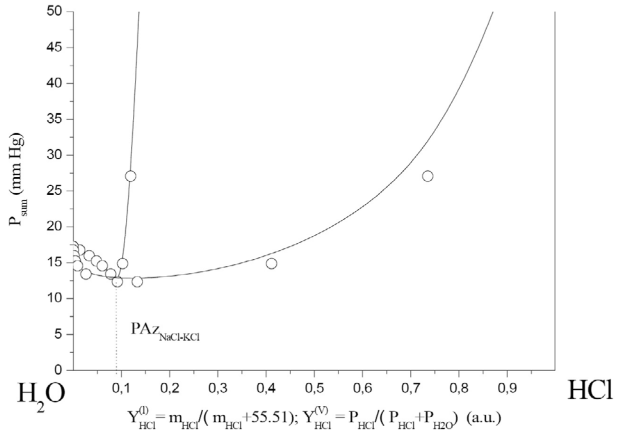

Fig. 9.3. Liquid-vapor phase diagram in the KCl – NaCl – HCl – H_2O system at 25 °C in variables: the total vapor pressure of volatile components is the Yanecke HCl index; $P_{AzNaCl-KCl}$ is a pseudo-azeotrope when moving along the KCl and NaCl co-crystallization branch

$$n^{(new)}_{\mathrm{MgCl_2 \cdot CaCl_2 \cdot 12H_2O}} = n^{(old)}_{\mathrm{CaCl_2}}, \quad n^{(new)}_{\mathrm{MgCl_2 \cdot 6H_2O}} = n^{(old)}_{\mathrm{MgCl_2}} - n^{(old)}_{\mathrm{CaCl_2}},$$

$$n^{(new)}_{\mathrm{HCl}} = n^{(old)}_{\mathrm{HCl}}, \qquad n^{(new)}_{\mathrm{H_2O}} = n^{(old)}_{\mathrm{H_2O}} - 6\left[n^{(old)}_{\mathrm{MgCl_2}} + n^{(old)}_{\mathrm{CaCl_2}}\right] - $$

$$- 12 n^{(old)}_{\mathrm{CaCl_2}}.$$

6.5. Application of the suggested analogues of the Gibbs–Konovalov and Gibbs–Roozeboom rules to ternary and quaternary systems

Fig. 9.1–9.3 demonstrate some examples of the suggested analogues of the Gibbs–Konovalov and Gibbs–Roozeboom rules implemented for univariant curves of three-phase equilibrium in ternary systems (HCl – H_2O – NaCl and HCl – H_2O – KCl at 25 °C) and a quaternary system (HCl – H_2O – NaCl – KCl at 25 °C). In the first case, three-phase equilibria (*s*–*l*–*v*) were considered, and in the second case – four-phase equilibria (s_1–s_2–*l*–*v*). In the first case, the concentration space was reduced with respect to NaCl, and in the second case it was reduced with respect to NaCl and KCl. In both cases, the variables of the composition were the Janecke indices of the volatile components of the system – Y_{HCl}, Y_W. Fig. 9.1–9.3 show that the three systems are in complete agreement with the suggested analogues of the three rules. Each system has one pseudo-azeotrope – P_{Azj} (index *j* corresponds to the solid phase(s) with respect to which the considered solution is saturated). P_{Azj} complies with the minimum $P_{\mathrm{sum}} = P_W + P_{\mathrm{HCl}}$. All the diagrams are also limited from above by the boiling point of the solution at P_{sum} = 760 mm Hg.

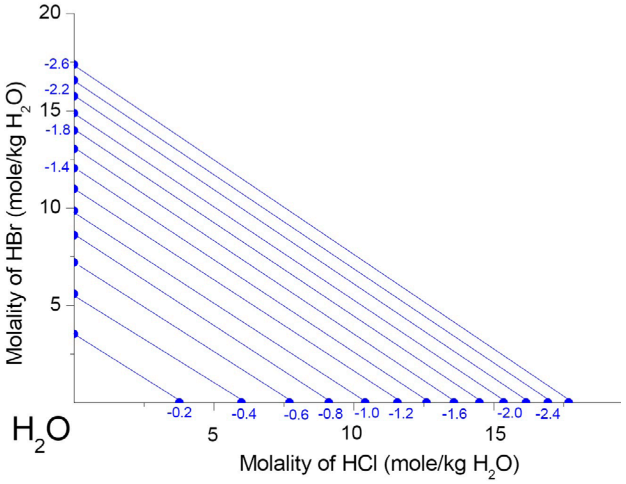

Fig. 10.1. Water isoacivates in the ternary HCl – HBr – H_2O system at 25 °C, ln a_W values are shown in blue

7. Ternary systems with three volatile components (HCl – HBr – H_2O) at 25 °C

To demonstrate the possibility of the calculation of phase diagrams of ternary systems with three volatile components, we considered the HCl – HBr – H_2O system at 25 °C. Solid phases cannot be formed in such systems under the defined conditions. So, naturally, there is the only type of equilibrium diagram, which we consider below.

7.1. An algorithm for the calculation of vapor-liquid equilibrium diagrams in unsaturated solutions

F1) Define a_W.

F2) Obtain linear water isoactivates with $P_W = P_W^{(0)}$ ($a_W = const$) based on the data regarding the binary subsystems (see Fig. 10.1).

F3) Curvilinear isoactivates or isobars of partial pressures P_{HCl} = *const* are obtained by solving equations of the following type: $a^0_{\mathrm{HCl}} Z_{\mathrm{HCl}} K^m_{\mathrm{H,HCl}} = const$ with various a_W, finding Z_{HCl} and the corresponding compositions of solutions (m_{HCl}, m_{KCl}) (see (13)), followed by combining the solutions to the equations in a continuous smooth curve.

F4) Curvilinear isoactivates or isobars of partial pressures P_{HBr} = *const* are obtained by solving equations of the following type:

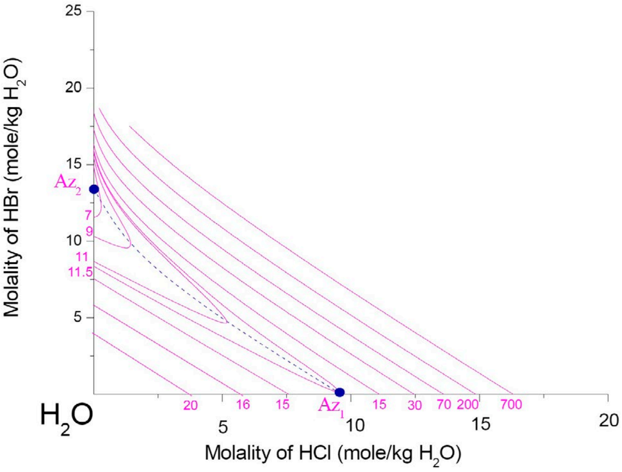

Fig. 10.2. Lines of equal total pressures of volatile components in the ternary HCl – HBr – H_2O system at 25 °C, P_{sum} values in mm Hg are shown in violet. The dotted blue line is the line of local extrema of the Psum function, i.e. a negative fold on the $P_{\mathrm{sum}}(m_{\mathrm{HCl}}, m_{\mathrm{HBr}})$ surface [7, 8]; the blue dots are binary azeotropes in the subsystems HCl – H_2O and HBr – H_2O

$a^{0}_{\mathrm{HBr}} Z_{\mathrm{HBr}} K^{m}_{\mathrm{H,HBr}} = const$ with various a_W, finding Z_{HBr} and the corresponding compositions of solutions (m_{HCl}, m_{KCl}) (see (13)).

F5) Curvilinear isobars of the total pressures of volatile components $P_{\mathrm{sum}} = const$ are obtained by solving equations of the following type: $a^{0}_{\mathrm{HCl}} Z_{\mathrm{HCl}} K^{m}_{\mathrm{H,HCl}} + a^{0}_{\mathrm{HBr}} \left(1 - Z_{\mathrm{HCl}}\right) K^{m}_{\mathrm{H,HBr}} + P_W = const$ with various a_W, finding the corresponding Z_{HCl} and the compositions of solutions (m_{HCl}, m_{KCl}), followed by combining the solutions to the equations in a continuous smooth curve. The latter curves, i.e. isobars of the total pressure in the considered ternary system, are given in Fig 10.2. Both figures demonstrate a univariant line of local extrema of function P_{sum} (local minimums), i.e. a negative fold on the surface of $P_{sum}(m_{\mathrm{HCl}}, m_{salt})$ [7, 26, 27]. This fold lies between the binary azeotrope Az_1 and another binary azeotrope Az_2, (see Fig. 10.2).

8. Conclusions

The article presented an algorithm for the calculation of vapor-liquid phase equilibria in multicomponent quasi-simple systems complying with Zdanovskii's rule. The algorithm is based entirely on the data regarding binary subsystems. The algorithm was tested using three- and four-component water-electrolyte systems with one, two, or three volatile components. The results of the calculations are in good agreement with the experimental data. Analogues of the Gibbs–Konovalov and Gibbs–Roozeboom rules were formulated and proved for the compositions of the solutions moving along univariant curves of n-phase equilibria in n-component systems at a constant temperature.

Author contributions

All authors made an equivalent contribution to the preparation of the publication.

Conflict of interests

The authors declare that they have no known competing financial interests or personal relationships that could have influenced the work reported in this paper.

References

1.Zdanovskii A. B. Patterns in the property changes of mixed solutions*. *Proceedings of the salt laboratory AN SSSR*. 1936;6: 1-70. (In Russ.)

2. Ryasanov M. A. *Selected chapters from the theory of solutions**. Syktyvkar: SGU Publ.; 1997. 205 p. (In Russ.)

3. Mikulin G. I. *Thermodynamics of mixed solutions of strong electrolytes. Issues of physical chemistry of electrolyte solutions**. Leningrad: Khimiya Publ.: 1968. p. 202–231. (In Russ.)

4. Charykova M. V., Charykov N. A. *Thermodynamic modeling of evaporite sedimentation processes**. S-Petersburg: Nauka Publ.; 2003. 261 p. (In Russ.)

5. Filippov V. K. Systems complying with Zdanovskii's rule*. *Vestnik of Saint Petersburg university: Physics and Chemistry*. 1977;3: 98–105. (In Russ.)

6. Charykov N. A., Rumyantsev A. V., Keskinov V. A., Letenko D. G., Charykova M. V. Universal algorithm for calculation of liquid-vapor diagrams of quasi-simple multicomponent systems. *Journal of Chemical & Engineering Data*. 2024;69(11): 4089–4097. https://doi.org/10.1021/acs.jced.4c00307

7. Storonkin A. V. *Thermodynamics of heterogeneous systems**. Book 1. Part I, II. Leningrad: LGU Publ.; 1967. 467 p. (In Russ.)

8. Storonkin A. V. *Thermodynamics of heterogeneous systems**. Book 2. Part III. Leningrad: LGU Publ.; 1969. 270 p. (In Russ.)

9. Münster A. *Chemische thermodynamik*. Berlin: Akademie — Verlag; 1969. 261 p.

10. Korjinskii A. D. *Theoretical bases of mineral paragenesis analysis**. Moscow: Nauka Publ.; 1973. 288 p. (In Russ.)

11. Filippov V. K. About the connection between chemical potentials, pressure, temperature and composition in multicomponent multiphase systems. In: *Aspects of thermodynamics of heterogeneous systems and theory of surface phenomena**. Collection of articles. A. V. Storonkin and V. T. Zharov (eds.). Leningrad: LGU Publ.; 1973. Vol. 2. p. 20–36. (In Russ.)

12. Filippov V. K. About the conditions of equilibrium and stability of heterogeneous systems. In: *Aspects of thermodynamics of heterogeneous systems and theory of surface phenomena**. Collection of articles. V. K. Filippov (ed.). Leningrad: LGU Publ.;1992. Vol. 9. p. 6–33. (In Russ.)

13. Stromberg A. G., Semchenko D. P. *Physical chemistry**. Moscow: Vysshaya shkola Publ.; 2001. 529 p. (In Russ.)

14. Pitzer K. S., Kim J. J. Thermodynamics of electrolytes. IV. Activity and osmotic coefficients for mixed electrolytes. *Journal of the American Chemical Society*. 1974;96: 5701–5707. https://doi.org/10.1021/ja00825a004

15. Rabinovich V. A., Khavin Z. Ya. *Brief chemical reference**. Ed. 2-nd: Corr. and add. Leningrad: Khimiya Publ.; 1978. 285 p. (In Russ.). Available at: http://es.niv.ru/doc/dictionary/chemical-manual/articles/660/parcialnye-davleniya-hcl-i-h2o.htm

16. *Chemist's Handbook**. Ed. 2-nd: Corr. and add. B. P. Nikol'skiy (ed.). Vol. 3. Moscow, Leningrad: Khimiya Publ.; 1964. 339 p. (In Russ.)

17. Reznik F. Ya. Isopiestic measurement of the vapor pressure in electrolyte solutions. In: *Physical chemistry of electrolyte solutions**. G. I. Mikulin (ed.). 1968. p. 222–239. (In Russ.)

18. *Reference book on the solubility of salt systems**. Leningrad: Khimiya Publ.; 1975. Vol. II-1. 552 p. (In Russ.)

19. *Reference book on the solubility of salt systems**. Leningrad: Khimiya Publ.; 1973. Vol. I-2. 568–1069 p. (In Russ.)

20. *Reference book on the solubility of salt systems**. Leningrad: Khimiya Publ.; 1973. Vol. I-1. 567 p. (In Russ.)

21. Eusseltova J. Solubility of lithium nitrate in solutions of lithium halides. *Monatshefte für Chemie - Chemical Monthly*. 2005;136(9): 1567–1572. https://doi.org/10.1007/s00706-005-0345-4

22. Armstrong H., Eyre J., Paddison W. Studies of the processes operative in solutions. In: *Proceedings of the Royal Society of London. Series A*. 1907;79: 570 and 1911;84: 128.

23. Storonkin A. V., Markuzin N. P. Investigation of vapor pressure in saturated and unsaturated solutions of potassium chloride in hydrochloric acid*. *Russian Journal of Physical Chemistry A*. 1955;29(1): 110–119. (In Russ.)

24. *Reference book. Experimental data on the solubility of multicomponent systems. Vol. 2. Quaternary and more complex systems. Book 1, 2**. A. D. Pel'sh (ed.). Leningrad: Khimiya Publ.; 1063 p. (In Russ.)

25. Efimov N. V., Rozendorn E. R. *Linear algebra and multidimensional geometry**. 2023. 552 p. (In Russ.)

26. *Multidimensional geometry**. O. V. Yakunin (ed.). Penza: PSU Pub.; 2013. 156 p. (In Russ.)

27. Charykov N. A., Rumyantsev A. V., Semenov K. N., … Blokhin A. A. Topological isomorphism of liquid-vapor, fusibility, and solubility diagrams. Analogues of Gibbs–Konovalov and Gibbs–Roozeboom laws for solubility diagrams. Processes. 2023;11(5): 1405. https://doi.org/10.3390/pr11051405

** Translated by author of the article*

Information about the authors

Nikolay A. Charykov, Dr. Sci. (Chem.), Professor at the Department of Physical Chemistry, Saint-Petersburg State Technological Institute (Technical University) (Saint-Petersburg, Russian Federation).

https://orcid.org/0000-0002-4744-7083
ncharykov@yandex.ru

Alexey V. Rumyantsev, Dr. Sci. (Chem.), Head of the Department of Engineering Radioecology and Radiochemical Technology, Saint-Petersburg State Technological Institute (Technical University) (Saint-Petersburg, Russian Federation).

https://orcid.org/0000-0003-3985-2086
radioecology_dept@technolog.edu.ru

Viktor A. Keskinov, Cand. Sci. (Chem), Leading Researcher «Veritas» Center, Kazakhstan State Technical University (Ust-Kamenogorsk, Republic of Kazakhstan).

https://orcid.org/0000-0003-3227-122X
keskinov@mail.ru

Konstantin N. Semenov, Dr. Sci. (Chem.), Professor, Head of the Department of General and Bioorganic Chemistry, Pavlov First Saint Petersburg State Medical University (Saint-Petersburg, Russian Federation).

https://orcid.org/0000-0003-2239-2044
knsemenov@gmail.com

Valerya A. German, graduate student at the Department of Physical chemistry, Saint-Petersburg State Technological Institute (Technical University) (Saint-Petersburg, Russian Federation).

ilao2010@mail.ru

Natalya A. Kulenova, Cand. Sci. (Chem), Head of «Veritas» Center, Kazakhstan State Technical University (Ust-Kamenogorsk, Republic of Kazakhstan).

https://orcid.org/0000-0002-7063-4899
3007kulenova53@gmail.com

Marina V. Charykova, Dr. Sci. (Geol.), Professor, Head of the Department of Geochemistry of the Faculty of Geology, Saint-Petersburg State University (Saint-Petersburg, Russian Federation).

https://orcid.org/0000-0001-8311-0325
m-char@yandex.ru

Mariia V. Keskinova, Assistant of the Department of Theoretical Foundations of Materials Science, Saint-Petersburg State Technological Institute (Technical University) (Saint-Petersburg, Russian Federation).

https://orcid.org/0000-0002-8359-9594
keskinova88@mail.ru

Mikhail Yu. Arshinov, graduate student at the Department of Physical chemistry, Saint-Petersburg State Technological Institute (Technical University) (Saint-Petersburg, Russian Federation).

ilao2010@mail.ru

Received 17.05.2024; approved after reviewing 24.09.2024; accepted for publication 15.10.2024; published online 25.03.2025.

Translated by Yulia Dymant

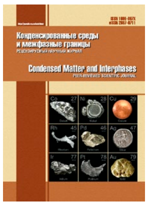

ISSN 1606-867X (Print)
ISSN 2687-0711 (Online)
Condensed Matter and Interphases
Kondensirovannye Sredy i Mezhfaznye Granitsy
https://journals.vsu.ru/kcmf/

Articles of issue 1

Original articles

Research article
https://doi.org/10.17308/kcmf.2025.27/12624

Analysis of the crystalline quality of bulk $In_{0.83}Ga(Al)_{0.17}$ layers formed on metamorphic InAlAs/InP buffer layers with linear and nonlinearcomposition gradients

E. I. Vasilkova[1,2]✉, **E. V. Pirogov**[1], **V. N. Nevedomsky**[3], **O. V. Barantsev**[1], **K. O. Voropaev**[4], **A. A. Vasiliev**[4], **L. Ya. Karachinsky**[1,5], **I. I. Novikov**[1,5], **M. S. Sobolev**[1,2,5]

[1]*Alferov University,*
8/3 Khlopina st., Saint Petersburg 194021, Russian Federation

[2]*St. Petersburg Electrotechnical University "LETI",*
5 Professora Popova ul., Saint Petersburg 197022, Russian Federation

[3]*Ioffe Institute,*
26 Politekhnicheskaya st., Saint Petersburg 194021, Russian Federation

[4]*JSC "OKB-Planeta",*
13a, room 1n Bolshaya Moskovskaya st., Velikiy Novgorod 173004, Russian Federation

[5]*LLC "Connector Optics",*
16 litera B Domostroitelnaya ul., Saint Petersburg 194292, Russian Federation

Abstract

This paper investigates the effectiveness of metamorphic InAlAs buffer layers with linear and root-like dependence of the In mole fraction in the composition for the growth of bulk $In_{0.83}Ga(Al)_{0.17}As$ layers on InP substrates. The analysis of the X-ray diffraction reciprocal space maps showed that in both cases $In_{0.83}Ga(Al)_{0.17}As$ layers were partially strain-free. One of the mechanisms of strain relaxation during the growth of the linearly graded buffer layer is the rotation of the crystal lattice, while the mechanism of strain relaxation during the growth of the convex-graded buffer layer is a 0.82° tilt of the crystal lattice without any rotation. According to the images obtained by transmission electron microscopy, the density of threading dislocations in the upper InGaAs layers grown on the buffer layer with a linear composition gradient is ~ $5 \cdot 10^8$ cm^{-2}.

Keywords: Metamorphic buffer layers, Reciprocal space mapping of X-ray diffraction intensity, Transmission electron microscopy, Molecular beam epitaxy

Funding: The study was funded by the Russian Science Foundation, research project No. 22-79-00146.

For citation: Vasilkova E. I., Pirogov E. V., Nevedomsky V. N., Barantsev O. V., Voropaev K. O., Vasiliev A. A., Karachinsky L. Ya., Novikov I. I., Sobolev M. S. Analysis of the crystalline quality of bulk $In_{0.83}Ga(Al)_{0.17}As$ layers formed on metamorphic InAlAs/InP buffer layers with linear and nonlinearcomposition gradients. *Condensed Matter and Interphases*. 2025;27(1): 86–95. https://doi.org/10.17308/kcmf.2025.27/12624

Для цитирования: Василькова Е. И., Пирогов Е. В., Неведомский В. Н., Баранцев О. В., Воропаев К. О., Васильев А. А., Карачинский Л. Я., Новиков И. И., Соболев М. С. Анализ кристаллического качества объемных слоев $In_{0.83}Ga(Al)_{0.17}As$, сформированных на метаморфных буферных слоях InAlAs/InP с линейным и нелинейным градиентом состава. *Конденсированные среды и межфазные границы*. 2025;27(1): 86–950. https://doi.org/10.17308/kcmf.2025.27/12624

✉ Elena I. Vasilkova, e-mail: elenvasilkov@gmail.com

© Vasilkova E. I., Pirogov E. V., Nevedomsky V. N., Barantsev O. V., Voropaev K. O., Vasiliev A. A., Karachinsky L. Ya., Novikov I. I., Sobolev M. S., 2025

The content is available under Creative Commons Attribution 4.0 License.

1. Introduction

The possibility of growing semiconductor layers on lattice-mismatched substrates has become an important factor contributing to the rapid development of epitaxial technologies. This achievement has allowed observing new electrophysical and optical effects in heterostructures and has considerably expanded the range of components for heterostructural nano- and optoelectronics. One of the traditional epitaxy-based approaches to obtaining semiconductor layers on substrates with a critically large mismatch in the crystal lattice parameters is the metamorphic growth. Metamorphic buffer layers (MBL) create a transition from the substrate lattice constant to the lattice constant required for the growth of the functional layers of the heterostructure. One way to enable such a transition is to gradually change the composition of the buffer layer, which means changing material fluxes during the MBL epitaxial growth. The change of the composition can be either smooth, for example, when a linear dependence is involved, or step-like. Typically, the thickness of the MBLs is a few micrometers. The MBL formation must result in a planar epitaxial surface for the subsequent strain-free growth of the active layers. The MBL technology is currently widely used for the manufacture of transistors with high mobility of electrons, lasers, solar cells, photodiodes, etc. [1–6]. Various designs, thicknesses, and materials of buffer layers are studied and applied depending on the active layers of the heterostructure and its application in devices.

This paper is devoted to the study of possible designs of a metamorphic buffer layer for the growth of $In_{0.83}Ga_{0.17}As$ triple solid solutions on InP substrates. These two materials are used for the manufacture of near-infrared spectral photodetectors, in which the peak wavelength of the photoresponse depends on the indium content in the photo-absorbing layer of InGaAs. The most common option is an absorbing layer of a $In_{0.53}Ga_{0.47}As$ solid solution, which is lattice-matched with InP. The high quality of InP substrates, as well as the excellent characteristics of photodiodes and matrix photodetectors based on $In_{0.53}Ga_{0.47}As$/InP, allowed InGaAs to become the leading material for the manufacture of photodetectors operating in the wavelength of 1–1.7 μm. With an increase in the indium content to the mole fraction of $x = 0.83$, the detection range shifts to a longer wavelength region of 2.2–2.6 μm. Thus, by varying the composition of the absorbing layer, a wider near-infrared region of the spectrum can be covered within the same system of materials. However, due to a large relative mismatch between the lattice parameters of $In_{0.83}Ga_{0.17}As$ and the InP substrate of ~ 2%, the critical thickness for the pseudomorphic growth of the active layer is 1-2 orders of magnitude less than the thickness required for the effective absorption of the emission [7]. Therefore, in order to avoid the appearance of a large number of misfit dislocations in the active region during the growth of the $In_{0.83}Ga_{0.17}As$ layer on the surface of InP, it is necessary to grow transitional metamorphic buffer layers. In this case, MBLs contribute to the pseudomorphic growth of the InGaAs absorbing layers and, consequently, reduce the density of the resulting misfit dislocations, and also stop the penetration of threading dislocations into the active layers of the photodetectors. Dislocations have adverse effects on photodetectors since they contribute to some mechanisms of dark current formation, which leads to a reduced detectivity of devices [8].

2. Experimental

The research involved growing experimental samples containing MBLs of various designs by means of molecular-beam epitaxy using a Riber MBE49 unit (Fig. 1). The samples were InAlAs/InGaAs heterostructures on n^+-InP (100) "epi-ready" doped substrates. The heterostructures included a ~ 0.1 μm thick layer of $In_{0.52}Al_{0.48}As$ which was lattice-matched with the substrate, InAlAs MBLs of ~ 2 μm of various configurations, an active region of $In_{0.83}Ga_{0.17}As$ with a thickness of ~ 1.5 μm, and upper contact layers of $In_{0.83}Al(Ga)_{0.17}As$ with a thickness of ~ 650 nm (Fig. 1). The MBLs were grown at a constant temperature of the substrate, which was 70 °C lower than the growth temperature of the active region (490 °C). The process was concluded with a thermal cycling: the peak temperature rose to 530 °C followed by cooling to 100 °C. The buffer layers were doped with silicon to a level of $1\cdot10^{18}$ cm^{-3} (n^+), while the contact layers were doped with

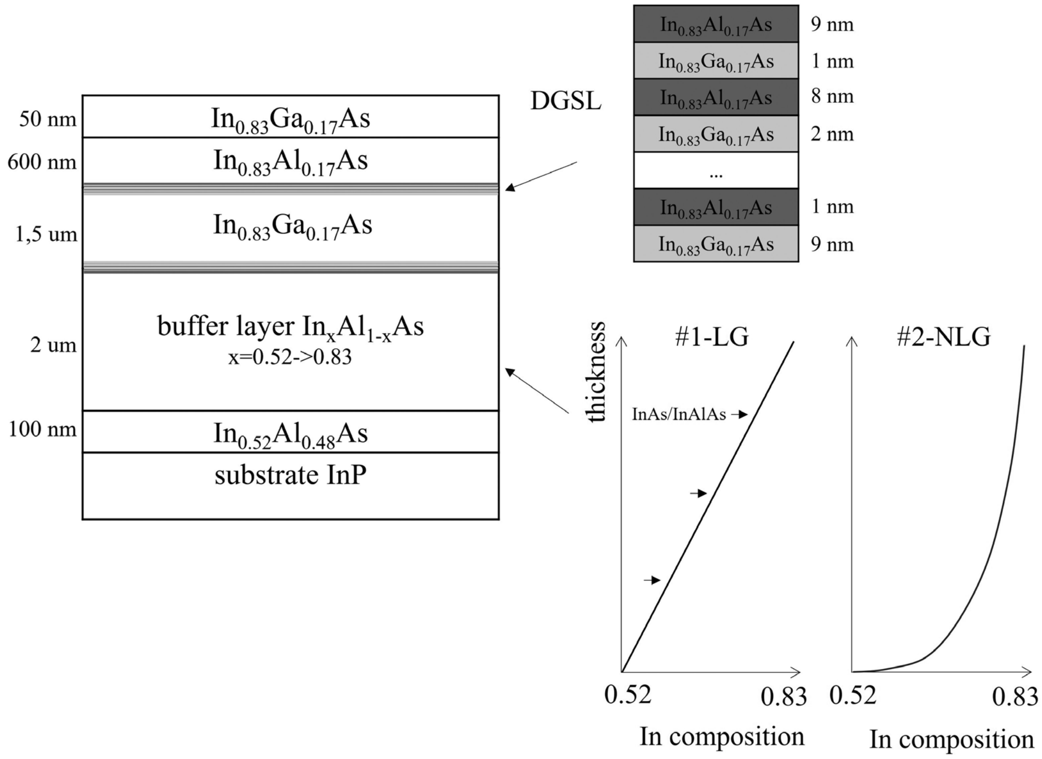

Fig. 1. Schematic image representing the layer composition of metamorphic heterostructures #1-LG и #2-NLG

beryllium, with an impurity concentration of $2\cdot10^{18}$ cm^{-3} (p^+). The active region of InGaAs was also doped with silicon at a low concentration of $2\cdot10^{16}$ cm^{-3}. The type and concentration of the dopant in each layer were selected in order to obtain a diode heterostructure for the subsequent manufacture of PIN photodiode crystals with an absorbing layer of $In_{0.83}Ga_{0.17}As$.

Sample 1-LG contained $In_xAl_{1-x}As$ MBLs with a linear gradient of indium composition from $x = 0.52$ to $x = 0.83$ and with intermediate inserts of three InAs(4 Å)/InAlAs(10 Å) periods every 500 nm. Buffer layers of a similar design showed an advantage over the stepwise changing of the composition and the linear changing of the composition without inserts [9]. The demonstrated benefit of using this type of MBLs was in the lower density of threading dislocations in the functional layers and the existence of a dislocation-free region d_{free} in the buffer layer.

The buffer layer of the 2-NLG sample was the $In_xAl_{1-x}As$ layer whose composition changed following the nonlinear convex gradient which approximated the square root-like dependence. The fraction of InAs in the composition also varied from 0.52 to 0.83. The main difference between the 1-LG and 2-NLG samples was that when the convex gradient of the composition was applied, the MBL crystal lattice parameter grew faster in its lower region bordering the substrate, and, conversely, more smoothly when approaching the active layers. Therefore, it can be assumed that dislocations formed more actively in the lower part of the MBLs, which was most distant from the functional layers of the heterostructure. Previous studies used metamorphic InAlAs layers on GaAs substrates to demonstrate the advantages of such a design as compared to a linear profile in terms of more effective elastic strain relaxation [10]. Also, using the example of the InAlAs/GaAs system of materials, it was experimentally confirmed that the root-like dependence of the indium composition in MBLs resulted in a lower density of dislocations and the formation of a thicker d_{free} region [11].

To reduce the conduction band discontinuity between InGaAs and InAlAs and the dislocation density, the so-called digital-graded superlattices (DGSL) were introduced into the structure of the heterostructures from above and below the absorbing layer, which consisted of 9-period $In_{0.83}Ga_{0.17}As/In_{0.83}Al_{0.17}As$ superlattices with a total thickness of about 90 nm [12]. The well-to-barrier ratio in the DGSL period ranged from 1:9 to 9:1 in the case of the lower superlattice (MBL-active region heterointerface) and was mirrored in the case of the upper superlattice (active region-contact layer heterointerface). These superlattices created a stepped barrier for charge carriers at the point of conduction band discontinuity in the heterostructure. What is more, the additional heterointerfaces that DGSLs created were expected to facilitate a smoother transition from the lattice constant of InGaAs to InAlAs if there was any residual strain in InGaAs. Therefore, DGSL regions were inserted in both samples before the growth of the $In_{0.83}Ga_{0.17}As$ absorbing layer and after its complete formation.

The main experiments aimed at studying the crystalline properties of the samples of metamorphic heterostructures were preceded by their electrochemical capacitance–voltage (ECV) measurements. A comparison of the profiles of the distribution of the charge carriers concentration in the 1-LG and 2-NLG samples along the depth of the structure is shown in Fig. 2. The profile of the 1-LG sample was smoother and more comparable to the structure of the heterostructure in terms of layer thickness. It also did not have spikes and abrupt changes in concentration, unlike the 2-NLG sample. This may be evidence of a higher defectiveness of the 2-NLG sample with the root profile of the buffer layer composition. Based on the obtained results of the ECV measurements, the 1-LG sample with a linear MBL was selected as a reference for the study by the destructive transmission electron microscopy (TEM). In addition, X-ray reflection spectra were measured for both samples, and reciprocal space maps of X-ray diffraction intensity were constructed and analyzed.

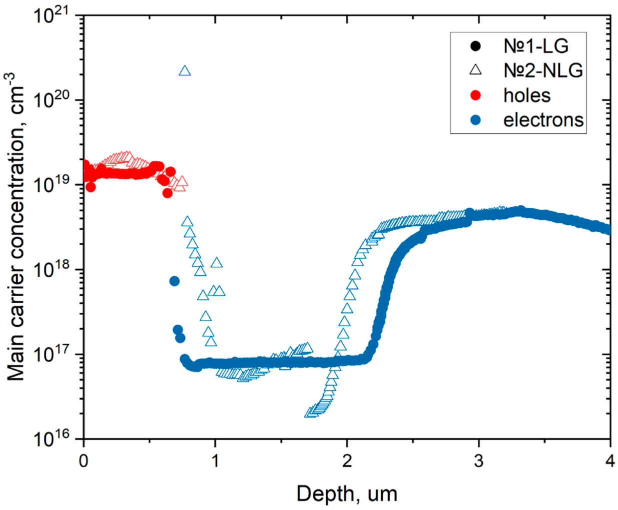

Fig. 2. Main carrier concentration profiles, obtained by electrochemical capacitance-voltage profiling

3. Results and discussion

3.1. Transmission electron microscopy

The 1-LG sample was examined by SEM in the cross-section geometry (110) on a JEM2100F (Jeol) electron microscope at an accelerating voltage of 200 kV. A standard method was used to prepare the sample, which involved thinning by precision grinding and spraying with argon ions during the final stage prior to perforation.

The obtained TEM image (Fig. 3) allowed identifying the regions of the MBLs, the InGaAs absorbing layer, and the InAl(Ga)As contact layers. In the image, the InP substrate is at the bottom and is separated from the metamorphic heterostructure by a bright white band. In the MBL, there was a large number of misfit dislocations in the form of horizontal dark bands and threading dislocations in the form of inclined dark lines. The dislocations were evenly distributed over the thickness of the MBL, and a rough estimate of the density of the extended defects in the buffer layer was ~ $1 \cdot 10^{11}$ cm^{-2}. Fig. 3

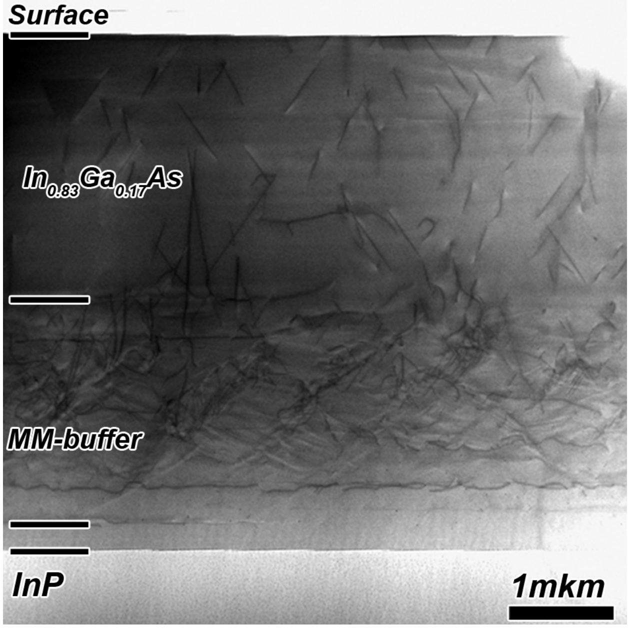

Fig. 3. STEM image of sample #1-LG

shows that some dislocations were directly under the heterointerfaces of the InAs/InAlAs inserts, especially during the initial stages of the MBL growth. Also, threading dislocations were bending on various heterointerfaces, including in the DGSL region, however, their complete bending and annihilation occurred less often.

Earlier studies of test MBL heterostructures with a linear composition gradient revealed the existence of a dislocation-free region d_{free} [9]. Based on current images, it was impossible to judge whether the d_{free} region was present. What is more, the density of defects in the sample was much higher than the density of defects in the test MBL structure. Thus, according to the TEM images in the cross-sectional geometry, the density of the threading dislocations revealed in the functional layers of the $In_{0.83}Al_{0.17}As$ and $In_{0.83}Ga_{0.17}As$ heterostructures was ~ $5 \cdot 10^8$ cm^{-2}, while in the test structure, the density of dislocations in the $In_{0.83}Ga_{0.17}As$ layer with a thickness of 500 nm was below the detection limit of the method, i.e. < $1 \cdot 10^6$ cm^{-2} [9]. Perhaps this was due to the absence of the inverse step in the InAlAs composition gradient, which was introduced into the MBL design of the test structure. The absence of the inverse step could also affect the density of threading dislocations in the InGaAs absorbing layer.

3.2. X-ray diffractometry and reciprocal space mapping of X-ray diffraction intensity

Information about the presence of elastic strain, misfit dislocations, and crystal lattice disorientation can be obtained from the X-ray diffraction reciprocal space mapping [13]. The X-ray diffraction reciprocal space map is a projection of the three-dimensional intensity distribution of the X-ray reflection intensity from the sample on the orthogonal axes of the reciprocal space qX <110> and qZ [001] which are parallel to the surfaces of the heterostructure and orthogonal to the surface of the heterostructure, respectively. The reciprocal space map is a set of contours of equal intensity, the greatest contribution to which is made by diffraction reflections from the selected family of crystalline planes. The X-ray scattering was recorded in the angular coordinates ω-2θ, which were then converted into the reduced coordinates of the reciprocal space qX and qZ. X-ray diffraction spectra were recorded on a DRON-8 X-ray diffractometer (Burevestnik, Russia) with a Bartels monochromator and the radiation at the X-ray tube of Cu$K\alpha 1$ = 0.15406 nm. The maps were converted and processed with the accompanying software package Reciprocal Space Mapping by *Burevestnik*.

Reciprocal space maps of X-ray diffraction intensity for reflections (224) for the samples were constructed and analyzed (Fig. 4). The reciprocal space mapping of X-ray diffraction intensity in the case of asymmetric reflection, for example, from a set of planes (224), allowed making judgements about the residual strain in the epitaxial layers. In Figures 4a and 4b, broad maxima of high intensity characterize diffraction on the functional layers of $In_{0.83}Al_{0.17}As/In_{0.83}Ga_{0.17}As$ of the 1-LG and 2-NLG samples, respectively. Lines drawn in the images in Fig. 4 characterize an entirely strain-free (solid line) and entirely pseudomorphic (dashed line) state of the crystal in relation to the substrate [14]. The line of the entire stain relaxation for reflection (224) always passes through the peak of the substrate, therefore, the position of the InGaAlAs maximum relative to this line can be used to conclude about the degree of strain relaxation in this layer. In both studied samples, the lines of strain relaxation passed near the reflection from the InGaAlAs layers, however, they did not cross its maximum. Thus, the active layers in both 1-LG sample and 2-NLG sample were partially strain-free.

The measurements of symmetric (004) reflections of the samples allowed making conclusions about the imperfection of the crystal lattice of the grown layers since the broadening of the intensity contours along the qX direction indicated dislocations or a mosaic structure, while the broadening along the qZ direction meant there was a fluctuation of the perpendicular component of the lattice parameter [15]. Let us assume that direction [110] of the X-ray beam incidence along the base cut of the substrate is an azimuthal angle of 0°, while direction [$1\underline{1}0$], which is perpendicular to the base cut is an azimuth of 90°. X-ray scattering patterns from a set of reflecting planes (004) of the 1-LG and 2-NLG samples in the reciprocal space are shown in Fig. 5. The narrower and more intense

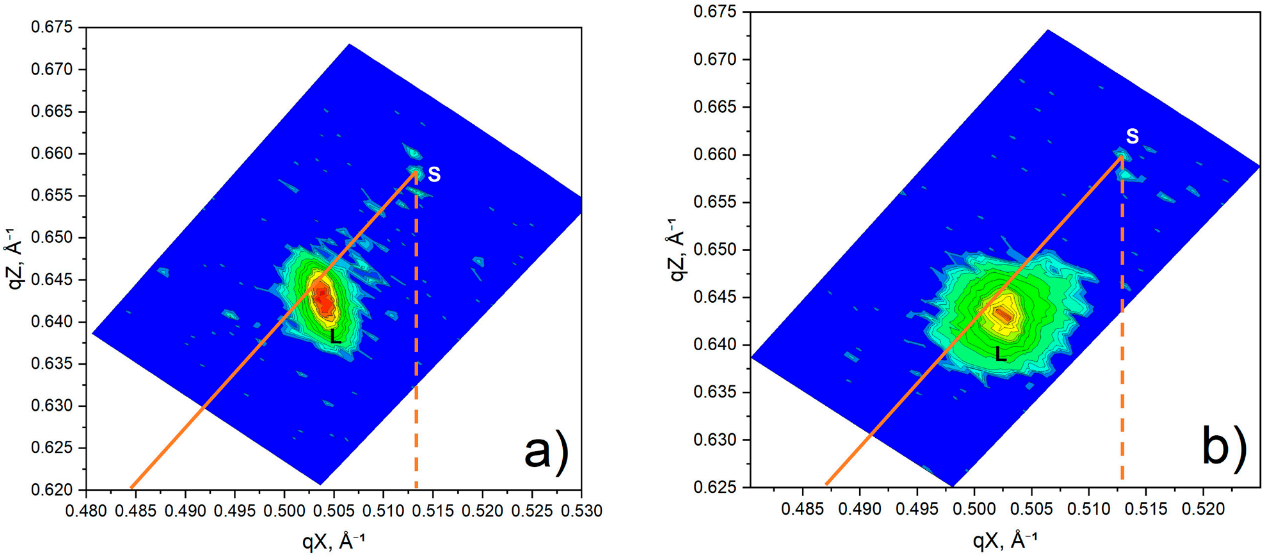

Fig. 4. Reciprocal space maps of asymmetric (224) reflection: a) sample #1-LG, б) sample #2-NLG. Labels S and L stand for reflection peaks from InP substrate and $In_{0.83}Ga(Al)_{0.17}As$ active layers. Orange lines represent fully relaxed (solid) and pseudomorphic (dashed) states

maximum at the top of all images corresponds to the InP substrate and is comparable to the angular coordinate $2\theta = 63.34°$.

Let us consider Fig. 5a for a symmetrical reflection of the 1-LG sample with an azimuthal angle of 0° corresponding to the *qX* direction [110]. A continuous green region of medium intensity, elongated along the *qZ* axis, is characteristic of MBLs with a smooth composition gradient. The experimental maximum of the functional layers of $In_{0.83}Al_{0.17}As/In_{0.83}Ga_{0.17}As$ (individual maxima of each layer are difficult to distinguish due to very close values of the lattice constant), located lower along the *qZ* axis, is shifted along the *qX* axis relative to the maximum of the substrate, and, as compared to it, has a more pronounced ellipticity. The coordinate of the $In_{0.83}Ga(Al)_{0.17}As$ peak along the *qZ* axis corresponds to an angle of $2\theta = 61.79°$. This peak, as compared to the peak of the substrate, is much more stretched along both axes and its width in the *qX* direction exceeds many times the spread along *qZ*. Thus, we can assume that active layers of this sample have more local strain-free regions than regions with an elastically deformed lattice [15].

In the scattering pattern of the 2-NLG sample with similar conditions depicted in Fig. 5c, the maxima of diffraction intensity on the substrate and on the active layer are at the same positions along the *qZ* axis. However, in the case of the 2-NLG sample, the reciprocal space mapping did not reveal any significant reflection continuously stretched from the gradient buffer layer along the *qZ* axis. In addition, unlike the 1-LG sample, the maximum of the InGaAs layer was on the $qX = 0$ line. What is more, it was elongated mainly along the *qZ* axis and was characterized by a much less expressed diffusion scattering along the *qX* axis than in Fig. 5a. As we noted above, the broadening of the peak along *qZ* may be due to a fluctuation of the lattice constant in a direction perpendicular to the scanning planes. Thus, a significant blurring of the maximum along the vertical axis may indicate the existence of local deformed regions of the crystal lattice and an inhomogeneous strain distribution over the crystal.

The half-width peaks of the intensity of the reflected X-ray emission along the ω axis in the angular coordinates of direct space ω-2θ characterizes the defectiveness of the structure, which in the metamorphic heterostructure is mainly contributed by misfit dislocations of the screw type. The assessment of the dependence of the half-width intensity peaks relative to the ω axis on the normal lattice parameter $c = 2\lambda/sin(\theta)$ [16] and the TEM images allowed characterizing the distribution of defects in the 1-LG sample. The results showed that the defectiveness of the linear MBL first increased with a thickness, was maximum in the middle and upper parts

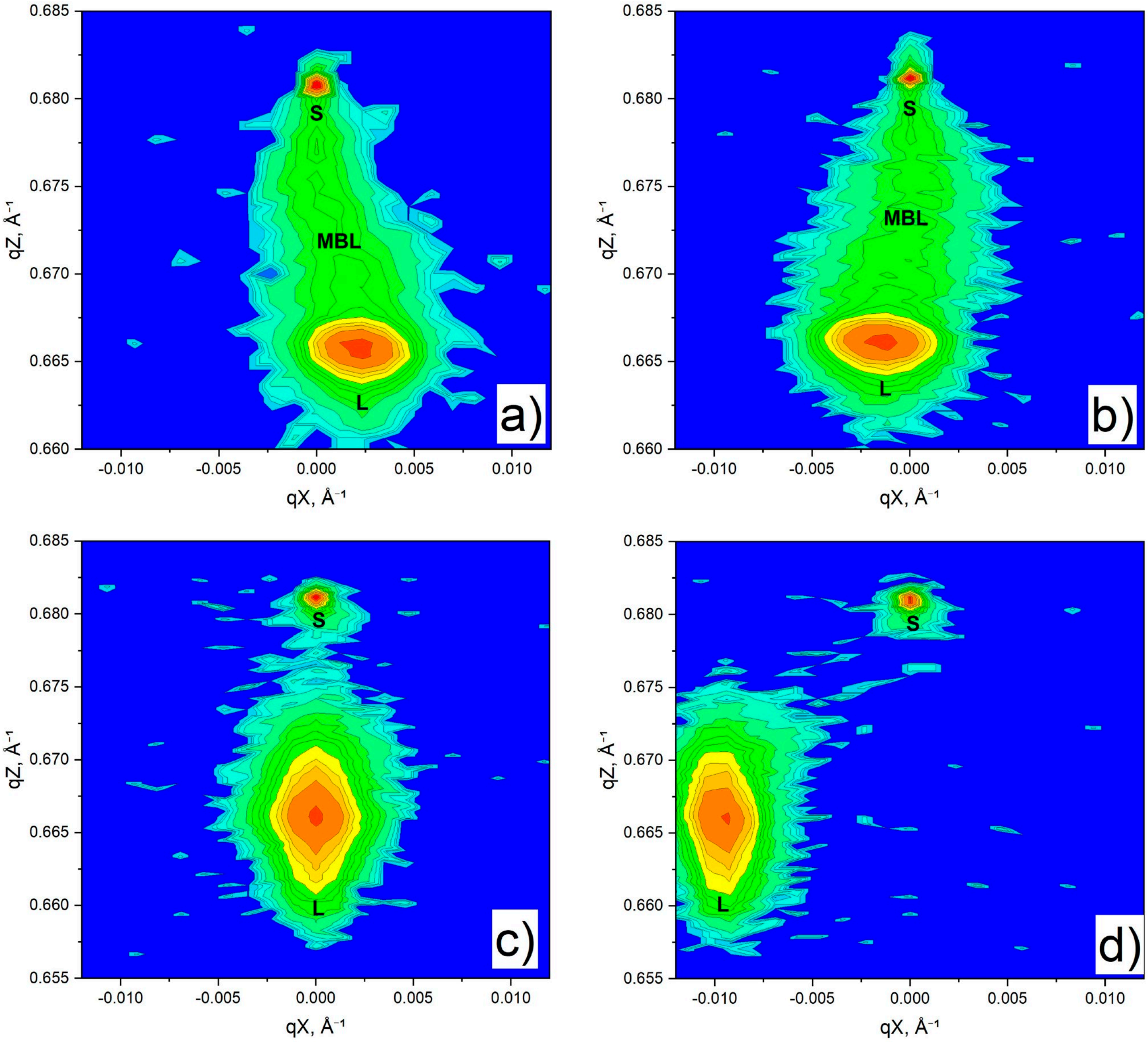

Fig. 5. Reciprocal space maps of symmetric (004) reflection of sample #1-LG (top) for azimuthal angles 0° (a) и 90° (b) and sample #2-NLG (bottom) for 0° (c) and 90° (d). Labels S, L and MBL stand for reflection peaks from InP substrate, $In_{0.83}Ga(Al)_{0.17}As$ active layers and $In_xAl_{1-x}As$ metamorphic buffer layer

of the buffer layer, and then decreased slightly just before the formation of the DGSL and the absorbing layer.

It should be noted that when rotating the 1-LG sample by an azimuthal angle of 90° (Fig. 5b), the maximum lateral coordinate of $In_{0.83}Ga(Al)_{0.17}As$ changed its sign relative to the $qX = 0$ axis, while the position of the peak along the qZ axis remained unchanged. However, similar to the case shown in Fig. 5a, the intensity spot from the linear MBL shifted uniformly towards the positive or negative qX, respectively. Fig. 5d shows images for the 2-NLG sample with an azimuthal angle of 90°. When rotating the sample with the root MBL by 90°, there was also a discrepancy between the maximum coordinates of the absorbing layer, however, in this case there was an abrupt change in the coordinate relative to $qX = 0$.

The mismatch between the maximum coordinates of the active layers and the substrate in the qX direction for the studied case of symmetrical reflection indicated the disorientation of the crystal lattice of the active layers relative to plane (001) [15]. The angle of the epitaxial layer disorientation relative to the substrate was characterized by inclination, rotation, or torsion. In lattice-mismatched heterostructures on substrates with orientation (001), disorientation could occur due to uneven distribution of dislocations over the surface relative to directions [110] and [$1\underline{1}0$] [17]. This resulted in anisotropy of residual strain along these directions and could affect the angle of disorientation.

The reciprocal space mapping in the geometry of symmetrical reflections allowed estimating the inclination and rotation angles of the crystal lattice in the active layer relative to the plane of the substrate (001). For calculations, we used the relations given in [18, 19]:

$$\mathrm{tg}(\alpha_{0^\circ,90^\circ}) = \frac{\left|\Delta qX^{004}\right|_{0^\circ,90^\circ}}{4/a_{sub} - \left|\Delta qZ^{004}\right|_{0^\circ,90^\circ}}$$

$$\mathrm{tg}(\varphi) = \alpha_{0^\circ} / \alpha_{90^\circ},$$

where α_{sub} = 5.8687 Å is the lattice constant of the substrate, qX^{004} is the difference in qX coordinates of the maxima of the layer and the substrate during symmetrical scanning (004), qZ^{004} is the difference in qZ coordinates of the maxima of the layer and the substrate during symmetrical scanning (004), α_{0° and α_{90° are the inclination angles of the crystal lattice at azimuthal angles of 0° and 90°, and φ is the azimuth of the zero inclination of the layer.

From Figures 5a and 5b, according to the given formulas, we obtained the inclination angles: $\alpha_{0^\circ} = 0.19^\circ$, $\alpha_{90^\circ} = 0.12^\circ$, and $\varphi = 57.7^\circ$. By performing similar calculations and by using the data presented in Fig. 5c and 5d for the 2-NLG sample, we obtained $\alpha_{0^\circ} = 0^\circ$, $\alpha_{90^\circ} = 0.82^\circ$, and $\varphi = 0^\circ$. Therefore, in the case of root-like MBLs, the disorientation of the crystal lattice of the InGaAs layer was mainly affected by the inclination of the layer relative to plane (001). What is more, there was no torsion of the lattice, which can also be indirectly confirmed by scanning at coordinates ω–φ. According to [17], large values of angles α correlate with low efficiency of elastic strain relaxation in the structure through the formation of dislocations. Therefore, the disorientation of the crystal lattice is a secondary mechanism for relieving residual strain. In the case of the 2-NLG sample, this may mean that during the early stages of the buffer layer growth, the strain relaxation mechanism was mainly due to the formation of dislocations, while further it was a tilt of the lattice that was responsible for the release of excessive strain.

4. Conclusions

In our study, for the growth of active layers of $In_{0.83}Ga(Al)_{0.17}As$ on InP substrates, we proposed two alternative designs of the metamorphic buffer layer: one following a linear law of the composition variation and the other following a nonlinear law, which in the studied case had a square root-like dependence. To determine the effectiveness of these metamorphic buffer layers, we used transmission electron microscopy and the reciprocal space mapping of X-ray diffraction intensity to study the crystalline quality of the bulk $In_{0.83}Ga(Al)_{0.17}As$ layers grown on the buffer layers. The reciprocal space mapping for asymmetric reflections from a set of planes (224) showed that the active layers were partially strain-free in heterostructures with both linear and nonlinear buffer layer. They also revealed the formation of misfit dislocations. The reciprocal space mapping in the geometry of symmetrical reflections (004) allowed establishing that in both samples elastic strain was relieved through the disorientation of the crystal lattice relative to the plane of the substrate. The density of threading dislocations in the active layers of $In_{0.83}Ga(Al)_{0.17}As$ in the heterostructure with a linear metamorphic buffer layer calculated from the images of transmission electron microscopy was ~ $5 \cdot 10^8$ cm^{-2}. Presumably, in order to reduce it and to obtain a dislocation-free region in the heterostructure, the growth of the linear metamorphic buffer layer must be completed with an inverse step with an increase in the mole fraction of indium in the composition of the buffer layer relative to the composition of the active layers.

Contribution of the authors

The authors contributed equally to this article.

Conflict of interests

The authors declare that they have no known competing financial interests or personal relationships that could have influenced the work reported in this paper.

References

1. Galiev G. B., Vasil’evskii I. S., Pushkarev S. S., ... Dwir E. I. Suvorova metamorphic InAlAs/InGaAs/InAlAs/GaAs HEMT heterostructures containing strained superlattices and inverse steps in the metamorphic buffer. *Journal of Crystal Growth*. 2013;366: 55–60. https://doi.org/10.1016/j.jcrysgro.2012.12.017

2. Kettler T., Karachinsky L. Ya., Fiol G., ... Ledentsov N. N. Degradation-robust single mode continuous wave operation of 1.46 μm metamorphic quantum dot lasers on GaAs substrate. *Applied Physics Letters*. 2006;89(4): 041113. https://doi.org/10.1063/1.2236291

3. Egorov A. Yu., Karachinsky L. Ya., Novikov I. I., Babichev A. V., Nevedomskiy V. N., Bugrov V. E. Optical properties of metamorphic GaAs/InAlGaAs/InGaAs heterostructures with InAs/InGaAs quantum wells, emitting light in the 1250–1400 nm spectral range. *Semiconductors*. 2016;50(5): 612–615. https://doi.org/10.1134/S1063782616050079

4. Egorov A. Yu., Karachinsky L. Ya., Novikov I. I., Babichev A. V., Berezovskaya T. N., Nevedomskiy V. N. Metamorphic distributed Bragg reflectors for the 1440–1600 nm spectral range: epitaxy, formation, and regrowth of mesa structures. *Semiconductors*. 2015;49(10): 1388–1392. https://doi.org/10.1134/S1063782615100073

5. Garcia I., France R. M., Geisz J. F., McMahon W. E., Steiner M. A., Johnston S., Friedman D. J. Metamorphic III–V solar cells: recent progress and potential. *IEEE Journal of Photovoltaics*. 2015;6(1): 366–373. https://doi.org/10.1109/JPHOTOV.2015.2501722

6. Liu Y., Ma Y., Li X., ... Gong H. High temperature behaviors of 1–2.5 μm extended wavelength $In_{0.83}Ga_{0.17}As$ photodetectors on InP substrate. *IEEE Journal of Quantum Electronics*. 2021;57(4): 1–7. https://doi.org/10.1109/JQE.2021.3087324

7. Gendry M., Drouot V., Santinelli C., Hollinger G. Critical thicknesses of highly strained InGaAs layers grown on InP by molecular beam epitaxy. *Applied Physics Letters*. 1992;60(18): 2249–2251. https://doi.org/10.1063/1.107045

8. Ji X., Liu B., Tang H., ... Yan F. 2.6 μm MBE grown InGaAs detectors with dark current of SRH and TAT. *AIP Advances*, 2014;4(8): 087135. https://doi.org/10.*1063*/1.4894142

9. Vasilkova E. I., Pirogov E. V., Sobolev M. S., Ubiyvovk E. V., Mizerov A. M., Seredin P. V. Molecular beam epitaxy of metamorphic buffer for InGaAs/InP photodetectors with high photosensitivity in the range of 2.2–2.6 um. *Condensed Matter and Interphases*. 2023;25(1): 20–26. https://doi.org/10.17308/kcmf.2023.25/10972

10. Pobat D. B., Solov’ev V. A., Chernov M. Yu., Ivanov S. V. Distribution of misfit dislocations and elastic mechanical stresses in metamorphic buffer InAlAs layers of various constructions. *Physics of the Solid State*. 2021;63(1): 84–89. https://doi.org/10.1134/s1063783421010170

11. Solov’ev V. A., Chernov M. Yu., Sitnikova A. A., Brunkov P. N., Meltser B. Ya., Ivanov S. V. Optimization of the structural properties and surface morphology of a convex-graded $In_xAl_{1-x}As$ ($x = 0.05–0.83$) metamorphic buffer layer grown via MBE on GaAs (001). *Semiconductors*. 2018;52(1): 120–125. https://doi.org/10.1134/s1063782618010232

12. Chen X., Gu Y., Zhang Y. Epitaxy and device properties of InGaAs photodetectors with relatively high lattice mismatch. *Epitaxy*. 2018: 203. https://doi.org/10.5772/intechopen.70259

13. Fewster P. F. Reciprocal space mapping. *Critical Reviews in Solid State and Material Sciences*. 1997;22(2): 69–110. https://doi.org/10.1080/10408439708241259

14. Bellani V., Bocchi C., Ciabattoni T., ... Trevisi G. Residual strain measurements in InGaAs metamorphic buffer layers on GaAs. *The European Physical Journal B*. 2007;56: 217–222. https://doi.org/10.1140/epjb/e2007-00105-8

15. Fewster P. F. X-ray diffraction from low-dimensional structures. *Semiconductor Science and Technology*. 1993;8(11): 1915. https://doi.org/10.1088/0268-1242/8/11/001

16. Vasil’evskii I. S., Pushkarev S. S., Grekhov M. M., Vinichenko A. N., Lavrukhin D. V., Kolentsova O. S. Features of the diagnostics of metamorphic InAlAs/InGaAs/InAlAs nanoheterostructures by high-resolution X-ray diffraction in the ω-scanning mode. *Semiconductors*. 2016;50(4): 559–565. https://doi.org/10.1134/s1063782616040242

17. Lee D., Park M. S., Tang Z., Luo H., Beresford R., Wie C. R. Characterization of metamorphic $In_xGa_{1-x}As$/GaAs buffer layers using reciprocal space mapping. *Journal of Applied Physics*. 2007;101(6):063523, https://doi.org/10.1063/1.2711815

18. Aleshin A. N., Bugaev A. S., Ermakova M. A., Ruban O. A. Investigation of MHEMT heterostructure with In0.4Ga0.6As channel, grown by MBE on GaAs substrate, using reciprocal space mapping. *Semiconductors*. 2015;49(8):1065. Available at: https://journals.ioffe.ru/articles/viewPDF/42087

19. Chauveau J.-M., Androussi Y., Lefebvre A., Persio J. Di, Cordier Y. Indium content measurements in metamorphic high electron mobility transistor structures by combination of X-ray reciprocal space mapping and transmission electron microscopy. *Journal of Applied Physics*. 2003;93(7): 4219–4225. https://doi.org/10.1063/1.1544074

Information about the authors

Elena I. Vasilkova, postgraduate student, Engineer, Alferov University (Saint Petersburg, Russian Federation).
https://orcid.org/0000-0002-0349-7134
elenvasilkov@gmail.com

Evgeny V. Pirogov, Researcher, Alferov University (Saint Petersburg, Russian Federation).
https://orcid.org/0000-0001-7186-3768
zzzavr@gmail.com

Vladimir N. Nevedomskiy, Senior Researcher, Ioffe Physical-Technical Institute of the Russian Academy of Sciences (Saint Petersburg, Russian Federation).
https://orcid.org/0000-0002-7661-9155
vladimir.nevedomskiy@connector-optics.com

Oleg V. Barantsev, student, Lab Assistant, Alferov University (Saint Petersburg, Russian Federation).
https://orcid.org/0009-0001-6873-8488
ovbarantsev@gmail.com

Kirill O. Voropaev, Head of the Group, JSC “OKB-Planeta” (Velikiy Novgorod, Russian Federation).
https://orcid.org/0000-0002-6159-8902
kirill.voropaev@novsu.ru

Andrey A. Vasil’ev, Engineer-Technologist, JSC “OKB-Planeta” (Velikiy Novgorod, Russian Federation).
https://orcid.org/0009-0009-2615-6795
Wasiliew.andre@yandex.ru

Leonid Ya. Karachinsky, Dr. Sci. (Tech.), Chief Researcher, Alferov University and Leading Researcher, ITMO University (Saint Petersburg, Russian Federation).
https://orcid.org/0000-0002-5634-8183
karach@switch.ioffe.ru

Innokenty I. Novikov, Cand. Sci. (Phys.–Math.), Senior Researcher, Alferov University and Senior Researcher, ITMO University (Saint Petersburg, Russian Federation).
https://orcid.org/0000-0003-1983-0242
novikov@switch.ioffe.ru

Maxim S. Sobolev, Cand. Sci. (Phys.–Math.), Head of the Laboratory, Alferov University (Saint Petersburg, Russian Federation).
https://orcid.org/0000-0001-8629-2064
sobolevsms@gmail.com

Received 15.04.2024; approved after reviewing 30.04.2024; accepted for publication 06.05.2024; published online 25.03.2025.

Translation by Irina Charychanskaya

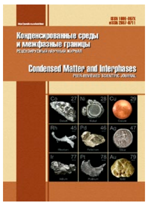

ISSN 1606-867X (Print)
ISSN 2687-0711 (Online)
Condensed Matter and Interphases
Kondensirovannye Sredy i Mezhfaznye Granitsy
https://journals.vsu.ru/kcmf/

Original articles

Research article
https://doi.org/10.17308/kcmf.2025.27/12486

Study of hyperfine interactions in spinel cobalt ferrite $CoFe_2O_4$ doped with Hf, Lu, and Yb using Mössbauer spectroscopy and perturbed γ-γ angular correlation

V. M. Vakhtel[4]✉, A. I. Velichkov[1,2], D. V. Karaivanov[1,2], M. M. Milanova[3], Yu. G. Segal[4], N. T. Temerbulatova[1,5], D. V. Filosofov[1], M. P. Tsvetkov[3]

[1]*Joint Institute for Nuclear Research,*
6 Joliot-Curie st., Dubna 141980, Moscow Region, Russian Federation

[2]*Institute for Nuclear Research and Nuclear Energy of the Bulgarian Academy of Sciences,*
72 72 Blvd. "Tsarigradsko Shose", Sofia 1784, Bulgaria

[3]*Sofia University "St. Kliment Ohridski",*
15 Tzar Osvoboditel Blvd., Sofia 1504, Bulgaria

[4]*Voronezh State University,*
1 Universitetskaya pl., Voronezh 394018, Russian Federation

[5]*Institute of Nuclear Physics,*
1 Ibragimov st., Almaty 050032, the Republic of Kazakhstan

Abstract

We studied hyperfine interactions (HFI) in spinel cobalt ferrite (ferrospinel) $CoFe_2O_4$ doped with Lu, Yb, and Hf (1 wt. %) by Mössbauer spectroscopy (MS) on ^{57}Fe nuclei. The interactions indicate the presence ($CoFe_2O_4$:Lu – 11 %, $CoFe_2O_4$:Yb – 23.4%) and the absence ($CoFe_2O_4$:Hf) of additional phases. The study revealed a significant change in the HFI parameters on ^{57}Fe nuclei in the octahedral sites in ferrospinels doped with Hf, Lu, and Yb. However, the relative influence of the impurity on ^{57}Fe nuclei in the tetrahedral sites was insignificant.

The parameters of hyperfine fields on ^{172}Yb nuclei in cobalt ferrite were obtained by the method of perturbed γ-γ angular correlations (PAC). The ^{172}Yb ions were introduced into the sample using two methods: by adding ^{172}Hf and ^{172}Lu isotopes. A significant difference in the HFI parameters for these two cases was revealed. The local environment of ^{172}Yb ions appears to be different in the two variants of isotope introduction into the sample (Hf or Lu). The difference in the HFI parameters persisted in the temperature range of 300 - 1000 K.

It was determined that the different effects of Hf and Lu on the parameters (electric field gradient, magnetic field, and isomer shift) of the HFI in the sample are revealed by both MS and PAC methods, irrespective of the amount of the dopant. According to the MS data, Hf and Lu do not lead to significant changes in the HFI parameters in the tetrahedral sites ("Sextet 1"), but have a significantly different effect on the same parameters in the octahedral sites ("Sextet 2"). A similar pattern was observed using the PAC method: replacing Hf with Lu did not reveal any changes in the HFI parameters in one of the sites (the octahedral site), but indicated a significant change in the other site.

Keywords: Mössbauer spectroscopy, Perturbed correlations, Spinels, Oxides, Ferrites

Acknowledgements: The authors are grateful to the Centre for Collective Use of Scientific Equipment of Voronezh State University for research using X-ray powder diffraction.

✉ Viktor M. Vakhtel, e-mail: vakhtel@phys.vsu.ru

© Vakhtel V. M., Velichkov A. I., Karaivanov D. V., Milanova M. M., Segal Yu. G., Temburlatova N. T., Filosofov D. V., Tsvetkov M. P., 2025

The content is available under Creative Commons Attribution 4.0 License.

For citation: Vakhtel V. M., Velichkov A. I., Karaivanov D. V., Milanova M. M., Segal Yu. G., Temburlatova N. T., Filosofov D. V., Tsvetkov M. P. Study of hyperfine interactions in spinel cobalt ferrite $CoFe_2O_4$ doped with Hf, Lu, and Yb using Mössbauer spectroscopy and perturbed γ-γ angular correlation. *Condensed Matter and Interphases*. 2025;27(1): 96–103. https://doi.org/10.17308/kcmf.2025.27/12486

Для цитирования: Вахтель В. М., Величков А. И., Караиванов Д. В., Миланова М. М., Сегал Ю. Г., Тембурлатова Н. Т., Философов Д. В., Цветков М. П. Исследования сверхтонких взаимодействий в ферритах кобальта со структурой шпинели $CoFe_2O_4$, легированных Hf, Lu и Yb с использованием методов мессбауэровской спектроскопии и возмущенных угловых γγ-корреляций. *Конденсированные среды и межфазные границы*. 2025;27(1): 96–103. https://doi.org/10.17308/kcmf.2025.27/12486

1. Introduction

Ferrites are mixed metal oxides with the general formula MFe_2O_4, where the metal (M) may be represented by Fe, Ni, Co, Zn, etc. They have a number of properties (high resistivity, high magnetic permeability, and high penetration depth of microwave field) that contribute to their application in various fields [1–9]. Cobalt ferrite ($CoFe_2O_4$) is one of the most widely used magnetic materials. In modern technologies, ferrites are often doped, because even small (≈ 1 %) amounts of additives significantly change their properties. Currently, rare earth elements (RE) are considered as dopants [6–15]. In the case of modification with RE^{3+} ions, taking into account their typical oxidation state of +3, we can expect them to replace Fe^{3+} [11–15]. On the other hand, considering that the ionic radius of the RE is larger than the ionic radius of Fe^{3+}, such substitution is difficult, and an additional phase may be formed [14]. Ferromagnetic spinel semiconductors $CdCr_2Se_4$ and $CdCr_2S_4$ were studied by the PAC method at the ISOLDE on-line separator (CERN) [16]. But in that work, ferrites were not studied, and besides the introduced isotopes (^{111}In, ^{111m}Cd, ^{111}Ag, ^{117}Cd, and ^{199m}Hg) were not rare earth elements. In work [17], non-rare earth impurities of $CoFe_2O_4$ were studied by Mössbauer spectroscopy.

The aim of this work was to study the hyperfine interactions in spinel cobalt ferrite (ferrospinel) $CoFe_2O_4$ doped with Lu, Yb, and Hf by Mössbauer spectroscopy (MS) and perturbed angular correlation (PAC) methods.

2. Experimental

2.1. Synthesis of samples

For the study, samples of cobalt ferrite $CoFe_2O_4$ were obtained by adding dopants during the synthesis. In the first case (the MS method), natural Yb, Lu, and Hf were added in the amount of 1 wt. % of the total weight of the sample. For the PAC measurements, $CoFe_2O_4$ was produced with the addition of radionuclides during the synthesis.

Ferrites were synthesized from mixed aqueous solutions of Fe and Co salts with a molar ratio of 2:1 by precipitation with 1 M NaOH solution to the pH of 11–12. To modify the samples with stable Yb, Lu, and Hf or radionuclides, solutions of Yb, Lu, or Hf nitrates or solutions of ^{172}Lu or ^{172}Hf radionuclides were added to the initial aqueous solutions of Fe(III) and M(II) (M = Co) salts. The procedure was described in detail in [13, 14, 15]. The preparation of radionuclides was described in [18]. The final washing of the precipitate was carried out with a 50/50 (v/v) water/acetone mixture. The washed samples were dried at 80 °C overnight and then heat treated at 750 °C in air for 5 hours. The obtained mixed metal oxides based on $CoFe_2O_4$ were labelled as CFO.

2.2. Mössbauer spectroscopy

The Mössbauer spectra were measured on a MS-1104Em spectrometer [20] in the sample mass range from 1 to 5 mg. The spectrometer was operated in transmission geometry at room temperature. The ^{57}Co radiation source was modulated in a mode in which the dependence of the Doppler velocity over time has a triangular shape. A ^{57}Co source in a Cr matrix with an activity of 30 mCi produced by Ritverc JSC was used as a resonant source of γ-quanta. A scintillation detector based on a NaI scintillator was used. It was calibrated against the metallic α-Fe. The speed was 12.11 mm/s, the triangular velocity profile of the absorber was used to record the Mössbauer spectra at forward and reverse movement. The Mössbauer spectra were approximated by Lorentzian lines according to the χ^2 criterion.

2.3. Perturbed γ-γ angular correlation method

The PAC method used in studies [20, 21, 22] is based on the introduction of a radioactive isotope into the sample, the decay of which is accompanied by the emission of cascade γ-rays. The advantage of the PAC method is the very low concentration of probe nuclei, so it does not change the properties of the studied sample. We used the isotopes ^{172}Lu(^{172}Yb) and ^{172}Hf(^{172}Lu(^{172}Yb)) for the PAC measurements, the daughter nuclides are provided in brackets.

The PAC measurements were performed using a 4-detector (BaF$_2$ crystals) spectrometer [22]. The detectors were positioned in the same plane at 90° to each other. The studied sample was placed in the center between them. The anisotropy of angular correlation is determined by the formula:

$$R(t) = A_2 G_2(t) Q_2 = 2\frac{S(180°,t) - S(90°,t)}{S(180°,t) + 2S(90°,t)}, \qquad (1),$$

where S (90°, t) are the gamma spectra of delayed coincidences when the detectors were placed at 90° (eight possible combinations of two detectors); S (180°, t) are the spectra of delayed coincidences when the detectors were placed at 180° (four possible combinations of two detectors); and Q_2 is a geometric factor (corresponding to the sizes and types of detectors and sources). The maximum time interval for obtaining delayed coincidence spectra was 800 ns. The timing resolution (^{60}Co, 1173-1332 keV) for a BaF$_2$ scintillator was 400 ps.

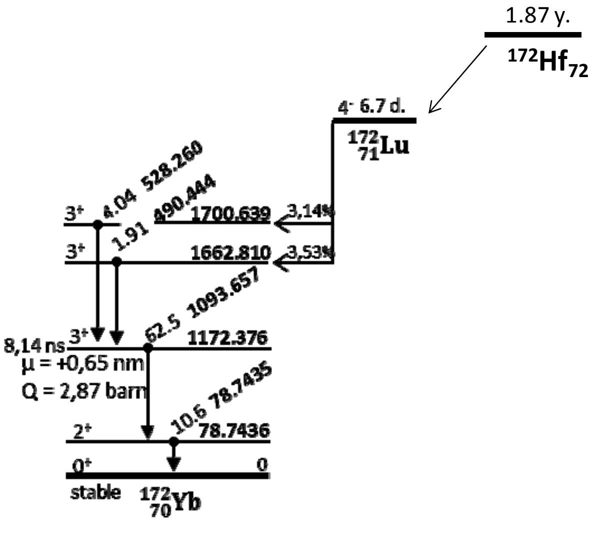

Fig. 1. Schemes of the decay of ^{172}Hf and ^{172}Lu in the target region for the PAC measurements on ^{172}Yb [24]

The decay scheme of ^{172}Lu and the used cascades of ^{172}Yb γ-quanta are presented in Fig. 1. Since ^{172}Hf decays into ^{172}Lu [23], either ^{172}Lu or ^{172}Hf were incorporated into the sample for the PAC measurements with the isotope ^{172}Yb.

3. Results and discussion

3.1. Studies of ferrites with the addition of 1% stable Hf, Yb, and Lu

Powder samples of CFO spinel (CoFe$_2$O$_4$) doped with Hf, Lu, and Yb (1 wt. %) were studied. Hereinafter they are denoted as CoFe$_2$O$_4$:Hf, CoFe$_2$O$_4$:Yb, and CoFe$_2$O$_4$:Lu. Fig. 2 shows the ^{57}Fe Mössbauer spectra for these samples. The spectra were measured at room temperature.

In the crystal lattice of a spinel ferrite, iron cations occupying the B sites (octahedral) have oxidation degrees +2 and +3, while in the A sites (tetrahedral) they have only +3. Each site has its own sextet in the spectrum ('Sextet_1' – (CoFe$_2$O$_4$)A and 'Sextet_2' – [CoFe$_2$O$_4$]B), which carries information about magnetic dipole and electric quadrupole interactions. Both sextets are indicated by the smooth fit lines against the spectrum background. Also, the spectra clearly show the manifestation of the impurity doublet (additional phase) in the cases of Lu and Yb. In the case of Hf, there is no impurity doublet (phase). All parameters for processing Mössbauer spectra are presented in Table 1. X-ray diffraction studies of powdered CoFe$_2$O$_4$:Hf, CoFe$_2$O$_4$:Yb, and CoFe$_2$O$_4$:Lu samples were carried out using a DRON-3 diffractometer at the *K*aMo line in the reflection mode [24]. The X-ray diffraction of our samples showed the presence of an additional phase only in CoFe$_2$O$_4$:Yb. In an earlier study [15], no second phases were also observed in the X-ray diffraction patterns of CoFe$_2$O$_4$ samples doped with Lu and Hf.

The analysis of the parameters of the Mössbauer spectra showed that the CoFe$_2$O$_4$:Hf sample contains 100 % standard spinel sextets (CoFe$_2$O$_4$)A and [CoFe$_2$O$_4$]B, the CoFe$_2$O$_4$:Lu sample contains 11 % of the impurity CoFe phase besides the standard sextets, and the CoFe$_2$O$_4$:Yb sample contains 23.4 % of the impurity CoFe phase.

The data for the ^{57}Fe isomer shifts (Fig. 3) in CoFe$_2$O$_4$ (1 wt. %) Hf, Lu, and Yb indicate a strong influence of the impurity on ^{57}Fe in the B sites and

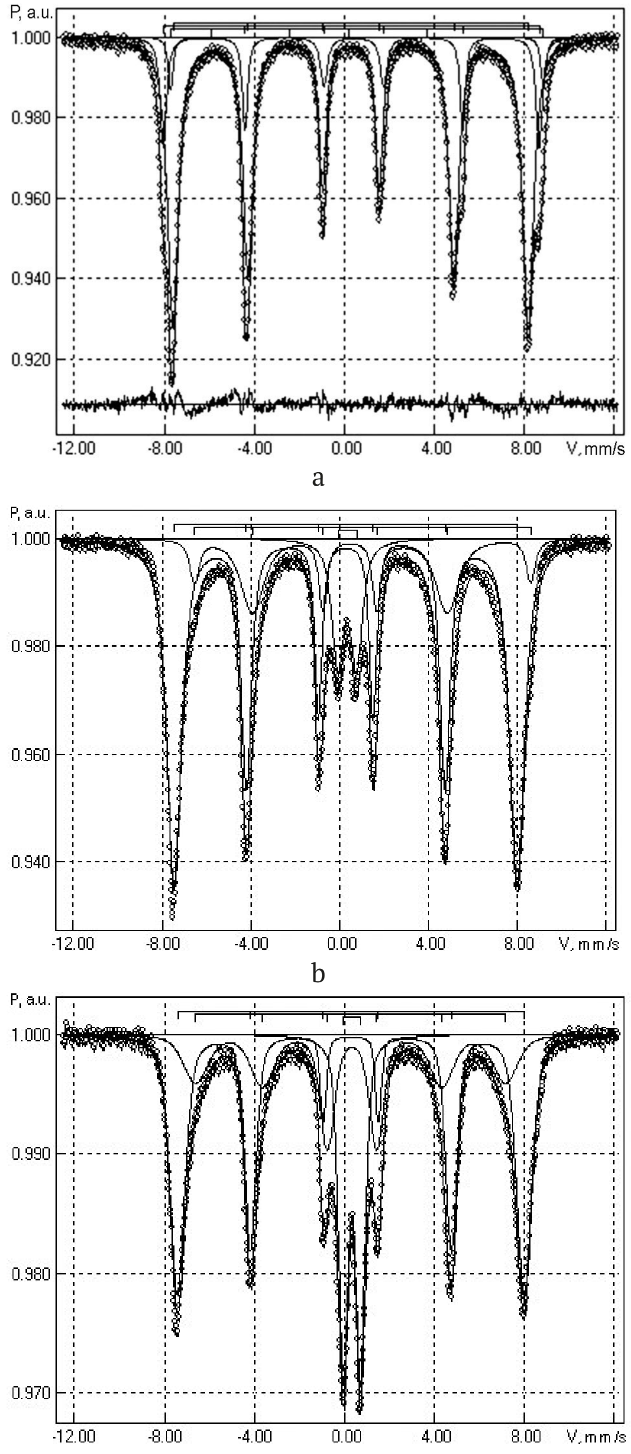

a

b

c

Fig. 2. Mössbauer spectra for ^{57}Fe in samples: a) $CoFe_2O_4$:Hf; b) $CoFe_2O_4$:Lu, and c) $CoFe_2O_4$:Yb, measured at 298 K

a negligible influence in the A sites.

Studying the ^{57}Fe quadrupole state in $CoFe_2O_4$ (1 wt. %) Hf, Lu, and Yb ferrites (Fig. 4) also provided important results. We observed a large ^{57}Fe quadrupole splitting in $CoFe_2O_4$ (1 wt. %) Lu relative to ferrites containing Yb and Hf. In addition, the ^{57}Fe quadrupole splitting appears only in the $[CoFe_2O_4]$B sites.

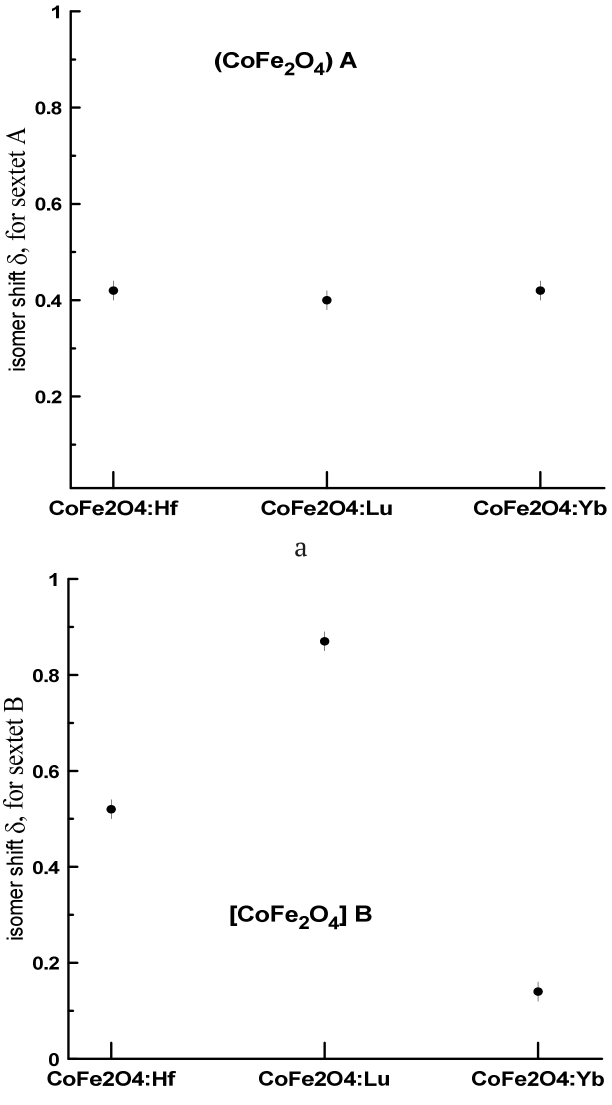

a

b

Fig. 3. The ^{57}Fe isomer shift in $CoFe_2O_4$ (1 wt. %) Lu, Yb, and Hf in the sites: a) $(CoFe_2O_4)$A and b) $[CoFe_2O_4]$B

The results for the ^{57}Fe hyperfine magnetic field in $CoFe_2O_4$ (1 wt. %) Hf, Lu, and Yb are shown in Fig. 5a, b. We observed a significant change in the ^{57}Fe hyperfine field in the $[CoFe_2O_4]$B site depending on the impurity element. The influence of the impurity element on ^{57}Fe in the $[CoFe_2O_4]$A sites was negligible.

3.2. Studies of $CoFe_2O_4$ ferrites by the PAC method

For the PAC measurements on ^{172}Yb nuclei, we can add either ^{172}Lu or ^{172}Hf radioactive

Table 1. Mössbauer parameters of $CoFe_2O_4$ samples. δ is the isomer shift, $\Delta E_Q{}^a$ is the quadrupole splitting, G is the line width, H is the Fe magnetic field, and A is the area under the spectrum

Sample	Sextet in the spectrum	δ (mm/s)	ΔE_Q^a (mm/s)	G (mm/s)	H (kOe)	A (%)	Component
$CoFe_2O_4$ +1 % Hf	«Sextet_1» «Sextet_2»	0.42 0.52	-0.00 -0.06	0.56 0.44	490 518	77.40 22.60	$(CoFe_2O_4)$A $[CoFe_2O_4]$B
$CoFe_2O_4$ +1 % Lu	«Sextet_1» «Sextet_2» «Doublet_1»	0.40 0.87 0.47	-0.00 0.57 0.84	0.80 0.50 0.63	480 470	68.50 20.46 11.04	$(CoFe_2O_4)$A $[CoFe_2O_4]$B CoFe
$CoFe_2O_4$ +1 % Yb	«Sextet_1» «Sextet_2» «Doublet_1»	0.42 0.14 0.14	-0.00 -0.06 0.74	0.79 1.29 0.51	478 427	48.83 27.87 23.39	$(CoFe_2O_4)$A $[CoFe_2O_4]$B CoFe

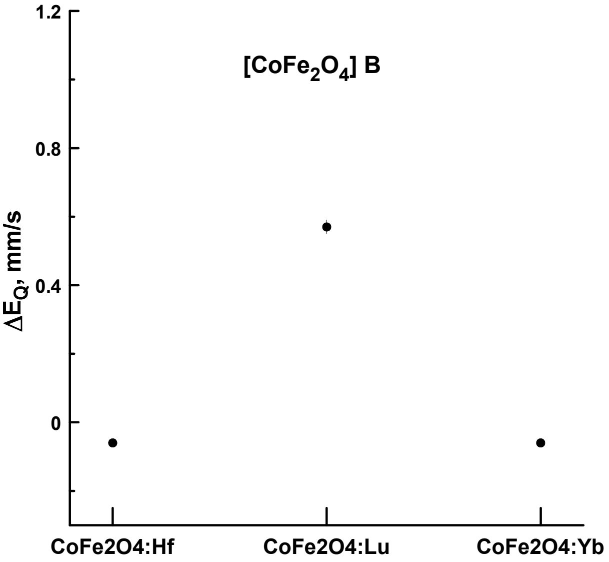

Fig. 4. The ^{57}Fe quadrupole splitting in $CoFe_2O_4$ (1 wt. %) Hf, Lu, and Yb ferrites

isotope to the sample. It should be noted that the radioactive isotopes were added without a carrier. An important assumption, apparently quite obvious, is that the position of the probe nucleus in the sample matrix coincides with the position of the parent nucleus.

The results at room temperature (considerably below the Curie temperature) showed that the $CoFe_2O_4$ ferrite (CFO) with incorporated ^{172}Hf (Fig. 6, above) provided two states of ^{172}Yb, characterized by two magnetic fields B_{hf1} = 14(1) T and B_{hf2} = 17(1) T with a population ratio of ~ 2:1. In the case of incorporated ^{172}Lu (Fig. 6, below), the processing of the spectrum indicated the presence of a single magnetic field B_{hf} = 18(1) T. This significant difference can be explained by the assumption that at room temperature ^{172}Lu is introduced preferentially into only one type of crystal lattice sites.

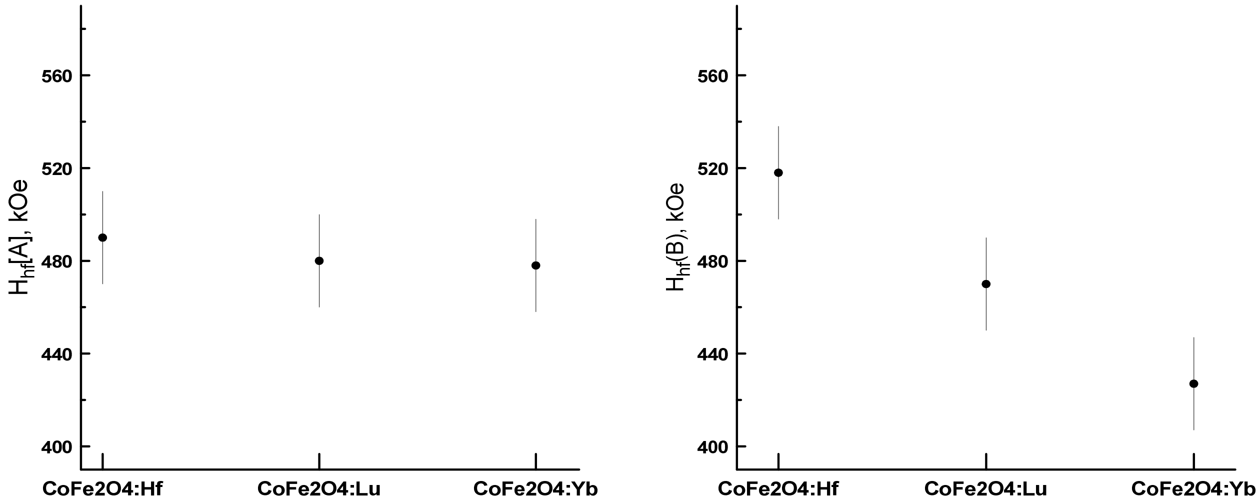

a b

Fig. 5. The ^{57}Fe hyperfine magnetic field in $CoFe_2O_4$ (1 wt. %) Lu, Yb, and Hf ferrites in the sites: a) $(CoFe_2O_4)$A and b) $[CoFe_2O_4]$B

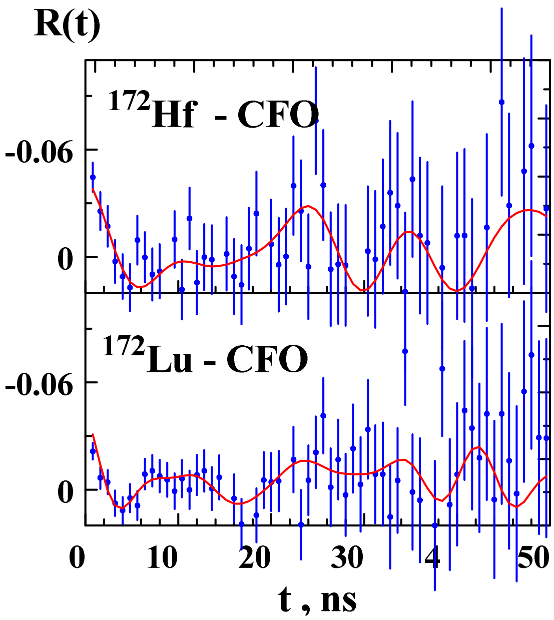

Fig. 6. The ^{172}Yb PAC spectra in $CoFe_2O_4$ ferrite measured at 298 K, after the introduction of ^{172}Hf (above) and ^{172}Lu (below) into the sample

It should be noted that below the Curie temperature, the hyperfine field is a mix of magnetic dipole and electric quadrupole fields. To reveal more clearly the influence of dopant ions (Hf and Lu) on the electric quadrupole interaction (directly related to the position of the dopant ion in the crystal lattice), we carried out measurements above the Curie temperature (1000 K). Table 2 shows the obtained quadrupole frequency, electric field gradient, and relative site occupancy parameters for ^{172}Yb in $CoFe_2O_4$(CFO), after introducing ^{172}Lu or ^{172}Hf into the sample.

The observed difference in the parameters can be explained by the assumption that the $^{3+}$Lu and $^{4+}$Hf ions are distributed differently when introduced into two non-equivalent lattice sites: in addition to the different charges of these ions, the lutetium ion has a larger ionic radius.

Basically, the post-effects of nuclear decay may influence the local environment of ^{172}Yb in CFOs. However, in crystalline phases, these effects usually have no significant influence on the HFI parameters.

4. Conclusions

Using the Mössbauer spectroscopy on ^{57}Fe nuclei, we studied the hyperfine interactions in $CoFe_2O_4$ ferrites doped with Hf, Lu, and Yb (1 wt. %). It was shown that doping with Lu and Yb leads to the formation of additional non-magnetic phases (Lu – 11 % and Yb – 23.4 %). In the ferrite doped with hafnium Hf, no additional phase was observed. A significant change in the HFI parameters was revealed for ^{57}Fe in the octahedral sites of $CoFe_2O_4$ ferrites doped with Hf, Yb, or Lu, respectively. However, the relative influence of the impurity on ^{57}Fe nuclei in the tetrahedral sites was insignificant. The formation of a new phase in the case of Yb and Lu can be attributed to the fact that the ionic radii of Yb and Lu are about 14-13 % larger than the ionic radius of Hf.

The parameters of hyperfine interactions on ^{172}Yb nuclei in $CoFe_2O_4$ ferrites were obtained by the PAC method. The ^{172}Yb ions were introduced (10^{-7} - 10^{-8} wt. %) into the samples in two ways: via ^{172}Hf ($^{172}Hf \rightarrow {}^{172}Lu \rightarrow {}^{172}Yb$ chain) or via the parent ^{172}Lu. A significant difference in the HFI parameters for these two cases was revealed. The difference in the HFI parameters persisted in the temperature range of 300–1000 K. The observed difference is due to the different distribution of $^{3+}$Lu and $^{4+}$Hf over the lattice sites due to different charges and ionic radii of these ions.

Notably, the different effects of Hf and Lu on the parameters (electric field gradient, magnetic field, and isomer shift) of the HFI in the samples were revealed by both MS and PAC methods, irrespective of the amount of the dopant. Specifically, according to MS, Hf, and Lu did not cause significant changes in the HFI parameters in the tetrahedral sites (“Sextet 1”),

Table 2. The parameters of the hyperfine interactions (above the Curie temperature) for ^{172}Yb upon the introduction of ^{172}Lu or ^{172}Hf into CFOs: quadrupole frequency ω_Q, electric field gradient *Vzz*, and relative site occupation *f*

	ω_{Q1}, Мрад/с	*Vzz*, 10^{21} В/м^2	*f*(ω_1), %	ω_{Q2}, Мрад/с	*Vzz*, 10^{21}В/м^2	*f*(ω_2), %
^{172}Hf(^{172}Lu(^{172}Yb))	220(15)	10.12(69)	65(8)	60(8)	2.76(37)	35(7)
^{172}Lu(^{172}Yb)	231(5)	10.63(56)	55(7)	108(9)	4.97(41)	45(8)

but had significantly different effects on the same parameters in the octahedral sites (“Sextet 2”). A similar situation was observed using the PAC method: substitution of Hf by Lu did not reveal a change in the HFI parameters in one of the sites (according to [15], it is the octahedral site), but indicated a significant difference (see Table 2) in the other site.

Contribution of the authors

The authors contributed equally to this article.

Conflict of interests

The authors declare that they have no known competing financial interests or personal relationships that could have influenced the work reported in this paper.

References

1. Casbeer E., Sharma V. K., Li X.-Zh. Synthesis and photocatalytic activity of ferrites under visible light: a review. *Separation and Purification Technology*. 2012;87: 1–14. https://doi.org/10.1016/j.seppur.2011.11.034

2. Tsoncheva T., Manova E., Velinov N., … Mitov I. Thermally synthesized nanosized copperferrites as catalysts for environment protection. *Catalysis Communications*. 2010;12: 105–109. https://doi.org/10.1016/j.catcom.2010.08.007

3. Manova E., Tsoncheva T., Estournés Cl., … Petrov L. Nanosized iron and iron–cobalt spinel oxides as catalysts for methanol decomposition. *Applied Catalysis A: General*. 2006;300(2): 170–180. https://doi.org/10.1016/j.apcata.2005.11.005

4. Behra Y., Singh N. B. Solid state properties of zinc ferrite in presence of dopants. *Materials Today: Proceedings*. 2018;5(7): 15451-15457. https://doi.org/10.1016/j.matpr.2018.05.032

5. Sun L., Zhang R., Ni Q., Cao E., Hao W., Zhang Y., Ju L. Magnetic and dielectric properties of $Mg_xCo_{1-x}Fe_2O_4$ ferrites prepared by the sol-gel method. *Physica B: Condensed Matter*. 2018;545: 4–11.https://doi.org/10.1016/j.physb.2018.05.030

6. Wu X., Ding,Z., Song N., Li L., WangW. Effect of the rare-earth substitution on the structural, magnetic and adsorption properties in cobalt ferrite nanoparticles. *Ceramics International*. 2016;42(3): 4246–4255.https://doi.org/10.1016/j.ceramint.2015.11.100

7. Zhao X., Wang W., Zhang Y., Wu S., Li F., Liu J. P. Synthesis and characterization of gadolinium doped cobalt ferrite nanoparticles with enhanced adsorption capability for Congo Red. *Chemical Engineering Journal*. 2014;250: 164–174. https://doi.org/10.1016/j.cej.2014.03.113

8. Bulai G., Diamandescu L., Dumitru I., Gurlui S., Feder M., Caltun O. F. Effect of rare earth substitution in cobalt ferrite bulk materials. *Journal of Magnetism and Magnetic Materials*. 2015;390: 123–131. https://doi.org/10.1016/j.jmmm.2015.04.089

9. Bulte J. W. M., Douglas T., Mann S., … Frank J. A. Magnetoferritin: characterization of a novel superparamagnetic MR contrast agent. *Journal of Magnetic Resonance Imaging*. 1994;4(3): 497–505. https://doi.org/10.1002/jmri.1880040343

10. Zipare K. V., Bandgar S. S., Shahane G. S. Effect of Dy-substitution on structural and magnetic properties of MnZn ferrite nanoparticles. *Journal of Rare Earths*. 2018;36(1): 86–94. https://doi.org/10.1016/j.jre.2017.06.011

11. Wu X., Chen W., Wu W., Wu J., Wang Q. Improvement of the magnetic moment of NiZn ferrites induced by substitution of Nd^{3+} ions for Fe^{3+} ions. *Journal of Magnetism and Magnetic Materials*. 2018;453: 246–253. https://doi.org/10.1016/j.jmmm.2018.01.057

12. Shoba M., Kaleemulla S. Structural, optical and dielectric studies of Er substituted zinc ferrite nanospheres. *Journal of Physics and Chemistry of Solids*. 2017;111: 447–457. https://doi.org/10.1016/j.jpcs.2017.08.028

13. Tsvetkov M., Milanova M., Pereira L. C. J., … Mitov I. Magnetic properties of binary and ternary mixed metal oxides $NiFe_2O_4$ and $Zn_{0.5}Ni_{0.5}Fe_2O_4$, doped with rare earths by sol–gel synthesis. *Chemical Papers*. 2016;70(12): 1600–1610. https://doi.org/10.1515/chempap-2016-0097

14. Tsvetkov M., Milanova M., Ivanova I., … Abrashev M. Phase composition and crystal structure determination of cobalt ferrite, modified with Ce^{3+}, Nd^{3+} and Dy^{3+} ions by X-ray and neutron diffraction. *Journal of Molecular Structure*. 2019;1179: 233–241. https://doi.org/10.1016/j.molstruc.2018.07.083

15. Temerbulatova N. T., Tsvetkov M. P., Karaivanov D. K., Velichkov A. I., Filosofov D. V., Milanova M. M. Rare earths doped ferrites, characterized by time differential $\gamma\gamma$ perturbed angle correlations method. *Journal of Solid State Chemistry*. 2019;277: 281–289. https://doi.org/10.1016/j.jssc.2019.05.029

16. Samokhvalov V., Unterricker S., Burlakov I., … The ISOLDE Collaboration. Investigation of ferromagnetic spinel semiconductors by hyperfine interactions of implanted nuclear probes. *Journal of Physics and Chemistry of Solids*. 2003;64(9-10): 2069–2073. https://doi.org/10.1016/s0022-3697(03)00152-5

17. Sawatzky G. A., van der Woude F., Morris A. H. Cation distributions in octahedral and tetrahedral sites of the ferrimagnetic spinel $CoFe_2O_4$. *Journal of Applied Physics*. 1968;39: 1204. https://doi.org/10.1063/1.1656224

18. Dadakhanov J. A., Lebedev N. A., Velichkov A. I., … Filosofov D. V. ^{172}Hf → ^{172}Lu radionuclide generator based on a reverse-tandem separation scheme. *Radiochemistry*. 2018;60(4): 415–426. https://doi.org/10.1134/s1066362218040112

19. MS-1104Em Mössbauer spectrometer, manufactured by the Research Institute of Physics of the Southern Federal University (formerly Rostov State University). Available at: https://www.sfedu.ru/www/stat_pages22.show?p=ELS/inf/D&x=ELS/-240

20. Abraham A., Pound R. V. Influence of electric and magnetic fields on angular correlations. *Phys. Rev*. 1953;92(4): 943. https://doi.org/10.1103/physrev.92.943

21. Brudanin V. B., Filosofov D. V., Kochetov O. I., … Akselrod Z. Z. PAC spectrometer for condensed matter investigation. *Nuclear Instruments and Methods in Physics Research Section A*. 2005;547(2–3): 389 399. https://doi.org/10.1016/j.nima.2005.04.002

22. Rinneberg H. H. Application of perturbed angular correlations to chemistry and related areas of solid state physics. *Atomic Energy Review*. 1979;17: 477.

23. Table of isotopes. Version 1.0. R. B. Fierstone, V. S. Shirley (eds.). New York: Wiley; 1996.

Information about the authors

Viktor M. Vakhtel, Cand. Sci. (Phys.–Math.), Associate Professor, Department of Nuclear Physics, Voronezh State University (Voronezh, Russian Federation).

vakhtel@phys.vsu.ru

Atanas I. Velichkov, Cand. Sci. (Phys.–Math.), Senior Researcher, Sector No. 4 of Radiochemistry, Scientific and Experimental Department of Nuclear Spectroscopy and Radiochemistry, Joint Institute for Nuclear Research (Dubna, Moscow Region, Russian Federation).

aiv@jinr.ru

Dimitar V. Karaivanov, Cand. Sci. (Phys.–Math.), Senior Researcher, Sector No. 4 of Radiochemistry, Scientific and Experimental Department of Nuclear Spectroscopy and Radiochemistry, Joint Institute for Nuclear Research (Dubna, Moscow Region, Russian Federation).

dvk@jinr.ru

Maria M. Milanova, Dr. Sci., Professor, Department of Inorganic Chemistry, Faculty of Chemistry and Pharmacy, Sofia University "St. Kliment Ohridski" (Sofia, Bulgaria).

nhmm@chem.uni-sofia.bg

Yuri G. Segal, Head of the Laboratory of Nuclear Spectrometry, Department of Nuclear Physics, Voronezh State University (Voronezh, Russian Federation).

ysemov@gmail.com

Nargiza Temerbulatova, Junior Researcher, Sector No. 4 of Radiochemistry, Scientific and Experimental Department of Nuclear Spectroscopy and Radiochemistry, Joint Institute for Nuclear Research (Dubna, Moscow Region, Russian Federation).

Dmitry V. Filosofov, Cand. Sci. (Chem.), Head of Sector No. 4 of Radiochemistry, Scientific and Experimental Department of Nuclear Spectroscopy and Radiochemistry, Joint Institute for Nuclear Research (Dubna, Moscow Region, Russian Federation).

filosofov@jinr.ru

Martin P. Tsvetkov, Dr. Sci., Associate Professor, Department of Inorganic Chemistry, Faculty of Chemistry and Pharmacy, Sofia University "St. Kliment Ohridski" (Sofia, Bulgaria).

nhmt@chem.uni-sofia.bg

Received 01.07.2024; approved after reviewing 30.07.2024; accepted for publication 16.09.2024; published online 25.04.2025.

Translated by Anastasiia Ananeva

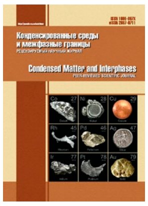

ISSN 1606-867X (Print)
ISSN 2687-0711 (Online)
Condensed Matter and Interphases
Kondensirovannye Sredy i Mezhfaznye Granitsy
https://journals.vsu.ru/kcmf/

Original articles

Research article
https://doi.org/10.17308/kcmf.2025.27/12488

Chemical vapor deposition of $Tm_3Fe_5O_{12}$ epitaxial films, investigation of their structure and properties in the terahertz range

M. N. Markelova✉, A. A. Hafizov, Shi Xiaoyu, I. E. Graboy, M. S. Shanin, M. R. Konnikova, A. P. Shkurinov, A.R. Kaul

[1]Lomonosov Moscow State University,
1 Leninskie Gory, Moscow 119991, Russian Federation

Abstract

In this study, for the search and development of new spintronic materials, thin films of $Tm_3Fe_5O_{12}$ iron garnet were obtained by the metalorganic chemical vapor deposition (MOCVD) on single-crystal $Gd_3Ga_5O_{12}$(111) – GGG and $Y_3Al_5O_{12}$(111) – YAG substrates. The $Tm_3Fe_5O_{12}$ films were investigated using X-ray diffraction, Energy dispersive X-Ray microanalysis, Raman spectroscopy and terahertz (THz) pulsed spectroscopy.

The epitaxial nature of films deposited on substrates of both types demonstrated. It was found that the growth of garnet film under the high-temperature vacuum conditions of MOCVD on a GGG substrate is complicated by the evaporation of gallium oxide, which causes the introduction of iron oxide into the surface layer of the substrate, enrichment of the adjacent layer of the film with thulium oxide and the formation of non-stoichiometric garnet with antisite defects.

It was concluded that YAG substrates are more promising, since the heteroepitaxy of iron garnets on them does not have such complications.

Keywords: Thin films, Iron garnets, MOCVD, Structure, Antisite defects, Raman spectroscopy, Terahertz spectroscopy

Funding: Work on MOCVD film production was carried out using equipment purchased using funds from the Moscow University Development Program. The study was carried out with the financial support of the Interdisciplinary Scientific and Educational Schools of Moscow University (Project No. 24-Ш06-13).

For citation: Markelova M. N., Hafizov A. A., Shi X., Graboy I. E., Shanin M. S., Konnikova M. R., Shkurinov A. P., Kaul A. R. Chemical vapor deposition of $Tm_3Fe_5O_{12}$ epitaxial films, investigation of their structure and properties in the terahertz range. *Condensed Matter and Interphases*. 2025;27(1): 104–114. https://doi.org/10.17308/kcmf.2025.27/12488

Для цитирования: Маркелова М. Н., Хафизов А. А., Ши С., Грабой И. Э., Шанин М. С., Конникова М. Р., Шкуринов А. П., Кауль А. Р. Химическое газофазное осаждение эпитаксиальных пленок $Tm_3Fe_5O_{12}$, исследование их структуры и свойств в терагерцовом диапазоне. *Конденсированные среды и межфазные границы*. 2025;27(1): 104–114. https://doi.org/10.17308/kcmf.2025.27/12488

✉ Maria N. Markelova, e-mail: maria.markelova@gmail.com
© Markelova M. N., Hafizov A. A., Shi X., Graboy I. E., Shanin M. S., Konnikova M. R., Shkurinov A. P., Kaul A. R., 2025

The content is available under Creative Commons Attribution 4.0 License.

1. Introduction

The successes achieved in the last decade in the development of new areas of electronics – spintronics and magnonics are based on the development and application of new materials, including those combining several functional properties [1]. One of the main trends in modern engineering is the miniaturization of electronic devices, so research and development of multifunctional materials in the form of thin films is of particular interest. This direction of development is especially relevant for spintronics and magnonics, which use ferrimagnets with a garnet structure in the form of ultra-thin (from units to tens of nanometers) epitaxial films as the main materials [1]. To obtain such thin films, the liquid-phase epitaxy method, which has long been the most popular method for synthesizing garnets (the thickness of the films obtained in this case is a few micrometers [2, 3]), cannot be used; therefore, new technological approaches to obtaining thin films of iron garnets are required. One of the promising synthesis methods is the metalorganic chemical vapor deposition (MOCVD) using , which has become the main method in the synthesis of epitaxial heterostructures of semiconductors [4]. Using b-diketonates and alcoholates as volatile substances, MOCVD can also be quite successfully applied to the epitaxy of functional materials based on simple and complex oxides [5].

The structural class of garnets belongs to the space group *Ia*3*d*. The cubic body-centered unit cell of garnet contains 8 identical octants corresponding to the formula composition $\{RE\}_3[Fe]_2(Fe)_3O_{12}$, where the curly brackets { } denote the dodecahedral positions of the rare earth element (RE), and the brackets [ ]- and ( )- correspond to the octahedral and tetrahedral positions occupied by Fe^{3+} ions. Thus, the features of iron-based garnets are: a multi-sublattice magnetic structure, have wide possibilities for varying the elemental composition and, as a consequence, a variety of their magnetic properties [6].

Iron garnets of rare earth elements (REE) have high resistance and, accordingly, high transparency in the visible and near IR ranges, which gives them an advantage over metallic ferromagnets (Fe, Ni, etc.), since it allows the use of the pump-probe technique in the study of ultra-fast magnetization dynamics [1,7]. Spin pumping is also a way to excite magnons in magnetic systems. Recently, spin wave propagation in a lutetium iron garnet/heavy metal ($Lu_3Fe_5O_{12}$/Pt) is demonstrated in [8]. The results of such studies, along with great fundamental interest, open up prospects for the creation of ultra-high-speed devices for recording and processing information using thin ferrimagnetic films [9].

Spin-flip transitions of some rare earth iron garnets occur in the frequency range from 0.1 THz to 10 THz. Therefore, terahertz radiation can potentially affect the spin state of such systems and can be used to obtain important results in the study of magnetic dynamics under the influence of laser radiation [10], however, research in this direction is in the initial phase of its development. Systematic studies of the spectral properties of iron garnet films in the THz range and their changes in a number of rare earth elements are of great interest.

Thus, the aim of this study was the MOCVD synthesis of thin films of $Tm_3Fe_5O_{12}$ iron garnet, comparative analysis of the results of epitaxy on isomorphic $Gd_3Ga_5O_{12}$ and $Y_3Al_5O_{12}$ (111) substrates, investigation of the structure of the obtained films by X-ray diffraction, Raman spectroscopy, and also study of their spectral characteristics by time-resolved pulsed THz spectroscopy.

2. Experimental

Thin $Tm_3Fe_5O_{12}$ films were synthesized on single-crystal $Ga_3Ga_5O_{12}$ (GGG) and $Y_3Al_5O_{12}$ (YAG) substrates with the (111) orientation by metal-organic chemical vapor deposition (MOCVD). Dipivaloylmethanates $Tm(thd)_3$ and $Fe(thd)_3$ (thd – 2,2,6,6-tetramethylheptane-3,5-dionate anion) were used as volatile compounds (precursors). In our previous study, we discussed in detail a new principle of dosing precursor vapor into the reactor, which ensures smooth, well-controlled and reproducible "feeding" of the growing film [11]. The scheme of the modernized setup using this principle and applied in this study is shown in Fig. 1. The system operates by passing a cotton thread impregnated with an metalorganic precursor solution through two separate vacuum zones – a low-temperature solvent evaporation zone and a higher-temperature zone where precursors sublimate. The solvent vapors (toluene was used) are condensed in a nitrogen trap, and the precursor vapors are transferred by a carrier gas flow (Ar) into a vertical hot-wall reactor, where their oxidative thermolysis occurs with the formation of an oxide film on a heated substrate. The substrate holder with the substrate fixed to it rotates around a vertical axis in order to increase the lateral homogeneity of the films by thickness. The vacuum in the system is created by a fore vacuum pump equipped with a valve for regulating the overall pressure in the film deposition zone. The temperature of the hot lines through which the precursor vapors are supplied and the temperature of the substrate holder were 190 and 910 °C respectively; the total pressure was 10 mbar, the partial pressure of oxygen was 1 mbar, the film growth rate was 3 nm/min. After film deposition, the setup was filled with oxygen to atmospheric pressure and oxidative annealing was carried out at the spraying temperature for 20 min, after which the setup was cooled. The thickness of the films was 900 nm.

The Fe/Tm ratio in the obtained films was determined by Energy dispersive X-Ray microanalysis (EDX) data using a Zeiss EVO 50 SEM scanning electron microscope with an e2v Sirius SD EDX analyzer. The phase composition and orientation of the obtained films were determined based on X-ray θ-2θ scanning data using a Rigaku SmartLab diffractometer (Cu*K*α, graphite monochromator). Measurement in the θ-2θ scanning mode was carried out in the angle range of 5–80° with a step of 0.02°, the signal accumulation time was 1 s. Phase analysis was performed using the ICDD PDF database. For the determination of the in-plane orientation of the films and confirm epitaxial growth, X-ray ϕ-scanning was performed.

Raman spectra at wavelengths of 532 and 785 nm were obtained using a HORIBA Scientific Raman spectrometer and microscope. The measurement range was from 80 to 2000 cm^{-1}. Raman spectroscopy was performed with a 100x objective at an incident radiation intensity of 140 W/cm^2 for $\lambda = 532$ nm and $3.6 \cdot 10^3$ W/cm^2 for $\lambda = 785$ nm. Three independent measurements were performed, each of which was averaged over 30 scans with an accumulation time of 0.5 s at each point. The background component of the spectrum was subtracted using the Voight

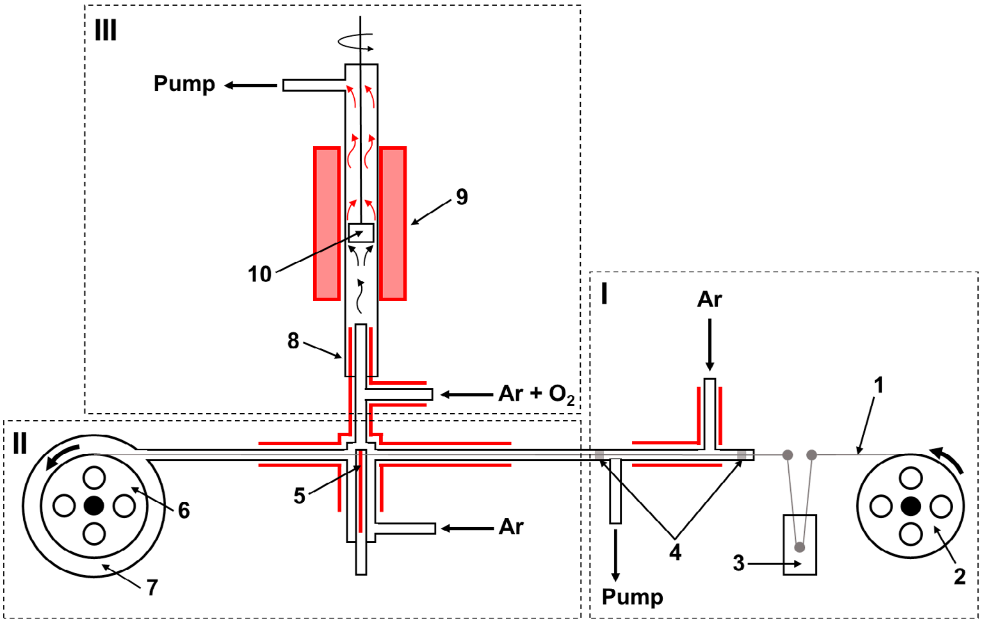

Fig. 1. Schematic diagram of MOCVD setup with thread-solution feeder. **I** – Thread feeding and solvent evaporation unit: *1* – cotton thread, *2* – feeding reel, *3* – reservoir for precursor solution, *4* – dies. **II** – Precursor evaporation unit: *5* – precursor evaporator, *6* – receiving reel, *7* – vacuum cover of the receiving reel. **III** – Film deposition unit: *8* – quartz reactor, *9* – reactor furnace, *10* – rotating substrate holder. Heated lines are marked in red

function approximation of the obtained Raman spectra.

Terahertz spectroscopy in both transmission and reflection geometry was performed using a commercial TeraSmart THz spectrometer (Menlo Systems GmbH, Germany). Linear p-polarized THz pulses are generated in a fiber-coupled photoconductive antenna (Fe:InGaAs/INASAS) and measured by two photoconductive detectors (LT InGaAs/InAlAs), which simultaneously measure the transmitted and reflected THz beams. The spectrometer has a dynamic range of 95 dB, a spectral range of 0.2–3.6 THz and a scan window of 110 ps, providing a frequency resolution of 7.3 GHz. The spectral range for measurements is limited in the low-frequency region by the sample aperture (4 mm), and in the high-frequency region (above 3.6 THz) by the detectors' absorption lines. The THz radiation was focused onto the sample by two parabolic mirrors, and the THz beam size on the sample was about 500 µm at the $1/e^2$ level. In this study, the incidence angle was 35°. To reduce the effect of water vapor absorption, the experiments were conducted using a dry air system that maintained a relative humidity of 20% in the chamber. In addition, to reduce systematic error, 3 independent measurements of 1000 pulses each were performed for each sample, the results of which were averaged.

The method for obtaining the absorption coefficient and refractive index for the transmission configuration is described in [12,13]. Determination of the dependence of the amplitude of the transmitted field on the frequency (w) is possible using the Fourier transforms (FFT) of the time profile of the THz pulse $E(t)$:

$$E_{\text{sample}}(\omega) = FFT\big(E(t)\big). \quad (1)$$

The transmittance coefficient $T_w(\omega)$ of the sample is calculated as the ratio of the amplitude of the field passed through the sample to the amplitude of the field without the sample (air):

$$T_w(\omega) = \frac{\text{substrate}(\omega)}{E_{\text{air}}(\omega)}. \quad (2)$$

From here the absorption index of the sample is calculated as:

$$\alpha(\omega) = \frac{-\ln\big(T_w(\omega)\big) + \ln(1 - R^2)}{d}, \quad (3)$$

$$n(\omega) = n_{\text{aver}} + \arg(T_w(\omega))\frac{c}{\omega d}, \quad (4)$$

where d – sample thickness, $R = \frac{n_{\text{aver}} - 1}{n_{\text{aver}} + 1}$ – reflection coefficient, $n_{\text{aver}} = 1 + \Delta t \cdot \frac{c}{d}$ – average refractive index, Δt – pulse delay when passing through the sample, c – the speed of light.

3. Results and discussion

For deposition of $Tm_3Fe_5O_{12}$ films two substrates with a garnet structure were selected – GGG(111) and YAG(111) with very different unit cell parameters (Fig. 2), which leads to different values of the unit cell parameter mismatch (e) at the film/substrate interface. Values e, calculated using the formula:

$$\varepsilon = \frac{a_{\text{substrate}} - a_{\text{film}}}{a_{\text{substrate}}} \cdot 100\ \%, \quad (5)$$

were 0.4% and -2.8% for films on GGG(111) and YAG(111), respectively. As can be seen from the calculated values, during epitaxy on YAG, the substrate compresses the film in-plane, and in the case of GGG, on the contrary, the substrate stretches the film in-plane. Thus, during the growth of $Tm_3Fe_5O_{12}$ films on these substrates, significant elastic stresses can be expected in the films, which usually lead to changes in many physical properties, in particular magnetic ones.

The θ/2θ diffraction patterns of $Tm_3Fe_5O_{12}$ films, obtained by simultaneous deposition on GGG(111) and YAG(111) substrates are shown

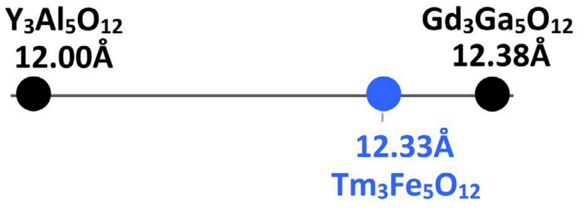

Fig. 2. Schematic illustration of the difference in the unit cell parameters of $Gd_3Ga_5O_{12}$(111) and $Y_3Al_5O_{12}$(111) garnet substrates and $Tm_3Fe_5O_{12}$ film

in Fig. 3a. It is evident that in both diffraction patterns, in addition to the substrate peaks, there were peaks from the $Tm_3Fe_5O_{12}$ film (444), however, on the GGG(111) substrate there were also additional peaks, designated **2** and **3** (Fig. 3a, b). This result is identical to recently observed in our study of the structure of lutetium iron garnet $Lu_3Fe_5O_{12}$ films on GGG substrates [14]. Under MOCVD synthesis conditions ($T_{deposition}$ = 890-950 °C and low partial pressure of oxygen ~1 mbar) surface chemical instability of the $Gd_3Ga_5O_{12}$ substrate was observed due to the volatility of gallium oxide Ga_2O. This leads to the formation of a surface layer of $Gd_3(Fe_xGa_{5-x})O_{12}$ in the substrate, which occurred as a result of filling vacancies formed during partial loss of gallium with Fe^{3+} ions. It is obvious that vacancies $V_{Ga}^{¢¢¢}$, occupied by iron ions, were formed primarily in octahedral positions. The diffraction peak **2** in Fig. 3 indicates the formation of the epitaxial layer of $Gd_3(Fe_xGa_{5-x})O_{12}$. The calculated unit cell parameter for the $Gd_3(Fe_xGa_{5-x})O_{12}$ layer was 12.46 Å, which was close to the unit cell parameter for $Gd_3Fe_5O_{12}$ = 12.50 Å.

Diffraction peak **3** (Fig. 3a, b) we interpret as belonging to the intermediate Tm-excessive layer of garnet of composition $Tm_3(Tm_xFe_{5-x})O_{12}$, similar to $Lu_3(Lu_xFe_{5-x})O_{12}$, observed in [14] and formed as a result of partial occupation of octahedral positions of garnet by Lu^{+3} ions and a decrease in their occupation by Fe^{+3} ions. Since the ionic radius of Tm^{+3} (coordination number = 6) is higher than that of Fe^{+3} (0.88 Å and 0.65 Å, respectively [15]), then such a substitution leads to a strong increase in the unit cell parameter of the Tm^{+3} compositions as the x value increases, which is manifested in a shift in the X-ray reflection of garnet (444) to the region of smaller angles. The possibility of the location of REE ions not only in dodecahedral but also in octahedral positions was pointed out by Geller in his classic study in 1967 on the crystallography of garnets [6]. Also the theoretical study[16], which examined these possibilities in detail and proposes an algorithm for calculating the degree of occupation of oxygen octahedra in garnet single crystals by REE ions, as well as the study [17], in which the formation of such antisite defects in a number of garnets, studied by the EXAFS method, was considered as the cause of a decrease in the cubic symmetry of garnets should be mentioned. At the same time, systematic and convincing experimental evidence of such a redistribution of REE ions by positions, as well as reliably established information about the region of non-stoichiometry of garnets in the systems “REE oxide – A_2O_3 (A = Al, Ga, Fe)” could not be found in the literature. In addition, it should be noted that the possibility of formation of antisite defects $[RE_{Fe}]^{3+}$ in heteroepitaxial films and autonomous phases (powders, single crystals)

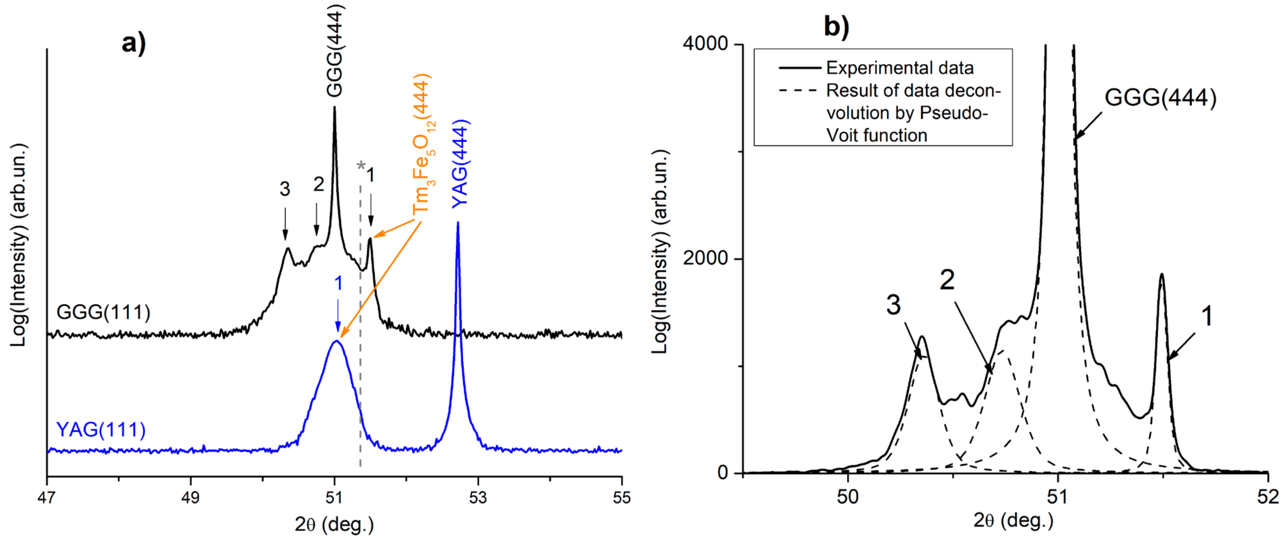

Fig. 3. (a) X-ray diffractograms of $Tm_3Fe_5O_{12}$ films deposited on GGG(111) and YAG(111) substrates. The dashed line indicates the (444) peak position of bulk $Tm_3Fe_5O_{12}$. (b) Magnified fragment of the diffractogram of $Tm_3Fe_5O_{12}$ film deposited on GGG(111) with description of the pseudo-Voit function of the film peaks (peaks **1**–**3**) and the substrate peak

of the same composition, can differ significantly, since the films in the immediate vicinity of the interface with the substrate are always strained (in-plane tensile or compressive strain), which can, depending on the sign of the deformation, promote or counteract the formation of films enriched in REE, with an increased parameter in the plane of the interface. During the growth of $Tm_3Fe_5O_{12}$ on GGG a positive ε value, which means the in-plane tensile of the film, can lead to the growth of the film with an increased unit cell parameter, i.e. contribute to the formation of antisite defects $[RE_{Fe}]^{3+}$ and the formation of a layer of Tm-enriched garnet.

Based on the established sequence of growth of the interface layers, it is possible to assume a common cause and diffusion mechanism for their occurrence: the removal of gallium from the surface layer of the substrate causes a counter diffusion flow of iron ions into the substrate from the adjacent thin layer of stoichiometric $Tm_3Fe_5O_{12}$ garnet which leads to enrichment of the latter with a rare earth component. It should be noted that both interface layers have a garnet structure and therefore do not impair the epitaxial character and orientation of the deposited layer, considered at full thickness. Epitaxial nature of $Tm_3Fe_5O_{12}$ films on GGG(111) and YAG(111) substrates was confirmed by X-ray φ-scanning (Fig. 4a, b): since the position of the reflections (800) of the film and substrate on the φ-scans coincided, it can be concluded that during $Tm_3Fe_5O_{12}$/GGG(111) and $Tm_3Fe_5O_{12}$/YAG(111) film growth, cube-on-cube heteroepitaxy occurs.

Garnet of the “correct stoichiometry” 3:5 on the diffraction pattern of the $Tm_3Fe_5O_{12}$/GGG sample corresponds to the peak number **1** (Fig. 3a, b). It corresponds to the reflection from the (444) plane, and its position corresponds to that expected based on the powder diffraction pattern (the position of the $Tm_3Fe_5O_{12}$(444) peak for the powder is indicated by a dashed line) taking into account the above-described nature of epitaxial deformations: in-plane tensile strain)and the resulting reduction in interplanar distances in the direction perpendicular to the substrate (out-of-plane). The fact that the deviation of the (444) reflex from the line for the powder is relatively small indicates a small amount of film deformation during heteroepitaxy on a substrate with a very different unit cell parameter. In accordance with theoretical concepts of heteroepitaxy [18], partial elimination of elastic stresses arising due to the parametric difference between the film and the substrate occurs in this case due to the emergence of misfit dislocations (MD) in the film. It is natural to assume that in this case the MD are formed at the boundary of the Tm-excess layer of $Tm_3(Tm_xFe_{5-x})O_{12}$ and stoichiometric layer $Tm_3Fe_5O_{12}$, which differ most significantly by the unit cell parameter.

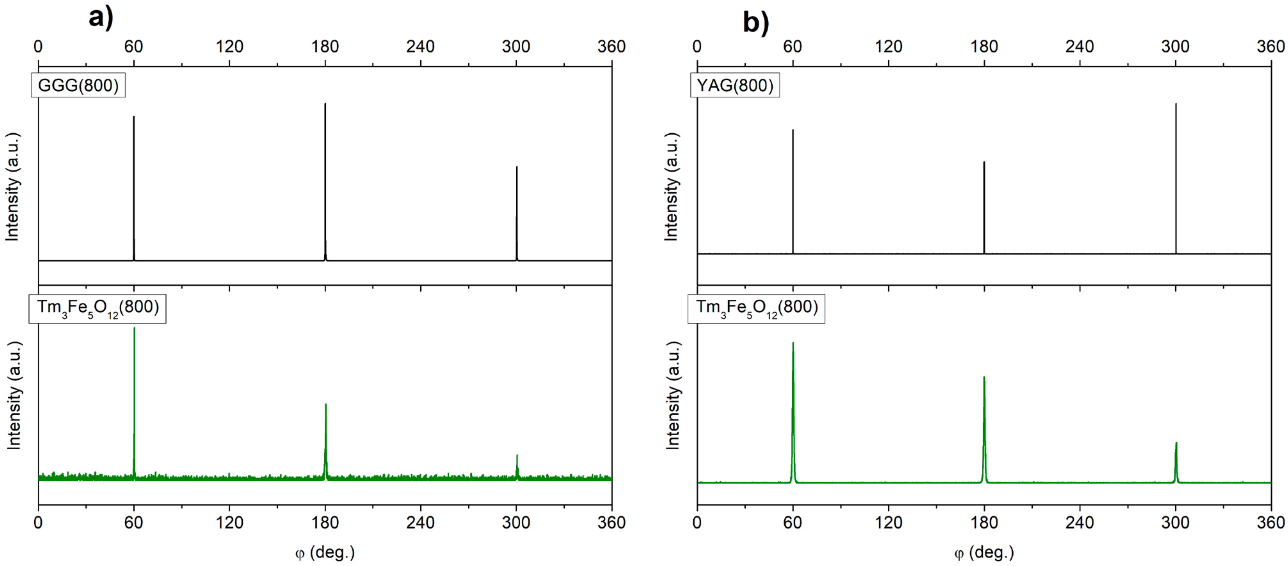

Fig. 4. X-ray φ-scans results for $Tm_3Fe_5O_{12}$ films on GGG(111) (a) and YAG(111) (b) substrates

As the result of the deposition of $Tm_3Fe_5O_{12}$ films on a YAG(111) substrate, which has a lower unit cell parameter than the film and a larger parametric mismatch, was the formation of highly strained film, as indicated by the large deviation of the (444) reflex from its position for the powder sample (Fig. 3a). In this case, the stress is of compressive nature along the substrate, which, in accordance with the elastic nature of the deformation, led to stretching of the film along the normal to the substrate (as was indicated by the shift of the film peak towards smaller angles relative to the peak for the powder). Strong elastic strains in the film were manifested not only as a large shift of the (444) reflex, but also as its significant broadening: the width at half maximum (FWHM) was 0.31°. The magnitude of elastic strains s is of interest. The value of s was calculated based on the relative change of unit cell parameter of the film's e compared to a $Tm_3Fe_5O_{12}$ single crystal using the ratios:

$$\varepsilon = \frac{a_{\text{film}} - a_{\text{Tm}_3\text{Fe}_5\text{O}_{12}}}{a_{\text{Tm}_3\text{Fe}_5\text{O}_{12}}}, \tag{6}$$

$$\sigma = \frac{E}{1-\nu}\varepsilon, \tag{7}$$

where a_{film} = 12.391 Å (the unit cell parameter determined based on XRD data for the $Tm_3Fe_5O_{12}$ film) and $a_{\text{Tm}_3\text{Fe}_5\text{O}_{12}}$ = 12.327 Å (the unit cell parameter for the $Tm_3Fe_5O_{12}$ single crystal), E – Young's modulus, ν – Poisson's ratio. Since the elastic constants for $Tm_3Fe_5O_{12}$ are not available in the literature, we used E = 187 GPa and ν = 0.29 for yttrium iron garnet $Y_3Fe_5O_{12}$ for the calculation [19]. The compressive stresses determined in this way was 1.4 GPa. It is obvious that, despite its large value, the compressive stresses characterizes only the stress remaining after part of it has been eliminated by the appearance of MD at the film/substrate interface. The value of the theoretically possible elastic stress arising in the absence of the dislocation relaxation mechanism was estimated according to the formula:

$$\sigma = \frac{E}{1-\nu}\cdot\frac{a_{\text{Tm}_3\text{Fe}_5\text{O}_{12}} - a_{\text{YAG}}}{a_{\text{YAG}}} \tag{8}$$

and composed ~7 GPA (a_{YAG} = 12.010 Å). Thus it becomes clear that the elastic stresses at the interface $Tm_3Fe_5O_{12}$ with YAG substrate by» 80% are eliminated by mismatch dislocations.

In conclusion of the discussion of the X-ray diffraction results, it is necessary to state the degradation of $Gd_3Ga_5O_{12}$-based substrates during gas-phase deposition, which led to the formation of additional phases in the composition of the $Tm_3Fe_5O_{12}$ film and to the impossibility of using GGG(111) substrates to obtain iron garnet films for applied research, including for studying their behavior in the terahertz region. In this regard, YAG substrates, which are quite stable under high-temperature conditions of film deposition using vacuum methods, despite the greater parametric mismatch, show a significant advantage.

The Raman scattering studies of synthesized $Tm_3Fe_5O_{12}$/YAG(111) film and YAG substrates were conducted at wavelengths λ = 532 nm (Fig. 5a) and λ = 785 nm (Fig. 5b). The iron garnets belong to the space group *Ia*3*d* and according to [20] have the following set of vibrational modes:

$$\Gamma = 3A_{1g} + 6E_g + 9T_{2g} + 9T_{1u}. \tag{1}$$

The YAG belongs to the same space group, and as studies of the YAG structure have shown [21], yttrium ions have 24 c-bonds with dodecahedral coordination, and aluminum ions have 16 a-bonds with octahedral coordination and 24 d-bonds with tetrahedral oxygen coordination. These 160 atoms (metals and oxygen) per unit cell create 18 phonon branches (17 optical and 1 acoustic T_{1u}). It should be noted that 18 Raman-active modes A_{1g}, E_g and T_{2g}, and 9 IR-active oscillations T_{1u} are possible for the space group *Ia*3*d* [22].

Our Raman study showed that the best resolution of vibrational modes of the $Tm_3Fe_5O_{12}$ film against the background of a single-crystal YAG substrate was observed at λ = 532 nm (Fig. 5a): the spectrum allows modes at 117 (T_{2g}), 182, 469, 650, 1114, 1284, 1817, 1910 and 1960 cm^{-1}. With less energy irradiation with a longer wavelength λ = 785 nm, weak differences were observed between the spectrum of the YAG substrate and the spectrum of the film (Fig. 5b): only 2 vibrational modes were allowed at 116 (T_{2g}) and 251 cm 1 (E_{2g}). This is due to the fact that with a decrease in wavelength, starting from 800 nm, the absorption of rare earth iron garnets increases significantly. This, in turn, was associated with intense interband transitions and charge transfer

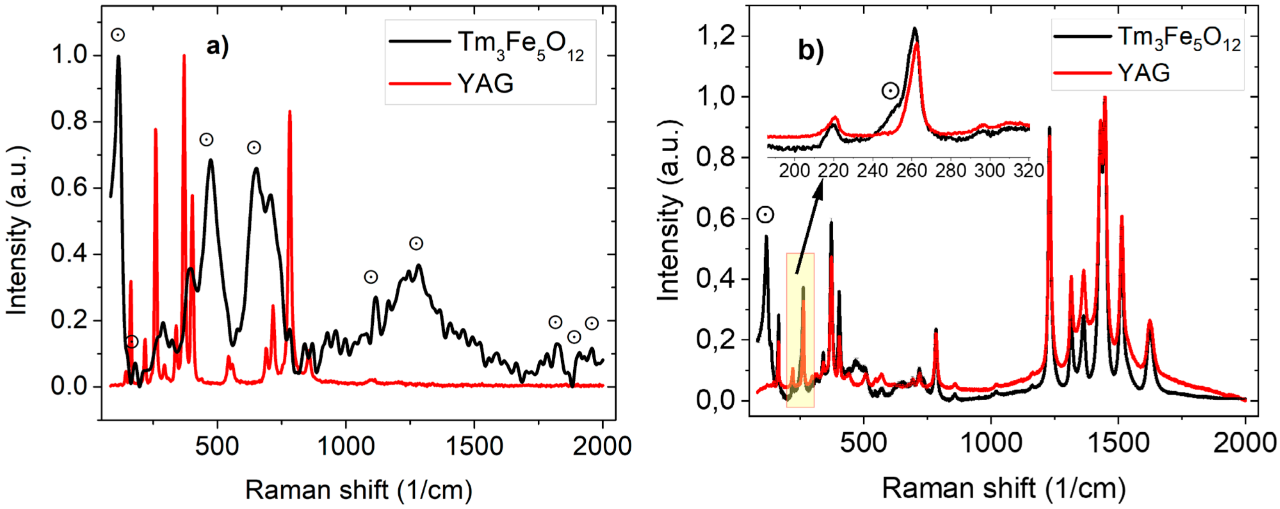

Fig. 5. Raman spectra of $Tm_3Fe_5O_{12}$ film on YAG(111) substrate at wavelengths of 532 nm (a) and 785 nm (b). ⊙ – vibrational modes related to the $Tm_3Fe_5O_{12}$ film

transitions from O^{2-} to Fe^{3+} or to the rare earth element ion RE^{3+} [23]. The obtained Raman shifts 116 and 251 cm^{-1} were consistent with the data for $Tm_3Fe_5O_{12}$ films with the thickness of 20–300 nm on a substituted gallium-gadolinium garnet ($Gd_{2.6}Ca_{0.4}Ga_{4.1}Mg_{0.25}Zr_{0.65}O_{12}$) substrate with orientation (111), in the Raman spectra of which 2 modes were observed – 130 and 250 cm^{-1} when shooting up to 300 cm^{-1} was performed [24].

The study [22] demonstrated that Raman spectra have a relatively low signal-to-noise ratio at frequencies below a few terahertz (150 cm^{-1}). In this regard, as another method of vibrational spectroscopy, we performed THz-pulse spectroscopy, which allows restoring the dielectric characteristics of various materials in the frequency range from 0.1 to 10 Thz. In this study, the dielectric characteristics of GGG and YAG substrates (with thicknesses of 513 μm and 502 μm, respectively) were investigated based on measurements of THz radiation transmission (Fig. 6). These measurements also indicate that the YAG(111) substrate is more promising than the GGG(111) substrate, since its characteristic spectrum does not show significant absorption in a wider frequency range from 0.25 to 3.0 THz, while GGG substrates have an absorption line at a frequency of 2.5 THz, which reduces the spectral range for film analysis to 0.2–2.2 THz. Thus, despite the stressed nature of the $Tm_3Fe_5O_{12}$ films, obtained on a YAG(111) substrate, such films appear more promising for further terahertz research. A resonant absorption mode was detected for the YAG(111) substrate at a frequency of 3.25 THz (108 cm^{-1}). The observed resonant absorption mode can be explained by a two-phonon difference process, as a result of which an acoustic phonon is transferred to the optical branch [22].

Due to the low film thickness compared to the wavelength of THz radiation, we simultaneously measure THz fields reflected and transmitted through the $Tm_3Fe_5O_{12}$ film on the YAG substrate. This approach improves the accuracy of the reconstruction of THz characteristics of thin films [25, 26]. The transmittance/reflectance spectra of the YAG(111) substrate and $Tm_3Fe_5O_{12}$ film on

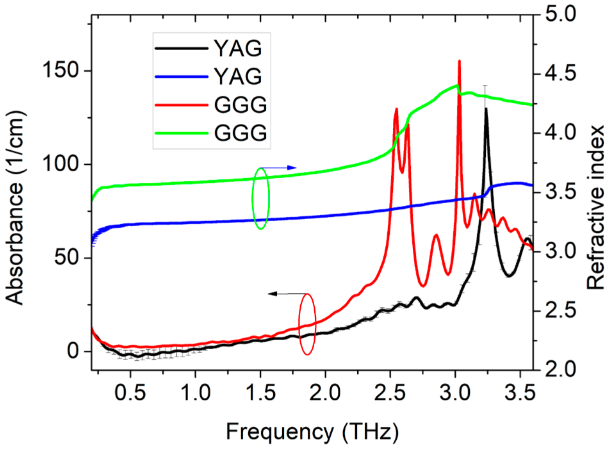

Fig. 6. Absorption coefficient and refractive index spectra of GGG(111) and YAG(111) substrates in the frequency range from 0.2 to 3.6 THz

this substrate are shown in Fig. 7a. As a result of the reconstruction of the THz characteristics [26], the spectra of the absorption coefficient and refractive index of the thulium iron garnet film on the YAG substrate were obtained (see Fig. 7b). The absorption coefficient tends to increase slowly in the high frequency region. The refractive index of the film has a large dispersion. At a fixed frequency of 2 THz, the absorption coefficient of the film was 13 cm^{-1}, and the refractive index was 2.8, which is typical for materials with low conductivity.

4. Conclusions

Thin $Tm_3Fe_5O_{12}$ iron garnet films were obtained on single-crystal GGG(111) and YAG(111) substrates using the MOCVD method. It was found that due to the volatility of gallium(I) oxide under deposition conditions (910 °C and P_{O2} = 1 mbar) the introduction of iron oxide into the surface layer of the substrate and enrichment of the adjacent layer of the film with thulium oxide occurs, which leads to the formation of non-stoichiometric garnet $Tm_3(Tm_xFe_{5-x})O_{12}$ with antisite defects [Tm_{Fe}^{3+}]. Thus, the epitaxial film of stoichiometric garnet $Tm_3Fe_5O_{12}$ grows on a GGG substrate with two interface layers. On the YAG substrate, the thulium iron garnet film is deposited without chemical interaction at the interface, but experiences strong in-plane compressive stress from the substrate. Films on a YAG substrate, transparent up to a frequency of 3.5 THz, have an advantage over films on GGG from the point of view of potential application in THz-range technology. As a result of the reconstruction of the THz characteristics, the frequency dependences of the absorption coefficient and the refractive index of the $Tm_3Fe_5O_{12}$ film on a YAG substrate were obtained.

Author contributions

Markelova M. N. – scientific supervision, research concept, processing of X-ray diffraction results and text writing. Hafizov A. A., Shi X. – conducting experiments on gas-phase deposition of thin films, processing the results of X-ray diffraction. Graboy I. E. – development of methodology, text writing. Shanin M. S., Konnikova M. R. – conducting experiments on Raman spectroscopy and terahertz spectroscopy. Shkurinov A. P. – scientific supervision, research concept, methodology development. Kaul A. R. – scientific supervision, research concept, methodology development, text editing.

Conflict of interests

The authors declare that they have no known competing financial interests or personal relationships that could have influenced the work reported in this paper.

References

1. Nikitov S. A., Kalyabin D. V., Lisenkov I. V. ... Pavlov E. S. Magnonics: a new research area in spintronics

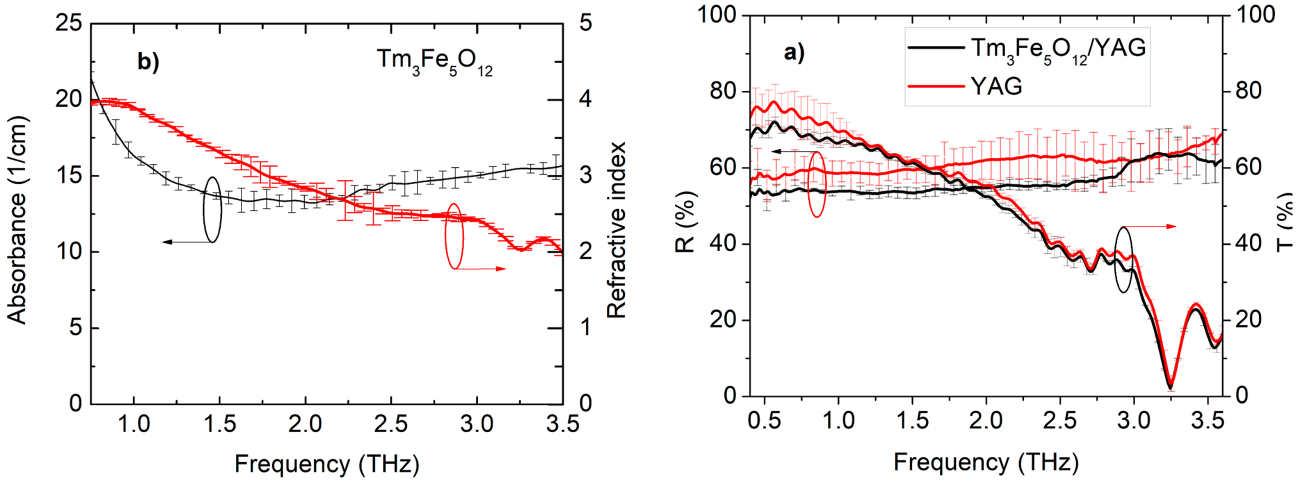

Fig. 7. Transmission, reflection (a), absorption and refractive index spectra of $Tm_3Fe_5O_{12}$ film (b) on YAG substrate in the THz frequency range. The standard deviation is calculated for three independent averages of 1000 accumulations each

and spin wave electronics. *Physics-Uspekhi*. 2015;58: 1002–1028. https://doi.org/10.3367/UFNr.0185.201510m.1099

2. Robertson J. M. Liquid phase epitaxy of garnets. *Journal of Crystal Growth*. 1978;45: 233–242. https://doi.org/10.1016/0022-0248(78)90441-4

3. Hibiya, T., Görnert, P. *Liquid phase epitaxy of garnets. Liquid phase epitaxy of electronic, optical and optoelectronic materials*. P. Capper and M. Mauk (eds.). John Wiley & Sons Limited, US; 2007. p. 305–339. https://doi.org/10.1002/9780470319505.ch11

4. Akchurin R. H., Marmalyuk A. A. *MOC-hydrid epitaxy in the technology of materials for photonics and electronics**. Technosphera Publ.; 2018. 488 p. (In Russ.)

5. Kaul A. R., Gorbenko O. Yu., Kamenev A. A. The role of heteroepitaxy in the development of new thin-film oxide-based functional materials. *Russian Chemical Reviews*. 2004;73(9): 861–880. https://doi.org/10.1070/rc2004v073n09abeh000919

6. Geller S. Crystal chemistry of the garnets. *Zeitschrift für Kristallographie*; 1967;125: 1–47. https://doi.org/10.1524/zkri.1967.125.16.1

7. Blank T. G. H., Mashkovich E. A., Grishunin K. A., … Kimel A. V. Effective rectification of terahertz electromagnetic fields in a ferrimagnetic iron garnet. *Physical Review B*. 2023;108: 094439. https://doi.org/10.1103/PhysRevB.108.094439

8. Volkov D. A., Gabrielyan D. A., Matveev A. A., … Nikitov S. A. Spin pumping from $Lu_3Fe_5O_{12}$. *JETP Letters*. 2024;119(5): 357–362. https://doi.org/10.1134/S0021364024600150

9. Kudasov Yu. B., Logunov M. V., Kozabaranov R. V., … Svetlov A. S. Magnetooptic properties of bismuth-substituted ferrite–garnet films in strong pulsed magnetic fields. *Physics of the Solid State*; 2018;60(11): 2207–2210. https://doi.org/10.1134/S106378341811015X

10. Kirilyuk A., Kimel A. V., Rasing T. Ultrafast optical manipulation of magnetic order. *Reviews of Modern Physics*. 2016;88: 039904. https://doi.org/10.1103/RevModPhys.82.2731

11. Kaul A. R., Nygaard R. R., Ratovskiy V. Yu., Vasiliev A. L. TSF-MOCVD – a novel technique for chemical vapour deposition on oxide thin films and layered heterostructures. *Kondensirovannye sredy i mezhfaznye granitsy = Condensed Matter and Interphases*. 2021;23(3): 396–405. https://doi.org/10.17308/kcmf.2021.23/3531

12. Nazarov M. M., Makarova S. A., Shkurinov A. P., Okhotnikov O. G. The use of combination of nonlinear optical materials to control terahertz pulse generation and detection. *Applied Physics Letters*. 2008;92: 021114. https://doi.org/10.1063/1.2831658

13. Coutaz J.-L., Garet F., Wallace V. *Principles of terahertz time-domain spectroscopy*. (1st ed.). New York: Jenny Stanford Publishing; 2018. 640 p. https://doi.org/10.1201/b22478

14. Hafizov A. A., Markelova M. N., Gu R., … Kaul A. R. Gas-phase deposition, structure and ferrimagnetic resonance of epitaxial garnet films of $Lu_3Fe_5O_{12}$*. *Solid state chemistry and functional materials – 2024: Proc. XIII All-Russ. Conf., 16–20 September 2024.* St. Petersburg: Novbytkhim Publ.; 2024. p. 405. (In Russ.)

15. Shannon R. D. Revised effective ionic radii and systematic studies of interatomic distances in halides and chalcogenides. *Acta Crystallographica Section A*. 1976;A32: 751–767. https://doi.org/10.1107/S0567739476001551

16. Karban' O. V. *Defects, crystal ordering, properties of oxides with garnet structure**. Cand. Phys. and Math. diss. Abstr. Izhevsk: 1999. 169 p. (In Russ.). Available at: https://www.dissercat.com/content/defekty-kristallograficheskoe-uporyadochenie-svoistva-oksidov-so-strukturoi-granata

17. Dong J., Lu K. Non-cubic symmetry in garnet structures studied using extended x-ray absorption fine-structure spectra. *Physical Review B*. 1999;43(11): 8808–8821. https://doi.org/10.1103/PhysRevB.43.8808

18. Efimov A. N., Lebedev A. O. *Geometric aspects of heteroepitaxy**. St. Petersburg: SPbGETU «LETI» Publ.; 2012. 110 p. (In Russ.)

19. Rabkin L. I., Soskin S. A., Epshtein B. Sh. *Ferrites. Structure, properties, production technology**. Leningrad: Energy Publ.; 1968. 384 p. (In Russ.)

20. Bilbao Crystallographic Server. Available at: https://www.cryst.ehu.es/

21. McDevitt N. T. Infrared lattice spectra of rare-earth aluminum, gallium, and iron garnets. *Journal of the Optical Society of America*. 1969;59(9): 1240–1244. https://doi.org/10.1364/josa.59.001240

22. Gaume R., Steere D., Sundaram S. K. Effect of nonstoichiometry on the terahertz absorption of $Y_3Al_5O_{12}$ optical ceramics. *Journal of Materials Research*. 2014;29(19): 2338–2343. https://doi.org/10.1557/jmr.2014.236

23. Pavlov V. V., Pisarev R. V., Fiebig M., Fröhlich D. Optical harmonic generation in magnetic garnet epitaxial films near the fundamental absorption edge. *Physics of the Solid State*; 2003:45(4): 662–669. https://doi.org/10.1134/1.1569002

24. Sharma A., Ciubotariu O. T., Matthes P., … Salvan G. Optical and magneto-optical properties of pulsed laser-deposited thulium iron garnet thin films. *Applied Research*. 2024;3: e202200064. https://doi.org/10.1002/appl.202200064

25. Konnikova M. R., Tretyakov A. K., Shevchenko A. R., … Shkurinov A. P. PCM for driving active THz modulators: frequency and polarization sensitivity. *2024 International Conference Laser Optics (ICLO)*, Saint Petersburg, Russian Federation, 2024: c. 326–326. https://doi.org/10.1109/ICLO59702.2024.10624176

26. Konnikova M., Tretyakov A., Kistenev Y., Ozheredov I., Coutaz J.-L., Shkurinov A. Novel method for extracting electromagnetic parameters of thin films based on dual-mode terahertz time-domain spectroscopy measurements. *Journal of Infrared, Millimeter, and Terahertz Waves*; 2024. (in press)

* *Translated by author of the article*

Information about the authors

Maria N. Markelova, Cand. Sci. (Chem.), Research Fellow at the Department of Chemistry, Lomonosov Moscow State University (Moscow, Russian Federation).

https://orcid.org/0000-0002-1014-9437
maria.markelova@gmail.com

Abduvosit A. Hafizov, graduate student at the Higher School of Material Science, Lomonosov Moscow State University (Moscow, Russian Federation).

https://orcid.org/0009-0003-0740-8180
abduvosithafizov220@gmail.com

Xiaoyu Shi, master degree student at the Higher School of Material Science, Lomonosov Moscow State University (Moscow, Russian Federation).

https://orcid.org/0009-0007-4025-9032
s1169608828@gmail.com

Igor E. Graboy, Cand. Sci. (Chem.), Senior Research Fellow at the Department of Chemistry, Lomonosov Moscow State University (Moscow, Russian Federation).

https://orcid.org/0009-0003-7011-2200
graboi@inorg.chem.msu.ru

Maxim S. Shanin, graduate student, Junior Research Fellow at the Department of Physics, Lomonosov Moscow State University (Moscow, Russian Federation); Research Fellow at National Research Centre "Kurchatov Institute" (Moscow, Russian Federation).

https://orcid.org/0009-0007-7215-4024
shaninms@my.msu.ru

Maria R. Konnikova, Junior Research Fellow at the Department of Physics, Lomonosov Moscow State University (Moscow, Russian Federation); Junior Research Fellow at National Research Centre "Kurchatov Institute" (Moscow, Russian Federation).

https://orcid.org/0000-0003-4701-6483
konnikova.mr20@physics.msu.ru

Alexander P. Shkurinov , Dr. Sci. (Phys.–Math.), Corresponding member of the Russian Academy of Sciences, Full Professor at the Chair of General Physics and Wave Processes, Lomonosov Moscow State University (Moscow, Russian Federation).

https://orcid.org/0000-0002-6309-4732
ashkurinov@physics.msu.ru

Andrey R. Kaul, Dr. Sci. (Chem.), Full Professor at the Chair of Inorganic Chemistry, Lomonosov Moscow State University, Moscow, Russian Federation

https://orcid.org/0000-0002-3582-3467
arkaul@mail.ru

Received 14.08.2024; approved after reviewing 10.09.2024; accepted for publication 16.09.2024; published online 25.03.2025.

Translation by Valentina Mittova

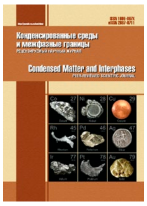

ISSN 1606-867X (Print)
ISSN 2687-0711 (Online)
Condensed Matter and Interphases
Kondensirovannye Sredy i Mezhfaznye Granitsy
https://journals.vsu.ru/kcmf/

Original articles

Research article
http://doi.org/10.17308/kcmf.2025.27/12489

Topography and microrelief electroless Ni-P coatings at different loading densities

I. V. Petukhov✉, N. A. Medvedeva

Perm State University,
15 ul. Bukireva, Perm 614990, Russian Federation

Abstract

The aim of this study was to investigate the growth processes of Ni-P coatings at different loading densities of the electroless nickel plating bath. The Ni-P coatings can be used to improve the thermal and corrosion resistance of optical fiber used to manufacture sensors of various physical quantities.

When depositing coatings on optical fiber, the loading density is an important parameter. The study investigated the influence of loading density on the topography, microrelief, roughness, and growth mechanism of Ni-P coatings using non-contact high-resolution optical profilometry. An increase in loading density from 0.5 to 3.0 dm^2/l did not lead to a significant change in the roughness parameters of the coatings. During the growth of coatings, “spheroids” strongly elongated in the plane of the substrate were formed on the surface. An analysis of growth processes was carried out within the framework of the layered growth mechanism. The growth rates of spheroids in normal and lateral directions were assessed. An increase in the loading density led to a decrease in the growth of spheroids in the normal direction, while the growth rate in the lateral direction was maximal at a loading density of 2 dm^2/l. Statistical analysis of the sizes of the “spheroids” showed that their distribution deviated from the normal law, which may be due to the fact that not only individual spheroids, but also their aggregates were considered in calculations. Another reason for the deviation may be a decrease in the proportion of the active surface on which the coating is deposited as the loading density increases.

Since increasing the loading density from 0.5 to 3.0 dm^2/l did not lead to a significant change in the roughness parameters even with coating thickness of ~ 8 μm or higher; deposition of coatings with the thickness up to 3.5 μm thick on optical fibers can be carried out at the specified loading densities with acceptable surface roughness.

Keywords: Optical fiber, Ni-P coatings, Electroless deposition, Non-contact profilometry, Topography, Microrelief, Roughness, Growth mechanism, “Spheroids”, Statistical analysis

Acknowledgements: The research was supported by the PERM SCIENTIFIC AND EDUCATIONAL CENTER “RATIONAL SUBSOIL USE”, 2023.

For citation: Petukhov I. V, Medvedeva N. A. Topography and microrelief electroless Ni-P coatings at different loading densities. *Condensed Matter and Interphases*. 2025;27(1): 115–127. http://doi.org/10.17308/kcmf.2025.27/12489

Для цитирования: Петухов И. В., Медведева Н. А. Влияние плотности загрузки на топографию и микрорельеф Ni-P покрытий. *Конденсированные среды и межфазные границы*. 2025;27(1): 115–127. http://doi.org/10.17308/kcmf.2025.27/12489

✉ Igor V. Petukhov, e-mail: petukhov-309@yandex.ru

© Petukhov I. V, Medvedeva N. A., 2025

The content is available under Creative Commons Attribution 4.0 License.

1. Introduction

Chemically electroless Ni-P coatings have a variety of applications in mechanical engineering, power engineering, and electronics [1] due to the ability to deposit hard, corrosion-resistant, heat-resistant coatings on products of complex configuration and also on dielectrics [2–6].

Currently, optical fiber (OF) is used not only for transmitting information, but also for the production of sensors of various physical quantities (temperature, stress, pressure, etc.) in the oil, gas, and nuclear energy industries [7–10]. Operating conditions of sensors may include temperatures up to 600 °C and aggressive environments. Usually, the OF is produced with a polymer protective and strengthening coating, which protects it from external mechanical influences and moisture [11–12]. Such optical fiber can operate at temperatures up to 200 °C [13]. In order to increase the operating temperature, metallized OF are used, in which a protective and strengthening coating of copper or aluminum is applied directly in the drawing column from molten metal. The operating temperature of such fibers in air is 350–400 °C. However, the copper coating does not sufficiently protect the optical fiber at high temperatures [14]. Nickel-coated optical fiber has higher corrosion resistance [15].

A layer of Ni-P coating can be applied over the metallized copper layer to increase corrosion resistance and heat resistance [16–17]. Such coatings were used in the manufacture of pressure sensors [18]. The coating can be two-layer, a thin layer of Ni-P coating and a thicker layer of electrodeposited nickel [19].

The roughness of the coatings [19–21], determined by the deposition conditions and the composition of the solution, is of great importance. In addition, the lower the roughness of the coatings, the less probable the formation of cavities due to stresses arising from temperature differences [20].

Thus, the application of nickel coatings to metallized optical fiber can be carried out in two ways: electrochemical or electroless nickel plating. In the first case, continuous pulling of the fiber through the nickel plating bath will be required; in the second case, due to the peculiarities of the process, the coating can be applied to a spool of optical fiber. The influence of a number of parameters on the microrelief and growth processes of Ni-P coatings was previously studied [22–25]. In electroless deposition, one of the significant factors is the loading density (the ratio of the area of the surface to be coated to the volume of the solution). In this study, the influence of loading density on the roughness and microrelief of Ni-P coatings was investigated using polished steel samples as the model objects.

2. Experimental

The coatings were deposited on polished samples of 20X13 steel and optical fiber with a quartz core diameter of 125 µm and a copper layer thickness of 18 µm. A copper layer was deposited on the optical fiber from the melt directly in the fiber drawing column.

Mechanical polishing of steel was carried out using a STRUERS LaboPol-2 polishing machine. The coatings copy the microrelief of the substrate, therefore, to eliminate the influence of the microrelief of the substrate on the microrelief of the deposited coatings, careful polishing of the substrate was performed.

Initially, polishing was carried out on Sic-Paper grinding wheels of class 220÷1000, which corresponds to a grain size of 50÷10 µm. Next, DiaPro diamond suspensions with particle sizes from 9 to 1 µm (Struers) were used. For the deposition of coatings, only steel samples with R_a (roughness) not exceeding 4 nm were selected.

Coatings were deposited on 20X13 steel samples for the investigation of the topography and microstructure of Ni-P alloys. The size of the samples was determined by the loading density, which varied from 0.5 to 3.0 dm^2/l.

Before deposition, the samples were degreased with alcohol, washed with distilled water and pickled in HCl (1:1) for 30–60 s. Deposition was carried out at 358 K under thermostatted conditions from a solution of the following composition, (M): $NiCl_2$ – 0.12; NaH_2PO_2 – 0.114; CH_3COONa – 0.12. The temperature was maintained with an accuracy of ±1°, the pH of the solution was 4.5. The reagents for the preparation of solutions were of chemically pure and analytical reagent grade (NaH_2PO_2) and were recrystallized twice. The required pH value was set by adding HCl (extra pure grade).

The thickness of Ni-P coatings on optical fiber was 3.5–4.0 µm. The plasticity of the optical fiber decreased with a higher coating thickness.

The coating thickness was determined gravimetrically, taking the coating density for Ni-P deposits to be 8.0 g/cm^3 [1].

The growth of the coatings and their phosphorus content were studied using a Hitachi S3400N scanning electron microscope and New View-7300 non-contact profilometer (Zygo). The following parameters were analyzed: PV – the maximum difference in height between the highest and lowest points of the profile surface; R_A - roughness, rms – standard deviation from the central line, R_z – the average absolute value of the five highest peaks and the five deepest depressions. The phosphorus content in the coatings was determined using energy dispersive analysis.

In addition, the average radii ($\bar{r}$), heights of "spheroids" ($\bar{h}$) and the average ratio of these values $\overline{\left(\frac{r}{h}\right)}$ were determined directly from the obtained microprofiles. The analysis of the obtained results was carried out using the MS Excel package. The confidence probability was adopted equal 0.95 for calculations of confidence intervals.

3. Results and discussion

Electroless Ni-P coatings on the surface of the optical fiber must be uniform (Fig. 1a), with a smoothed microstructure and low roughness, which in turn is determined by the deposition conditions, the composition of the elecrtoless nickel plating solution and the loading density. The microrelief of the coatings is determined by the presence of "spheroids" on the surface (Fig. 1b). These are formations elongated in the plane of the substrate with a fairly high ratio of the radius to the height of the "spheroid" [22–23].

The usually used loading density for deposition of coatings does not exceed 2.0 dm^2/l [1]. The study considers the influence of this technological parameter on the growth processes of Ni-P coatings.

The deposition rate had a steady tendency to decrease with an increased loading density (Table 1), which was described earlier [1].

The deposition rate decreased almost twofold with an increase in loading density from 0.5 to 3.0 dm^2/l (Table 1). Starting from a loading density of 1.0 dm^2/l the decrease in deposition rate with increasing loading density occurred almost linearly. An increase in the loading density caused a rapid decrease in the pH of the electroless nickel plating solution (Table 1), a decrease in the concentration of nickel ions and the reducing agent, thus the deposition almost stopped after some time. This was evidenced by a comparison of the dependences of the coating thickness obtained with deposition times of 40 and 60 min (Fig. 2). At a loading density of 3.0 dm^2/l the thickness of the coatings were almost identical.

The substrate had a significant influence on the topography of the growing coatings, since

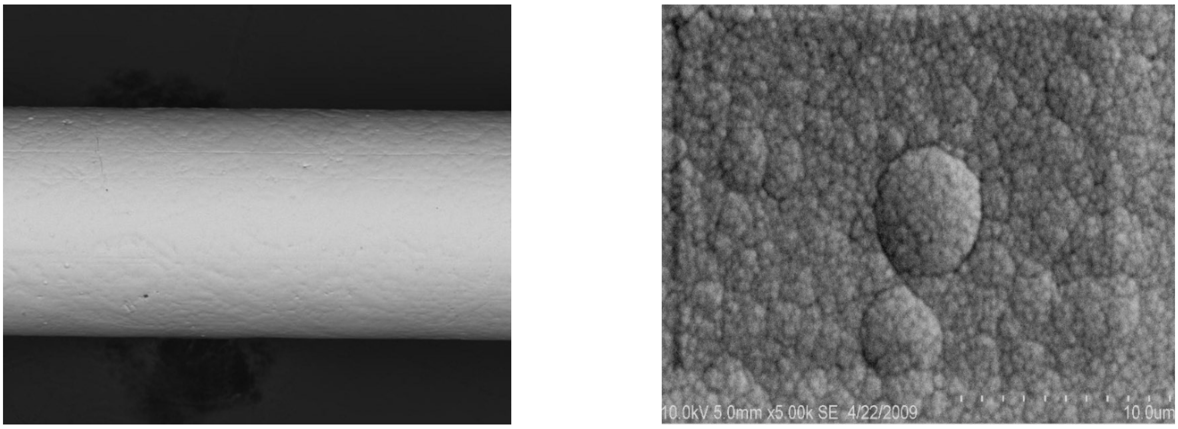

a b

Fig. 1. (a) Micrograph (250x magnification) of Ni-P coating on the surface of copper protective layer on the optical fiber, and (b) "spheroidal" structure of coating (5000× magnification)

Table 1. Coating deposition rate, phosphorus content and change in pH value of electroless nickel plating solution (ΔpH) after deposition at different loading densities

Loading, dm^2/l	Deposition rate, μm/h	Phosphorus content, wt. %	ΔpH
0.5	13.6±1.2	8.1±0.4	0.24±0.06
1.0	13.1±0.5	8.7±0.2	0.39±0.04
1.5	11.9±0.6	9.4±0.2	0.48±0.05
2.0	9.9±0.5	9.8±0.3	0.72±0.07
3.0	7.5±0.5	10.7±0.4	0.85±0.04

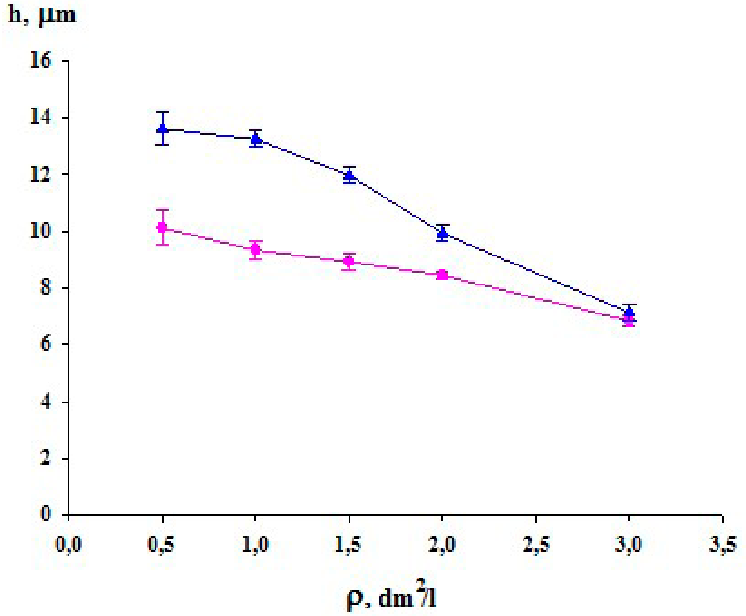

Fig. 2. Dependence of the coating thickness on the loading. Deposition time, minutes: 40 (●), 60 (▲)

Ni-P coatings accurately copied all the details of the substrate surface relief. The decrease in the deposition time will result in a reduction in the coating thickness, which may cause the substrate microrelief to affect the coating's surface topography. Taking this into account, the deposition duration in further studies was 60 min. Deposition at minimum loading density (0.5 dm^2/l) led to the formation of a typical surface relief of Ni-P coatings (Fig. 3). The surface of the coating contained numerous "spheroids", most of which overlapped into agglomerates of various shapes. At the same time, the surface relief was quite smooth, since the height of most "spheroids" did not exceed 30-40 nm.

Increase in the loading density did not qualitatively change the surface topography of the coatings (Fig. 4). The number of "spheroids" on the surface of the coating increased, they become smaller and formed agglomerates of various shapes. For this reason, the detection of clearly distinguishable spheroids was a difficult task.

Individual pores on the surface were detected on the surface, probably formed as a result of the adsorption of hydrogen bubbles, which prevented the deposition of the coating in this area.

The formation of grooves with a linear shape on the surface can probably be associated with the paths of hydrogen bubble removal from the coating surface. Another reason for their occurrence may be insufficient polishing of the steel substrate.

Increase in loading density up to 2 dm^2/l led to an increase in the radii of the "spheroids", which can be concluded from a comparison of the micrographs (Figs. 4 and 5). At the same time, the height of the "spheroids" became

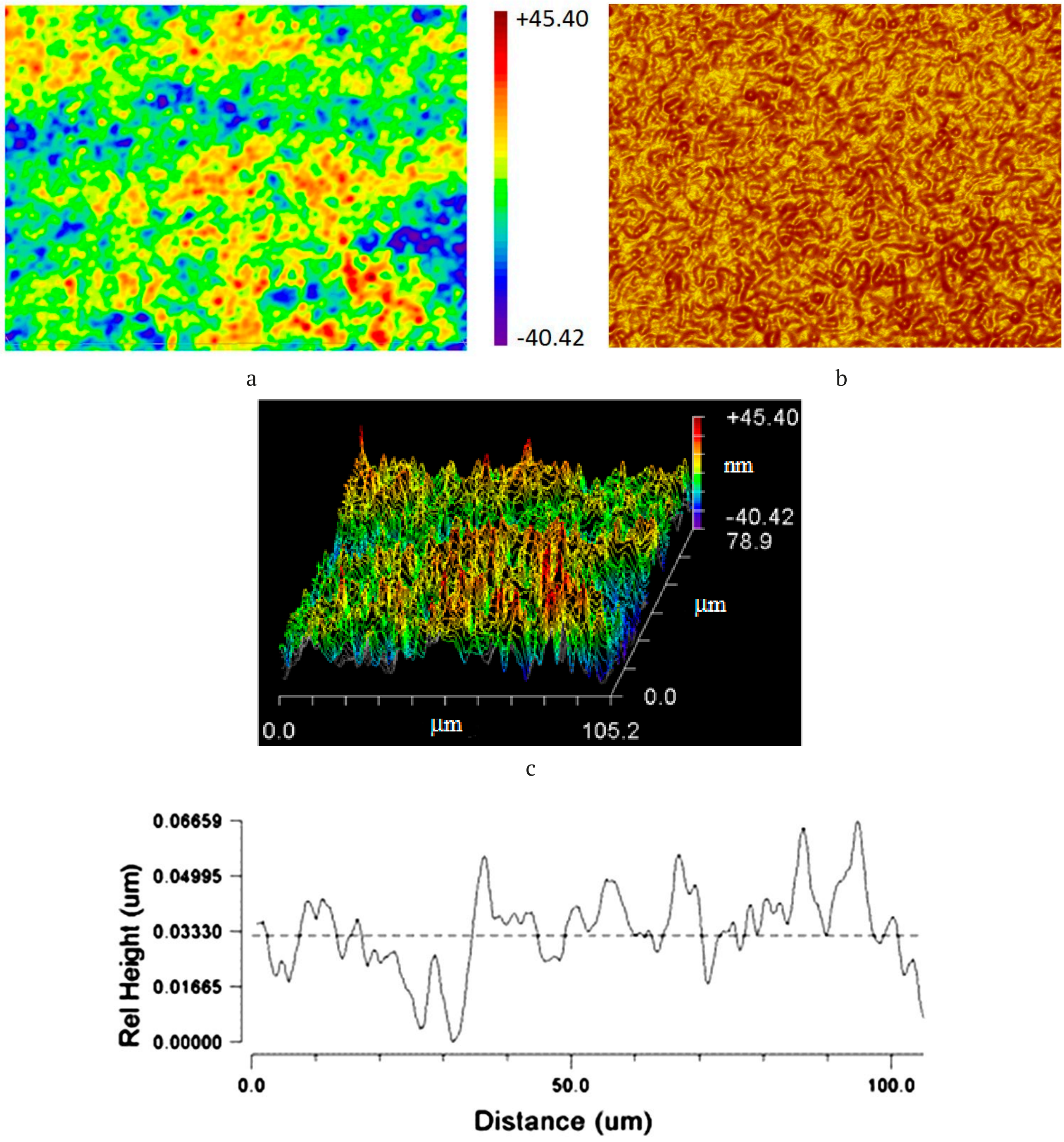

a b

c

d

Fig. 3. Topography and microrelief of the coating formed at loading of 0.5 dm^2/l: a – topographical height map; b – map of gradient; c – 3D image of the surface; d – microprofile along the selected direction

smaller. The topography and microrelief of the growing coating did not change fundamentally at the maximum loading density in our series of experiments of 3.0 dm^2/l; in addition to the “spheroids”, the same characteristic structural elements – pores and linear grooves.

For a more detailed comparison of roughness, the roughness parameters of the coatings obtained at the studied loading densities were analyzed (Table 2).

The comparison of the microroughness parameters of the coatings indicates that with an

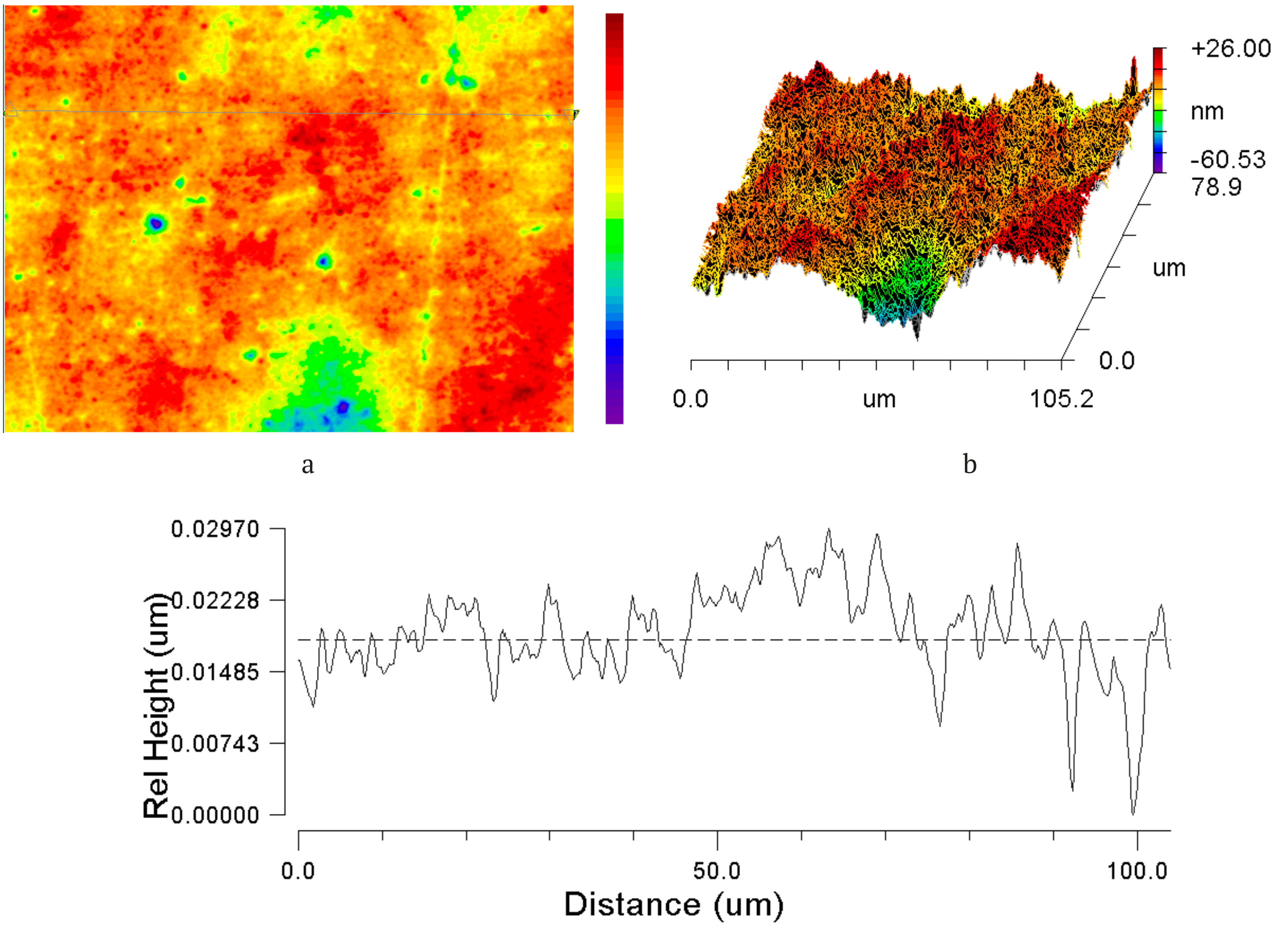

a

b

c

Fig. 4. Topography and microrelief of the coating formed at loading of 1 dm²/l: a – topographical height map; b – 3D image of the surface; c – microprofile along the selected direction

Table 2. Parameters of microroughness of Ni-P coatings, formed at different loadings

Loading, dm²/l	R_a, nm	*rms*, nm	R_z, nm	*PV*, nm
0.5	8.5±2.1	10.8±2.6	54.7±23.9	81.1±17.4
1.0	7.1±1.4	9.3±1.5	62.5±4.9	95.6±12.6
2.0	4.7±1.2	6.2±1.6	26.8±1.3	50.3±7.4
3.0	5.2±1.3	7.4±0.3	51.3±16.6	72.5±25.0

increase in the loading density, the roughness of the coatings did not tend to increase. Moreover, the parameters of microroughness of the coatings obtained at a loading density of 2.0 dm²/l were minimal in the studied series of samples.

At a loading density of 3.0 dm²/l, the microroughness parameters were also comparatively low. Some increase of parameters was possibly due to the fact that at a given loading density, localization of coating growth occurred at the end of deposition. This caused the appearance of irregularly shaped formations on the coating surface with a height of ~100 nm, protruding above the rest of the smoothed surface (Fig. 6). The approximate diameter of such formations was 100–250 μm.

The reason for the occurrence of such formations may be due to the low rate of the deposition process, the surface of the coating does not have time for renewal, and is poisoned by impurity compounds adsorbed from the solution. Only separate areas of the growing surface remain active, which causes localization of the growth of the coating.

Since the process of coating growth occurred through the formation of “spheroids”, further treatment of the results consisted of finding the

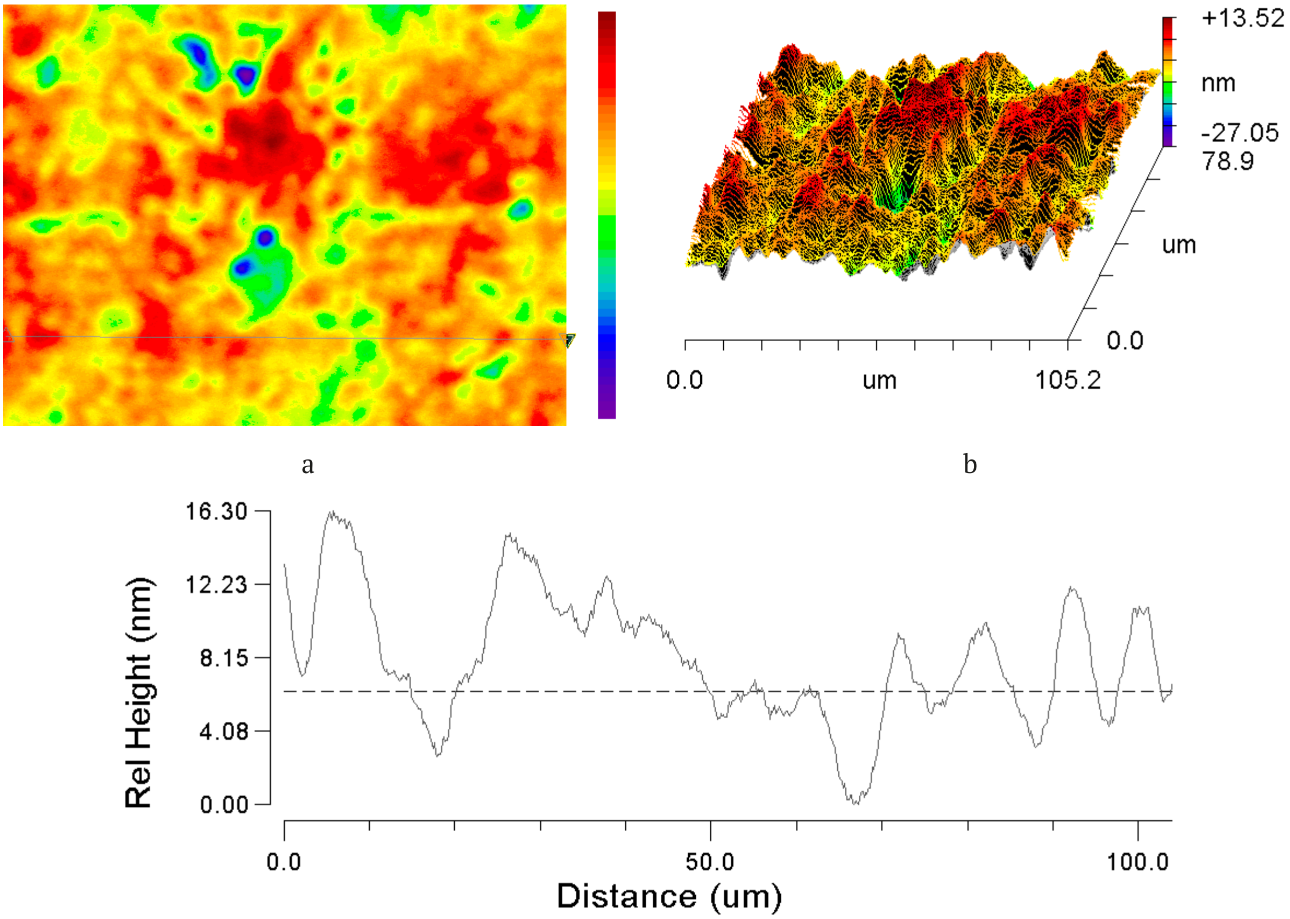

a

b

c

Fig. 5. Topography and microrelief of the coating formed at loading of 2 dm²/l: a – topographical height map; b – 3D image of the surface; c – microprofile along the selected direction

average values of the height ($\bar{h}$), the radius of the "spheroids" ($\bar{r}$) and the relationship of these parameters $\left(\overline{\frac{r}{h}}\right)$ (Fig. 7) based on profilograms. For processing fragments of profilograms where the "spheroids" clearly did not overlap were used.

The average values for each of the loading densities were obtained by averaging several samples, each of which yielded from 70 to 200 experimental values. The results of the treatment are presented in Table 3.

As can be seen from Table 3, changes of the parameters $\bar{h}$, $\bar{r}$, and the $\left(\overline{\frac{r}{h}}\right)$ ratio were non-monotonic. With increasing loading density up to 1 dm²/l the radii and heights of the "spheroids" decreased, while the $\left(\overline{\frac{r}{h}}\right)$ ratio practically did not change. The latter circumstance indicates a similar nature of growth of the coatings. At the same time, the decrease in the average radii and heights of the "spheroids" may be associated with an increase in passivation phenomena during the growth of the coating. A higher loading density caused more intensive acidification of the near-electrode layer of the solution, a decrease in the deposition rate, and increased inhibition of the deposition process by products.

Further increase in loading density up to 2.0 dm²/l led to a noticeable increase in the radii of the "spheroids" with a slight decrease in their heights. These opposite trends in the change of the parameters of the "spheroids" significantly increased the $\left(\overline{\frac{r}{h}}\right)$ ratio.

One of the probable reasons for the increase in the radii of the "spheroids" may be the insufficient

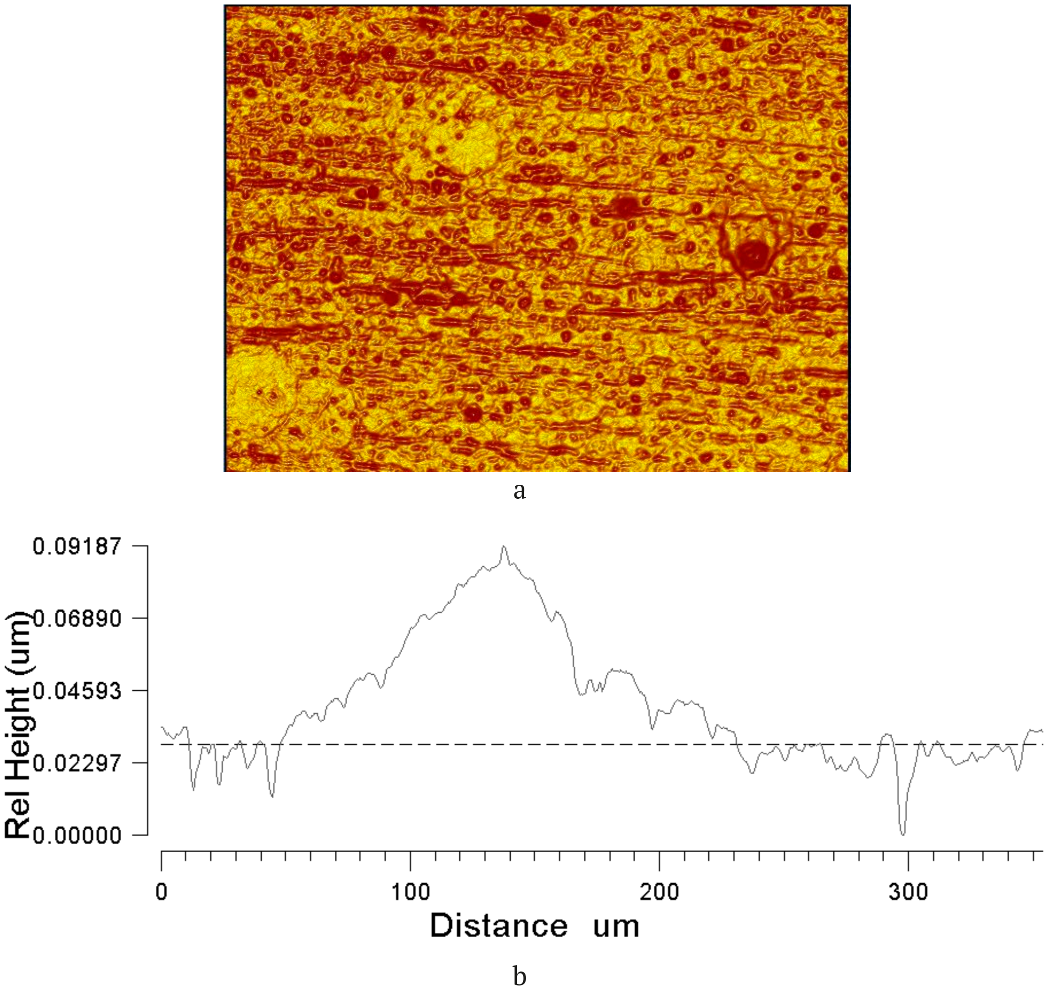

b

Fig. 6. Topography and microrelief of Ni-P coatings obtained at the loading of 3.0 dm^2/l: a – map of gradient; b – microprofile along the selected direction

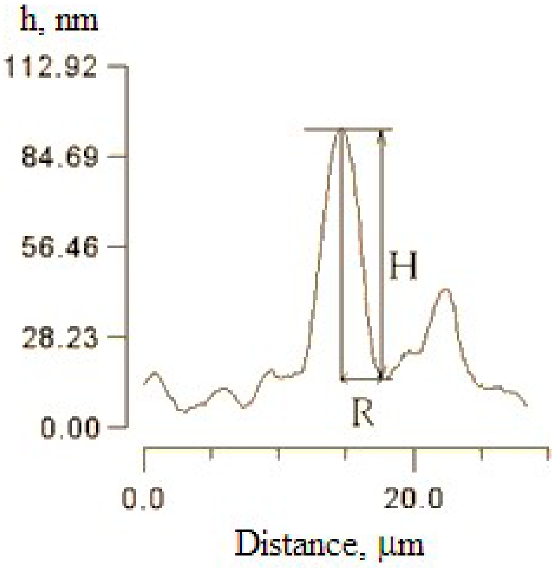

Fig. 7. The scheme of profilogram treatment

resolution of interference microscopy and 3D profilography methods for the study of the fine structure of the resulting "spheroids". It is possible that the "spheroids" observed under these conditions were aggregates of smaller "spheroids". The complex structure of "spheroids" was indicated by the results obtained by the AFM method [25–27]. At the same time, it cannot be ruled out that under conditions of sufficiently low catalytic activity of coating and a low deposition rate, the only possibility for growth was growth in the horizontal direction, which allows the generation of a juvenile coating surface. Similar phenomena were observed during the growth of coatings in the presence of stabilizing additives [23].

A decrease in the radii and the $\overline{\left(\frac{r}{h}\right)}$ ratio with a slight change in the height of the "spheroids"

Table 3. Parameters determined the size of “spheroids” and their growth rates in vertical plane (V_v) and substrate plane (V_s)

Loading, dm²/l	$\bar{r}$, μm	$\bar{h}$, nm	$\overline{\left(\frac{r}{h}\right)}$	$V_г$, nm/s	$V_в$, nm/s
0.5	2.77±0.14	21.22±1.46	143±9	880±46	6.74±0.44
1	1.53±0.08	11.1±0.7	155±9	994±59	6.40±0.01
2	3.63±0.26	8.1±0.7	478±29	2319±139	4.85±0.01
3	2.35±0.18	10.7±1.4	264±26	1073±107	4.05±0.01

was observed at a loading density of 3.0 dm²/l (Table 3).

Despite the complex nature of the change in the parameters of the “spheroids”, we attempted to use the layered growth mechanism to describe their growth processes [22-23, 25]. Within the framework of this mechanism, the average growth rates of “spheroids” in the lateral (V_h) and normal directions (V_v) were determined (Table 3).

Analysis of the results shown in Table 3 indicates that increasing the loading density decreased the rate of normal growth. It should be noted that its increase from 0.5 to 1.0 dm²/l had a relatively weak effect on growth rates in both normal and lateral directions.

The main reason for the decrease in normal growth rate was the acidification of the electroless nickel plating solution during the deposition process (Table 1). The acidification of the surface layer of the solution was even more expressed [28]. These changes in the composition of the solution blocked vertical growth.

The decrease in normal growth rate with a decreasing pH of the solution has been described previously [23]. Acidification of the solution with increasing loading density should also lead to a decrease in lateral growth, but the results indicated an increase in the growth rate of the “spheroids” in this direction. This was probably due to the fact that in this case, using profilometric measurements, we recorded the dimensions of not a single “spheroid”, but a formation composed by several “spheroids”.

Further processing of the obtained results consisted of statistical analysis of samples of radii and heights of “spheroids”, *r/h* ratio for each of the studied loading densities.

For each loading density, histograms of the spheroid size distribution were obtained (separately, histograms of the distribution by *r* and *h*), and the distribution of the ratio of these values (*r/h*). Histograms of the distribution of the values of *r*, *h* and the *r/h* ratio for coatings obtained at different loading densities are shown in Figs. 8–9.

In order to assess the compliance of the obtained distributions with the normal law, the values of the coefficients of asymmetry (γ_1^*), excess (γ_2^*) and the values of these coefficients acceptable for the normal distribution were calculated [28]:

$$\left|\gamma_1^*\right| \le \gamma_{1,\text{norm}}^*, \tag{1}$$

$$\left|\gamma_2^*\right| \le \gamma_{2,\text{norm}}^*, \tag{2}$$

Maximum permissible values of asymmetry coefficients $\left(\gamma_{1,\text{norm}}^*\right)$ and excess $\left(\gamma_{2,\text{norm}}^*\right)$ were calculated using the following formulas:

$$\gamma_{1,\text{norm}}^* = 3\sqrt{D\left(\gamma_1^*\right)}, \tag{3}$$

$$\gamma_{2,\text{norm}}^* = 5\sqrt{D\left(\gamma_2^*\right)}, \tag{4}$$

where $D\left(\gamma_1^*\right)$ and $D\left(\gamma_2^*\right)$ – the dispersions of these values determined using the following equations:

$$D\left(\gamma_1^*\right) = \frac{6(n-1)}{(n+1)(n+3)}, \tag{5}$$

Table 4. Statistical parameters of spheroids’ radius distribution

Loading, dm²/l	*r*, μm	γ_1^*	γ_2^*	*n*	$\gamma_{1\ \text{normal}}^*$	$\gamma_{2\ \text{normal}}^*$
0.5	2.8±0.1	1.7 6	0.81	142	0.60	1.94
1	1.5±0.1	0.78	1.02	195	0.52	1.68
2	3.6±0.3	-0.11	0.46	82	0.78	2.46
3	2.4±0.2	0.28	0.59	71	0.84	2.62

Table 5. Statistical parameters of spheroids' height distribution

Loading, dm²/l	h, nm	γ_1^*	γ_2^*	n	$\gamma_{1\,\text{normal}}^*$	$\gamma_{2\,\text{normal}}^*$
0.5	21.2±1.5	1.10	0.90	142	0.60	1.94
1	11.1±0.7	1.52	1.15	195	0.52	1.68
2	8.1±0.7	1.64	0.95	82	0.78	2.46
3	10.7±1.4	1.25	1.18	71	0.84	2.62

Table 6. Statistical parameters of r/h ratio distribution

Loading, dm²/l	r/h	γ_1^*	γ_2^*	n	$\gamma_{1\,\text{normal}}^*$	$\gamma_{2\,\text{normal}}^*$
0.5	143±9	1.66	0.81	142	0.60	1.94
1	155±9	22.2	3.69	195	0.52	1.68
2	478±29	8.88	2.57	82	0.78	2.46
3	264±26	0.11	0.51	71	0.84	2.62

$$D\left(\gamma_2^*\right)=\frac{24n(n-2)(n-3)}{(n+1)^2(n+3)(n+5)}. \qquad (6)$$

The results of the calculations performed for samples obtained at different loading densities are shown in Tables 4–6.

A comparison of the asymmetry and excess coefficients calculated for a sample of experimental values of the "spheroid" parameters with similar coefficients for a normal distribution allows to conclude that for most loading densities, the distribution of "spheroids" by size does not obey the normal law. Deviations from the normal law are caused by an increase in asymmetry coefficient values. The most heterogeneous is the distribution of the parameter r/h. This is obvious even from the appearance of the histograms (Fig. 8c, 9c) without additional statistical processing. The excess coefficient for most cases corresponded to a normal distribution.

The fact that the distribution of "spheroids" by size corresponded to the normal law may indicate that all "spheroids" grow by the same mechanism. The possible simultaneous implementation of normal and layered growth mechanisms was mentioned in [24]. Under the deposition conditions used in the study, no "spheroids" with a low r/h ratio were observed, which is typical for the mechanism of normal growth. Therefore, deviations from the normal distribution may be associated with the fact that in a number of cases, instead of individual spheroids, we registered aggregates of these "spheroids". The used method did not provide the required horizontal resolution. In order to obtain the required resolution, atomic

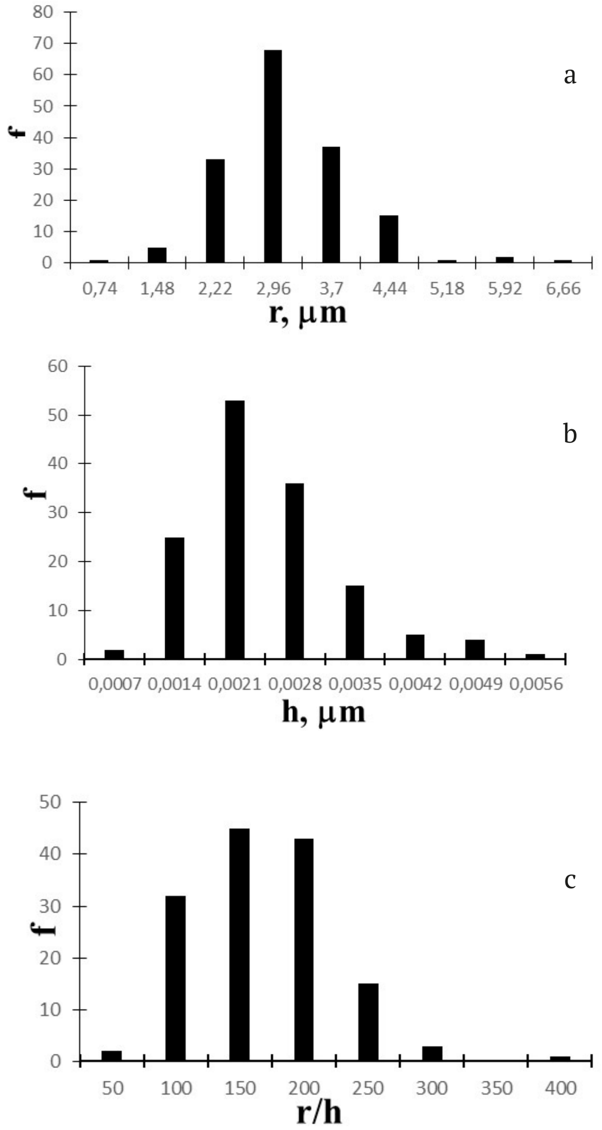

Fig. 8. r (a), h (b) and r/h ratio (c) distributions for spheroids obtained at loading of 0.5 dm²/l

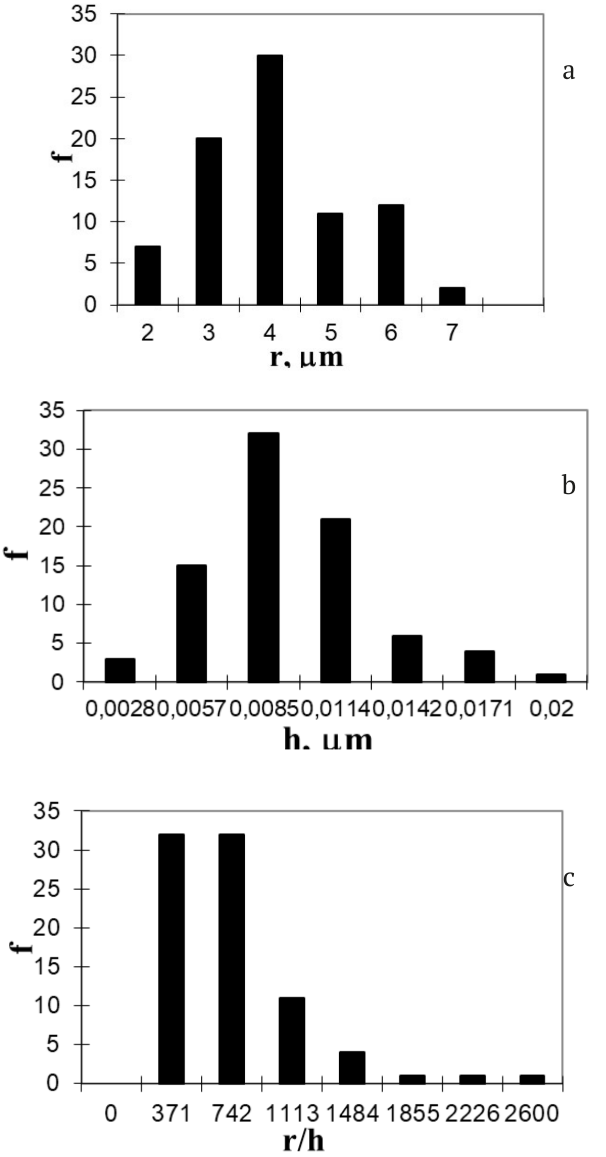

Fig. 9. *r* (a), *h* (b) and *r*/*h* ratio (c) distributions for "spheroids" obtained at loading of 2.0 dm^2/l

force microscopy should be used, but due to the labor intensity of the method, it will be difficult to obtain a similar sample size. The presence of individual "spheroids" and aggregates of them in one statistical sample may lead to deviations from the normal law.

At the same time, the obtained results do not contradict the layered growth mechanism, since during the coating deposition process, the pH of the electrolyte changes, the deposition rate decreases, which can enhance passivation phenomena on the growing surface. Due to this, the movement of individual atomic layers spreading over the surface can be blocked. For this reason, multiple growth centers (several growth layer packages) arise. These newly formed "spheroids" grow until they overlap with each other (Fig. 1b). In this way the structuring of the growing "spheroid" occurs. The rounded shape of these formations is determined by the fact that at this shape the surface energy is minimal at the spheroid-solution interface, since the amorphous structure of the coatings does not require crystalline faceting. If there is no change in the growth mechanism, it can be assumed that this will not have a significant impact on the calculation results presented in Table 3.

4. Conclusions

Thus, the investigation of growth processes at loading densities from 0.5 to 3.0 dm^2/l allows us to conclude that an increase in the loading density in the studied range of values does not lead to an increase in the roughness of the coatings. Probably, the condition for the transition to the normal growth mechanism and the corresponding increase in the roughness of the coatings is a sufficiently high catalytic activity of the surface accompanied by the discharge of nickel ions in the diffusion or diffusion-kinetic mode, which can occur with an increase in the temperature of the electroless nickel plating solution or with a decrease in the concentration of nickel ions [24].

An increase in the loading density increases the acidification of the electroless nickel plating solution during the deposition process, which contributes to an increase in the phosphorus content in the coatings and, as a consequence, a decrease in their catalytic activity in the oxidation reaction of the reducing agent (sodium hypophosphite), due to which the deposition rate significantly decreases.

Under condition of low deposition rates (low catalytic activity of coatings), conditions for the discharge of nickel ions in diffusion mode and the transition to the normal growth mechanism with the formation of dendritic deposits probably are not created. Therefore, with an increase in loading density, coatings with a smooth surface can be formed.

Some additional increase in roughness occurs only when the deposition rate is reduced to almost zero and the growth process occurs only on individual active areas of the coating surface.

The obtained results should be taken into account when depositing Ni-P coatings on the surface of optical fiber.

Contribution of the authors

The authors contributed equally to this article.

Conflict of interests

The authors declare that they have no known competing financial interests or personal relationships that could have influenced the work reported in this paper.

References

1. *Electroless nickel plating*: fundamentals to applications. Delaunois F., Vitry V., Bonin L. (eds.). *CRC Press*. 2019: 446. https://doi.org/10.1201/9780429466274

2. Sudagar J., Lian J., Sha W. Electroless nickel, alloy, composite and nano coatings – a critical review. *Journal of Alloys and Compounds*. 2013;571(15): 183–204. https://doi.org/10.1016/j.jallcom.2013.03.107

3. Chintada V. B., Koona R., Raju Bahubalendruni M. V. A. State of art review on nickel-based electroless coatings and materials. *Journal of Bio- and Tribo-Corrosion*. 2021;7(4): 1–14. https://doi.org/10.1007/s40735-021-00568-7

4. Muraliraja R., Selvan R. A. S., ... Sudagar J. A review of electroless coatings on non-metals: Bath conditions, properties and applications. *Journal of Alloys and Compounds*. 2023;960: 170723. https://doi.org/10.1016/j.jallcom.2023.170723

5. Biswas P., Das S. K., Sahoo P. Investigation of tribological and corrosion performance of duplex electroless Ni-P/Ni-Cu-P coatings. *Materials Today: Preceedings*. 2023;80(2): 1122–1129. https://doi.org/10.1016/j.matpr.2022.12.119

6. Oh S., Kim D., Kim K. Ch., Kim D.-I., Chung W., Shin B.-H. Electrochemical properties of electroless Ni plated super duplex stainless in 3.5% NaCl solution. *International Journal of Electrochemical Science*. 2023;18(10): 100287. https://doi.org/10.1016/j.ijoes.2023.100287

7. Lee B. Review of the present status of optical fiber sensors. *Optical Fiber Technology*. 2023;9: 57–79. https://doi.org/10.1016/S1068-5200(02)00527-8

8. Engelbrecht R. Fiber Optic strain and temperature sensing: overview of principles. *Proceedings Sensor*. 2017: 255–260. https://doi.org/10.5162/sensor2017/B6.1

9. Li J., Sun X., Huang L., Stolov A. Optical fiber for distributed sensing in harsh environments. *Fiber Optic Sensors and Applications XV, 13*. 2017; 106540E. https://doi.org/10.1117/12.2305433

10. Liu H. H., Hu D. J. J., Sun Q., ... Shum P. P. Specialty optical fibers for advanced sensing applications. *Opto-Electronic Science*. 2023;2(2): 220025. https://doi.org/10.29026/oes.2023.220025

11. Salunkhe T. T., Kim I. T. Sequential dual coating with thermosensitive polymers for advanced fiber optic temperature sensors. *Sensors*. 2023;23(6): 2898. https://doi.org/10.3390/s23062898

12. Janani R., Majumder D., Scrimshire A., ... Bingham P. A. From acrylates to silicones: a review of common optical fibre coatings used for normal to harsh environments. *Progress in Organic Coatings*. 2023;180: 107557. https://doi.org/10.1016/j.porgcoat.2023.107557

13. Popelka M., Stolov A. A., Hokansson A. S., Li J., Hines M. J. A new polyimide coating for optical fibers: demonstration of advantageous characteristics in harsh environments. *Optical Components and Materials XIX*. 2022;11997: 119970J. https://doi.org/10.1117/12.2608322

14. Popov S. M., Voloshin V. V., Vorobyov I. L., ... Chamorovski Y. K. Optical loss of metal coated optical fibers at temperatures up to 800 °C. *Optical Memory and Neural Networks (Information Optics)*. 2012;21(1): 45–51. https://doi.org/10.3103/S1060992X12010080

15. Lupi C., Vendittozzi C., Ciro E., Felli F., Pilone D. Metallurgical aspects of Ni-coating and high temperature treatments for FBG spectrum regeneration. *Materials*. 2023;*16*(8): 2943. https://doi.org/10.3390/ma16082943

16. Filas R. W. Metallization of silica optical fiber. *MRS Proceedings*. 1998;531: 263–268. https://doi.org/10.1557/PROC-531-263

17. Wysokiński K, Stańczyk T., Gibała K., ... Nasiłowski T. New methods of enhancing the thermal durability of silica optical fibers. *Materials*. 2014;7: 6947–6964. https://doi.org/10.3390/ma7106947

18. Rosolem J. B., Penze R. S., Bassan. F. R., ... Junior M. A. R. Electroless nickel-plating sealing in FBG pressure sensor for thermoelectric power plant engines applications. *Journal of Lightwave Technology*. 2019;37(18): 4791–4798. https://doi.org/10.1109/JLT.2019.2920120

19. Mei X., Jiang B. Thick nickel coating on surface of quartz optical fiber by electrochemical deposition method. *Applied Mechanics and Materials*. 2015;727-728: 51–55. https://doi.org/10.4028/www.scientific.net/AMM.727-728.51

20. Shiuea Sh.-Ts., Yang C.-H., Chub R.-Sh., Yang Ts.-J. Effect of the coating thickness and roughness on the mechanical strength and thermally induced stress voids in nickel-coated optical fibers prepared by electroless plating method. *Thin Solid Films*. 2005;485: 169–175. https://doi.org/10.1016/j.tsf.2005.04.024

21. Huang L., Wang Zh., Li Zh., Deng W.. Electroless nickel plating on optical fiber probe. *Chinese Optics Letters*. 2009;6: 472–474. https://doi.org/10.3788/COL20090706.0472

22. Petukhov I. V. Of the mechanism governing the growth of electrolessly deposits nickel-fhosphorus coatings. *Russian Journal of Electrochemistry*. 2007;43(1): 34–41. https://doi.org/10.1134/S1023193507010053

23. Petukhov I. V. The effect of component concentration in electroless nickel plating soluton on topography and microeliefof Ni-P coatings. *Russian Journal of Electrochemistry*. 2008;44(2): 147–157. https://doi.org/10.1007/s11175-008-2002-9

24. Petukhov I. V., Medvedeva N. A., Mushinskii S. S., Nabiullina M. R. Possible reasons for the appearance of metallic phase in electroless nickel plating solutions. *Russian Journal of Applied Chemistry*. 2012;85(1): 29–34. https://doi.org/ 10.1134/S1070427212010065

25. Petukhov I. V., Semenova V. V., Medvedeva N. A., Oborin V. A. Effect of deposition time on the formation of

Ni-P coating. *Bulletin of Perm University. CHEMYSTRY*. 2011;3(3): 47–56. Available at: https://www.elibrary.ru/item.asp?id=17563299

26. Wang J-Y., Peng B., Xie H-N., Cai W.-B. In situ ATR–FTIR spectroscopy on Ni–P alloy electrodes. *Electrochimica Acta*. 2009;54(6): 1834–184. https://doi.org/10.1016/j.electacta.2008.10.015

27. Elansezhian R., Ramamoorthy B., Kesavan N. The influence of SDS and GTAB surfactants on the surface morphology and surface topography of electroless Ni-P deposits. *Journal of Materials Processing Technology*. 2009;209: 233-240. https://doi.org/10.1016/j.jmatprotec.2008.01.057

28. Vashkyalis P.-A. Yu. *Regularities and mechanism of autocatalytic reduction of metals in aqueous solutions**. Dr. chem. sci. diss. Vilnius: 1982. 405 p. (In Russ.)

29. Akhnazarova S. L., Kafarov V. V. *Optimization of experiments in chemistry and chemical technology**. Moscow: Vysshaya Shkola Publ.; 1978. 319 p. (In Russ.)

** Translated by author of the article*

Information about the authors

Igor V. Petukhov, Cand. Sci. (Chem.), Associate Professor at the Department of Physical Chemistry, Perm State University (Perm, Russian Federation).

https://orcid.org/0000-0002-3110-668x
petukhov-309@yandex.ru

Natalia A. Medvedeva, Cand. Sci. (Chem.), Associate Professor, Head of the Department of Physical Chemistry, Perm State National Research University (Perm, Russian Federation).

https://orcid.org/0000-0002-0042-5418
nata-kladova@yandex.ru

Received 19.10.2023; approved after reviewing 18.04.2024; accepted for publication 15.05.2024; published online 25.03.2025.

Translated by Valentina Mittova

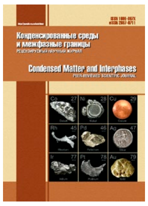

ISSN 1606-867X (Print)
ISSN 2687-0711 (Online)
Condensed Matter and Interphases
Kondensirovannye Sredy i Mezhfaznye Granitsy
https://journals.vsu.ru/kcmf/

Original articles

Research article
https://doi.org/10.17308/kcmf.2025.27/12490

Coulometric analysis method for determining the concentration and degree of oxidation of vanadium in the electrolyte of a vanadium flow battery using a hydrogen vanadium cell

E. A. Petukhova[1,2]✉, V. S. Ershova[1], A. V. Terentyev[1,2], E. A. Ruban[1], R. D. Pichugov[2,3], D. V. Konev[1], A. A. Usenko[1,2]

[1]*Federal Research Center of Problems of Chemical Physics and Medicinal Chemistry,
1 Academician Semenov ave., Chernogolovka 142432, Russian Federation*

[2]*InEnergy LLC,
2-nd Kotlyakovskiy Lane 18, Moscow 115201, Russian Federation*

[3]*D. I. Mendeleev Russian University of Chemical Technology,
9 Miusskaya pl., Moscow 125047, Russian Federation*

Abstract

Determining the vanadium content and the average degree of oxidation of vanadium ions in an electrolyte is a highly important task, both in the production and operation of vanadium flow batteries and in scientific research aimed at improving the performance characteristics of electrolytes throughout their entire life cycle. This article proposes a solution to this issue using the coulometric analysis of electrolyte samples circulating through a cell with a membrane-electrode unit consisting of a gas diffusion hydrogen electrode, a proton exchange membrane, and a liquid flow electrode. The coulometric analysis involves the oxidation of the sample to the highest degree of vanadium oxidation with further reduction to an oxidation state of +4. The parameters of the procedure (polarization modes and completion conditions) were chosen in order to minimize the relative error in determining the concentration of vanadium up to 5% and the average degree of oxidation up to 2% based on model composition electrolytes with different concentrations and degrees of vanadium oxidation, including sulfuric acid, as well as mixed acid (H_2SO_4 + HCl) compositions.

Keywords: Vanadium electrolyte, Vanadium flow batteries, Coulometry, Hydrogen electrode, Concentration, Degree of oxidation of vanadium

Funding: The study was supported by the Russian Science Foundation, project No. 22-73-00157.

For citation: Petukhova E. A., Ershova V. S. Terentyev A. V., Ruban E. A., Pichugov R. D., Konev D. V., Usenko A. A. Coulometric analysis method for determining the concentration and degree of oxidation of vanadium in the electrolyte of a vanadium flow battery using a hydrogen vanadium cell. *Condensed Matter and Interphases*. 2025;27(1): 128–138. https://doi.org/10.17308/kcmf.2025.27/12490

Для цитирования: Петухова Э. А., Ершова В. С., Терентьев А. В., Рубан Е. А., Пичугов Р. Д., Конев Д. В., Усенко А. А. Кулонометрический метод анализа для определения концентрации и степени окисления ванадия в электролите ванадиевой проточной батареи с использованием водородно-ванадиевой ячейки. *Конденсированные среды и межфазные границы*. 2025;27(1): 128–138. https://doi.org/10.17308/kcmf.2025.27/12490

✉ Elina A. Petukhova, e-mail: ea.petukhova@yandex.ru

© Petukhova E. A., Ershova V. S. Terentyev A. V., Ruban E. A., Pichugov R. D., Konev D. V., Usenko A. A., 2025

The content is available under Creative Commons Attribution 4.0 License.

1. Introduction

Redox flow batteries are a promising electrochemical technology for integrating with renewable energy sources due to their flexibility and scalability [1–3]. Vanadium flow batteries (VFB) have become obvious competitors in the future energy industry as dozens of projects have been implemented around the world, and their integration into energy networks continues [4, 5]. Vanadium flow batteries (VFB) consist of electrolyte tanks, graphite electrodes, ion exchange membranes, and circulation systems to ensure efficient energy storage. A significant part (from one third to one half) of the cost per kilowatt-hour (kWh) of energy accumulated using this technology is accounted for by electrolytes based on vanadium compounds [6]. Numerous studies have been aimed at optimizing the composition of vanadium electrolytes and their preparation methods, as well as their regular monitoring and performance improvement. The methods of electrolyte production and the study of reactions occurring in it are being constantly developed and improved due to continuous research [7–11].

The crossover of vanadium compounds [12, 13] and the occurrence of side electrode reactions during the operation of the VFB [14–16] result in decreased capacity due to a violation of the charge balance between positive and negative electrolytes (with the same volume of positive and negative electrolytes, the same concentration of vanadium compounds in them, and the total average degree of oxidation of the two electrolytes around +3.5). To solve this problem, various approaches are being developed, including passive and active rebalancing of the positive and negative capacity of the electrolyte: hydraulic shunting [17], pressure gradient [18], introduction of reducing agents [19], and auxiliary electrochemical devices that restore a vanadium electrolyte using water [20, 21] or hydrogen oxidation [22].

It should be noted that the production of an electrolyte and its operational maintenance require regular monitoring of the key characteristics of the electrolyte: the concentration and average degree of oxidation of vanadium ions. Several methods were proposed to solve this problem. For example, in [23–25] it was proposed to monitor the average oxidation state of a vanadium electrolyte using potentiometric measurements. To determine the total vanadium content in an electrolyte sample, another analytical method should also be used. In [26] it was proposed to add a reducing or oxidizing agent to transfer vanadium to a required valence state, while the concentration of vanadium in each valence state was calculated based on the volume of the initial sample and the amount of oxidizing/reducing agent added. The method can be supplemented by measurements of the absorption spectrum of the obtained solutions. The spectrophotometric method described in [27, 28] also requires preliminary calibration using references. The concentrations of vanadium compounds in the oxidation states of +3 and +4 in the test sample were determined based on these calibration dependencies. For electrolytes with a concentration of 1-2 M, the optical absorption ceased to depend linearly on the concentration, which complicated the calibration process. In addition, changes in the electrolyte composition regarding concentration and acid composition could cause shifts in the characteristic absorption peaks of vanadium compounds in the oxidation states of +3, +4, and +5 due to changes in the acidity of the solution and the appearance of new absorption bands caused by concentration-dependent complex vanadium compounds [29, 30]. The use of microelectrodes for amperometric studies seems promising, but its applicability was demonstrated only for reversible redox pairs of low-concentration vanadium electrolytes [31, 32].

The purpose of this study was to evaluate the applicability of the coulometric method for determining the characteristics of an electrolyte using a flow cell with a membrane-electrode assembly (MEA) of the composition H_2 (PtC)//proton exchange membrane//$V^{+(n-1)}/V^{+n}$ composition, where *n* ranged from 3 to 5. Previously, MEA of similar composition (combining gas diffusion hydrogen and liquid flow vanadyl/vanadate half-cells) were proposed for autonomous energy storage systems [33, 34] and as auxiliary devices for electrochemical rebalancing [35]. As far as we know, such MEA have not been used for analytical purposes in relation to the composition of the VFB electrolyte [36–38].

2. Experimental

Three samples were tested to determine the degree of oxidation and concentration of vanadium ions: 1 – sulfuric acid electrolyte with a composition of 1 M $VOSO_4$ in 4 M H_2SO_4 (vanadium oxidation state +4), 2 – sulfuric acid electrolyte with a concentration of 1.6 M vanadium and an average degree of vanadium oxidation of +3.5 in 2.4 M H_2SO_4 and 3 – mixed acid electrolyte from a commercial vanadium flow battery.

For sample 1, we used a sulfuric acid electrolyte prepared from vanadyl sulfate $VOSO_4{\cdot}3H_2O$ trihydrate of the reagent (Reakhim, Russia) and sulfuric acid (95%, Sigmatek, Russia) of the reagent grade. The vanadyl sulfate portion was dissolved in a pre-prepared 4 M sulfuric acid solution until a predetermined solution volume was reached.

For sample 2, we prepared a sulfuric acid electrolyte with a known vanadium concentration (1.6 M) and an average degree of vanadium oxidation of +3.5 in 2.4 M sulfuric acid from vanadium pentoxide V2O5 99.6% (Sigma-Aldrich, USA). The chemical reduction of vanadium pentoxide V_2O_5 to an oxidation state of +4 was conducted using oxalic acid (dihydrate, RG, VWR Chemicals, USA) in a 2.4 M solution of sulfuric acid with further electrolysis of a sulfuric acid solution of vanadium with an oxidation state of +4 divided into two portions to oxidation states of +3 and +5, respectively [39].

Sample 3 was a commercial mixed acid electrolyte synthesized according to the instruction received from LIAONING GREPALOFU NEW ENERGY CO.LTD within the ranges of precursor values provided by the company: vanadium (III) sulfate content – 10–15 wt. %, vanadium (IV) sulfate – 8–12 wt. %, sulfuric acid – 10–12 wt. %, water – 50–60 wt. %, hydrochloric acid – 10–12 wt. %. According to this instruction, the average concentrations in sample 3 were as follows: $C_v = 1.65$ M, $C(SO_4) = 2.7$ M, $C(Cl) = 3.014$ M. In this case, the concentration of vanadium in a commercial sample can be in the range from 1.32 to 1.98 M.

A background electrolyte solution was also prepared – a solution of sulfuric acid with a concentration of 4 M.

Electrochemical measurements were performed on the installation, the scheme of which is presented in Fig. 1, electrolyte tank (*2*), peristaltic pump (*3*) (BT100-1L, LongerPump, China). A hydraulic seal (*4*) was connected to the reservoir (*2*). The hydrogen source was the hydrogen generator GVCH-36A (*5*) (NPP Khimelectronics, Russia), and hydrogen was moistened through a Drexel flask filled with distilled water (*6*). The rate of hydrogen supply to the gas diffusion electrode was 2 l/h, the electrolyte circulation rate through the liquid flow electrode was 100 ml/min. Electrochemical measurements were performed on a P-20X galvanostat/potentiostat (Electrochemical Instruments) – (*7*). The potentiostat was connected to the cell (1) according to a two-electrode scheme: the working electrode was a liquid flow electrode, and the counter electrode was a hydrogen gas diffusion electrode. The description of the performed electrochemical measurements is presented in *3.1. Measurement parameters*.

A flow electrochemical cell used for measurements (see the diagram in Fig. 2) consisted of titanium end plates (1), Viton sheet plates (2), electrically conductive Graflex foil plates (3) (NPO Unimtek, Russia), nickel current collectors (4), graphite electrode plates (5, 8), Teflon flow frames (some with engraved flow channels 6a and the closing part 6b). The hydrogen gas diffusion electrode (7a) was

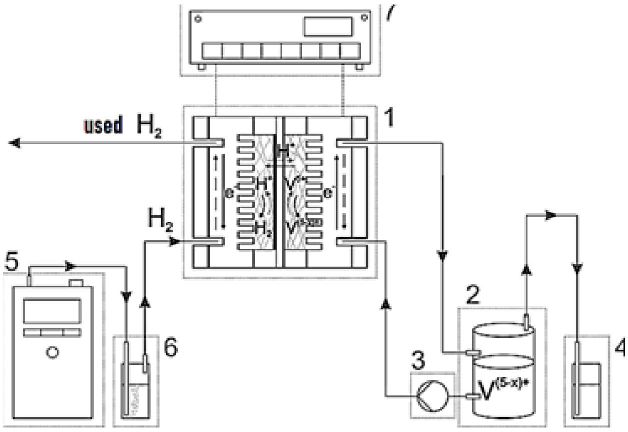

Fig. 1. Installation for determining the concentration and oxidation degree of vanadium in the electrolyte: *1* – flow electrochemical cell; *2* – reservoir for the analyzed electrolyte solution; *3* – peristaltic pump; *4* – water seal; *5* – hydrogen generator; *6* – hydrogen humidifier; *7* – potentiostat/galvanostat

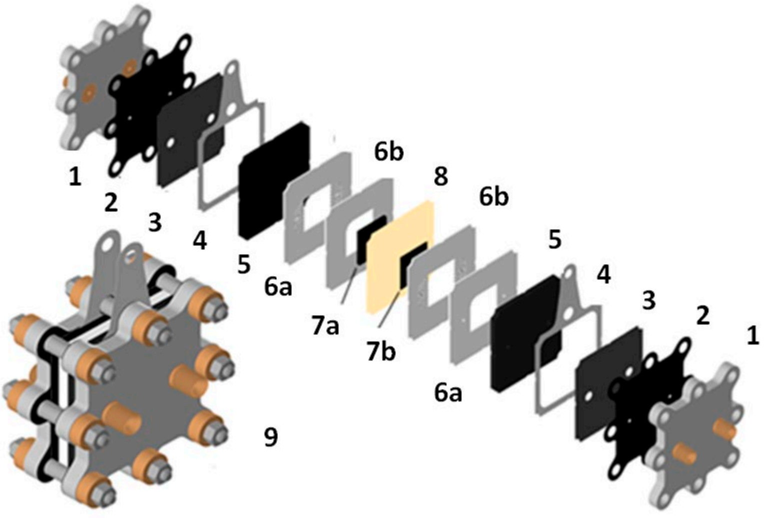

Fig. 2. Scheme of hydrogen-vanadium flow cell used in the experiment: *1* – end plates with fittings for supplying electroactive media (hydrogen and aqueous sulfate solution with vanadium electrolyte sample); *2* – elastomer sealing gasket; *3* – graphite foil gasket; *4* – metal foil terminals; *5* – graphite current-collector plates of the hydrogen electrode; *6* – flow frame of the electrode space area, consisting of two Teflon gaskets (*6*a, *6*b); *7*a – hydrogen gas diffusion electrode; *7*b – carbon felt electrode for vanadium half-cell; *8* – cation exchange membrane; *9* – scheme of assembled cell

a Freudenberg H23C8 carbon paper coated with Pt/C catalyst (0.516 mg/cm^2), and a carbon felt (Sigracell GFD 4.65EA-TA, SGL GmbH, Germany) (7b) was used as a porous flow electrode, while the proton exchange membrane (8) was made of a perfluorinated cation exchange membrane IEM-N102 (Zhongding New Energy Co., Ltd, China).

2.1. Measurement method for determining the concentration and average degree of oxidation of vanadium ions in a vanadium electrolyte using coulometric analysis

To analyze the sample, we used the apparatus presented in Fig. 1. For testing, we assembled a membrane electrode block (Fig. 2). The MEA was connected to the potentiostat using a two-electrode scheme so that the working electrode was made of a carbon felt, and a hydrogen gas diffusion electrode with a catalytic layer of Pt/C was the counter electrode.

The hydrogen was to be supplied to the gas diffusion electrode. To do this, we turned on a hydrogen generator (5) (GVCh-36A (NPP Khimelectronika, Russia)) and a peristaltic pump which circulated hydrogen through a moistening tank (6). Thus, a constant excess pressure of hydrogen ~20 mbar was maintained in the tank, regardless of whether hydrogen was consumed or generated on the cell during the measurements.

The carbon felt had to be moistened on the cathode side with a background electrolyte of 4 M H_2SO_4. To do this, we poured 20 ml of background electrolyte into the reservoir (2) and switched on the peristaltic pump (3). The pumping procedure of the background electrolyte for the newly assembled membrane electrode unit lasted about 30 minutes. The rate of hydrogen pumping through the gas diffusion electrode was 2 l/h, and the rate of electrolyte pumping on carbon felt was 100 ml/min.

If the unit is used again, the carbon felt must be washed with a background electrolyte solution before analysis. To do this, we turned on the peristaltic pump (3), poured 20 ml of background electrolyte into the tank (2), waited 5-10 minutes, and drained this electrolyte from the tank. This procedure must be repeated two more times.

To determine the Q^0_i charges, a sample of the background electrolyte was introduced into the reservoir (2), and the electrochemical measurement procedure was conducted in 4 stages, described in *3.1. Measurement parameters*.

The background electrolyte was drained after the procedure.

For the analysis itself, we added 10 ml of the background electrolyte and 1 ml of the test sample to the tank (2). Vanadium electrolyte tends to remain on the walls of the pipette, which was used to take the 1 ml of the sample. Therefore, to reduce the error in the analysis, it is recommended to introduce the test sample using a pipette, then, after mixing the sample with a solution of background electrolyte, take a dilute sample solution into this pipette, and drain it back into the tank. This must be repeated 3 times. Thus the remaining vanadium electrolyte can be washed from the walls of the pipette. After that, we performed the electrochemical measurement procedure described in *3.1. Measurement parameters* for determining the values of Q_i charges.

1.2. Methodology of coulometric analysis

The proposed method is based on transferring an electrolyte sample with vanadium compounds that have an unknown total concentration of C_v and an average oxidation state of *OS* to a completely oxidized state at an oxidation state of +5 and then to oxidation state of +4. The balance of charges that are spent on the oxidation and reduction stages are presented in Fig. 3. The charge at the oxidation stage, Q_{OX}, is related to the volume of the electrolyte sample, *V*, and the unknown average degree of oxidation of vanadium in it, *OS*, by the following ratio:

$$Q_{OX} = (5 - OS) \cdot C_V \cdot F \cdot V, \qquad (1)$$

where C_V is the concentration of all vanadium forms in the sample and *F* is Faraday constant. The charge passed through at the recovery stage, Q_{RED}, can be calculated using the formula:

$$Q_{RED} = C_V \cdot F \cdot V. \qquad (2)$$

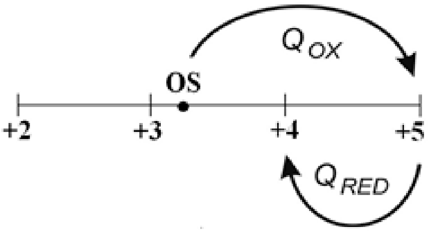

Fig. 3. Scheme of coulometric determination of the oxidation state and concentration of vanadium

Therefore, both unknowns, C_V and *OS*, were determined from the solution of the system of equations (1), (2):

$$OS = 5 - Q_{RED} / Q_{OX}, \qquad (3)$$

$$C_V = Q_{RED} / (F \cdot V). \qquad (4)$$

Thus, the task of finding C_V and *OS* is reduced to measuring Q_{OX} and Q_{RED}. And to do this, the conditions must be chosen that ensure the uniqueness of the electrochemical reactions of the conversion of vanadium redox forms, as well as to determine the conditions for conducting and completing the oxidation and reduction stages. This requires using a suitable coulometric cell, the development of a measurement procedure, and testing it on model compositions with known C_V and *OS*. The following part is devoted to this issue.

3. Results and discussion

3.1. Measurement parameters

In a hydrogen-vanadium cell with a membrane-electrode block of the composition H_2(Pt-C)|*IEM*|$V^{(n-1)+}/V^{n+}$, where *n* varies from 3 to 5, the following reactions occurred during the measurements:

$$V^{(OS)} \rightarrow V^{(+5)} + (5 - OS)e^-, \qquad (5)$$

$$V^{(+5)} + e^- \rightarrow V^{(+4)}, \qquad (6)$$

$$H^+ + e^- \leftrightarrow 1/2H_2, \qquad (7)$$

which means that the release/oxidation of hydrogen on a gas diffusion electrode was used in order to change the degree of oxidation of vanadium. Monitoring the potential of a liquid flow electrode was necessary to determine the completeness of the reactions (5, 6). In turn, the potential of a vanadium flow electrode can be controlled at a given cell voltage on condition that the hydrogen electrode is slightly polarizable. This was facilitated by the high exchange current of the reaction (7) as compared to both reactions (5, 6). To ensure the proper fulfilment of the condition of low polarizability of the gas diffusion electrode, hydrogen moistened at room temperature was supplied to it during the entire measurement, and the vanadium electrolyte sample was additionally diluted before measurement with an acidic background electrolyte in a ratio of 1:10. Such dilution not only reduced the polarization of the hydrogen electrode due to a decrease in flowing currents but also significantly decreased the number of vanadium ion transfers due to an increase in the ratio of concentrations of H+ and vanadium cations.

To select the cell voltages corresponding to the complete oxidation of vanadium to the oxidation state of +5 and its reduction to the oxidation state of +4, and at the same time excluding side reactions (oxidation of electrolyte components or electrode material in the first case and deeper reduction of vanadium in the second), voltammograms were recorded when a background electrolyte of 4 M H_2SO_4 and a vanadium electrolyte with an oxidation state of +4 were supplied to the liquid flow electrode (Fig. 4a, b).

The low current section on the background curve in Fig.4 (a) up to 1.3 V allowed assuming that at voltages less than 1.3 V, the current flowing through a cell with a vanadium electrolyte would be mainly determined by the conversion processes of vanadium compounds (i.e., the background current would be minimal). Judging by the curve in Fig. 5b, the undesirable process of vanadium reduction (+4) with a noticeable rate would begin at a voltage of less than 0.4 V. Thus, to ensure maximum current output of the first reaction (4), U_{max} = 1.3 V should not be exceeded, and excessive reduction of vanadium compounds to an oxidation state below +4 could be avoided if the second stage of coulometry was conducted at voltages not lower than U_{min} = 0.4 V.

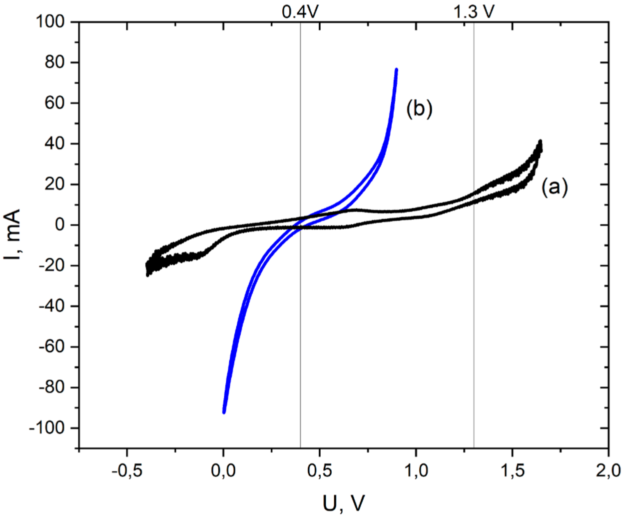

Fig. 4. Voltammograms of the hydrogen-vanadium cell measured at scan rate 20 mV/s for (a) 4 M sulfuric acid solution and (b) model electrolyte with vanadium oxidation state +4 supplied to the liquid electrode, respectively

To ensure the shortest duration of the sample analysis, the oxidation and reduction stages should be performed in a potentiostatic mode, setting the U_{max} and U_{min} measured above at the appropriate stages. However, the imposition of such great voltage surges will be accompanied by high pulse currents. The magnitude of these currents can be evaluated based on the data on the cell resistivity obtained by the electrochemical impedance method. This value calculated by the high-frequency cutoff of the hodograph, was about 0.4 Ohm×cm^2, which gave the pulse current density at the moment of switching U_{max} to U_{min}: $(U_{max}-U_{min})$/0.4 Ohm×cm^2 = 2.25 A/cm^2. The working surface area of the MEA (Fig. 2) was 4 cm^2, so the pulse current density for such MEA was ~ 9 A/cm^2.

As the total missed charge had to be accurately registered, measuring such currents (great at the beginning of each stage and close to zero at the end) significantly increased the requirements for the potentiostat in the installation. To get around this problem, each of the oxidation and reduction stages was divided into two steps: galvanostatic,

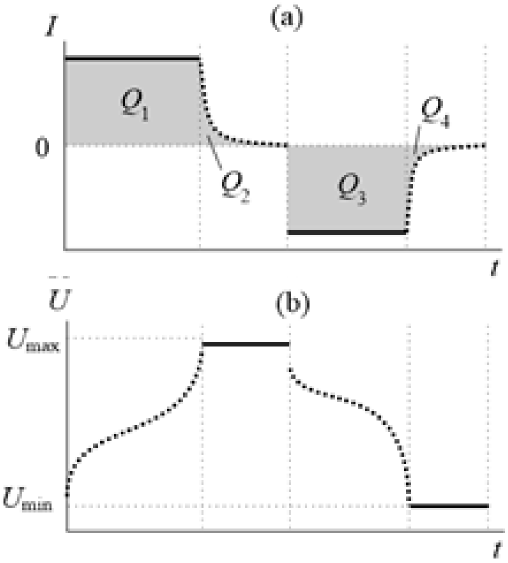

Fig. 5. Schematic dependencies of current (a) and voltage (b) on time during the two-step procedure of complete oxidation and partial reduction of vanadium compounds with each stage divided into galvanostatic and potentiostatic steps. Solid lines indicate the characteristics imposed on the cell, while dashed lines represent the measured values

on condition that it is completed upon reaching the limit voltage, and potentiostatic, that is maintaining the limit voltage until a small stationary current of the appropriate direction is reached. This scheme of two-stage cell polarization with the division of each stage into 2 steps is presented in Fig. 5, which shows separately the dependence of current (a) and voltage (b) on time. The Q_i charges measured at each of the four steps (where i is the step number) were related to Q_{RED} and Q_{OX} as follows: $Q_{OX} = Q_1 + Q_2$, a $Q_{RED} = Q_3 + Q_4$.

It should also be taken into account that when switching the current direction, the double electric layer (DES) was recharged on electrodes with a developed surface, as well as the electrochemical conversion of electroactive compounds that were not included in the aliquot of the analyzed electrolyte (the impurities contained in the background electrolyte, MEA materials and flow circuits of the installation, mainly the results of the analysis of the previous electrolyte portion with multiple repetition of the measurement). To reduce the errors caused by the above-mentioned factors, a preliminary measurement stage was introduced, which consisted of using the same polarization scheme of the cell (Fig. 5) with only the background electrolyte circulating in its liquid circuit. As a result, the values of Q^0_i were determined. These values were used to correct the Q_i charges measured during the analysis of the vanadium electrolyte. Thus, the final formulas for calculating the average degree of oxidation of *OS* and the concentration of C_v of a vanadium electrolyte sample were as follows:

$$OS = 5 - \frac{\left(Q_3 - Q_3^0\right) + \left(Q_4 - Q_4^0\right)}{\left(Q_1 - Q_1^0\right) + \left(Q_2 - Q_2^0\right)}, \tag{8}$$

$$c_V = \frac{\left(Q_3 - Q_3^0\right) + \left(Q_4 - Q_4^0\right)}{FV}. \tag{9}$$

Ratios (8) and (9) include the absolute values of the Q_i and Q_i^0 charges.

Figure 6 shows the results of applying this sequence of measurements to sample 1. As a condition for the termination of potentiostatic steps 2 and 4 we chose a decrease in the absolute current value to 3 mA/cm^2. This value was established experimentally as it was assumed by a stationary current that compensated for a change in the degree of oxidation of vanadium compounds as a result of crossover to the anode. Since this value was determined by the transport characteristics of the membrane and the catalytic layer of the anode with respect to vanadium compounds, its clarification was required for each new assembly of the MEA with materials of a different brand.

Table 1 shows the values of Q_i charges according to Fig. 6, as well as the values of Q^0_i at the preparatory stage of the background electrolyte analysis.

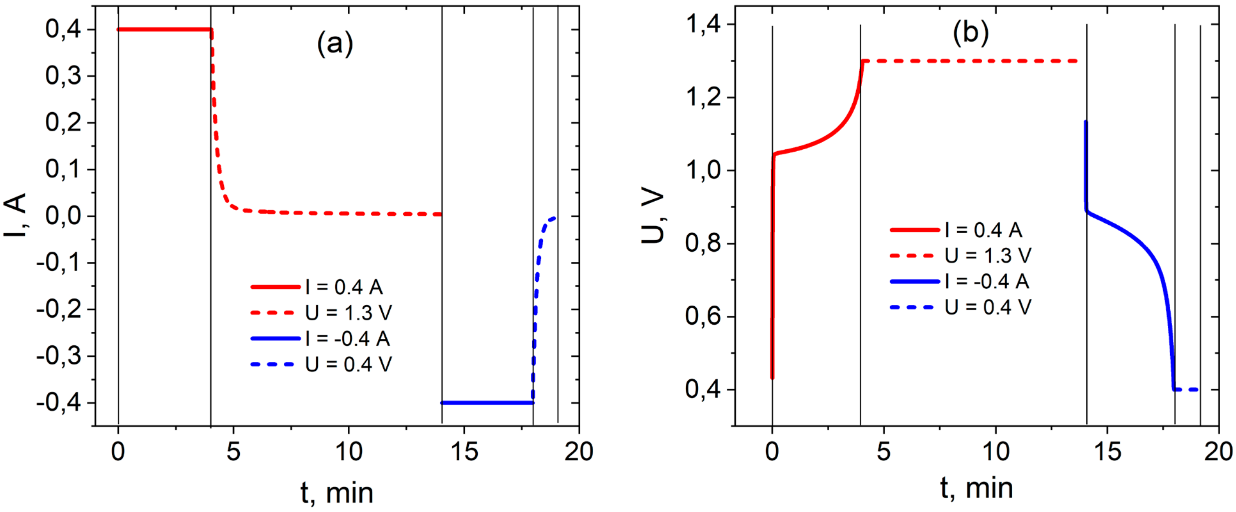

Fig. 6. Dependencies of current (a) and voltage (b) on time during the analysis of sample 1. Solid lines represent galvanostatic segments, while dashed lines represent potentiostatic segments. The legend denotes the parameters set at each of the 4 steps

Table 1. Charge values obtained during the analysis of sample 1 and the background electrolyte 4 M H_2SO_4

Procedure step number (i)	Sample 1	
	Q_i^0, C	Q_i, C
1	0.13	78.71
2	0.05	24.28
3	0.27	99.56
4	0.03	2.56

Based on the charge values indicated in Table 1, we calculated the concentration of vanadium ions C_v using formula (9), it was 1.05 M, and the average oxidation state of vanadium *OS* was calculated using formula (8), it was 3.99.

3.2. Reproducibility of research results

To assess the reproducibility of the method, we conducted a series of measurements on sample 1 and on sample 2. The results of these measurements are presented in tables 2 and 3, respectively.

To increase the accuracy of measurements of concentrations and degrees of oxidation, all experiments were performed on a single MEA. There was no increase in the deviation of the average concentration for sample 1 and sample 2 with the experiment number. It was random, which is an error in aliquot selection. The deviation of the values of the average degree of oxidation in all experiments for sample 1 and sample 2 was less than 1%.

Also, during the experiments we remeasured the correction values of charges on the background electrolyte $Q_{(i)}^0$ each time, while an increase in $Q_{(i)}^0$ charges, which could indicate contamination and/or degradation of MEA materials, was not observed. Therefore, the developed cell is expected to have a fairly large resource.

Table 2. Comparison of measurement results of the average oxidation state and vanadium concentration in sample 1 resulting from 4 experiments

Analysis No	Sample 1	
	C_V, M	*OD*
1	1.05	3.990
2	1.02	3.993
3	1.07	3.994
4	1.01	3.990
Average	1.04	3.992
	0.014	0.001
Confidence interval	1.04±0.04	3.992±0.003

3.3. Analysis of mixed acid electrolyte

To assess the performance of the proposed method for measuring the average degree of oxidation and concentration of vanadium electrolyte for other compositions of vanadium electrolytes in relation to mineral acids, we selected the mixed acid vanadium electrolyte, which is used in commercial vanadium flow batteries (sample 3).

To study the mixed acid electrolyte sample, we assembled a new cell where electrode materials and a membrane were replaced. The background electrolyte used to dilute the 1:10 sample was prepared according to the anionic composition of the studied mixed acid electrolyte.

Three experiments were conducted to determine the average degree of oxidation and concentration of the mixed acid vanadium electrolyte. Table 4 shows the values of the average degree of oxidation and concentration of vanadium electrolyte calculated using the measurement results for sample 3.

Table 3. Results of determining C_v and *OS* for sample 2

Analysis No	Sample 2	
	C_V, M	*OD*
1	1.610	3.51
2	1.597	3.49
3	1.602	3.49
4	1.612	3.49
Average	1.605	3.495
Standart deviation	0.004	0.005
Confidence interval	1.605±0.011	3.495±0.016

Table 4. Results of determining C_v and OS for sample 3

Analysis No	Sample 3	
	C_V, M	*OD*
1	1.440	3.38
2	1.460	3.39
3	1.480	3.39
Average	1.460	3.39
Standart deviation	0.011	0.003
Confidence interval	1.46±0.04	3.387±0.011

The average concentration of vanadium ions in a mixed acid electrolyte, calculated using the proposed method, was 1.46 M, which, according to the method, was within the range of permissible vanadium concentrations.

Although the spread of the results in the determined vanadium concentration for all three samples did not exceed 3% of the average value of the parameter being determined, it still significantly exceeded the spread of the *OS* measurement results (less than 0.3%). This parameter was determined with higher accuracy and reproducibility, as only coulometric data were used for its calculation, while the error in determining C_V included an error in aliquot selection.

4. Conclusions

We proposed a method for determining the main characteristics of the VFB electrolyte, which allowed obtaining values of the average degree of oxidation *OS* and concentration of vanadium ions C_v with a relative deviation from the average at 3% for concentration and 0.3% for degree of oxidation, with a duration of one measurement from several minutes to several dozens of minutes. At the same time, it required a laboratory with a fairly simple and inexpensive equipment: a hydrogen source, a peristaltic pump with a capacity of 20–100 ml/min, and a potentiostat operating with currents in the range from 1 mA to 0.5 A, as well as a measuring cell with a MEA area of several cm^2. This method will become popular at the sites of production of the VFB electrolyte, as well as in research laboratories dedicated to the development of the VFB area: the devices, installations, and materials necessary for its implementation are included in the basic equipment or are easily accessible, the measurement technique and result processing are simple, and the analytical characteristics are similar to the spectrophotometric method most commonly used for electrolyte analysis. The principle of the method, its experimental design, and the developed procedures (with slight variations) can be generalized to current-forming reactions with other electroactive substances in aqueous electrolytes, as they are based on their basic characteristic – the ability to conduct a redox transformation on electrodes with an approximate current output of 100% over a known potential range.

Author contributions

D. V. Konev – research concept, methodology development, scientific supervision. E. A. Petukhova – conducting research, text writing. E. A. Ruban, V. S. Ershova – conducting experiments. A.V. Terentyev – review writing. R. D. Pichugov – scientific editing of the text. A. A. Usenko – project administration.

Conflict of interests

The authors declare that they have no known competing financial interests or personal relationships that could have influenced the work reported in this paper.

References

1. Lourenssen K., Williams J., Ahmadpour F., Clemmer R., Tasnim S. Vanadium redox flow batteries: A comprehensive review. *Journal of Energy Storage*. 2019;25: 100844. https://doi.org/10.1016/j.est.2019.100844

2. Aluko A., Knight A. A review on vanadium redox flow battery storage systems for large-scale power systems application. *IEEE Access*. 2023;11: 13773–13793. https://doi.org/10.1109/ACCESS.2023.3243800

3. Daniel M., Byron N. P., Krowne C. M. Harnessing redox flow batteries for industrial applications: Opportunities and future directions. *Journal of Power Sources*. 2024;591: 233889. https://doi.org/10.1016/j.jpowsour.2023.233889

4. Jiang H. R., Sun J., Wei L., Wu M. C., Shy W., Zhao T. S. A high power density and long cycle life vanadium redox flow battery. *Energy Storage Materials*. 2020;24: 529–540. https://doi.org/10.1016/j.ensm.2019.07.005

5. Li J., Wang Q., Zhang J. Design and development of large-scale vanadium redox flow batteries for engineering applications. *Journal of Power Sources*. 2024;591: 233855. https://doi.org/10.1016/j.jpowsour.2023.233855

6. Minke C., Turek T. Techno-economic modelling and evaluation of flow batteries. In: *Flow batteries: from fundamentals to applications. Volume 2*. C. Roth, J. Noack, M. Skyllas-Kazacos (eds.). Wiley, VCH GmbH; 2023. p. 463–485. https://doi.org/10.1002/9783527832767.ch20

7. Sum E., Skyllas-Kazacos M. A study of the V (II)/V (III) redox couple for redox flow cell applications. *Journal of Power Sources*. 1985;15(2-3): 179–190. https://doi.org/10.1016/ 0378-7753(85)80071-9

8. Rahman F., Skyllas-Kazacos M. Solubility of vanadyl sulfate in concentrated sulfuric acid solutions. *Journal of Power Sources* 1998;72(2): 105–110. https://doi.org/10.1016/S0378-7753(97)02692-X

9. Li W., Zaffou R., Sholvin C. C., Perry M. L., She Y. Vanadium redox-flow-battery electrolyte preparation with reducing agents. *ECS Transactions*. 2013;53(7): 93. https://doi.org/10.1149/05307.0093ecst

10. Skyllas-Kazacos M., Cao L., Kazacos M., Kausar N., Mousa A. Vanadium electrolyte studies for the vanadium

redox battery—a review. *ChemSusChem*. 2016;9(13): 1521–1543. https://doi.org/10.1002/cssc.201600102

11. Fenton A. M., Jha R. K., Neyhouse B. J., ... Brushett F. R. On the challenges of materials and electrochemical characterization of concentrated electrolytes for redox flow batteries. *Journal of Materials Chemistry A*. 2022;10(35): 17988–17999. https://doi.org/10.1039/D2TA00690A

12. Lei Y., Zhang B. W., Zhang Z. H., Bai B. F., Zhao T. S. An improved model of ion selective adsorption in membrane and its application in vanadium redox flow batteries. *Applied Energy*. 2018;215: 591–601. https://doi.org/10.1016/j.apenergy.2018.02.042

13. Cecchetti M., Toja F., Casalegno A., Zago M. A comprehensive experimental and modelling approach for the evaluation of cross-over fluxes in vanadium redox flow battery. *Journal of Energy Storage*. 2023;68: 107846. https://doi.org/10.1016/j.est.2023.107846

14. Sun C. N., Delnick F. M., Baggetto L., Veith G. M., Zawodzinski T. A. Hydrogen evolution at the negative electrode of the all-vanadium redox flow batteries. *Journal of Power Sources*. 2014;248: 560–564. https://doi.org/10.1016/j.jpowsour.2013.09.125

15. Wei L., Zhao T. S., Xu Q., Zhou X. L., Zhang Z. H. In-situ investigation of hydrogen evolution behavior in vanadium redox flow batteries. *Applied Energy*. 2017;190: 1112–1118. https://doi.org/10.1016/j.apenergy.2017.01.039

16. Schilling M., Zeis R. Investigating the V (II)/V (III) electrode reaction in a vanadium redox flow battery – a distribution of relaxation times analysis. *Electrochimica Acta*. 2024;477: 143771. https://doi.org/10.1016/j.electacta.2022.141058

17. Bhattarai A., Ghimire P. C., Whitehead A., Schweiss R., Scherer G. G., Wai N., Hng H. H. Novel approaches for solving the capacity fade problem during operation of a vanadium redox flow battery. *Batteries*. 2018;4(4): 48. https://doi.org/10.3390/batteries4040048

18. Yan L., Li D., Li S., Xu Z., Dong J., Jing W., Xing W. Balancing osmotic pressure of electrolytes for nanoporous membrane vanadium redox flow battery with a draw solute. *ACS Applied Materials & Interfaces*. 2016;8(51): 35289–35297. https://doi.org/10.1021/acsami.6b12068

19. Cao L., Skyllas-Kazacos M., Menictas C., Noack J. A review of electrolyte additives and impurities in vanadium redox flow batteries. *Journal of Energy Chemistry*. 2018;27(5): 1269–1291. https://doi.org/10.1016/j.jechem.2018.04.007

20. Loktionov P., Konev D., Pichugov R., Petrov M., Antipov A. Calibration-free coulometric sensors for operando electrolytes imbalance monitoring of vanadium redox flow battery. *Journal of Power Sources*. 2023;553: 232242. https://doi.org/10.1016/j.jpowsour.2022.232242

21. Noack J., Roznyatovskaya N., Pinkwart K., Tübke J. Vanadium proton exchange membrane water electrolyser. *Journal of Power Sources*. 2017;349: 144–151. https://doi.org/10.1016/j.jpowsour.2017.03.039

22. Feng W., Zeng Y., Deng F., Yang P., Dai S. A hydrogen-vanadium rebalance cell based on ABPBI membrane operating at low hydrogen concentration to restore the capacity of VRFB. *Journal of Energy Storage*. 2023;74: 109363. https://doi.org/10.1016/j.est.2023.109363

23. Kim B. G., Lee S. J. *Method for preparing electrolyte for vanadium redox flow battery using vanadium oxide*. Патент US: № 9406961B2. Опубл. 02.08.2016.

24. Rudolph S., Schröder U., Bayanov I. M. On-line controlled state of charge rebalancing in vanadium redox flow battery. *Journal of Electroanalytical Chemistry*. 2013;703: 29–37. https://doi.org/10.1016/j.jelechem.2013.05.011

25. Haisch T., Ji H., Weidlich C. Monitoring the state of charge of all-vanadium redox flow batteries to identify crossover of electrolyte. *Electrochimica Acta*. 2020; 36: 135573. https://doi.org/10.1016/j.electacta.2019.135573

26. Li L., Liu Y., Sun C. *Methods for determining and/or adjusting redox-active element concentrations in redox flow batteries*. Патент US: № 9846116B2. Опубл. 17.12.2019.

27. Wu H., Liu S., Liu C. *Method for online detection of concentration of electrolyte of vanadium battery*. Патент CN: № 102621085B. Опубл. 06.11.2013.

28. Wu X., Wang J., Liu S., Wu X., Li S. Study of vanadium (IV) species and corresponding electrochemical performance in concentrated sulfuric acid media. *Electrochimica Acta*. 2011;56(27): 10197–10203. https://doi.org/10.1016/j.electacta.2011.09.006

29. Agarwal H., Florian J., Goldsmith B. R., Singh N. V2+/V3+ redox kinetics on glassy carbon in acidic electrolytes for vanadium redox flow batteries. *ACS Energy Letters*. 2019;4(10): 2368–2377. https://doi.org/10.1021/acsenergylett.9b01423

30. Petchsingh C., Quill N., Joyce J. T., ... Buckley D. N. Spectroscopic measurement of state of charge in vanadium flow batteries with an analytical model of VIV-VV absorbance. *Journal of The Electrochemical Society*. 2015;163(1): A5068. https://doi.org/10.1149/2.0091601jes

31. Stolze C., Meurer J. P., Hager M. D., Schubert U. S. An amperometric, temperature-independent, and calibration-free method for the real-time state-of-charge monitoring of redox flow battery electrolytes. *Chemistry of Materials*. 2019;31(15): 5363–5369. https://doi.org/10.1021/acs.chemmater.9b02376

32. Neyhouse B. J., Tenny K. M., Chiang Y. M., Brushett F. R. Microelectrode-based sensor for measuring operando active species concentrations in redox flow cells. *ACS Applied Energy Materials*. 2021;4(12): 13830–13840. https://doi.org/10.1021/acsaem.1c02580

33. Yufit V., Hale B., Matian M., Mazur P., Brandon N. P. Development of a regenerative hydrogen-vanadium fuel cell for energy storage applications. *Journal of The Electrochemical Society*. 2013;160(6): A856. https://doi.org/10.1149/2.086306jes

34. Hsu N. Y., Devi N., Lin Y. I., ... Chen Y. S. Study on the effect of electrode configuration on the performance of a hydrogen/vanadium redox flow battery. *Renewable Energy*. 2022;190: 658–663. https://doi.org/10.1016/j.renene.2022.03.151

35. Pichugov R., Loktionov P., Pustovalova A., ... Antipov A. Restoring capacity and efficiency of vanadium redox flow battery via controlled adjustment of electrolyte composition by electrolysis cell. *Journal of Power Sources*. 2023;569: 233013. https://doi.org/10.1016/j.jpowsour.2023.233013

36. Nolte O., Volodin I. A., Stolze C., Hager M. D., Schubert U. S. Trust is good, control is better: a review on monitoring and characterization techniques for flow battery electrolytes. *Materials Horizons*. 2021;8(7): 1866–1925. https://doi.org/10.1039/D0MH01632B

37. Zhao X., Nam J., Jung H. Y., Jung S. Real-time state of charge and capacity estimations of vanadium redox flow battery based on unscented Kalman filter with a forgetting factor. *Journal of Energy Storage*. 2023;74: 109146. https://doi.org/10.1016/j.est.2023.109146

38. Puleston T., Serra M., Costa-Castelló R. Vanadium redox flow battery capacity loss mitigation strategy based on a comprehensive analysis of electrolyte imbalance effects. *Applied Energy*. 2024;355: 122271. https://doi.org/10.1016/j.apenergy.2023.122271

39. Konev D. V., Loktionov P. A., Pichugov R. D., ... Kashin A. M. *Method for producing electrolyte for a vanadium redox flow battery**. Patent RF No.: 2803292C1. Pub.12.09.2023, bull. No. 26.

* Translated by author of the article.

Information about the authors

Elina A. Petukhova, Research Engineer, Federal Research Center of Problems of Chemical Physics and Medicinal Chemistry (Chernogolovka, Russian Federation).

https://orcid.org/0000-0003-2875-0324
ea.petukhova@yandex.ru

Valeria S. Ershova, Laboratory Assistant, Federal Research Center of Problems of Chemical Physics and Medicinal Chemistry (Chernogolovka, Russian Federation).

https://orcid.org/0009-0003-8261-3475
ershova.vs@yandex.ru

Alexander V. Terentyev, Engineer, Federal Research Center of Problems of Chemical Physics and Medicinal Chemistry (Chernogolovka, Russian Federation).

https://orcid.org/0000-0002-7591-9973
terentev.alxndr@yandex.ru

Evgeniy A. Ruban, Junior Research Fellow, Federal Research Center of Problems of Chemical Physics and Medicinal Chemistry (Chernogolovka, Russian Federation).

https://orcid.org/0000-0003-3832-1611
evgeny.ruban991@gmail.com

Roman D. Pichugov, Cand. Sci. (Phys.–Math.), Associate Professor, D. I. Mendeleev Russian University of Chemical Technology (Moscow, Russian Federation).

https://orcid.org/0000-0001-7353-2938
pichugov.r.d@muctr.ru

Dmitry V. Konev, Cand. Sci. (Chem.), Senior Research Fellow, Federal Research Center of Problems of Chemical Physics and Medicinal Chemistry (Chernogolovka, Russian Federation).

https://orcid.org/0000-0002-2188-9254
dkfrvzh@yandex.ru

Andrey A. Usenko, Cand. Sci. (Phys.–Math.), Research Fellow, Federal Research Center of Problems of Chemical Physics and Medicinal Chemistry (Chernogolovka, Russian Federation).

https://orcid.org/0000-0002-4119-5292
andy4uday@gmail.com

Received 23.04.2024; approved after reviewing 03.05.2024; accepted for publication 06.05.2024; published online 25.03.2025.

Translated by Marina Strepetova

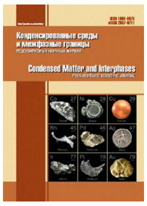

ISSN 1606-867X (Print)
ISSN 2687-0711 (Online)
Condensed Matter and Interphases
Kondensirovannye Sredy i Mezhfaznye Granitsy
https://journals.vsu.ru/kcmf/

Original articles

Research article
https://doi.org/10.17308/kcmf.2025.27/12490

The role of nanofillers of various nature in the morphological changes of the polymer binder for plywood production

E. V. Yushchenko[1]✉, L. I. Belchinskaya[1], A. V. Kostyuchenko[2], D. A. Zhukalin[3]

[1]*Voronezh State University of Forestry and Technologies named after G. F. Morozov,
8 ul. Timiryazeva, Voronezh 394087, Russian Federation*

[2]*Voronezh State Technical University,
84 ul. 20 let Oktyabrya, Voronezh 394006, Russian Federation*

[3]*Voronezh State University,
1 Universitetskaya pl., Voronezh 394018, Russian Federation*

Abstract

Nanomodification of the adhesive composition is one of the promising methods for improving the quality of wood laminated materials. Morphological changes in nanostructures make it possible to control the functional characteristics of the resulting nanocomposites. The shape and distribution of nanomodifiers of nanocellulose and multi-walled carbon nanotubes of urea-formaldehyde resin used to produce plywood have been studied by atomic force microscopy. The phase composition and crystal structure of biological and carbon nanofillers of the binder are investigated. Data on the qualitative and quantitative composition, structural state of nanocrystalline cellulose and multi-walled carbon nanotubes, as well as cured resin in pure and modified form, were obtained by X-ray diffractometry. The microrelief of the surface of the cured binder in the presence of multi–walled carbon nanotubes is characterized by uniformly distributed nanoclusions of 50 nm – 1 μm; and nanoclusions of 70 nm - 2 μm in the case of resin modification with nanocrystalline cellulose. Unmodified urea-formaldehyde resin is characterized by a low degree of crystallinity: the crystallite size is 10 nm. When modifying the resin with multi–walled carbon nanotubes, the crystal size increases to 18 nm, and when modified with nanocrystalline cellulose - up to 15 nm. The most probable type of lattice of the resin under study is a primitive cubic one with a parameter $a = 0.840$ nm. An increase in the volume of the unit cell of resin modified with multi-walled carbon nanotubes ($a = 0.844$ nm) and nanocrystalline cellulose ($a = 0.842$ nm) is observed. An increase in the size of the crystalline regions in the resin, as well as an increase in the volume of the resin unit cell as a result of the use of nanomodifiers, can help improve the performance of plywood.

Keywords: Crystal lattice, Urea-formaldehyde resin, Multi-walled carbon nanotubes, Nanocrystalline cellulose, Modification

Acknowledgments: Authors thank the reviewers for their contribution to the peer review.

For citation: Yushchenko E. V., Belchinskaya L. I., Kostyuchenko A. V., Zhukalin D. A. The role of nanofillers of various nature in the morphological changes of the polymer binder for plywood production. *Condensed Matter and Interphases*. 2025;27(1): 139–145. https://doi.org/10.17308/kcmf.2025.27/12719

Для цитирования: Ющенко Е. В., Бельчинская Л. И., Костюченко А. В., Жукалин Д. А. Роль нанонаполнителей различной природы в морфологических изменениях полимерного связующего для производства фанеры. *Конденсированные среды и межфазные границы*. 2025;27(1): 139–145. https://doi.org/10.17308/kcmf.2025.27/12719

✉ Ekaterina V. Yushchenko, e-mail: katerina.vgltu@yandex.ru
© Yushchenko E. V., Belchinskaya L. I., Kostyuchenko A. V., Zhukalin D. A., 2025

The content is available under Creative Commons Attribution 4.0 License.

1. Introduction

Russia is one of the leaders among plywood producing and exporting countries [1]. The need for plywood production is due to its wide range of applications in various fields of production [2]. A relevant direction in plywood production is the use of nanotechnology to improve the quality of laminated materials [3, 4]. Unlike other thermosetting resins, urea-formaldehyde resin has a crystalline structure, which makes it possible to strengthen the structure of the polymer matrix and improve its mechanical characteristics [5]. The crystalline regions are favorable for the hydrolytic stability of plywood [6]. Urea-formaldehyde (UF) resin nanomodification is able to influence the size and dispersion of crystalline regions in the resin and comprehensively improve the performance characteristics of the material [5]. It is known that the composition of CF resin affects the degree of crystallinity and crystal morphology in the binder structure [6]. The crystallinity of the resin is preserved during the curing of the CFS in contact with the wood veneer, but the order of the crystal lattice is disrupted [7]. Bio- and carbon nanomodifiers of carbamide-formaldehyde binder for plywood production were selected for the study: nanocellulose and multi-walled carbon nanotubes. Morphological changes of nanostructures allow controlling their functional characteristics.

Thus, the purpose of this work is to analyze by atomic-force microscopy (AFM) and X-ray diffractometry (XRD) the morphology of the nanostructure of urea-formaldehyde (UF) resin when nanocellulose (NCC) and multi-walled carbon nanotubes (MWCN) are introduced into it.

2. Objects and methods

The object of the study is a binder based on KF-Zh-F grade UF resin, modified with multi-walled carbon nanotubes and nanocrystalline cellulose.

For the experiment, carbamide-formaldehyde resin of the KF-Zh-F brand (Uralximplast PJSC, N. Tagil, Russia) was used as a polymer matrix. The nanofillers were MWCN with an average diameter of 9.5 nm and a length of 1.5 μm (Nanocyl Technology, Sambreville, Belgium) and NCC with an average particle size (width x length): 10–20 × 300–900 nm (Nanografi Nano Technology, Ankara, Turkey). The active substrate was peeled birch veneer (*Betula pendula* L.), produced by GalichLes LLC (Galich, Russia), and the passive substrate was glass. Ammonium chloride was used as a resin hardener (Komponent-Reagent LLC, Moscow, Russia).

A suspension of MWCN in an aqueous solution of lauryl sulfate, a surfactant, was obtained by ultrasonic dispersion under constant cooling for 30 minutes on an ultrasonic dispersant UZD-0.1/22 with a power of 100 W and a frequency of 22 kHz. The concentration of the dispersed phase in the suspension was 4.5%.

To obtain the UF resin/MWCN adhesive composition, the components were mechanically mixed for 10 minutes with the addition of MWCN at a concentration of 1.25 wt. %. Ultrasonic dispersion of the adhesive composition in the resin–filler system was carried out under constant cooling for 3 minutes on an ultrasonic dispersant UZK-1.3 with a power of 80 W and a frequency of 24 kHz. Cooling was carried out in a water bath to a temperature of 20 °C in order to avoid polymerization of the adhesive composition. The hardener was added in an amount of 1 wt. %. The adhesive composition of UF resin /NCC was obtained similarly by adding NCC with a concentration of 2 wt. %.

Then the samples of the modified and unmodified resin were cured in a drying cabinet chamber on an inert glass substrate and an active veneer substrate at a temperature of 115 °C, after which they were kept for 24 hours at room temperature and humidity of 65 ± 5% to complete the polymerization process.

The shape and distribution of nanofillers in the resin were studied using an NT-MDT scanning probe microscope in topology and phase contrast modes. Images of the surface of an unmodified binder cured on an active substrate (veneer), as well as a binder modified with MWCN or NCC, were obtained.

The phase composition and crystal structure of the initial MWCN and NCC powders were studied by electron diffraction in the “lumen” mode on an E’G-100M electronograph. Sample preparation was carried out by ultrasonic dispersion of the test material in surfactants, followed by application to a mesh and drying at a temperature of 20 °C until complete drying.

The phase (qualitative and quantitative) composition and structural state of the nanofillers and the cured resin in its pure and modified form were determined by X-ray diffractometry using a Burken D2-Phaser X-ray diffractometer (Germany). X-ray images of the samples were obtained using CuKa radiation (λ =1.5406 Å) in the angle range 2θ from 7 to 70°. During the survey, the samples were placed on a silicon wafer with a "zero" background. To determine the lattice parameters of the crystalline phases and estimate the average size of the crystallites, the profiles of X-ray diffractograms were analyzed using the Rietveld method in the HighScore Plus program.

3. Results and discussions

Atomic-force microscopy in the topology and phase contrast modes has been used to obtain images of the surface of a binder cured on an active substrate (veneer), modified with MWCN (Fig. 1) or NCC (Fig. 2).

The microrelief of the surface of the resin modified with MWCN is represented by inhomogeneities about 1 μm in size (Fig. 1a). The AFM scan obtained in the topology mode (Fig. 1b) shows nanoscale inhomogeneities in the form of protrusions with a lateral size of about 50 nm. The image obtained in phase contrast mode (Fig. 1c) shows rounded irregularities up to 70 nm in size, darker than the background (indicated by arrows in Fig. 1c). The absence of corresponding inhomogeneities in the image obtained in the surface topology mode indicates that the dark inhomogeneities are nanoinclusions with different mechanical properties compared to the polymer matrix. The nanoscale inhomogeneities very likely correspond to the location of the MWCN.

The microrelief of the resin surface modified by NCC (Fig. 2a) is represented by large,

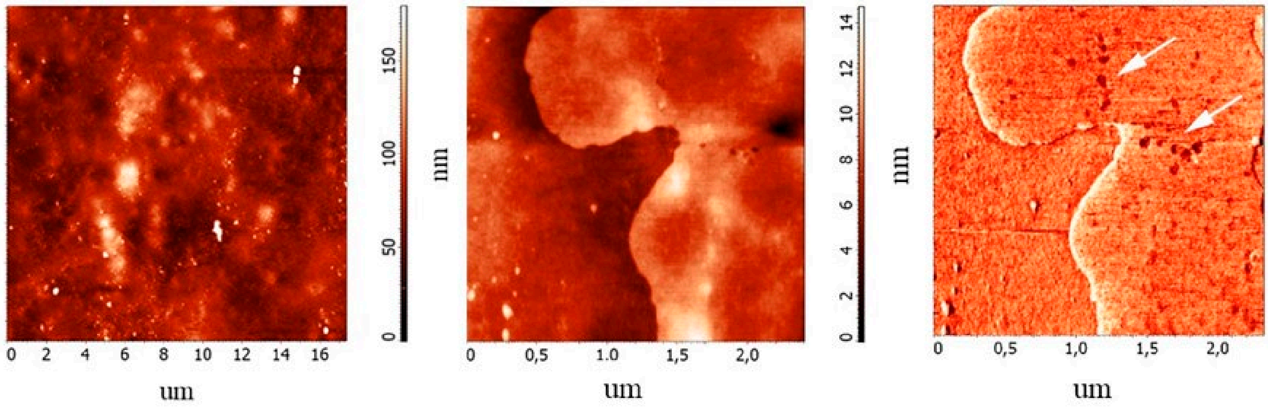

a b c

Fig. 1. Images of the surface of a binder modified by MWCN cured on an active substrate (veneer)

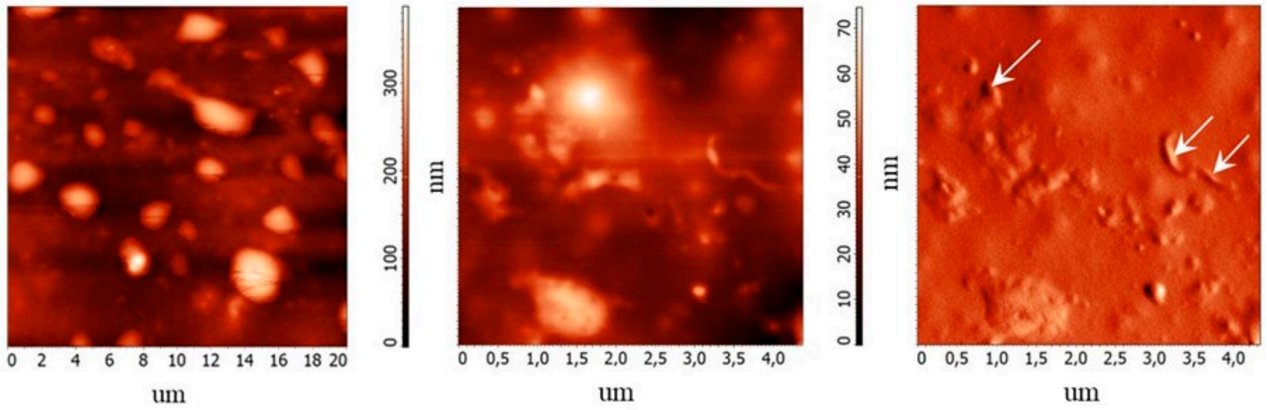

a b c

Fig. 2. Images of the surface of a binder modified by NCC cured on an active substrate (veneer)

evenly distributed inhomogeneities with a lateral size of 0.5-2 μm and a height of up to 0.5 μm. The microrelief is poorly developed between the inhomogeneities. The relief of the second level in the areas between large inhomogeneities is represented by irregularly shaped inhomogeneities measuring 70–300 nm (indicated by arrows in Fig. 2c), obviously corresponding to inclusions in the form of fibers (Fig. 2b, c). There is no pronounced phase contrast from the inclusions, which can be explained by the similar elastic-plastic characteristics of NCC and resin.

Figure 3 shows the electronograms of the initial components: powders of MWCN (a) and NCC (b).

The electronogram (Fig. 3a) shows a complete set of reflections corresponding to the MWCN [8]. In the electron diagram (Fig. 3b), all the observed reflections correspond to the crystal lattice of cellulose [9].

Figure 4 shows X-ray diffractograms (XRD) of NCC powder (Fig. 4, curve *1*); MWCN powder after dispersion in surfactants (sodium lauryl sulfate (SLS)) and subsequent drying (Fig. 4, curve *2*); mixtures of NCC and MWCN after dispersion in surfactants and subsequent drying (Fig. 4, curve *3*).

On the XRD of the NCC powder (Fig. 4, Curve *1*), very blurred maxima are observed, the position of which coincides with the reflection spectrum from the cellulose crystal lattice. The width of the maxima indicates the nanocrystalline structure of the cellulose.

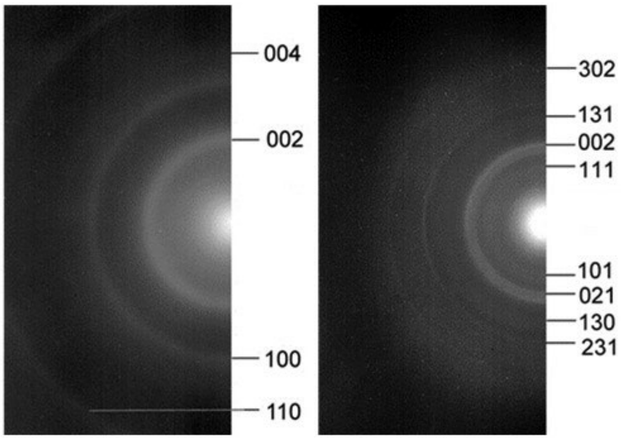

a b

Fig. 3. Electronograms of MWCN (a) and NCC (b) powders

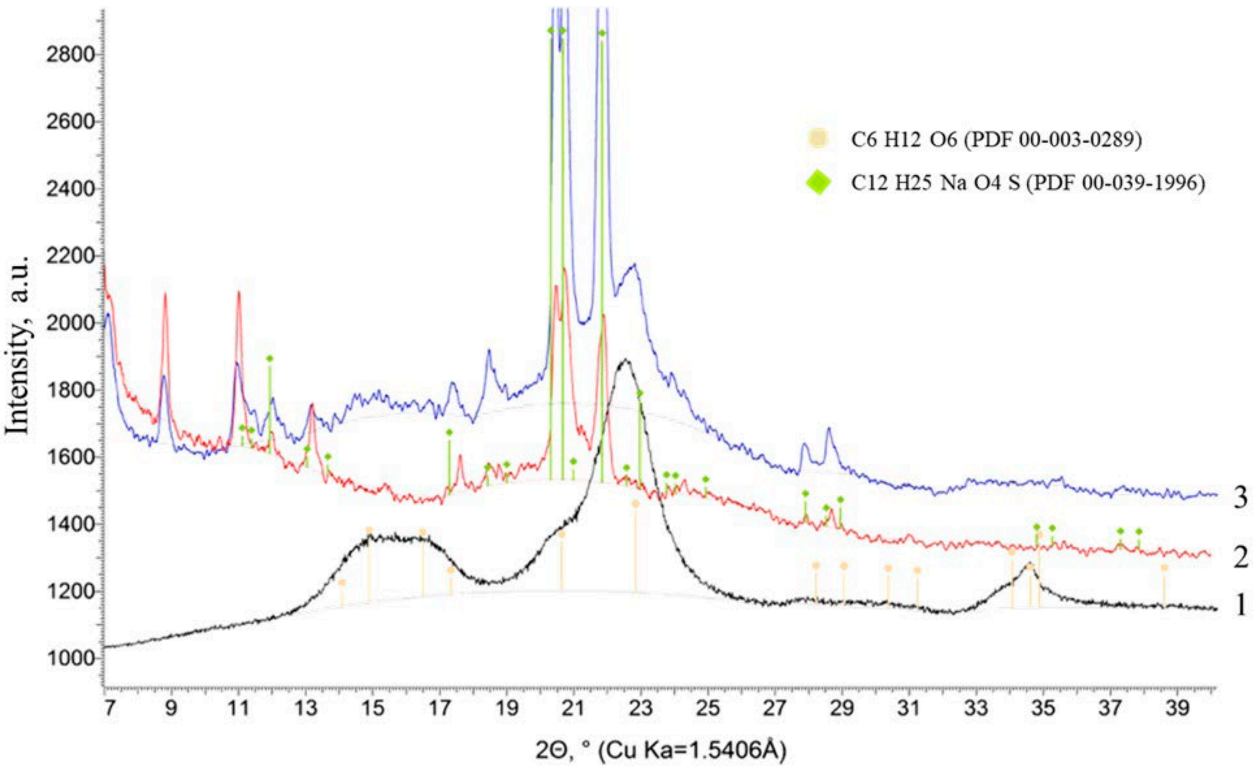

Fig. 4. X-ray diffractograms of NCC powder (*1*); MWCN powder dispersed in surfactants with subsequent drying (*2*); mixtures of NCC and MWCN dispersed in surfactants with subsequent drying (*3*)

All reflections corresponding to the crystalline SLS are observed on the MWCN + SLS XRD (Fig. 4, Curve *2*). The absence of reflections corresponding to MWCN is due to both the low-dimensional nature of the nanotubes and their relatively small number.

All the reflections present in the first two diffractograms are observed on the XRD from MWCN +NCC+ SLS (Fig. 4, Curve *3*). Reflections associated with phases other than NCC and LSN are not observed, which indicates the absence of crystalline products of the reaction of MNT with NCC in the sample.

Figure 5 shows X-ray diffractograms (XRD) of an unmodified binder (Fig. 5, curve *1*) and a binder modified by NCC (Fig. 5, curve *2*) and MWCN (Fig. 5, curve *3*).

The XRD of unmodified resin (Fig. 5, Curve *1*) is represented by wide maxima in the form of halos, the most intense of which is in the angle range 2θ = 18–28 °. A low-intensity peak with a peak of 2θ = 21.11° is observed against the background of this halo. The character of the maxima observed on the diffractogram indicates a low degree of crystallinity of the resin.

In the composite binder containing MWCN (Fig. 5, curve *3*), in addition to the halo, there are 2 pronounced maxima with a peak of 2θ = 21.03° and 23.6°. The higher intensity of the first maximum compared to the XRD of the resin without filler and the appearance of the second maximum indicate an increase in the degree of crystallinity of the resin with filler from MWCN (an increase in the size and proportion of crystallites). The reflections characteristic of MWCN are not observed on XRD, probably due to their small volume fraction in the binder.

Diffraction patterns similar to those of unmodified and modified CNTs of urea-formaldehyde resin are described in the work for formaldehyde resin with different molar ratios. [10]. The authors explain the appearance of pronounced peaks on the resin diffractograms by increasing the degree of polymer crystallinity due to the formation of hydrogen bonds between linear molecules [10].

A halo similar to the unmodified resin is observed on the RD of the resin modified by the NCC (Fig. 5, Curve *2*). There are also peaks with peaks of 2θ = 21.08° and 34.8°. According to [11], these maxima correspond to reflections from the cellulose crystal lattice.

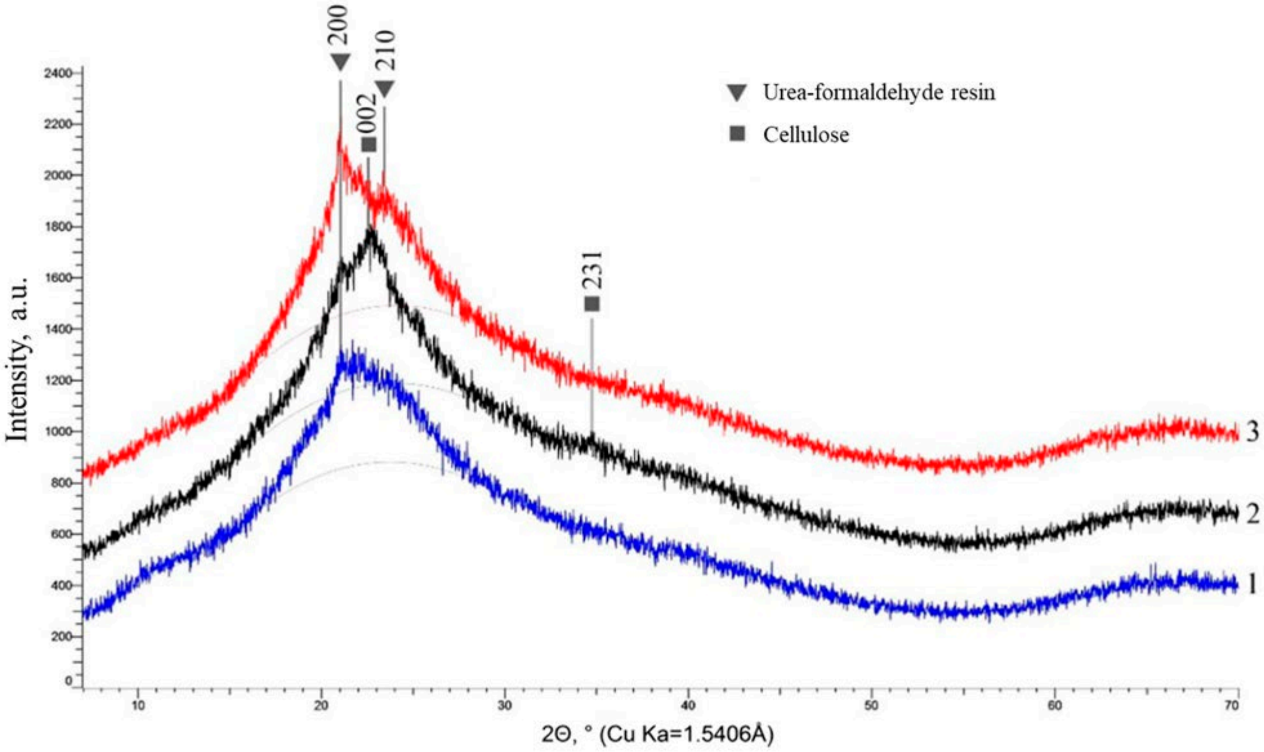

Fig. 5. X-ray diffractograms of unmodified binder (*1*) and binder modified by NCC (*2*) and MWCN (*3*)

The size of the crystallites (coherent scattering regions), calculated as a result of profile analysis of X-ray diffractograms in the region of the maximum with a peak of 21.1°, was about 10 nm for resin without filler, 15 nm for resin with nanocellulose, 18 nm for resin with MWCN. The effect of increasing the size of crystallites on the strength characteristics of the resulting nanocomposite plywood is confirmed by experimental data. Thus, the tensile strength when chipping through the adhesive layer of plywood modified with MWCN increases by 76% (from 0.68 MPa to 1.2 MPa), modified with NCC – by 194% (from 0.68 MPa to 2 MPa) compared with unmodified plywood [12].

Thus, based on comparative diffraction analysis of unmodified and modified resin samples, the following can be noted: a resin containing ultrasound-activated MWCN [12], after curing, has a higher degree of crystallinity compared with unmodified resin. Modification of the NCC resin activated by ultrasound [13] leads to a less pronounced increase in the degree of its crystallinity.

The most likely type of resin lattice is a primitive cubic one. The cubic lattice constant a was 0.840, 0.844, and 0.842 nm for pure resin, UF resin/ MWCN, and UF resin /NCC, respectively. There is a weak tendency to increase the volume of the unit cell when using MWCN as a nanomodifier of KF–Zh-F resin. For NCC resin, the indices of the observed reflections are 200 and 210. Such a set of reflections may indicate a virtually one-dimensional arrangement of polymer fibers parallel to each other with a relatively arbitrary radial rotation. The reflection indices 002 and 231 are characteristic of NCC powder, which is confirmed by the electronogram data (Fig. 3b).

4. Conclusion

The microrelief of the surface of the modified UF resin/MWCN binder cured on an active substrate is characterized by the presence of uniformly distributed MWCN nanoclusions measuring 50 nm – 1 μm. The microrelief of the resin surface modified by NCC shows the presence of evenly distributed nanocellulose inclusions measuring 70 nm – 2 μm. The sets of reflections observed on the electronograms of the nanomodifiers correspond to the MWCN and NCC.

The data of X-ray diffractometry of unmodified resin indicate a low degree of its crystallinity. The modification of the binder of both MWCN and NCC is accompanied by an increase in the degree of crystallinity of the polymer. The crystallite size of the resin without filler is 10 nm; the resin modified with nanocellulose is 15 nm; the resin nanomodified with MWCN is 18 nm. An increase in the size of the crystallites in the resin can lead to an increase in its density, strength, hardness of the material and chemical resistance.

The most probable type of UF resin lattice is a primitive cubic one with parameter $a = 0.840$ nm. The cubic lattice constant of the resin with MWCN and NCC is 0.844 and 0.842 nm, respectively, i.e. there is a weakly pronounced increase in the volume of the unit cell of the UF resin modified with MWCN.

Thus, the atomic force microscopy data allow us to conclude that the reinforcing components (MWCN, NCC) are evenly distributed in the polymer matrix. The AFM data on the morphology of the surface of composites with NCC obviously correlate with the XRD data: according to the first method, morphological signs of the presence of fibers are observed, according to the second, signs of the NCC crystal lattice. For MWCN, AFM morphology data correlate with electronography data. Electronography confirms that the reinforcing material has a crystalline structure of MWCN. And AFM reveals the presence of inclusions with other elastic-plastic properties in the polymer. Taken together, both methods indicate that the inclusions in the matrix are precisely the MWCN. X-ray diffractometry proved to be insensitive in the case of MWCN.

Contribution of the authors

The authors contributed equally to this article.

Conflict of interests

The authors declare that they have no known competing financial interests or personal relationships that could have influenced the work reported in this paper.

References

1. Nazarenko I. N., Nazarenko M. V. The state and prospects of development of plywood production. *Management Accounting*. 2022;1-2: 299–310. https://doi.org/10.25806/uu1-22022299-310 (In Russ., abstract in Eng.)

2. Churkina A.V. Analysis of the use of plywood as raw material. *Forum molodykh uchenykh.* 2019;2(30): 1645–1648. Available at: https://www.elibrary.ru/item.asp?id=38693672 (In Russ., abstract in Eng.)

3. Dorieh A., Selakjani P. P., Shahavi M. H., … Aghaei R. Recent developments in the performance of micro/nanoparticle-modified urea-formaldehyde resins used as wood-based composite binders: a review. *International Journal of Adhesion and Adhesives.* 2022;114: 103106. https://doi.org/10.1016/j.ijadhadh.2022.103106

4. Kantieva E. V., Ponomarenko L. V., Tomina E. V., Tomenko D. K. The effect of nanoscale silicon oxide on the operational characteristics of plywood. *Systems. Methods. Technologies.* 2022;3(55): 129–134. https://doi.org/10.18324/2077-5415-2022-3-129-134

5. Liu M., Rooban Venkatesh K. G. Thirumalai, Wu Y., Wan H. Characterization of the crystalline regions of cured urea formaldehyde resin. *RSC Advances*. 2017;7: 49536–49541. https://doi.org/10.1039/C7RA08082D

6. Singh A. P., Causin V., Nuryawan A., Park B-D. Morphological, chemical and crystalline features of urea–formaldehyde resin cured in contact with wood. *European Polymer Journal*. 2014;56: 185–193. https://doi.org/10.1016/j.eurpolymj.2014.04.014

7. Ferra J. M. M., Mendes A. M., Costa M. R. N., Carvalho L. H., Magalhães F. D. A study on the colloidal nature of urea-formaldehyde resins and its relation with adhesive performance. *Journal of Applied Polymer Science*. 2010;118 (4): 1956–1968. https://doi.org/10.1002/app.31112

8. Farbod M., Khajehpour Tadavani S., Kiasat A. Surface oxidation and effect of electric field on dispersion and colloids stability of multiwalled carbon nanotubes. *Colloids and Surfaces A: Physicochemical and Engineering Aspects.* 2011;384: 685–690. https://doi.org/10.1016/j.colsurfa.2011.05.041

9. Database: JCPDS, Powder Diffraction File Alphabetical Index Inorganic Compounds, Publication SMA - 27, Published by the JCPDS International Center for Diffraction Date

10. Li J., Zhang Y. Morphology and crystallinity of urea-formaldehyde resin adhesives with different molar ratios. *Polymers*. 2021;13: 673. https://doi.org/10.3390/polym13050673

11. Yudhanto F., Yudha V., Ridzuan M., … Sudarisman. Morphology, crystallinity and thermal properties of nanocrystalline cellulose isolated of sisal fiber by acid hydrolysis-ultrasonication. *International Journal of Nanoelectronics and Materials (IJNeaM)*. 2024;2(17): 180–188. https://doi.org/10.58915/ijneam.v17i2.657

12. Yushchenko E. V., Belchinskaya L. I., Zhuzhukin K. V., Zhukalin D. A. Multi-walled carbon nanotubes and ultrasound modified urea-formaldehyde resins: advantages of using for the production of magnetically processed composite plywood. *Lesotekhnicheskii Zhurnal.* 2024;14(3): 238–259. https://doi.org/10.34220/issn.2222-7962/2024.3/14 (In Russ., abstract in Eng.)

13. Yushchenko E. V., Belchinskaya L. I., Zhuzhukin K. V. Nanocomposite eco-plywood: morphological, ecological, IR spectroscopic substantiation of obtaining. *Lesotekhnicheskii zhurnal*. 2024;14(3): 260–283. https://doi.org/10.34220/issn.2222-7962/2024.3/15 (In Russ., abstract in Eng.)

Information about the authors

Ekaterina V. Yushchenko, postgraduate student of the Department of Wood Science, Voronezh State University of Forestry and Technologies named after G. F. Morozov (Voronezh, Russian Federation).

http://orcid.org/0000-0002-4827-2756
katerina.vgltu@yandex.ru

Larisa I. Belchinskaya, Dr. Sci. (Tech.), Professor, Chief Researcher of the Research Department, Voronezh State University of Forestry and Technologies named after G. F. Morozov (Voronezh, Russian Federation).

http://orcid.org/0000-0003-3921-8018
belbom@mail.ru

Aleksandr V. Kostyuchenko, Cand. Sci. (Phys.–Math.), Associate Professor, Department of Solid State Electronics, Voronezh State Technical University (Voronezh, Russian Federation).

http://orcid.org/0000-0002-0049-3664
av-kostuchenko@mail.ru

Dmitrii A. Zhukalin, Cand. Sci. (Phys.–Math.), Associate Professor, Department of Physics of Semiconductors and Microelectronics, Voronezh State University (Voronezh, Russian Federation).

http://orcid.org/0000-0002-0754-4989
d.zhukalin@mail.ru

Received 17.10.2024; approved after reviewing 13.12.2024; accepted for publication 16.12.2024; published online 25.03.2024.

Translated by the author

Condensed Matter and Interphases. 2025;27(1): 146–153

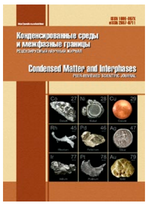

ISSN 1606-867X (Print)
ISSN 2687-0711 (Online)
Condensed Matter and Interphases
Kondensirovannye Sredy i Mezhfaznye Granitsy
https://journals.vsu.ru/kcmf/

Original articles

Research article
https://doi.org/10.17308/kcmf.2025.27/12492

Theoretical and experimental study of the niobium dioxide electronic structure

M. D. Manyakin✉, **S. I. Kurganskii, I. S. Kakuliia, S. S. Titova, O. A. Chuvenkova, S. Yu. Turishchev**

Voronezh State University,
1 Universitetskaya pl., Voronezh 394018, Russian Federation

Abstract

The investigation of the niobium dioxide electron-energy structure is presented in the paper. The electronic structure computer modeling of the NbO_2 with a rutile crystal structure has been performed using linearized augmented plane wave method. The energy band structure as well as total and partial densities of electronic states are calculated.

Experimental studies of the NbO_2 sample electronic structure were carried out using synchrotron and laboratory X-rays sources. The X-ray photoelectron spectrum of the valence band and subvalent states of NbO_2 and the spectrum of the X-ray absorption near edge structure near K-edge of the oxygen atom in NbO_2 have been recorded.

The spectra of the X-ray absorption near edge structure of the oxygen and niobium atoms K-edges are modeled. The calculated spectra make it possible to reliably interpret the data from the synchrotron experiment. It is shown that for NbO_2 the spectrum calculated for the ground energy state without using the supercell and core hole modeling method demonstrates high agreement with the experiment.

Keywords: Computer modeling, Niobium dioxide, Electronic structure, Density of states, XANES, XPS, Core hole, Rutile

Funding: The study was supported by the Russian Science Foundation grant no. 22-72-00145, https://rscf.ru/project/22-72-00145/.

For citation: Manyakin M. D., Kurganskii S. I., Kakuliia I. S., Titova S. S., Chuvenkova O. A., Turishchev S. Yu. Theoretical and experimental study of the niobium dioxide electronic structure. *Condensed Matter and Interphases*. 2025;27(1): 146–153. https://doi.org/10.17308/kcmf.2025.27/12492

Для цитирования: Манякин М. Д., Курганский С. И., Какулия Ю. С., Титова С. С., Чувенкова О. А., Турищев С. Ю. Теоретическое и экспериментальное исследование электронной структуры диоксида ниобия. *Конденсированные среды и межфазные границы*. 2025;27(1): 146–153. https://doi.org/10.17308/kcmf.2025.27/12492

✉ Maxim D. Manyakin, e-mail: manyakin@phys.vsu.ru

© Manyakin M. D., Kurganskii S. I., Kakuliia I. S., Titova S. S., Chuvenkova O. A., Turishchev S. Yu., 2025

The content is available under Creative Commons Attribution 4.0 License.

1. Introduction

Materials in which the metal-semiconductor phase transition is observed can be used to create various electronic, optical and other devices: memory elements, neuromorphic hardware devices, “smart windows”, devices for energy generation and storage, etc. [1–4]. Such materials include niobium dioxide NbO_2 [3, 5, 6]. Above the phase transition temperature (for NbO_2 Tc ≈ 808 °C), this material has a crystalline structure of the classical rutile type ($P4_2/mnm$ space group) and is a conductor of electric current [7, 8]. Below this temperature, the crystal structure of NbO_2 changes to a distorted rutile structure (space group $I4_1/a$) that accompanied by a change in the nature of the conductivity to semiconducting [7, 8].

In order to study the features of the electron-energy structure of niobium dioxide in the present work a comprehensive study is carried out including the use of ab initio methods of computer modeling, X-ray photoelectron spectroscopy (XPS) and X-ray absorption near edge structure (XANES) spectroscopy.

2. Calculation technique

The high-temperature phase of niobium dioxide has a rutile crystal structure, belongs to tetragonal syngony, and is characterized by the $P4_2/mnm$ space group [3, 7, 9]. The experimental values of the NbO_2 crystal structure parameters given in Table 1 [10] were used in the calculation, similar to other works [9, 11, 12]. The appearance of the NbO_2 unit cell and the corresponding first Brillouin zone are shown in Fig. 1a, b.

Calculations of the electronic structure were performed using the linearized augmented plane waves method using the Wien2k software package [13]. The Generalized Gradient Approximation (GGA) was used to account for the exchange-correlation energy [14]. The radii of muffin-tin spheres R_{mt} given in atomic units of lenght (numerically equal to the Bohr radius a_0), were 1.98 a.u. for the Nb atom and 1.79 a.u. for the O. The $R_{mt}\cdot K_{max}$ value that determines the number of the basis plane waves was 6.0. When integrating over the Brillouin zone 5000 k-points were used for calculating the unit cell and 200 k-points for calculating the supercell.

Table 1. Parameters of the NbO_2 crystal lattice

Space group	*P4₂/mnm*		
Unit cell parameters *a*, *b*, Å	4.8464		
Unit cell parameter *c*, Å	3.0316		
Atomic position	*x/a*	*y/b*	*z/c*
Nb_1	0.0	0.0	0.0
Nb_2	0.5	0.5	0.5
O_1	0.2925	0.2925	0.0
O_2	0.7075	0.7075	0.0
O_3	0.2075	0.7925	0.5
O_4	0.7925	0.2075	0.5

The XANES spectra were modeled for a unit cell in the ground energy state as well as for a 2×2×3 supercell using the core hole method. The formalism of this method is described in detail in our previous work [15]. Previously, this method was successfully tested when calculating the XANES spectra of various oxide materials [16, 17].

3. Experimental technique

The experimental part of the work consisted in conducting studies of the commercial NbO_2 powder sample produced by Sigma-Aldrich [18] using XPS and XANES spectroscopy. X-ray phase analysis of the sample showed that it has a crystalline structure of distorted rutile (space group $I4_1/a$).

The experiments were carried out at the NanoPES synchrotron radiation end-station including the ESCA module of the National Research Center “Kurchatov Institute” [19]. The pressure in the analytical chambers of the NanoPES workstation spectrometers was ~10^{-10} Torr. Electron energy analyzers Specs Phoibos 250 and Phoibos 150 were used. When using a laboratory monochromatic source, the excitation energy was 1486.6 eV.

We used a standard approach to data calibration based on recording the C 1s signal line of hydrocarbon contamination [20]. To compare and analyze the main features of the spectra, well-known databases were used from which the most relevant data were selected [20, 21].

4. Results and discussion

The band structure of NbO_2 is shown in Fig. 1c. The position of the Fermi level (E_F) is selected as the beginning of the energy count. The lower part of the valence band consists of

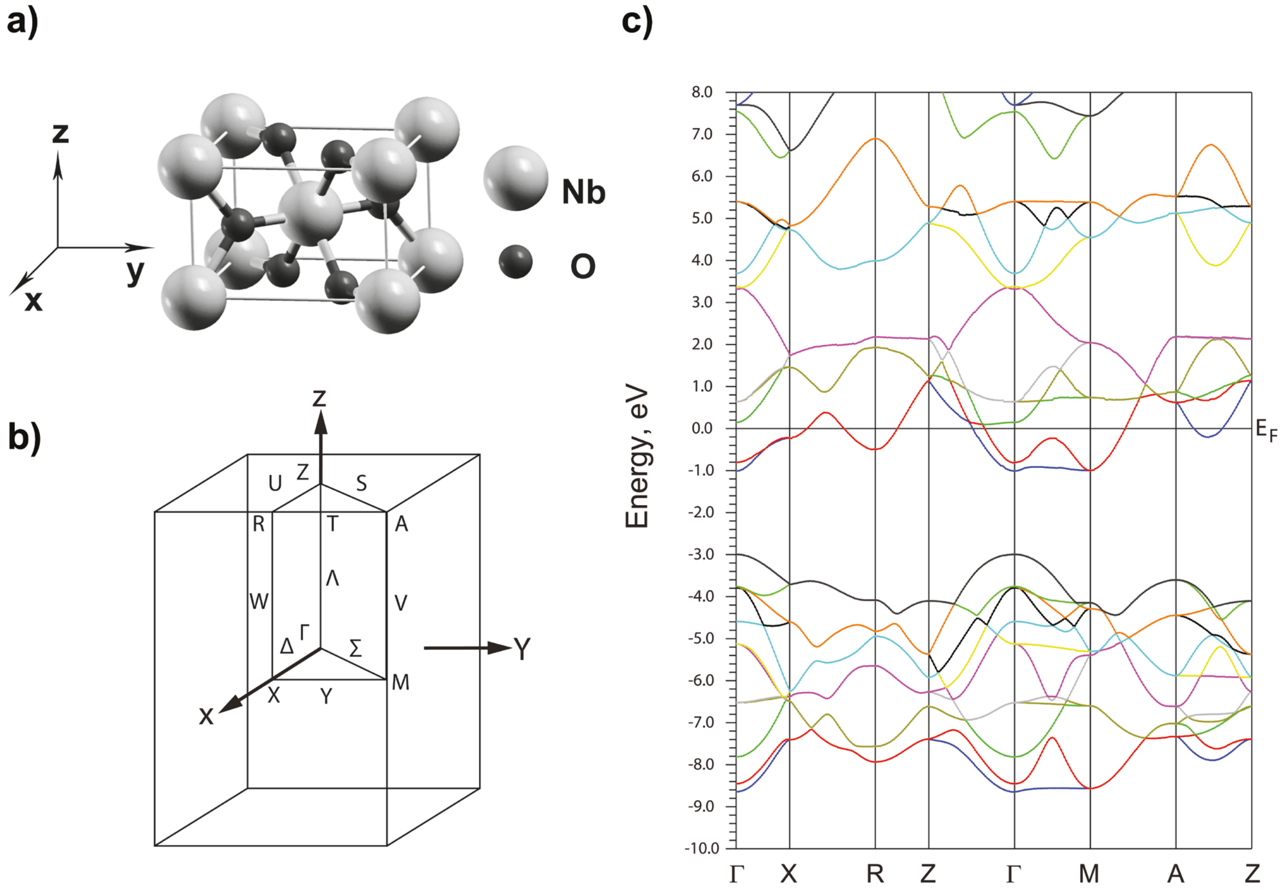

Fig. 1. NbO$_2$ unit cell with rutile crystalline structure (a). The first Brillouin zone of NbO$_2$ (b). Band structure of NbO$_2$ (c)

12 bands originating mainly from 2*p*-states of the oxygen with a small admixture of 4*d*-states of the niobium (see Fig. 2c, d), has a width of 5.65 eV and is located in the energy range of −8.65.. −3.0 eV. Above the top of this group of bands there is a 1.98 eV wide gap of forbidden energies. Even higher in the energy is a group of 10 bands originating mainly from 4*d*-states of niobium atoms with a certain proportion of 2*p*-states of oxygen atoms. According to the crystal field theory due to the octahedral surrounding of the niobium atom by oxygen atoms in NbO$_2$ the 4*d*-states of Nb are splitted into 6 low-energy bands with t_{2g} symmetry and 4 high-energy bands with e_g symmetry [9]. These two groups of 4*d* bands are well separated in the band structure with the exception of the point Γ vicinity where they slightly overlap [22].

A comparison of the performed calculations results with the data from [8, 9, 11, 22] shows a fairly high agreement which indicates their reliability. At the same time some differences are observed. Compared with the results of [11] there is a noticeable difference in the behavior of the uppermost t_{2g} band in the Z-A and Z-R directions connecting the center of the upper face of the Brillouin zone Z with its vertex A and the middle of its edge R respectively. In both cases the bands have an almost flat character but in our calculation this band lies ~ 1 eV lower in these directions (at an energy of ~ 2.2 eV above E_F) than in [11]. At the same time our picture of the band dispersion of the uppermost t_{2g} band is closest to the results of work [9]. However, in the calculation [9] as in [8] but unlike [11, 22] there is a gap of forbidden energies separating the upper t_{2g} band from the lower e_g band. In our calculation these two groups of bands converge in the vicinity of point Γ similar to the results of [11, 22].

In our calculation the forbidden energy gap dividing the valence band into two parts has a width of 1.98 eV. This is less than the values obtained in other works: 6.1 eV [8], 4.1 eV [22], ~ 3 eV [9].

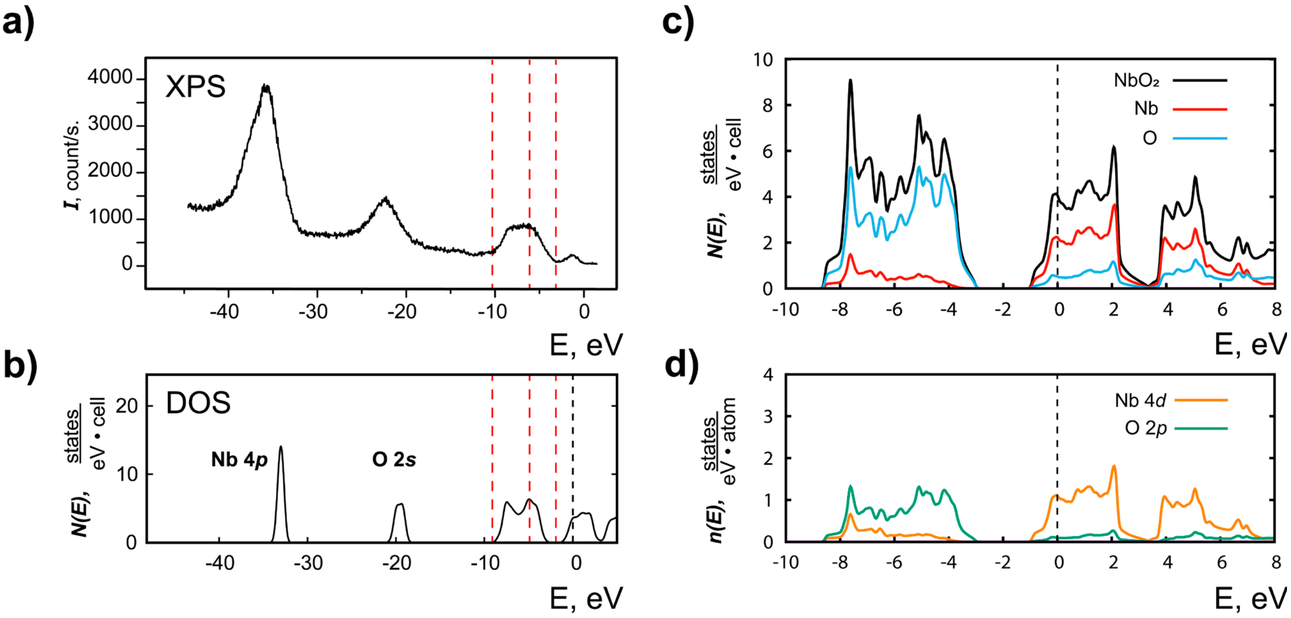

Fig. 2. XPS spectrum of NbO_2 (a). Total DOS of NbO_2 (b). Total DOS of the crystal and the Nb and O atoms in the valence region and near the bottom of the conduction band (c). Partial DOS of the Nb and O atoms (d)

In general, NbO_2 has a band structure typical of rutile-like transition metal oxides. The most important characteristic defining the unusual properties of NbO_2 is the position of the Fermi level which is explained by the following considerations. The free niobium atom has five electrons on the valence shell occupying $4d^4 5s^1$-states. During crystallization into the rutile structure the niobium valence shell electrons are transferring to more electronegative oxygen atoms. Formally the niobium atom in rutile-like NbO_2 has an oxidation state of Nb^{+4} and the filling of the *d*-subshell is $4d^1$ [23]. As a result, the energy bands formed from the *d*-states of niobium atoms are partially occupied by electrons. The Fermi level crosses a group of bands formed by Nb *4d*-states which acts as a conduction band and NbO_2 exhibits a metallic type of electrical conductivity.

The results of NbO_2 XPS spectroscopy provide important information about the features of occupied electronic states. Fig. 2a shows the X-ray photoelectron spectrum of the NbO_2 sample recorded in the range of binding energies from −45 to 0 eV. In the considered energy range 4 regions of occupied states are observed similar to the results of [24] and the experimental spectrum is generally consistent with the results of [11, 24–28]. The XPS spectrum was compared with the total density of states calculation results in the same energy range by combining the position of the valence band on the energy scale (Fig. 2b). At the same time the starting point of the experimental and calculated scales do not coincide. Fig. 2a, b shows a good agreement of the results which makes it possible to explain the features observed in the XPS spectrum. The intense peak at −35.8 eV in the experimental spectrum corresponds to the density of Nb 4*p*- states peak at the −33.0 eV on the calculation scale where the position of the Fermi level is taken as the starting point. The experimental peak at −22.25 eV corresponds to the density of O 2*s*- states peak at an energy of −19.5 eV on the calculation scale. The peaks position of the Nb 4*p*- and O 2*s*- states in the calculation turns out to be shifted closer to the Fermi level if compared with the experiment. At the same time the distance between the peaks in the calculation is 13.5 eV which is in excellent agreement with the experimental value of 13.55 eV.

Features in the energy range −10 .. 0 eV describes the structure of the valence band. This area as well as the bottom of the conduction band are shown on an enlarged scale in Fig. 2c, d. The total density of electronic states (DOS) of the NbO_2 crystal, the total atomic DOS for Nb and O atoms as well as the partial densities for Nb 4*d*- and O 2*p*- electronic states dominating in the considered energy range are shown. As mentioned above the valence band consists of two regions. Its lower part from −8.65 to −3.0 eV is formed mainly by 2*p*-oxygen states. Nb 4*d*-states dominate in the upper part of the valence band and at the bottom part of the conduction band in the range from −1 to +6 eV. It can be seen that there is a contribution of O 2*p*-states to the two upper groups of bands and Nb 4*d*-states to the lower group respectively that indicates the covalent component of the chemical bond [9]. In the low-energy group of states there are local maxima at the bottom and top of the considered range with the local minimum observed in its center. The Fermi level is located near the local DOS maximum which may indicate the instability of such an electronic structure and contribute to the metal–semiconductor phase transition observed in NbO_2. The calculated DOS spectra are in good agreement with the results of [11, 22].

Figure 3 shows a comparison of the experimentally recorded O K-edge XANES spectrum with the spectra calculated for a unit cell in the ground energy state (without core hole modeling) and for a 2×2×3 supercell calculated using the core hole method. The experimental spectrum contains three maxima designated as A, B and C at energies 531.1, 534.8, and 542.0 eV, respectively. Maximum A has the highest intensity. The intensities of maxima B and C are approximately equal. Experimental spectra of the O K-edge with the same intensity ratio between the maxima were obtained in [27] by the XANES method for NbO_2 thin films and in [12] by electron energy loss spectroscopy (EELS) for a commercial sample produced by Alfa Aesar. The relative intensity of peak A is less than the intensity of peak B but greater than the intensity of peak C in spectra obtained by EELS for commercial samples produced by Aldrich [29] and Alfa Aesar samples [30]. It can be concluded that the data presented in the literature are ambiguous and probably depend on the conditions of the experiment as well as the subsequent mathematical processing of the result.

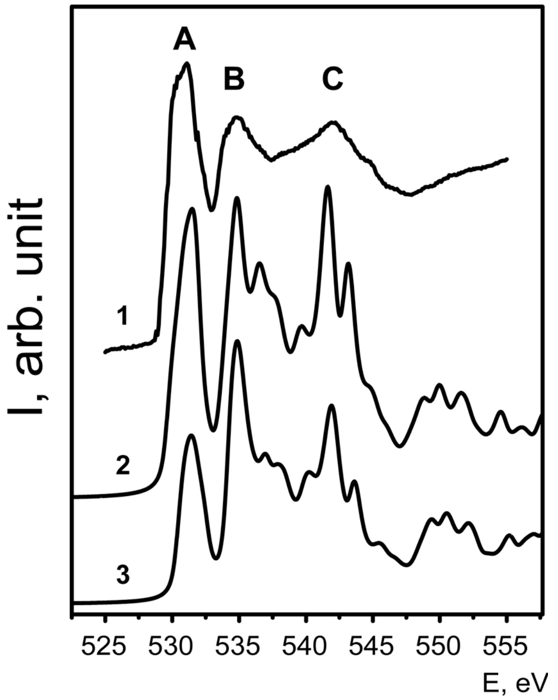

Fig. 3. O K-edge XANES spectrum. *1* – experimental, *2* – calculation for unit cell without core hole, *3* – calculation for supercell with core hole

The calculated spectra shown in Fig. 3 were compared with the experimental one based on the maximum B position at an energy of 534.8 eV. In our calculation performed for a unit cell in the ground energy state all three maxima have a similar intensity, but maximum A has the lowest value and maximum C has the highest. There are known papers [12, 27] in which calculations of the O K absorption edge were also performed using the Wien2k software package. In [27] the ratio of the maxima A and B have the same intensities as ours but unlike our result in [27] maximum C has the lowest intensity. In [12] maximum A is the most intense followed by least intense maximum B and C. Thus, in all three calculations including the present one the obtained results differ slightly in the ratio of the main spectrum features intensities. At the same time there is a good agreement between the calculated spectra and the experimental one in terms of the number of peaks and their position on the energy scale that makes it possible to unambiguously interpret the experimental data.

The use of the core hole method in the calculation does not lead to a change in the number of features in the spectrum or their position on the energy scale. However, the relative intensity of the A and C maxima is noticeably decreasing. The decrease of the first peak intensity in the calculated XANES O K-edge spectrum by the core hole method in transition metal oxides is a well-known effect [31]. According to our calculations and ones given in [23, 31] the hybridization of unoccupied O2*p*-electronic states and unoccupied states of metal atoms is observed in transition metal oxides. According to this approach the O K spectrum fine structure is explained as follows. Peak A in the spectrum reflects the density of oxygen 2*p*- states hybridized with niobium t_{2g} states, peak B – with niobium e_g states. Peak C reflects the hybridization of O 2*p*- states and 5*s*-, 5*p*- metal states. Thus, modeling a core hole leads to a systematic underestimation of the first peak intensity associated with t_{2g}-symmetry states [31].

Using the XANES O K spectrum as the example we conclude that the calculation for the NbO_2 unit cell without accounting the core hole gives results that are better consistent with experiment. Therefore, for the Nb K absorption edge the calculation was performed only for the unit cell. The result in comparison with the experimental spectrum [32] is given in Fig. 4. The calculated spectrum reproduces all the absorption edge fine structure main features presented in the experimental spectrum which indicates the correctness of the chosen modeling method and the reliability of the result obtained.

5. Conclusions

The electronic structure of niobium dioxide has been studied by the linearized augmented plane waves method. The band structure, total and partial densities of electronic states are calculated. The DOS spectrum allows reliable interpretation of XPS spectroscopy results.

The results of XANES spectra calculations for the Nb K-, O K- absorption edges are presented. For the O K absorption edge spectrum it is shown that the calculation for the ground energy state without using the supercell and core hole modeling method demonstrates high agreement with the synchrotron experiment.

The results obtained can be used in the analysis of experimentally studied samples of the Nb – O system.

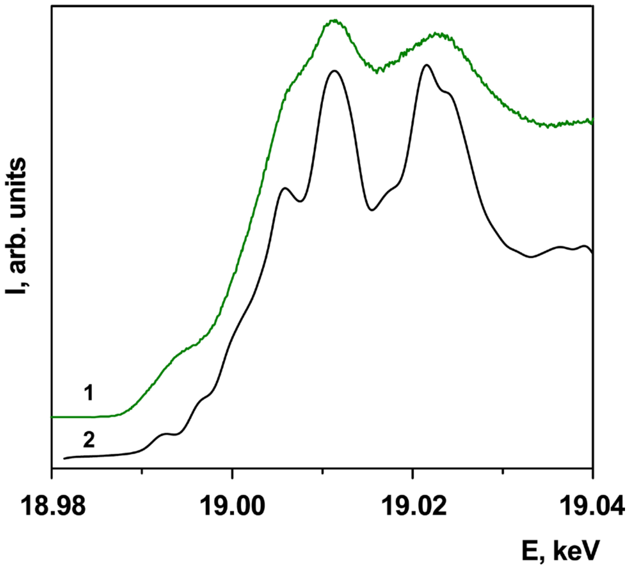

Fig. 4. Nb K-edge XANES spectrum. 1 – experimental [32], 2 – our calculation.

Contribution of the authors

All authors made an equivalent contribution to the preparation of the publication.

Conflict of interests

The authors declare that they have no known competing financial interests or personal relationships that could have appeared to influence the work reported in this paper.

References

1. Zhou Y., Ramanathan S. Mott memory and neuromorphic devices. *Proceedings of the IEEE*. 2015;103(8): 1289–1310. https://doi.org/10.1109/JPROC.2015.2431914

2. Joshi T., Cirino E., Morley S. A., Lederman D. Thermally induced metal-to-insulator transition in NbO_2 thin films: modulation of the transition temperature by epitaxial strain. *Physical Review Materials*. 2019;3: 124602. https://doi.org/10.1103/PhysRevMaterials.3.124602

3. Music D., Krause A. M., Olsson P. A. T. Theoretical and experimental aspects of current and future research on NbO_2 thin film devices. *Crystals*. 2021;11: 217. https://doi.org/10.3390/cryst11020217

4. Manning T. D., Parkin I. P., Pemble M. E., Sheel D., Vernardou D. Intelligent window coatings: atmospheric pressure chemical vapor deposition of tungsten-doped vanadium dioxide. *Chemistry of Materials*. 2004;16(4): 744–749. https://doi.org/10.1021/cm034905y

5. Fajardo G. J. P., Howard S. A., Evlyukhin E., ... Piper L. F. J. Structural phase transitions of NbO_2: bulk versus surface. *Chemistry of Materials*. 2021;33: 1416–1425. https://doi.org/10.1021/acs.chemmater.0c04566

6. Park J., Hadamek T., Posadas A. B., Cha E., Demkov A. A., Hwang H. Multi-layered $NiO_y/NbO_x/NiO_y$ fast drift-free threshold switch with high I_{on}/I_{off} ratio for selector

application. *Scientific Reports*. 2017;7: 4068. https://doi.org/10.1038/s41598-017-04529-4

7. Shapiro S. M., Axe J. D., Shirane G., Raccah P. M. Neutron scattering study of the structural phase transition in NbO_2. *Solid State Communications*. 1974;15: 377–381. https://doi.org/10.1016/0038-1098(74)90780-7

8. Posternak M., Freeman A. J., Ellis D. E. Electronic band structure, optical properties, and generalized susceptibility of NbO_2. *Physical Review B*. 1979;19: 6555–6563. https://doi.org/10.1103/PhysRevB.19.6555

9. Eyert V. The metal-insulator transition of NbO_2: an embedded Peierls instability. *Europhysics Letters*. 2002;58: 851–856. https://doi.org/10.1209/epl/i2002-00452-6

10. Bolzan A. A., Fong C., Kennedy B. J., Howard C. J. Structural studies of rutile-type metal dioxides. *Acta Crystallographica*. 1997;B53: 373–380. https://doi.org/10.1107/S0108768197001468

11. O'Hara A., Nunley T. N., Posadas A. B., Zollner S., Demkov A. A. Electronic and optical properties of NbO_2. *Journal of Applied Physics*. 2014;116: 213705. https://doi.org/10.1063/1.4903067

12. Jiang N., Spence J. C. H. Electron energy-loss spectroscopy of the O K edge of NbO_2, MoO_2, and WO_2. *Physical Review B*. 2004;70: 245117. https://doi.org/10.1103/PhysRevB.70.245117

13. Blaha P., Schwarz K., Tran F., Laskowski R., Madsen G.K.H., Marks L.D. WIEN2k: An APW+lo program for calculating the properties of solids. *The Journal of Chemical Physics*. 2020;152: 074101. https://doi.org/10.1063/1.5143061

14. Perdew J. P., Burke K., Ernzerhof M. Generalized gradient approximation made simple. *Physical Review Letters*. 1996;77: 3865-3868. https://doi.org/10.1103/PhysRevLett.77.3865

15. Manyakin M. D., Kurganskii S. I. Electronic structure of germanium dioxide with rutile structure according to ab initio computer simulation data. *Condensed Matter and Interphases*. 2023;25(4): 587–593. https://doi.org/10.17308/kcmf.2023.25/11478

16. Manyakin M. D., Kurganskii S. I. Electronic structure of stishovite SiO_2. *Journal of Physics: Conference Series*. 2019;1352: 012032. https://doi.org/10.1088/1742-6596/1352/1/012032

17. Turishchev S., Schleusener A., Chuvenkova O., ... Sivakov V. Spectromicroscopy studies of silicon nanowires array covered by tin oxide layers. *Small*. 2023;19(10): 2206322. https://doi.org/10.1002/smll.202206322

18. https://www.sigmaaldrich.com/RU/en

19. Lebedev A. M., Menshikov K. A., Nazin V. G., Stankevich V. G., Tsetlin M. B., Chumakov R. G. NanoPES photoelectron beamline of the Kurchatov synchrotron radiation source. *Journal of Surface Investigation: X-ray, Synchrotron and Neutron Techniques*. 2021;15(5): 1039–1044. https://doi.org/10.1134/S1027451021050335

20. Moulder J. F., Stickle W. F., Sobol P. E., Bomben K. D. *Handbook of X-ray photoelectron spectroscopy. Physical Electronics Division*. Eden Prairie, Minnesota: Perkin-Elmer Corporation; 1992. 261 p.

21. Crist B. V. *Handbook of Mmonochromatic XPS Spectra: the elements of native oxides*. Mountain View: Wiley; 2000. 500 p.

22. Xu J. H., Jarlborg T., Freeman A. J. Self-consistent band structure of the rutile dioxides NbO_2, RuO_2, and IrO_2. *Physical Review B*. 1989;40: 7939–7949. https://doi.org/10.1103/PhysRevB.40.7939

23. Frati F., Hunault M. O. J. Y., de Groot F. M. F. Oxygen K-edge X-ray absorption spectra. *Chemical Reviews*. 2020;120(9): 4056–4110. https://doi.org/10.1021/acs.chemrev.9b00439

24. Kuznetsov M. V., Razinkin A. S., Shalaeva E. V. Photoelectron spectroscopy and diffraction of surface nanoscale NbO/Nb(110) structures. *Journal of Structural Chemistry*. 2009;(50): 514–521. https://doi.org/10.1007/s10947-009-0079-y

25. Beatham N., Orchard A. F. X-ray and UV photoelectron spectra of the oxides NbO_2, MoO_2 and RuO_2. *Journal of Electron Spectroscopy and Related Phenomena*. 1979;16: 77–86. https://doi.org/10.1016/0368-2048(79)85006-9

26. Fujiwara K., Tsukazaki A. Formation of distorted rutile-type NbO_2, MoO_2, and WO_2 films by reactive sputtering. *Journal of Applied Physics*. 2019;125: 085301. https://doi.org/10.1063/1.5079719

27. Wahila M. J., Paez G., Singh C. N., ... Piper L. F. J. Evidence of a second-order Peierls-driven metal-insulator transition in crystalline NbO_2. *Physical Review Materials*. 2019;3: 074602. https://doi.org/10.1103/PhysRevMaterials.3.074602

28. Berman S., Zhussupbekova A., Boschker J. E., ... Zhussupbekov K. Reconciling the theoretical and experimental electronic structure of NbO_2. *Physical Review B*. 2023;108: 155141. https://doi.org/10.1103/PhysRevB.108.155141

29. Arnold A., Tao R., Klie R. F. Comparison of FEFF9 results of metallic niobium and niobium oxides to EELS. *Journal of Undergraduate Research*. 2012;5(1): 38–41. https://doi.org/10.5210/JUR.V5I1.7508

30. Bach D., Schneider R., Gerthsen D., Verbeeck J., Sigle W. EELS of niobium and stoichiometric niobium-oxide phases – part I: plasmon and near-edges fine structure. *Microscopy and Microanalysis*. 2009;15(6): 505–523. https://doi.org/10.1017/S143192760999105X

31. Liang Y., Vinson J., Pemmaraju S., Drisdell W. S., Shirley E. L., Prendergast D. Accurate X-ray spectral predictions: an advanced self-consistent-field approach inspired by many-body perturbation theory. *Physical Review Letters*. 2017;118: 096402. https://doi.org/10.1103/physrevlett.118.096402

32. Sahiner M. A., Nabizadeh A., Rivella D., Cerqueira L., Hachlica J., Morea R., Gonzalo J., Woicik J. C. Subtle local structural variations in oxygen deficient niobium germanate thin film glasses as revealed by x-ray absorption spectroscopy. *Journal of Physics: Conference Series*. 2016;712: 012103. https://doi.org/10.1088/1742-6596/712/1/012103

Information about the authors

Maxim D. Manyakin, Cand. Sci. (Phys.-Math.), Researcher, Joint Scientific and Educational Laboratory “Atomic and Electronic Structure of Functional Materials” of Voronezh State University and the National Research Center «Kurchatov institute», Voronezh State University (Voronezh, Russian Federation).

https://orcid.org/0000-0003-2260-6233
manyakin@phys.vsu.ru

Sergey I. Kurganskii, Dr. Sci. (Phys.-Math.), Professor of the Solid State Physics and Nanostructure Department, Voronezh State University (Voronezh, Russian Federation).

kurganskii@phys.vsu.ru

Iuliia S. Kakuliia, Teacher of General Physics Department, Voronezh State University (Voronezh, Russian Federation).

https://orcid.org/0000-0002-0953-9024
kakuliia@phys.vsu.ru

Sofiia S. Titova, Teacher of General Physics Department, Voronezh State University, (Voronezh, Russian Federation).

https://orcid.org/0000-0001-6860-401X
titova@phys.vsu.ru

Olga A. Chuvenkova, Cand. Sci. (Phys.-Math.), Senior Researcher, Joint Scientific and Educational Laboratory «Atomic and Electronic Structure of Functional Materials» of Voronezh State University and the National Research Center «Kurchatov Institute», Voronezh State University (Voronezh, Russian Federation).

https://orcid.org/0000-0001-5701-6909
chuvenkova@phys.vsu.ru

Sergey Yu. Turishchev, Dr. Sci. (Phys.-Math.), Associate Professor, Head of the General Physics Department, Voronezh State University (Voronezh, Russian Federation).

https://orcid.org/0000-0003-3320-1979
tsu@phys.vsu.ru

Received 02.04.2024; approved after reviewing 23.04.2024; accepted for publication 08.05.2024; published online 25.03.2025.

Translated by Sergey Turishchev

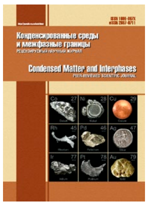

ISSN 1606-867X (Print)
ISSN 2687-0711 (Online)
Condensed Matter and Interphases
Kondensirovannye Sredy i Mezhfaznye Granitsy
https://journals.vsu.ru/kcmf/

Short communication

Short communication
https://doi.org/10.17308/kcmf.2025.27/12493

Monte Carlo simulation of interfacial adhesion between geopolymer binders and mineral aggregates

Y. M. Ermolov[1], **A. A. Vasilchenko**[2]✉, **V. B. Mischinenko**[2]

[1]Platov South-Russian State Polytechnic University (NPI),
132 Prosveshcheniya st., Novocherkassk 346428, Russian Federation

[2]Rostov State Transport University,
2 Rostovskogo Strelkovogo Polka Narodnogo Opolcheniya sq., Rostov-on-Don 344038, Russian Federation

Abstract

Silico-aluminophosphate and alkali-aluminosilicate geopolymers are increasingly popular as a green alternative to traditional Portland cement concrete used in the construction industry. In geopolymer concretes and mortars, the aggregate-matrix interface plays a major role in the fracture mechanisms. The adhesion strength between the mineral aggregate and the geopolymer matrix is mainly determined by the chemical nature of the components of the aggregate-geopolymer interface. However, this aspect remains insufficiently studied. Therefore, we used a Monte Carlo simulation to investigate adhesive behavior and interfacial interaction mechanisms of a cyclic aluminosilicate oligomer forming the structure of a geopolymer gel with mineral aggregates.

The study determined the low-energy equilibrium configurations of the structure of oligomers adsorbed on the surface of quartz, calcite, albite, and microcline, as well as the adsorption energies.

Keywords: Geopolymer, Interfacial adhesion, Mineral aggregate, Quartz, Calcite, Albite, Microcline, Monte Carlo method

Funding: The study was supported by the Russian Science Foundation grant No. 19-79-10266, https://rscf.ru/project/19-79-10266/.

For citation: Ermolov Y. M., Vasilchenko A. A., Mischinenko V. B. Monte Carlo simulation of interfacial adhesion between geopolymer binders and mineral aggregates. *Condensed Matter and Interphases*. 2025;27(1): 154–159. https://doi.org/10.17308/kcmf.2025.27/12493

Для цитирования: Ермолов Я. М., Васильченко А. А., Мищиненко В. Б. Моделирование межфазной адгезии между геополимерным вяжущим и минеральными заполнителями методом Монте-Карло. *Конденсированные среды и межфазные границы*. 2025;27(1): 154–159. https://doi.org/10.17308/kcmf.2025.27/12493

✉ Andrey M. Vasilchenko, e-mail: zmandr@mail.ru

© Ermolov Y. M., Vasilchenko A. A., Mischinenko V.B., 2025

The content is available under Creative Commons Attribution 4.0 License.

1. **Introduction**

Over the past few years, silico-alumino-phosphate and alkali-aluminosilicate geopolymers [1] have been considered as a green alternative to traditional Portland cement concrete used in the construction industry [2–4] and as promising binders for a wide range of applications [5, 6]. The adjustable pore microstructure of geopolymers makes them promising materials for thermal, acoustic, and vibration insulation [7–9]. Geopolymers also exhibit effective immobilization properties and can thus be used for the utilization and disposal of radioactive waste [10–12]. Owing to their strong bonding properties, geopolymers can also be used as repair binders for concrete and reinforced concrete structures [13, 14].

In geopolymer concretes and mortars, the aggregate-matrix interface plays a major role in the fracture mechanisms and hence determines the mechanical properties of the aggregate. The properties of the interface affect the process of deformation of geopolymer materials, which typically deteriorate within the interfacial layer. A weak interfacial adhesion between geopolymer binders and mineral aggregates often results in inferior mechanical properties [15]. The adhesion strength between the mineral aggregate and the geopolymer matrix is determined by frictional forces at the aggregate-geopolymer interface and the chemical nature of these components. The impact of the latter factor on the final adhesion strength is more significant. However, this aspect remains insufficiently studied.

In our study, we used a Monte Carlo simulation to investigate the adhesive behavior and the mechanism of interfacial interaction between a cyclic aluminosilicate oligomer forming the structure of a geopolymer gel and characteristic minerals in the structure of an inorganic aggregate (α-SiO_2, β-SiO_2, calcite, albite, and microcline). The article presents low-energy equilibrium configurations of the aluminosilicate oligomer on the surface of the considered minerals and the results of a comparative analysis of adsorption energies.

2. Experimental

To study the interfacial interaction between the geopolymer obtained by means of low-temperature alkali activation of aluminosilicates [16] and mineral aggregates, we used a cyclic aluminosilicate oligomer (CAO) with a ratio of Si/Al = 3 shown in Fig. 1a. The structure of the CAO was optimized using the Dmol3 software package [17]. The calculations were performed by means of exchange-correlation functional approximations using the Perdew–Burke–Ernzerhof (RPBE) functional [18]. The electron density was determined using a double numerical plus polarization (DNP) basis set [19]. In order to account for the van der Waals forces, we used a dispersion-corrected DFT (DFT-D) suggested by Grimme [20, 21].

The following surfaces were used for the simulation of the adsorption behavior of the CAO: (100) quartz (α-SiO_2) [22]; (100) quartz (β-SiO_2) [23], (010) calcite ($CaCO_3$) [24], (100) albite

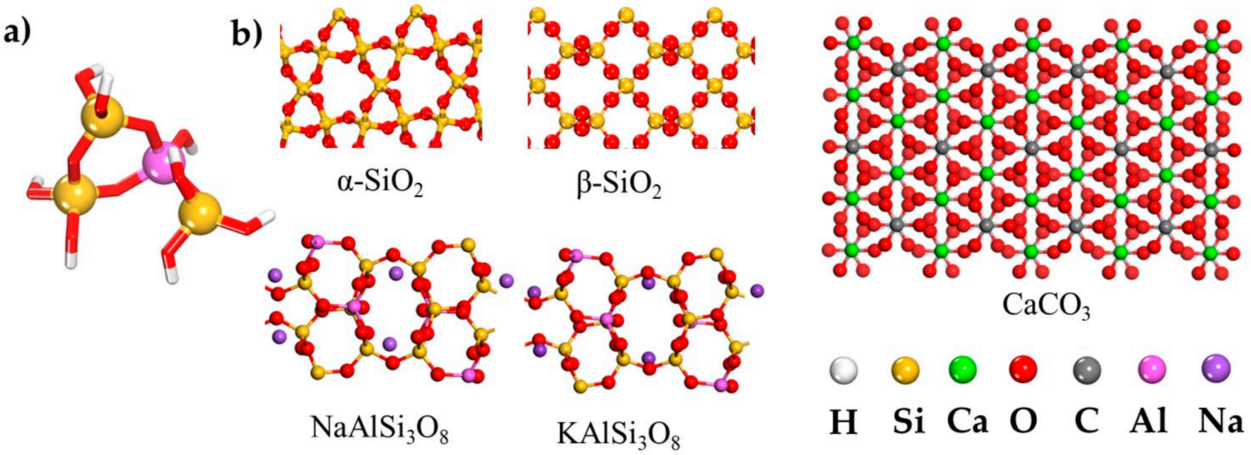

Fig. 1. (a) model of a ring-type aluminosilicate oligomer defining the structure of the N-A-S-H geopolymer gel; (b) surface models: (100) α-SiO_2; (100) β-SiO_2; (010) $CaCO_3$; (100) $NaAlSi_3O_8$; (100) $KAlSi_3O_8$

($NaAlSi_3O_8$) [25], and (100) microcline ($KAlSi_3O_8$) [26] shown in Fig. 1b. In order to eliminated the effect of the atomic layers associated with periodic boundary conditions when simulating a mineral surface, we used a 40 Å vacuum layer. The simulation was performed by means of the Monte Carlo technique in a gas phase using the Adsorption Locator software unit [17]. The calculations were based on the Metropolis–Hastings algorithm and involved simulated annealing with 20 measurement cycles at different temperatures and 2×10^5 steps for each cycle [27]. The energies were calculated using the COMPASS force field [28]. The van der Waals energy was calculated using the atomic method. The cut-off distance of the Lennard-Jones potential was 14 Å. The electrostatic interaction was described using the Ewald summation technique [29].

3. Results and discussion

The interfacial adhesion between the geopolymer binder and the aggregate was assessed based on the results of the Monte Carlo simulation of the adsorption of the cyclic aluminosilicate oligomer on the analyzed surfaces. In our study, we determined the most stable adsorption configurations of the CAO and its adsorption energies.

The adsorption energy (E_{ads}) was determined using the formula:

$$E_{ads} = E_{Total} - (E_{Adsorbate} + E_{Surface}),$$

where E_{ads} is the energy of the mineral surface-adsorbate configuration, $E_{Adsorbate}$ and $E_{Surface}$ are energies of the CAO and the mineral surface respectively.

The low-energy equilibrium configurations of the structure of the CAO adsorbed on mineral surfaces (α-SiO_2, β-SiO_2, $CaCO_3$, $NaAlSi_3O_8$, $KAlSi_3O_8$) determined as a result of the Monte Carlo simulation are demonstrated in Fig. 2. We can see that as a result of the adsorption, the CAO is oriented parallel to the mineral surface. This spatial conformation of the CAO allows for maximum number of interactions with the mineral surface. To determine the main types of interactions between the adsorbate and the mineral surface, we performed an analysis of bond lengths. The shortest distances between the atoms of the mineral surface and the nearest aluminum and silicon atoms of the adsorbed oligomer in the equilibrium state are given in Table 1. The distances were calculated based on the difference in the Cartesian coordinates. To calculate the number of bonds between the surface oxygen atoms and the hydroxyl groups of the oligomer, we used a geometric criterion, according to which the distance between the atoms forming the hydrogen bond cannot be more than 2.45 Å [30]. In our study, practically all the shortest bonds were less than 2.5 Å, which indicates the formation of a strong bond between chemisorbed oligomers and the mineral surface.

Fig. 3 presents the calculated E_{ads} for all the studied systems. Significantly negative E_{ads} values indicate the strongest and most stable adsorption. Fig. 3 demonstrates that the absolute values of the adsorption energy of the CAO on the studied

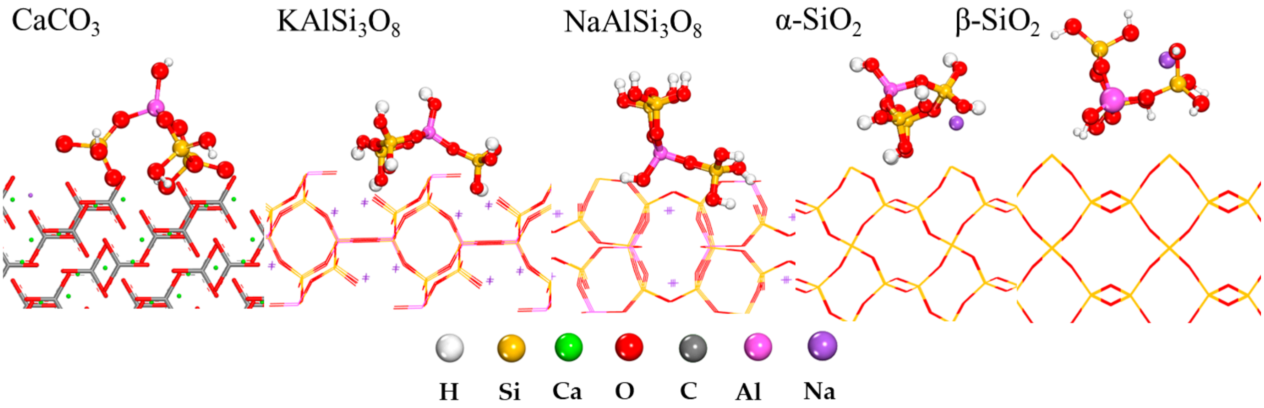

Fig. 2. Most stable low-energy configurations calculated by MC simulations for the adsorption of oligomer on the mineral surfaces of aggregate

Table 1. The distance (Å) between the layer of near-surface atoms and the atoms of the oligomer, as well as the number of bonds formed, calculated by the Monte Carlo method

Mineral aggregate	Al	Si	Si	Si	Number of bonds
$CaCO_3$	3.22	5.72	3.36	3.09	5
$KAlSi_3O_8$	2.78	1.99	2.52	4.83	4
$NaAlSi_3O_8$	5.07	2.04	5.32	5.67	3
α-SiO_2	3.89	1.49	6.61	2.97	2
β-SiO_2	2.52	4.31	2.05	4.31	2

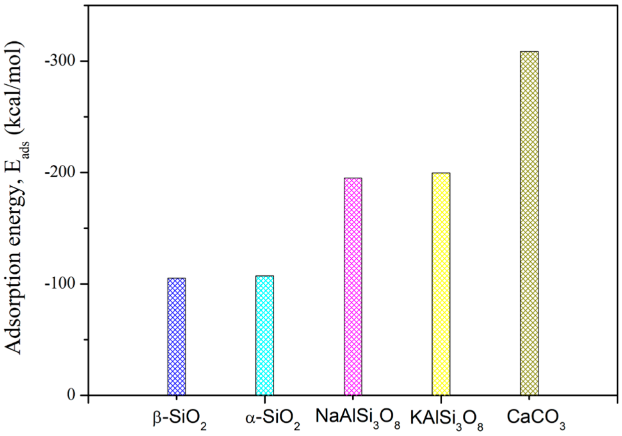

Fig. 3. Adsorption energies obtained from Monte Carlo simulations for oligomer adsorption on the surface of mineral aggregates in the gas phase

mineral surfaces decrease in the following order: $CaCO_3$ > $KAlSi_3O_8$ > $NaAlSi_3O_8$ > α-SiO_2> β-SiO_2. This tendency correlates well with the number of formed OH-bonds (Table 1). The calculated E_{ads} demonstrated that the best adhesion is observed during the interaction of the CAO with calcite, which is confirmed by the experimental data presented in [31, 32].

4. Conclusions

This study presents Monte Carlo simulation results investigating the adhesive behavior and the mechanism of interfacial bonding of a cyclic aluminosilicate oligomer and mineral aggregates. The study determined low-energy equilibrium configurations of the structure of oligomers adsorbed on the surface of (100) α-SiO_2, (100) β-SiO_2, (010) $CaCO_3$, (100) $NaAlSi_3O_8$, (100) $KAlSi_3O_8$, as well as the adsorption energies. The simulation demonstrated that cyclic aluminosilicate oligomers can be chemisorbed. The absolute values of the adsorption energy of the aluminosilicate oligomer on the studied surfaces are characterized by the following sequence: $CaCO_3$ > $KAlSi_3O_8$ > $NaAlSi_3O_8$ > α-SiO_2> β-SiO_2. This result is in good agreement with the number of the OH-bonds formed between the aluminosilicate oligomer and the mineral surface. The best adhesion effect was observed for calcite.

Contribution of the authors

The authors contributed equally to this article.

Conflict of interests

The authors declare that they have no known competing financial interests or personal relationships that could have influenced the work reported in this paper.

References

1. Davidovits J. Geopolymers: ceramic-like inorganic polymers. *Journal of Ceramic Science and Technology*. 2017;8(3): 335–350. https://doi.org/10.4416/JCST2017-00038

2. Jwaida Z., Dulaimi A., Mashaan N., Othuman Mydin M. A. Geopolymers. The green alternative to traditional materials for engineering applications. *Infrastructures*. 2023;8(6): 98. https://doi.org/10.3390/infrastructures8060098

3. Ansari M. A., Shariq M., Mahdi F. Geopolymer concrete for clean and sustainable construction – a state-of-the-art review on the mix design approaches. *Structures*. 2023;55: 1045–1070. https://doi.org/10.1016/j.istruc.2023.06.089

4. Martínez A., Miller S. A. A review of drivers for implementing geopolymers in construction: codes and constructability. *Resources, Conservation and Recycling*. 2023;199: 107238. https://doi.org/10.1016/j.resconrec.2023.107238

5. Manzoor T., Bhat J. A., Shah A. H. Performance of geopolymer concrete at elevated temperature – a critical review. *Construction and Building Materials*. 2024;420: 135578. https://doi.org/10.1016/j.conbuildmat.2024.135578

6. Goryunova K., Gahramanli Y., Muradkhanli V., Nadirov P. Phosphate-activated geopolymers: advantages and application. *RSC Advances*. 2023;13(43): 30329–30345. https://doi.org/10.1039/d3ra05131e

7. Matalkah F., Ababneh A., Aqel R. Synthesis of calcined kaolin-based geopolymer foam: assessment of mechanical properties, thermal insulation, and elevated temperature stability. *Ceramics International*. 2023;49(6): 9967–9977. https://doi.org/10.1016/j.ceramint.2022.11.174

8. Liu X., Hu C., Chu L. Microstructure, compressive strength and sound insulation property of fly ash-based geopolymeric foams with silica fume as foaming agen. *Materials*. 2020;13(14): 3215. https://doi.org/10.3390/ma13143215

9. Ettahiri Y., Bouargane B., Fritah K., ... Novais R. M. A state-of-the-art review of recent advances in porous geopolymer: applications in adsorption of inorganic and organic contaminants in water. *Construction and Building Materials*. 2023;395: 132269. https://doi.org/10.1016/j.conbuildmat.2023.132269

10. Liu J., Xu Y., Zhang W., Ye J., Wang R. Solidification performance and mechanism of typical radioactive nuclear waste by geopolymers and geopolymer ceramics: a review. *Progress in Nuclear Energy*. 2024;169: 105106. https://doi.org/10.1016/j.pnucene.2024.105106

11. Kasprzhitskii A., Ermolov Y., Mischinenko V., Vasilchenko A., Yatsenko E. A., Smoliy V. A. Mechanism of Cs immobilization within a sodalite framework: the role of alkaline cations and the Si/Al Ratio. *International Journal of Molecular Sciences*. 2023;24(23): 17023. https://doi.org/10.3390/ijms242317023

12. Zhu Y., Zheng Z., Deng Y., Shi C., Zhang Z. Advances in immobilization of radionuclide wastes by alkali activated cement and related materials. *Cement and Concrete Composites*. 2022;126: 104377. https://doi.org/10.1016/j.cemconcomp.2021.104377

13. Wang Y. S., Peng K. D., Alrefaei Y., Dai J. G. The bond between geopolymer repair mortars and OPC concrete substrate: Strength and microscopic interactions. *Cement and Concrete Composites*. 2021;119: 103991. https://doi.org/10.1016/j.cemconcomp.2021.103991

14. Tan J., Dan H., Ma Z. Metakaolin based geopolymer mortar as concrete repairs: Bond strength and degradation when subjected to aggressive environments. *Ceramics International*. 2022;48(16): 23559–23570. https://doi.org/10.1016/j.ceramint.2022.05.004

15. Xu F., Chen G., Li K., ... Zhang X. Interfacial bond behavior between normal OPC concrete and self-compacting geopolymer concrete enhanced by nano-SiO_2. *Construction and Building Materials*. 2024;411: 134617. https://doi.org/10.1016/j.conbuildmat.2023.134617

16. Guan X., Jiang L., Fan D., Garcia Hernandez, A., Li B., Do H. Molecular simulations of the structure-property relationships of N-A-S-H gels. *Construction and Building Materials*. 2022;329: 127166. https://doi.org/10.1016/j.conbuildmat.2022.127166

17. BIOVIA, Dassault Systemes, Materials Studio, 2020, San Diego: Dassault Systemes, 2020.

18. Perdew J. P., Burke K., Ernzerhof M. Generalized gradient approximation made simple. *Physical Review Letters*. 1996;77: 3865–3868. https://doi.org/10.1103/PhysRevLett.77.3865

19. Inada Y., Orita H. Efficiency of numerical basis sets for predicting the binding energies of hydrogen bonded complexes: evidence of small basis set superposition error compared to Gaussian basis sets. *Journal of Computational Chemistry*. 2008;29(2): 225–232. https://doi.org/10.1002/jcc.20782

20. Wu X., Vargas M. C., Nayak S. Towards extending the applicability of density functional theory to weakly bound systems. *Chemical Physics*. 2001;115(19): 8748–8757. https://doi.org/10.1063/1.1412004

21. Grimme, S. Semiempirical GGA-type density functional constructed with a long-range dispersion correction. *Journal of Computational Chemistry*. 2006;27(15): 1787–1799. https://doi.org/10.1002/jcc.20495

22. Lombard C. J., van Sittert C. G. C. E., Mugo J. N., Perry C., Willock D. J. Computational investigation of α-SiO_2 surfaces as a support for Pd. *Physical Chemistry Chemical Physics*. 2023;25 (8): 6121–6130. https://doi.org/10.1039/d2cp04722e

23. Wang C., Guo X., Wang H. Elastic, electronic and thermodynamic properties of β-SiO_2 doped by Ar: a first-principles investigation. *Materials Today Communications*. 2023;36: 106610. DOI: 10.1016/j.mtcomm.2023.106610

24. Graf D. L. Crystallographic tables for the rhombohedral carbonates Locality: synthetic. *American Mineralogist*. 1961;46: 1283–1316.

25. Harlow G. E., Brown G. E. Low albite: an X-Ray and neutron diffraction study. *American Mineralogist*. 1980;65: 986–995.

26. Bailey S. W. Refinement of an intermediate microcline structure. *American Mineralogist*. 1969;54: 1540–1545.

27. Metropolis N., Rosenbluth A. W., Rosenbluth M. N., Teller A. H, Teller E. Equation of state calculations by fast computing machines. *Chemical Physics*. 1953;21(6): 1087–1092. https://doi.org/10.1063/1.1699114

28. Sun H. Compass: an ab initio force-field optimized for condensed-phase applications - Overview with details on alkane and benzene compounds. *The Journal of Physical Chemistry B*. 1998;102(38): 7338–7364. https://doi.org/10.1021/jp980939v

29. Yeh I. C., Berkowitz M. L. Ewald summation for systems with slab geometry. *Chemical Physics*. 1999;111(7): 3155–3162. https://doi.org/10.1063/1.479595

30. Luzar A., Chandler D., Structure and hydrogen bond dynamics of water-dimethyl sulfoxide mixtures by computer simulations. *The Journal of Chemical Physics*. 1993;98: 8160–8173. https://doi.org/10.1063/1.464521

31. Chindaprasirt, P., Rattanasak, U. Calcium wastes as an additive for a low calcium fly ash geopolymer. *Scientific Reports*. 2023;13(1): 16351. https://doi.org/10.1038/s41598-023-43586-w

32. Yip C. K., Provis J. L., Lukey G. C., van Deventer J. S. J. Carbonate mineral addition to metakaolin-based geopolymers. *Cement and Concrete Composites*. 2008;30(10): 979-985. https://doi.org/10.1016/j.cemconcomp.2008.07.004

Information about the authors

Yakov M. Ermolov, Cand. Sci. (Tech.), Engineer of the Fuel Energy Waste Recycling Laboratory, Platov South-Russian State Polytechnic University (Novocherkassk, Russian Federation).

https://orcid.org/0000-0002-2065-6168
mr.yak.erm@gmail.com

Andrey A. Vasilchenko, Head of the Research Testing Laboratory "Testing and monitoring in civil and transport construction", Rostov State Transport University (Rostov-on-Don, Russian Federation).

https://orcid.org/0000-0001-6336-4379
zmandr@mail.ru

Vasily B. Mischinenko, Assistant at the Department of Transport Machines and Tribotechnics, Rostov State Transport University (Rostov-on-Don, Russian Federation).

https://orcid.org/ 0000-0002-9799-0519
m.vasbor@bk.ru

Received 02.04.2024; approved after reviewing 03.05.2024; accepted for publication 15.05.2024; published online 25.03.2025.

Translated by Yulia Dymant

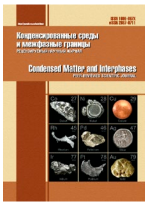

ISSN 1606-867X (Print)
ISSN 2687-0711 (Online)
Condensed Matter and Interphases
Kondensirovannye Sredy i Mezhfaznye Granitsy
https://journals.vsu.ru/kcmf/

Guide for Authors – 2025

Manuscripts should be submitted as single **Microsoft Word 2003** files.

Preferred font 12 pt Times New Roman (please, do not use any other fonts, except for Symbol), 1.5 spaced lines, 1.25 cm first-line indent. Decimal values (e.g. 0.1; 0.9; 2.3) should be written using a decimal point.

Review/Research article/Short communication
https://doi.org/10.17308/kcmf.2025.27/000

Modelling of interdiffusion and phase formation in thin-film two-layer systems of polycrystalline oxides of titanium and cobalt

(All proper nouns should be capitalized; titles and subtitles should be left-aligned)

N. N. Afonin[1]✉, V.A. Logacheva[2]

[1]Voronezh State Pedagogical University,
86 ul. Lenina, Voronezh 394043, Russian Federation
(Official name and address of the organisation)
[2]Voronezh State University,
1 Universitetskaya pl., Voronezh 394018, Russian Federation

Abstract
The abstract should be 200-250 words and include the following sections.

Purpose: States the problem considered in the article, its importance, and the purpose of the research.

Experimental: Provides information about the objects being studied and the methods used.

Conclusions: Provides a brief description of the principal results, major conclusions, and their scientific and practical relevance.

Keywords: Please, provide 5-10 keywords for the principal concepts, results, and terms used in the article.

Funding: The study was funded by the Russian Science Foundation, research project No.

Acknowledgments: The DTATGA, XRD and SEM studies were performed on the equipment of the Engineering Center of Saint Petersburg State Institute of Technology.

For citation: Afonin N. N., Logacheva V. A. Modelling of interdiffusion and phase formation in the thin-film two-layer system of polycrystalline oxides of titanium and cobalt. *Condensed Matter and Interphases.* 2025;27(1): 000-000. https://doi.org/10.17308/kcmf.2025.27/000

✉ Nikolay N. Afonin, e-mail: nafonin@vspu.ac
© Afonin N. N., Logacheva V. A., 2025
The content is available under the Creative Commons Attribution 4.0 License.

ARTICLE STRUCTURE (IMRAD)

1. Introduction

The introduction (1–2 pages) states the problem under consideration, its relevance, and the most important tasks that need to be resolved. Describe the scientific problems which have not yet been solved and which you sought to solve in your research. The introduction should contain a short critical review of previously published works in this field and their comparative analysis. It is recommended that the analysis is based on 20–30 studies (no more than 20% of references to the author's own works, at least 50% of the references should be to articles published within the previous 5 years). **The purpose** of the article is indicated by the problem statement.

The Vancouver reference style is used in the journal: bibliographic references in the text of the article are indicated by numbers in square brackets; in the references section, the references are numbered in the order they are mentioned in the text.

Example of references in-text citations:

Single crystals of difluorides of alkaline earth elements are widely used as photonics materials [1–3] as well as matrices for doping with rare-earth ions [4,10].

References should primarily be made to original articles published in scientific journals indexed by global citation databases. References should indicate the names of all authors, the title of the article, the name of the journal, year of publication, volume (issue), number, pages, and DOI (Digital Object Identifier https://search.crossref.org/). If a DOI is lacking, a link to the online source of the article must be indicated. References to dissertation abstracts are acceptable if the texts are available online. It is vital that our readers can find any of the articles or other sources listed in the reference section as fast as possible. Links to unpublished literature sources or sources not available online are unacceptable.

2. Experimental

The experimental section (2-3 pages) provides the details of the experiment, the methods, and the equipment used. The object of the study and the stages of the experiment are described in detail and the choice of research methods is explained.

3. Results and discussion

Results and discussion (6-8 pages) should be brief, but detailed enough for the readers to assess the conclusions made. It should also explain the choice of the data being analysed. Measurement units on graphs and diagrams should be separated with a coma. **Formulae should be typed using Microsoft Office Equation 3 or Math Type** and aligned on the left side. Latin letters should be in italics. Do not use italics for Greek letters, numbers, chemical symbols, and similarity criteria.

All subheadings should be in italics.

Example:

1.1. *X-ray diffraction analysis*

Example of figure captions in the text of the article: Fig. 1, curve *1*, Fig. 2b.

A complete list of figures should be provided at the end of the paper after the information about the authors.

Figures and tables should not be included in the text of the article. They should be placed on a separate page. Figures should also be **submitted as separate** *tif, *jpg, *cdr, or *ai. files. **All figures should have a minimum resolution of 300 dpi.** Name each figure file with the name of the first author and the number of the figure.

4. Conclusions

Conclusions (1 paragraph) should briefly state the main conclusions of the research. Do not repeat the text of the article. The obtained results are to be considered with respect to the purpose of the research. This section includes the conclusions, a summary of the results, and recommendations. It states the practical value of the research and outlines further research problems in the corresponding field.

Contribution of the authors

At the end of the Conclusions the authors should include notes that explain the actual contribution of each co-author to the work.

Example 1:

Nikolay N. Afonin – Scientific management, Research concept, Methodology development, Writing – original draft, Final conclusions.

Vera A. Logachova – Investigation, Writing – review & editing.

Example 2:

The authors contributed equally to this article.

Conflict of interests

The authors declare that they have no known competing financial interests or personal relationships that could have influenced the work reported in this paper.

References

(The references are to be formatted according to the Vancouver Style. The reference list should only include articles published in peer-reviewed journals)

Examples:

Journal article

1. Bahadur A., Hussain W., Iqbal S., Ullah F., Shoaib M., Liu G., Feng K. A morphology controlled surface sulfurized CoMn$_2$O$_4$ microspike electroncatalyst for water splitting with excellent OER rate for binder-free electrocatalytic oxygen evolution. *Journal of Materials Chemistry A*. 2021;20(9): 12255–12264. https://doi.org/10.1039/D0TA09430G

2. Alexandrov A. A., Mayakova M. N., Voronov V. V., Pominova D. V., Kuznetsov S. V., Baranchikov A. E., Ivanov V. K., Fedorov P. P. Synthesis upconversion luminophores based on calcium fluoride. *Condensed Matter and Interphases*. 2020;22(1): 3–10. https://doi.org/10.17308/kcmf.2020.22/2524

3. Kopeychenko E. I., Mittova I. Y., Perov N. S., Alekhina Y. A., Nguyen A. T., Mittova V. O., Pham V. Synthesis, composition and magnetic properties of cadmium-doped lanthanum ferrite nanopowders. *Inorganic Materials*. 2021;57(4): 367–371. https://doi.org/10.1134/S0020168521040075

Book: print

4. Nakamoto K. *Infrared and Raman spectra of inorganic and coordination compounds*. New York: John Wiley; 1986. 479 p.

5. Fedorov P. P., Osiko V. V. Crystal growth of fluorides. In: *Bulk Crystal Growth of Electronic. Optical and Optoelectronic Materials*. P. Capper (ed.). Wiley Series in Materials for Electronic and Optoelectronic Applications. John Wiley & Son. Ltd.; 2005. pp. 339-356. https://doi.org/10.1002/9780470012086.ch11

6. *Nanostructured oxide materials in modern micro-, nano- and optoelectronics*. V. A. Moshnikov, O. A. Aleksandrova (eds.). Saint Petersburg: Izd-vo SPbGETU “LETI” Publ., 2017. 266 p. (in Russ.)

Conference proceeding: individual paper

7. Afonin N. N., Logacheva V. A., Khoviv A. M. Synthesis and properties of functional nanocrystalline thin-film systems based on complex iron and titanium oxides. In: *Amorphous and microcrystalline semiconductors: Proc. 9th Int. Conf., 7–10 July 2014*. St. Petersburg: Polytechnic University Publ.; 2014. p. 356–357. (In Russ.)

Website

8. NIST Standard Reference Database 71. *NIST Electron Inelastic-Mean-Free-Path Database: Version 1.2.* Available at: www.nist.gov/srd/nist-standard-reference-database-71

Patent

9. Chekanov V. V., Kandaurova N. V., Rakhmanina Yu. A., Chekanov V. S. *Ultrasound indicator 2*. Patent RF, no. 2446384, 2012. Publ. 27.03.2012, bull. no. 9. (In Russ.)

Information about the authors

This section should include the full last and first name(s) of the author(s), their academic degree, academic title, affiliation, position, city, country. ORCID (register for an ORCID here https://orcid.org/register) and e-mail.

Nikolay N. Afonin, Dr. Sci. (Chem.), Research Fellow, Professor at the Department of Science and Technology Studies, Voronezh State Pedagogical University (Voronezh, Russian Federation).
https://orcid.org/0000-0002-9163-744X
nafonin@vspu.ac.ru

Vera A. Logachova, Cand. Sci. (Chem.), Research Fellow at the Department of General and Inorganic Chemistry, Voronezh State University (Voronezh, Russian Federation).
https://orcid.org/0000-0002-2296-8069
kcmf@main.vsu.ru

Tien Dai Nguyen, PhD in Advanced Materials Science and Engineering, Lecturer/ Research at Institute of Theoretical and Applied Research (ITAR), Duy Tan University (DTU), Hanoi, Vietnam.
https://orcid.org/0000-0002-9420-210X
nguyentiendai@duytan.edu.vn

Valery V. Voronov, Cand. Sci. (Phys.–Math.), Head of the Laboratory, Prokhorov General Physics Institute of the Russian Academy of Science (Moscow, Russian Federation).
https://orcid.org/0000-0001-5029-8560
voronov@lst.gpi.ru

Received __.__.2025; approved after reviewing __.__.2025; accepted for publication __.__.2025; published online __.__.2025.

A complete list of figures should be provided at the end of the paper after the information about the authors.

Example:

Fig. 1. Dependences of the parameters *a* and *c* of the tetragonal lattice of nanocrystalline PdO films on the oxidation temperature T_{ox}: *1* – single-phase PdO films, *2* – heterophase PdO + Pd films; *3* – data of the ASTM standard [22, 23]

Table 1. The values of relative electronegativity (ENE) of some chemical elements [30] and the proportion of the ionic component of the chemical bond in binary compounds of the AB composition formed by these elements

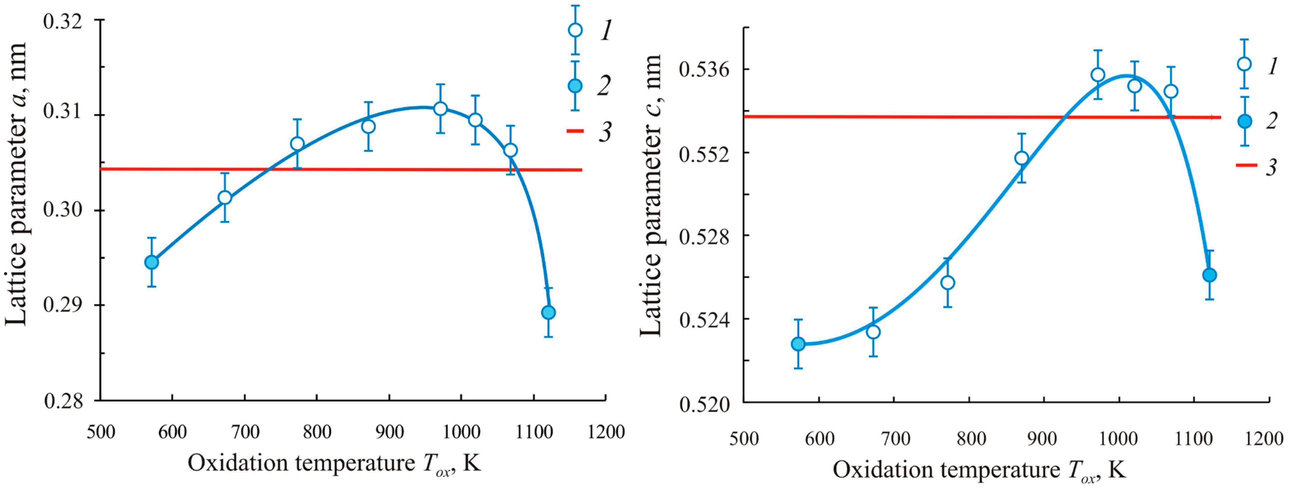

a *b*

Fig. 1. Dependences of the parameters *a* and *c* of the tetragonal lattice of nanocrystalline PdO films on the oxidation temperature T_{ox}: *1* – single-phase PdO films; *2* – heterophase PdO + Pd films; *3* – data of the ASTM standard [22, 23]

Table 1. Values of the ionic radii of palladium Pd^{2+} and oxygen O^{2-} [30–32]

Ion	Coordination number CN	Coordination polyhedron	Values of ionic radii R_{ion}, nm
Pd^{2+}	4	Square (rectangular)	0.078 [30]; 0.086 [31]; 0.078 [32]
O^{2-}	4	Tetragonal tetrahedron	0.132 [30]; 0.140 [31]; 0.124* [31]; 0.132 [32]

*The values of ionic radius were obtained on the basis of quantum mechanical calculations.

ACCOMPANYING DOCUMENTS

(The following documents should be submitted as PDF files)

1. Covering letter (with authorisation for open access publication)
2. License agreement *(signed by all authors)* https://journals.vsu.ru/kcmf/Licensingcontract
3. Manuscript.

EDITING AND PROOFREADING

When the layout is ready it is sent back to the authors for proofreading. The article should be sent back to the publisher within a maximum of three days. The authors may only correct printing mistakes.